A Metabolism-Wide *E. coli* CRISPRi Library to Screen Antibiotic Susceptibility and Metabolome Responses

Dissertation

der Mathematisch-Naturwissenschaftlichen Fakultät

der Eberhard Karls Universität Tübingen

zur Erlangung des Grades eines

Doktors der Naturwissenschaften

(Dr. rer. nat.)

vorgelegt von

Andreas Verhülsdonk

aus Geldern

Tübingen

2025

Gedruckt mit Genehmigung der Mathematisch-Naturwissenschaftlichen Fakultät der Eberhard Karls Universität Tübingen.

Tag der mündlichen Qualifikation:	24.11.2025
Dekan:	Prof. Dr. Thilo Stehle
1. Berichterstatter/-in:	Prof. Dr. Hannes Link
2. Berichterstatter/-in:	Prof. Dr. Lisa Maier

Table of Contents

Table of Contents

Table of Contents

Table of Contents

Acknowledgements

After nearly a decade of study, this work marks the conclusion of a long and rewarding academic journey. Along the way, I passed through many stations and places, so I am immensely grateful to everyone who supported me, both scientifically and emotionally, enabling me to reach this goal.

First and foremost, I would like to thank **Dominic Winter**, who welcomed me into his group for my bachelor's thesis. He was the first to believe in my scientific abilities, constantly challenging and encouraging me to grow. His infectious passion for science sparked my motivation to pursue a master's degree, making him the catalyst for this entire journey.

My deepest gratitude also goes to my supervisor, **Hannes Link**, for the opportunity to continue working in his lab after its move from Marburg to Tübingen, leading to both my master's thesis and this dissertation. While the flood of good scientific ideas at times exceeded our investigative capacity (keyword: meat grinder), our discussions were always insightful and inspiring. His guidance helped me to develop countless skills and complete my transformation into the scientist I am today.

I'm also thankful for the many amazing colleagues I met along the way, many of whom became close friends. A heartfelt thank you to the **Winter and Link Labs**, who made this journey so memorable. Special thanks to the **MTG group**, who continue to make me laugh (and rage) on a weekly basis.

I'd like to especially acknowledge my lab supervisors, **Michelle Kuntz** and **Alejandra Alverado**, not only for their practical guidance, but also for their patience with my somewhat *unique* sense of humor. I'm also grateful to my students **Amelie, Leo, and Tilmann** for letting me be a part of their scientific growth. Additionally, I am incredibly thankful to our lab technician **Felicia Troßmann**, whose constant support in and around my experiments was invaluable.

My thanks also go to **Prof. Lisa Maier**, **Prof. Andreas Peschel**, and **Prof. Klaus Hantke** for their time, input, and support, as well as to the **IGIM doctoral school** for offering valuable courses to help expand my skill set. A big thank you as well to everyone who helped spot (and correct) the inevitable mistakes in this manuscript.

Finally, I want to thank my family and friends for their unwavering support from afar throughout my time in Rheinbach, Marburg and Tübingen. Your encouragement helped me endure the many ups and downs of this journey.

Danke!

Abstract

Understanding gene function and stress response mechanisms in bacteria requires tools that enable precise and scalable genetic perturbations, coupled with comprehensive phenotypic readouts. In this work, an arrayed CRISPR interference (CRISPRi) library targeting the metabolic genes of *Escherichia coli* was developed and validated to facilitate high-resolution functional genomics. The library was constructed from a pooled resource and quality-controlled to ensure accurate and reproducible gene knockdowns, enabling systematic phenotypic analysis under defined experimental conditions.

The arrayed library was used to explore the impact of metabolic gene knockdowns on antibiotic susceptibility. A focused investigation of fosfomycin responses revealed that repression of specific metabolic genes, including *atpH* and *pykF*, modulates tolerance phenotypes through transcriptional and metabolic shifts. This work was extended to a broader antibiotic stress screen involving ciprofloxacin, gentamicin, rifampicin, and meropenem. Comparative analysis identified both antibiotic-specific and shared tolerance phenotypes, highlighting non-inherited survival strategies.

To support metabolomic applications, a high-throughput sampling workflow was established and optimized for reproducibility, throughput, and compatibility with untargeted mass spectrometry. This protocol was applied in a genome-wide screen using the arrayed CRISPRi library, resulting in the identification of metabolic bottlenecks, buffering mechanisms, and phenotypic consequences of gene repression. Targeted metabolite profiling data integration were used to validate and refine these observations.

Taken together, these findings demonstrate a platform that integrates gene perturbation with multi-omics profiling to investigate bacterial physiology. The arrayed CRISPRi library and associated workflows provide tools to dissect genotype–phenotype relationships and open avenues for applications in antibiotic development, metabolic engineering, and systems biology.

Zusammenfassung

Um die Genfunktion und Stressreaktionsmechanismen in Bakterien besser zu verstehen, sind Werkzeuge erforderlich, die präzise und skalierbare genetische Störungen ermöglichen und gleichzeitig umfassenden phänotypischen Auswertungen erlauben. In dieser Arbeit wurde eine array-basierte CRISPR-Interferenz-(CRISPRi)-Bibliothek entwickelt und validiert, die auf die Stoffwechsel Gene von *Escherichia coli* abzielt, um eine hochauflösende funktionelle Genomik zu ermöglichen. Die Bibliothek wurde aus einer gepoolten Ressource erstellt und mehreren Qualitätskontrollen unterzogen, um einen exakten und reproduzierbaren Gen-Knockdown zu gewährleisten, der eine systematische phänotypische Analyse unter definierten Versuchsbedingungen ermöglicht.

Die Bibliothek wurde genutzt, um den Einfluss von metabolischen Gen-Knockdowns auf die Antibiotikaempfindlichkeit zu untersuchen. Eine gezielte Analyse der Fosfomycin-Reaktionen ergab, dass die Repression spezifischer Stoffwechsel Gene, insbesondere *atpH* und *pykF*, Toleranzphänotypen durch transkriptionelle und metabolische Veränderungen beeinflusst. Diese Untersuchungen wurden auf ein erweitertes Antibiotika-Stress-Screening mit Ciprofloxacin, Gentamicin, Rifampicin und Meropenem ausgedehnt. Eine vergleichende Analyse identifizierte sowohl antibiotikaspezifische als auch gemeinsame Toleranzphänotypen und hob nicht-vererbte Überlebensstrategien hervor.

Zur Unterstützung metabolomischer Anwendungen wurde ein Hochdurchsatz-Probenahme-Workflow etabliert und hinsichtlich Reproduzierbarkeit, Durchsatz und Kompatibilität mit ungerichteter Massenspektrometrie optimiert. Dieses Protokoll wurde in einem Genom-weiten Screening unter Verwendung der array-basierten CRISPRi-Bibliothek angewendet, was zur Identifizierung von Stoffwechselengpässen, Puffermechanismen und phänotypischen Folgen der Genrepression führte. Zur Validierung und Verfeinerung dieser Beobachtungen wurden gerichtete Metabolitenprofile integriert.

Insgesamt präsentiert diese Arbeit die Etablierung einer Plattform, die gezielte genetische Perturbationen mit Multi-Omics-Analysen kombiniert, um bakterielle Physiologie detailliert zu untersuchen. Die array-basierte CRISPRi-Bibliothek und die entwickelten Arbeitsabläufe stellen ein leistungsfähiges Instrument für die Erforschung von Genotyp-Phänotyp-Beziehungen bereit und eröffnet neue Perspektiven für Anwendungen in der Antibiotikaforschung, dem metabolischen Engineering und der Systembiologie.

List of Figures and Tables

Abbreviations

Abbreviation	Definition
μ	Growth rate
AcN	Acetonitril
Amp	Ampicillin
aTc	Anhydrotetracycline
atpH	ATP synthetase
AUC	Area under the curve
AUC_{norm}	Normalized AUC
bp	Base pair
CFU	Colony forming units
Cip	Ciprofloxacin
CRISPR	Clustered regularly interspaced short palindromic repeats
CRISPRa	CRISPR activation
CRISPR-Cas	CRISPR and their associated proteins
CRISPRi	CRISPR interference
crRNAs	CRISPR RNAs
CV	Coefficient of variation
dCas9	Catalytically inactive Cas9
E. coli	*Escherichia coli*
$E_{CRISPRi}$	Enzyme levels CRISPRi strain
EHEC	Enterohemorrhagic *Escherichia coli*
EIC	Extracted ion chromatogram
ESBL	Extended-spectrum β-lactamase
ESR	Envelope stress response
E_{WT}	Wild-type enzyme-levels
FI-TOF MS	Flow-injection analysis time-of-flight mass spectrometry
FI-MS	flow injection mass spectrometry
Fosfo	Fosfomycin
Genta	Gentamicin
HILIC	Hydrophilic Interaction Liquid Chromatography
IspB	Octaprenyl diphosphate synthase
K	Carrying capacity
LC	Liquid chromatographic
LC-MS/MS	Liquid chromatography-tandem mass spectrometry
LPS	Lipopolysaccharide

Abbreviation	Definition
m/z	Mass to charge (m/z)
MeOH	Methanol
MEP	Methylerythritol phosphate
Mero	Meropenem
MGM	Institute for Medical Microbiology and Hygiene
MIC	Minimal inhibitory concentration
MS	Mass spectrometry
NTP	Nucleoside triphosphate
OD	Optical density
OD_{600}	Optical density at 600 nm
PAM	Protospacer Adjacent Motif
PBP	Penicillin-binding proteins
pfkA/pfkB	Phosphofructokinases
PMF	Proton motive force
PurL	FGAM synthetase
PVDF	Polyvinylidene fluoride
PykA	Pyruvate kinase 2
PykF	Pyruvate kinase 1
QqQ MS	Triple quadrupole mass spectrometry
Q-TOF MS	Quadrupole time-of-flight mass spectrometry
Quenching solution	Acetonitrile/methanol/water, 40:40:20
Rif	Rifampicin
RNA-seq	RNA sequencing
RNR	Ribonucleotide reductase
ROS	Reactive oxygen species
sgRNA	Single guide RNA
TCA	Tricarboxylic acid
TPM	Transcripts per million
UPEC	Uropathogenic *Escherichia coli*
UTI	Urinary tract infection
wwPTFE	water wettable Polytetrafluoroethylene

Metabolite Abbreviations

Abbreviation	Definition
FBP	Fructose-1,6-bisphosphate
2-Cema	N-Acetyl-S-(2-carboxyethyl)-L-cysteine
2dda7p	2-dehydro-3-deoxy-arabino-heptulosonate-7-phosphate
2mecdp	2-C-methyl-D-erythritol 2,4-cyclodiphosphate
3dhq	3-dehydroquinate
3dhsk	3-dehydroshikimate
3psme	5-*O*-(1-carboxyvinyl)-3-phosphoshikimate
acgam6p	N-acetyl-D-glucosamine 6-phosphate
acmum6p	*N*-acetylmuramate 6-phosphate
aicar	5-amino-1-(5-phospho-d-ribosyl)imidazole-4-carboxamide
anhgm	N-Acetyl-D-glucosamine(anhydrous)N-Acetylmuramic acid
anhm	1,6-anhydrous-N-Acetylmuramate
ATP	Adenosine triphosphate
cAMP	Cyclic AMP
cpppg3	Coproporphyrinogen III
dtdp4addg	DTDP-4-amino-4,6-dideoxy-D-galactose
dUMP	Deoxyuridine-phosphate
Fe–S	Iron–sulfur
fgam	N^2-formyl-N^1-(5-phospho-β-d-ribosyl)glycinamide
FPP	Farnesyl pyrophosphate
LPG(16:0)	1-hexadecanoyl-sn-glycerol 3-phosphate
Nac-hcpc	S-(3-hydroxy-3-carboxy-n-propyl)homocysteine
PEP	Phosphoenolpyruvate
SAM	*S*-adenosylmethionine
skm5p	Shikimate-5-phosphate
u23ga	UDP-2,3-bis(3-hydroxytetradecanoyl)glucosamine
uacmamu	UDP-N-acetyl-D-mannosaminouronate
/	Homolanthionine
/	N-acetylcystathionine
/	N-acetylmethionylserine

Chapter 1: General Introduction

Escherichia coli

***Escherichia coli* (*E. coli*)** is a Gram-negative, facultative anaerobe, rod-shaped bacterium that belongs to the *Enterobacteriaceae* family and is usually found within the intestine of mammals as a commensal or pathogen[1,2]. In humans it plays a role in the synthesis of vitamins such as vitamin K and in maintenance of intestinal health[3,4]. *E. coli* is a widely used model organism for research, making it one of the most studied organisms in the world[5]. It is favored for its high replication rate, robustness, receptiveness to genetic modifications, and ease of cultivation, making it ideal for biotechnological industries[5–7].

Even though most strains of *E. coli* that are found within the human gut are harmless, some variants are pathogenic and can cause gastrointestinal diseases[8,9]. The pathogenic *E. coli* strains are classified by their mechanisms of infection and their virulence factors, including enterohemorrhagic (EHEC) and uropathogenic (UPEC) types, among others[10,11]. While these strains were initially easily treatable with antibiotics, rising numbers of antibiotic-resistant strains cause concerns in medical sciences[12–14].

From a scientific perspective, *E. coli* plays a central role in genetic engineering and biotechnology. The *E. coli* genome was one of the first organisms to be sequenced, and recombinant *E. coli* is used worldwide to produce therapeutic proteins like insulin[15–17]. Additionally, *E. coli* is a pivotal tool in systems biology and synthetic biology to develop and test biological circuits and gene regulation models[18,19].

To summarize, *E. coli* is both a central model for biological research and a member of the human microbiome, while pathogenic or antibiotic-resistant strains pose significant risks to human health.

Antibiotics

Antibiotics are antimicrobial agents that are effective against a wide range of bacterial species. They are used to treat infections, either by inhibiting bacterial growth (bacteriostatic) or by directly killing bacterial cells (bactericidal)[20]. Antibiotics rank among the most impactful discoveries in modern medicine, having reduced mortality from bacterial diseases[21–23]. The introduction of the first widely produced antibiotic, penicillin, in the 1940s profoundly transformed medical practice, making it possible to cure previously fatal infections[23–25]. In the decades that followed, the availability of antibiotics enabled more complex medical interventions requiring bacteria-free environments, such as organ transplantation and chemotherapy[26,27].

Antibiotics exert their effects by targeting and hindering essential cellular processes in bacteria. These inhibited processes include synthesis of proteins (e.g. aminoglycosides, macrolides, tetracyclines), the cell wall (e.g. β-lactams, cephalosporins), and nucleic acids (e.g. rifamycins, fluoroquinolones), but also of metabolic pathways (e.g. sulfamides)[20,28–30]. Their selectivity is based on structural and functional differences between bacterial and mammalian cells, allowing them to act against pathogens without significantly harming host tissues[30,31].

Antibiotics are classified according to their mode of action, spectrum of activity, chemical structure, and origin, whether natural, synthetic, or semisynthetic[32]. Narrow-spectrum antibiotics are highly effective against specific bacterial groups, whereas broad-spectrum agents target a wider array of bacteria, including both Gram-positive and Gram-negative organisms[33,34]. Such classifications provide the basis for selecting empirical therapies, allowing clinicians to match antibiotic properties with suspected pathogens before diagnostic results are available.

Over the past decades, the inappropriate and widespread use of antibiotics has led to the emergence and spread of antibiotic resistance, which has become a major global health threat[25,41]. Resistance mechanisms include target site modifications, efflux pump activation, and enzymatic degradation of antibiotics[42]. In Gram-negative bacteria in particular, horizontal gene transfer facilitates the rapid dissemination of resistance traits. These developments have made many once-treatable infections harder to manage, contributing to higher mortality rates, longer hospitalization, and rising healthcare costs[43].

Among the many antibiotics, a particularly interesting example of an older antibiotic with renewed clinical relevance is **fosfomycin**, discovered in 1969[35]. It inhibits the enzyme **MurA**, which plays a key role in the early stages of peptidoglycan synthesis, a process critical for bacterial cell wall construction[36]. This mechanism is unique among antibiotics. Fosfomycin was initially used to treat urinary tract infections, but its use declined due to the emergence of broader-spectrum alternatives and early concerns about resistance[36,37]. In recent years, however, the rise of multidrug-resistant organisms, such as extended-spectrum β-lactamase (ESBL)-producing *Enterobacteriaceae* and *Staphylococcus aureus*, has renewed interest in fosfomycin[38,39]. Its low toxicity, ease of oral administration, and efficacy against certain carbapenem-resistant strains make it a valuable option for uncomplicated infections and, in combination therapy, for more severe cases[40].

Compounding the problem of reduced antibiotic treatment efficacy, the pipeline for new antibiotics has slowed markedly. Regulatory hurdles, high development costs, and poor financial incentives — given that new antibiotics are often reserved for limited, last-resort use — have discouraged pharmaceutical companies from investing in antibiotic development[44,45]. As a result, there is renewed focus on the clinical potential of older antibiotics like fosfomycin, as well as on alternative strategies such as antibiotic combination therapies, bacteriophage therapy, and immune system modulation[40,46].

Antibiotic Survival Strategies

When exposed to antibiotics, bacterial populations are placed under strong selective pressure, driving the emergence of diverse survival mechanisms[47–49]. These mechanisms allow bacteria to withstand antibiotic treatment either by actively neutralizing the drug or by entering temporary physiological states that reduce their vulnerability[50,51]. Bacterial survival under antibiotic stress can be broadly grouped into four strategies — resistance, heteroresistance, tolerance, and persistence — each defined by distinct mechanisms and clinical implications[52,53]. Each of these contributes to reduced treatment effectiveness and ultimately to the growing global challenge of antimicrobial resistance.

Antibiotic resistance is the most well-characterized survival strategy. It refers to the bacterial ability to grow in the presence of an antibiotic that would normally kill or inhibit susceptible strains[54]. As illustrated in Figure 1 (top panel), resistant cells survive and proliferate during antibiotic treatment, ultimately dominating the population. Resistance is typically inherited and can involve several mechanisms, including modification of antibiotic targets, such as changes in penicillin-binding proteins, or reduced membrane permeability[54–56]. Additionally, active efflux of antibiotics and enzymatic degradation, for example via β-lactamases, are well characterized mechanisms[54,57]. Most of these traits are acquired by chromosomal mutation or horizontal gene transfer of mobile genetic elements[58,59]. Bacterial resistance leads to increased **minimal inhibitory concentrations (MICs)** making standard treatments less effective and require the use of alternatives or combinatory therapies[60].

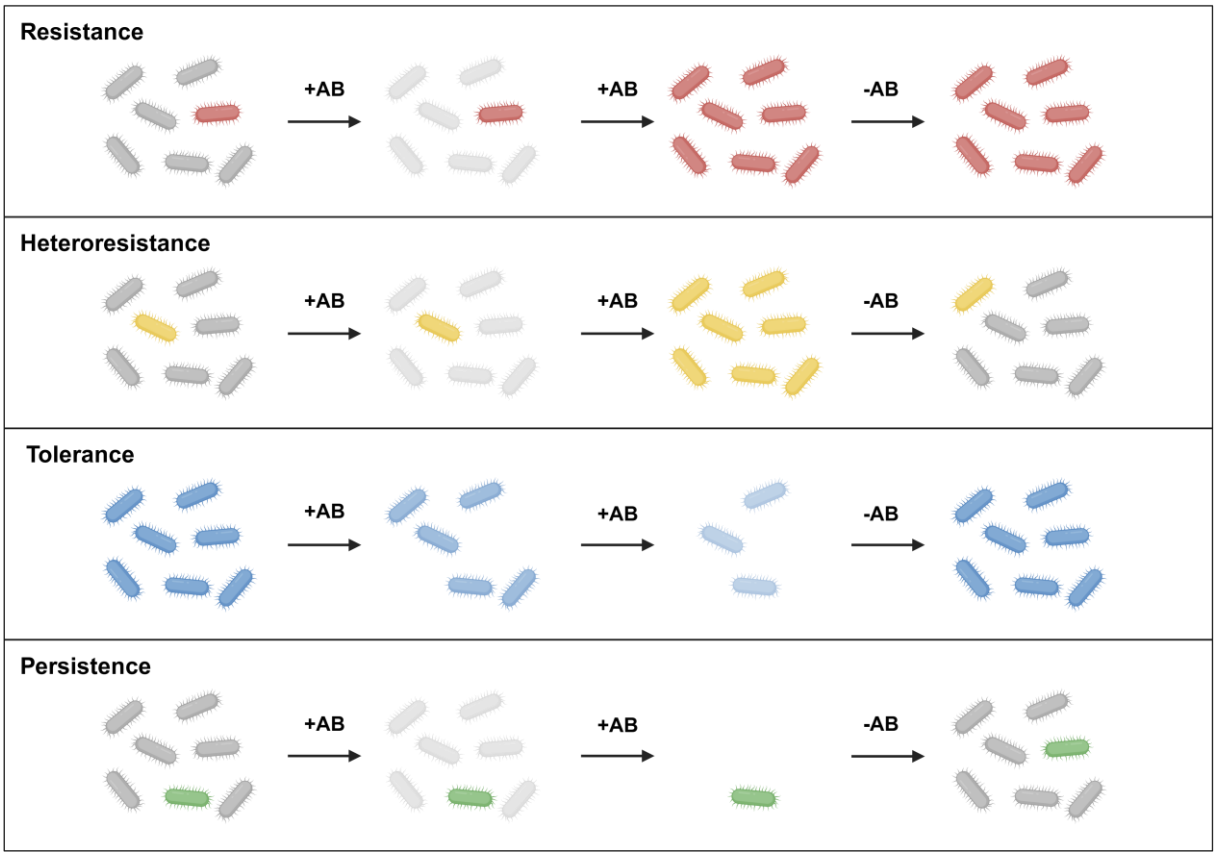

Figure 1. Antibiotic survival strategies towards antibiotic treatment. The figure illustrates the four major bacterial mechanisms to survive antibiotic exposure. **Resistance**: resistant cells (red) proliferate during antibiotic exposure, leading to population domination. **Heteroresistance**: a genetically similar subpopulation (yellow) with enhanced resistance proliferates under antibiotic pressure, while reverting to original population compositions when antibiotic exposure stops. **Tolerance**: tolerant cells (blue) die at a decreased rate during antibiotic exposure but resume growth after treatment ceases. **Persistence**: persister cells (green) are dormant during antibiotic treatment, surviving without cell division, and regrow to the original population composition after antibiotic pressure is removed, contributing to relapse or chronic infections.

Heteroresistance refers to a situation in which a bacterial population contains a small subpopulation of cells with significantly higher antibiotic resistance than the majority, despite being genetically similar[61,62]. In Figure 1 (second panel), a minority of resistant cells expands under antibiotic pressure, even though most of the population appears susceptible, while reverting to original population compositions within the next generations. Heteroresistance can result from gene amplifications, mutations of low stability, or stochastic gene expression[53,63,64]. Because most cells remain susceptible, heteroresistance often goes undetected in standard antibiotic susceptibility testing. However, under antibiotic pressure, the resistant minority can expand, potentially leading to treatment failure and the development of stable resistance[65,66].

Antibiotic tolerance differs fundamentally from resistance. Tolerant bacteria can survive exposure to bactericidal antibiotics without acquiring heritable resistance mutations[67,68]. In Figure 1 (third panel), tolerant cells do not proliferate during antibiotic exposure but survive the treatment longer and resume growth once the antibiotic is removed, particularly if treatment durations are insufficient. Most of these cells are either in a metabolic inactive state or slow-growing, rendering them less susceptible to antibiotics that target actively dividing cells[69]. While tolerance does not increase the MIC, the treatment duration required for bacterial eradication is elevated[70]. It can be induced by the formation of biofilms, limitation of nutrients, or environmental stress[71,72]. Tolerant populations are often correlated to treatment delays, acting as reservoirs for the emergence of resistant clones[73].

Persistence is a specialized form of tolerance involving a small subpopulation of dormant cells, known as **persisters**[52,72]. As shown in Figure 1 (bottom panel), persister cells survive antibiotic treatment without replicating and later regrow once the antibiotic is removed, leading to relapse or chronic infection. These cells are genetically identical to the rest of the population but temporarily adopt a phenotype that allows them to survive high concentrations of antibiotics[52,72,74]. Persistence plays a key role in biofilm-associated infections and is particularly relevant in pathogens such as *E. coli*, *Staphylococcus aureus*, and *Mycobacterium tuberculosis*[72,75].

These survival strategies illustrate the remarkable ability of bacteria to adapt to antibiotic stress, complicating eradication efforts. While resistance has long been considered the most dangerous and clinically important mechanism, growing evidence points to the significant roles of tolerance, heteroresistance, and persistence. Therapeutic progress will require approaches that target not only classical resistance but also tolerance, persistence, and heteroresistance, since all four contribute to treatment failure and resistance evolution.

Clustered Regularly Interspaced Short Palindromic Repeats (CRISPR) Variants

Clustered Regularly Interspaced Short Palindromic Repeats and their associated proteins (**CRISPR-Cas**) constitute an adaptive immune system present in many bacteria and archaea[76,77]. It provides protection against invading genetic elements such as DNA injected by bacteriophages via integrating short fragments of foreign DNA into specific regions of the host genome known as CRISPR loci[77–80]. These fragments are transcribed into CRISPR RNAs (crRNAs), which form complexes with Cas nucleases scanning the cell for target sequences[76,81]. The crRNAs guide the nuclease to complementary sequences in the foreign DNA, enabling cleavage and neutralization of the threat [81,82].

Two major CRISPR–Cas system classes exist: Class I, in which multiple Cas proteins cooperate to degrade foreign genetic elements, and Class II, which relies on a single large Cas protein[83]. While **Cas9** from the Class II CRISPR-Cas system, originally discovered in *Streptococcus pyogenes*, is the most widely used, other differently targeting CRISPR effectors such as Cas12 and Cas13 have been adapted for DNA and RNA targeting, respectively[84,85].

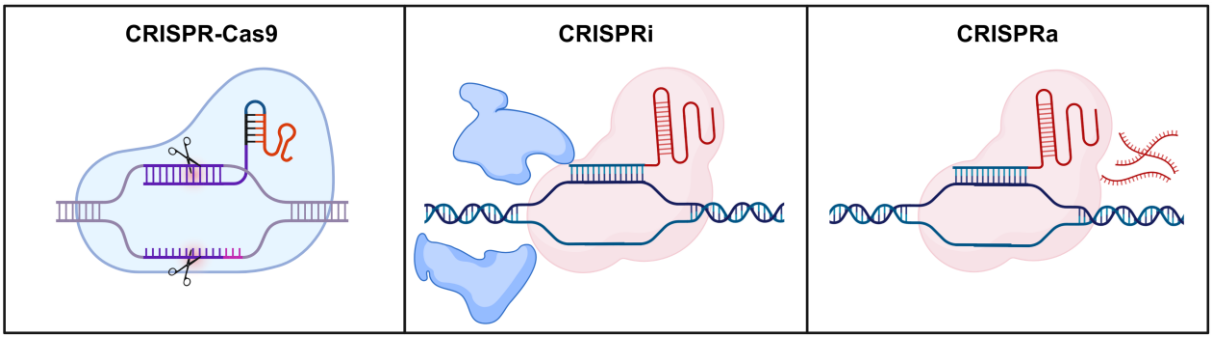

Figure 2. Schematic representation of laboratory adapted CRISPR-Cas9 and modified derivatives. Left: CRISPR-Cas9, where the Cas9 endonuclease introduces a double strand break at a target DNA sequence guided by a single guide RNA (sgRNA), consisting of a spacer sequence (purple) and the scaffold region (red). Error prone repair pathways can be exploited to knock out genes and providing a donor template enables precise sequence integration. **Middle:** CRISPR interference (CRISPRi) uses a catalytically inactive Cas9 (dCas9) with an sgRNA that binds the target DNA, physically blocking RNA polymerase (blue) and thereby preventing transcription. **Right:** CRISPR activation (CRISPRa) uses dCas9 with transcriptional activators, either fused to dCas9 or recruited via engineered sgRNAs, to enhance gene expression without introducing DNA breaks.

Laboratory adaptation of CRISPR systems has enabled precise genome engineering and programmable gene regulation in diverse organisms (Figure 2, left)[86]. One such modification, known as **CRISPR interference (CRISPRi)**, allows for targeted repression of gene expression without inducing double-stranded DNA breaks[87,88]. In this system, the catalytic activity of Cas9 is inactivated by point mutations, generating a nuclease-deficient variant known as dCas9[87]. Guided by single-guide RNAs (sgRNA), dCas9 binds directly or next to complementary DNA sequences, physically blocking elongation or binding of RNA polymerase (Figure 2, Middle)[89]. This results in effective transcriptional repression but requires the presence of a short sequence, the Protospacer Adjacent Motif (PAM), downstream of the binding site for target site recognition[90,91]. Although this requirement restricts potential target regions, it also enhances targeting specificity[90].

CRISPRi offers several advantages, including reversible and tunable gene knockdown. Gene silencing occurs only in the presence of the dCas9-sgRNA complex, and expression as well as targets of sgRNAs can be controlled[92,93]. Importantly, CRISPRi induces no DNA damage, making it a pivotal and safe tool to study essential genes and to perform genetic screens[94].

A related technique uses dCas9 fused to transcriptional activator domains to enhance gene expression. This **CRISPR activation (CRISPRa)** utilizes the dCas9-activator to bind to enhancer or promoter regions causing an increase in target gene transcription (Figure 2, right)[95–97]. Beyond gene regulation dCas9 can be fused to other functional domains, including fluorescent proteins or transcriptional repressors for utilization in epigenetics or cell imaging[98,99].

Together, CRISPRi and CRISPRa provide complementary approaches for modulating gene expression without altering DNA sequences, making them valuable tools in both prokaryotic and eukaryotic research[100].

Genetic Libraries and CRISPR-Based Screening

Bacterial strain libraries provide systematic access to mutant collections, enabling direct investigation of gene function and cellular physiology[101–103]. These libraries typically consist of mutant strains with specific gene disruptions, deletions, or modifications[103,104]. In bacterial systems, common formats include transposon mutant libraries, gene knockout collections, and overexpression libraries[104–106].

Knockout libraries consist of defined gene deletions and are widely used to study metabolic pathways, gene essentiality, and synthetic lethality[104,107,108]. A well-established example is the Keio library in *E. coli*[104]. However, these libraries have limitations: essential genes cannot be

deleted, polar effects can complicate interpretation, and generating new mutants for different conditions or strains requires substantial time and effort[101,109,110]. Similarly, transposon mutant libraries can only target non-essential genes, since disruption of essential genes prevents growth[111]. Overexpression libraries, in contrast, impose a high metabolic burden on cells from the outset, often leading to unwanted or unpredictable effects, and they do not provide insight into loss-of-function phenotypes[112].

CRISPR-based methods have transformed functional genomics by enabling programmable perturbations of gene expression. In particular, CRISPRi and CRISPRa provide alternatives to traditional strain libraries[113,114]. CRISPRi enables tunable and reversible repression, while CRISPRa allows targeted upregulation[113,114]. Together, these approaches support genome-wide analyses with a level of flexibility not achievable through knockouts or overexpression alone.

Leveraging the versatility of CRISPR-Cas9-based systems, genome-wide CRISPRi/a libraries have been developed to systematically investigate gene function[113,115]. These libraries allow the repression or activation of thousands of genes simultaneously and are typically implemented in either pooled or arrayed formats[115]. As this study employed CRISPRi, the following sections will focus on this approach.

In **pooled CRISPRi libraries**, diverse sgRNA collections targeting multiple genes are integrated into single cell populations. Each cell receives a single sgRNA, resulting in a mixed population where each cell harbors a unique gene knockdown. This format is well suited for high-throughput screening under selective conditions such as antibiotic treatment, stress, or nutrient limitation[102,116]. Changes in sgRNA abundance can be quantified by next-generation sequencing to identify genes that influence survival or fitness[117]. While pooled libraries are highly scalable and cost-efficient, they are limited to population-level phenotypes[118]. Moreover, indirect effects and cross-rescue between strains can obscure interpretation, making follow-up validation essential[119,120].

In contrast, **arrayed CRISPRi libraries** consist of individually isolated strains, each containing a defined sgRNA. Stored in multi-well plates, they enable direct and separate analysis of individual gene knockdowns. This format allows a wider range of phenotypic assays that are difficult to perform in pooled settings, including biochemical profiling, growth analysis, and fluorescence microscopy[121,122]. Although arrayed libraries require more resources to construct and maintain, they facilitate straightforward experimental reproducibility and easier validation of results[121,123].

In this dissertation, specifically in Chapter 2, an arrayed CRISPRi library was created by isolating individual clones from a pooled strain library. The pooled library used for arraying in this work was developed previously[124]. It includes 2–5 sgRNAs targeting each metabolic gene, based on the iML1515 genome-scale metabolic model. This approach preserved the coverage and density of the original screen while enabling precise and controllable analysis of individual gene knockdowns under defined experimental conditions. The arrayed format was applied in metabolic and antibiotic stress screens, as described in Chapters 3, 4, and 6. To investigate the cellular consequences of gene perturbations introduced through CRISPRi, this work combines a functional library with multi-omics profiling. By integrating CRISPRi with multi-omics readouts, this work maps regulatory and metabolic responses from gene-level perturbations to systems-scale outcomes.

Transcriptomics, Proteomics, and Metabolomics

High-throughput omics approaches in systems biology quantify RNA, proteins, and metabolites to capture cellular responses under defined conditions. These methods offer a detailed view of how cells respond to genetic or environmental changes by measuring e.g. gene expression, protein levels, and metabolite concentrations on a global scale[125,126]. When coupled with strain libraries, omics readouts directly connect gene-level perturbations to transcriptional, proteomic, and metabolic consequences[127].

Transcriptomics focuses on the large-scale analysis of RNA transcripts, typically using RNA sequencing (RNA-seq)[128,129]. This method allows for quantification of genome-wide expression levels and reveals transcriptional regulation under specific conditions[129]. Transcriptomic data is highly sensitive, offers strong quantitative resolution, and is suitable for high-throughput formats[128,130]. One limitation is the inconsistent correlation between mRNA and protein levels, due to post-transcriptional regulation[131,132]. This makes the integration of additional data layers from other omics approaches important for interpretation.

Proteomics directly quantifies protein abundance and chemical modifications, offering insight into regulatory layers not captured by transcriptomic data[133]. In addition, proteomic studies highlight mechanisms such as post-translational modifications and protein stability differences, which are missed when relying solely on transcript levels[134,135]. Nevertheless, proteomic workflows involve more complex protein extraction and quantification steps, often requiring additional optimization and resulting in lower coverage compared to transcriptomics[136,137].

Metabolomics refers to the systematic analysis of small molecules and metabolites, providing snapshots of cellular physiology and metabolic activity[138–140]. This approach is particularly useful for studying responses to environmental stress, antimicrobial treatments, or nutrient shifts[141,142]. Because metabolites have short half-lives and are tightly regulated, changes in the metabolome occur more rapidly than transcriptional or proteomic shifts[143]. Metabolomics can be performed in untargeted formats, to broadly detect changes across the metabolic landscape, or in targeted formats, focusing on specific pathways or reactions[144]. Although data interpretation poses challenges due to identification uncertainties and compound diversity, metabolomics is an essential complement to transcriptomics and proteomics data[145].

Integrating transcriptomic, proteomic, and metabolomic data provides a multi-layered view of cellular responses and improves the interpretation of gene function, particularly when combined with CRISPRi-based perturbations[124,127,146]. Integrating multiple omics allows researchers to follow the regulatory cascade from gene repression to metabolic phenotype.

In this dissertation, all three omics approaches were applied to different extents. In Chapter 3, targeted analyses of CRISPRi strains under antibiotic treatment were used to investigate metabolic and transcriptomic shifts. Chapter 5 focused on metabolomics, as a high-throughput metabolite sampling method was developed. Chapter 6 centered on a CRISPRi library-wide untargeted metabolomic screen, supplemented with targeted metabolite profiling and proteomics data integration.

Metabolic Analysis

Mass spectrometry (MS) has become the central method for metabolome analysis, enabling high-resolution detection of cellular metabolites under defined conditions[147]. As mentioned in the previous section, MS-based metabolomics is typically categorized into untargeted and targeted approaches. Targeted MS offers high-quality, quantitative signals but requires longer acquisition times, often several minutes per measurement[148]. In contrast, untargeted MS can acquire data within seconds, enabling a very high throughput, though usually at the cost of increased data processing complexity and reduced quantification accuracy[149]. In this dissertation, two complementary MS methods were applied: untargeted flow-injection time-of-flight (FI-TOF) MS, measured on a quadrupole time-of-flight (Q-TOF) instrument operated in transmission mode (Q1 not used for filtering), and targeted triple quadrupole (QqQ) MS.

FI-TOF MS enables global metabolome profiling without chromatographic separation, making it suitable for high-throughput measurements[150]. After sample injection and ionization, metabolites directly pass into the time-of-flight analyzer (Figure 3 A). Here, ions are separated according to their flight time, with lighter ions reaching the detector earlier than heavier ones. This approach captures thousands of features in a single run with high mass accuracy[150]. However, the lack of chromatographic separation complicates the identification of isomers, rendering the results more semi-quantitative than absolute[151,152].

QqQ MS, in contrast, is regarded as the gold standard for the precise and sensitive quantification of predefined metabolites[153]. After ionization, metabolites enter the first quadrupole (Q1), which filters precursor ions by mass (Figure 3B). These ions are then fragmented in the collision cell (Q2), and the resulting product ions are filtered in the third quadrupole (Q3) before detection. This targeted approach provides a wide dynamic range, high sensitivity, and excellent reproducibility[152]. Because the analysis focuses on specific metabolites within a narrow mass range, it requires prior knowledge of targets and is therefore less suitable for hypothesis-free discovery[154].

Modern metabolomics workflows often combine FI-TOF and QqQ MS, using the former for broad profiling and the latter for precise quantification[155]. FI-TOF MS is well suited for broad metabolite profiling and untargeted discovery, while QqQ MS provides precise follow-up quantification and validation of key metabolites[155].

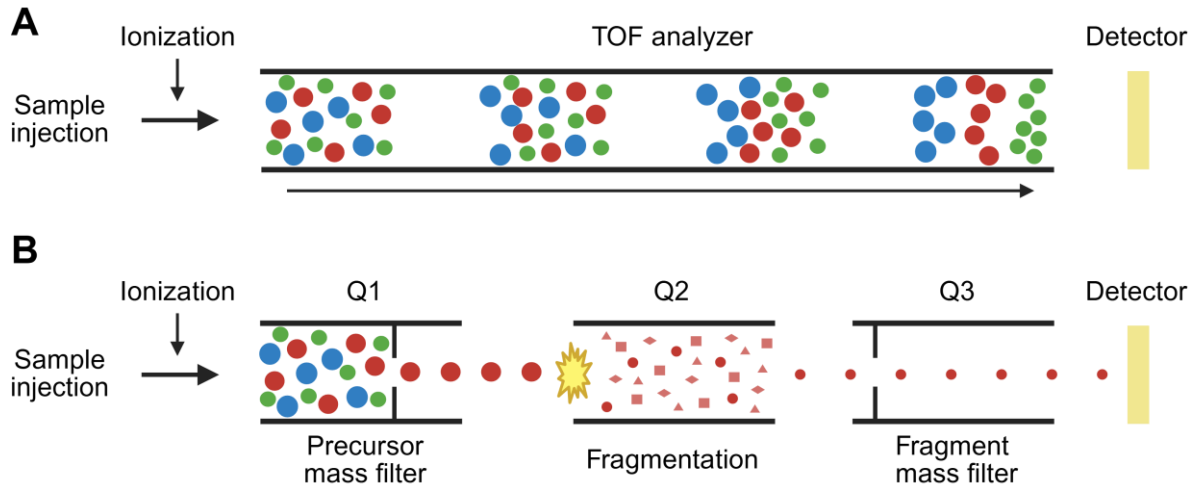

Figure 3. Comparison of flow-injection time-of-flight (FI-TOF) and triple quadrupole (QqQ) mass spectrometry (MS). (A) In FI-TOF MS, ions are separated by their flight time in the analyzer tube, where lighter ions reach the detector faster than heavier ions. This enables fast untargeted metabolite measurements with high coverage. **(B)** In QqQ MS, ions are initially filtered by their precursor mass in Q1, then fragmented by collision with inert gas in Q2, and filtered by their fragment mass in Q3 before reaching the detector. This allows sensitive and reproducible metabolite quantification.

In this dissertation, FI-TOF MS was applied as a rapid, high-throughput tool for broad metabolite profiling, particularly in the CRISPRi library-wide screen in Chapter 6 and in the development of high-throughput metabolite sampling of Chapter 5. QqQ MS was employed for targeted quantification in Chapter 3 and for validating untargeted findings in Chapter 6. By combining FI-TOF and QqQ MS, this work linked large-scale metabolic changes with precise metabolite quantification, providing a foundation for integration with transcriptomic and proteomic datasets across the dissertation.

Dissertation Overview and Chapter Structure

This dissertation is organized into five additional chapters (Table 1). **Chapter 2** describes the construction of an arrayed CRISPRi library from an existing pooled screen, enabling systematic and high-resolution gene perturbation studies. **Chapter 3** investigates antibiotic-induced phenotypes using the arrayed CRISPRi library, focusing on fosfomycin resistance mechanisms and integrating transcriptomic and metabolomic profiling. **Chapter 4** focuses on additional antibiotic stress screens, performed in four antibiotics of different types and modes of action. **Chapter 5** presents the development of a new high-throughput metabolite sampling protocol, optimized for use with arrayed libraries and untargeted metabolomics. **Chapter 6** applies the arrayed library in a genome-wide untargeted metabolomics screen to identify gene knockdowns associated with metabolite accumulation. The chapter also incorporates targeted MS and bioengineering strategies.

Table 1. Overview of experimental workflow in this dissertation.

Chapter	Focus	Main Tool	Data Type	Key Output
1	Introduction	Literature review	Published literature	Background knowledge
2	Pooled → arrayed CRISPRi library	CRISPRi	sgRNA mapping	Arrayed strain library
3	Antibiotic stress screen	CRISPRi + Metabolomics + Transcriptomics	Multi-omics	Resistance and tolerance insights
4	Antibiotic stress screen	CRISPRi	Growth data	Resistance and tolerance insights
5	Sampling method development	Metabolomics	Untargeted MS	High-throughput workflow
6	Metabolic screens	CRISPRi + Metabolomics + Proteomics	Integrated Omics	Phenotype mapping

Aim of the Dissertation

Despite major advances in pooled CRISPRi screening and multi-omics technologies, studying bacterial gene function is still limited by a lack of scalable, single-strain perturbation systems that work across different omics workflows. Pooled approaches often mask individual phenotypes and are difficult to combine with methods that require defined genetic perturbations.

The main aim of this dissertation is to establish an arrayed CRISPRi library for functional genomics in *E. coli*, combining systematic gene perturbation with omics-based readouts. As part of this work, I developed a high-throughput metabolite sampling method and used transcriptomics, proteomics, and metabolomics to analyze gene function, metabolism, and antibiotic responses.

Bibliography

(1) Tenaillon, O.; Skurnik, D.; Picard, B.; Denamur, E. The Population Genetics of Commensal *Escherichia Coli*. *Nat Rev Microbiol* **2010**, *8* (3), 207–217. https://doi.org/10.1038/nrmicro2298.

(2) Ramos, S.; Silva, V.; Dapkevicius, M. de L. E.; Caniça, M.; Tejedor-Junco, M. T.; Igrejas, G.; Poeta, P. *Escherichia Coli* as Commensal and Pathogenic Bacteria among Food-Producing Animals: Health Implications of Extended Spectrum β-Lactamase (ESBL) Production. *Animals* **2020**, *10* (12), 2239. https://doi.org/10.3390/ani10122239.

(3) Ellis, J. L.; Karl, J. P.; Oliverio, A. M.; Fu, X.; Soares, J. W.; Wolfe, B. E.; Hernandez, C. J.; Mason, J. B.; Booth, S. L. Dietary Vitamin K Is Remodeled by Gut Microbiota and Influences Community Composition. *Gut Microbes 13* (1), 1887721. https://doi.org/10.1080/19490976.2021.1887721.

(4) Lai, Y.; Masatoshi, H.; Ma, Y.; Guo, Y.; Zhang, B. Role of Vitamin K in Intestinal Health. *Front. Immunol.* **2022**, *12*. https://doi.org/10.3389/fimmu.2021.791565.

(5) İncir, İ.; Kaplan, Ö. *Escherichia Coli* as a Versatile Cell Factory: Advances and Challenges in Recombinant Protein Production. *Protein Expression and Purification* **2024**, *219*, 106463. https://doi.org/10.1016/j.pep.2024.106463.

(6) Huang, C.-J.; Lin, H.; Yang, X. Industrial Production of Recombinant Therapeutics in *Escherichia Coli* and Its Recent Advancements. *Journal of Industrial Microbiology and Biotechnology* **2012**, *39* (3), 383–399. https://doi.org/10.1007/s10295-011-1082-9.

(7) Rosano, G. L.; Ceccarelli, E. A. Recombinant Protein Expression in *Escherichia Coli*: Advances and Challenges. *Front. Microbiol.* **2014**, *5*. https://doi.org/10.3389/fmicb.2014.00172.

(8) Stromberg, Z. R.; Van Goor, A.; Redweik, G. A. J.; Wymore Brand, M. J.; Wannemuehler, M. J.; Mellata, M. Pathogenic and Non-Pathogenic *Escherichia Coli* Colonization and Host Inflammatory Response in a Defined Microbiota Mouse Model. *Dis Model Mech* **2018**, *11* (11), dmm035063. https://doi.org/10.1242/dmm.035063.

(9) Katouli, M. Population Structure of Gut *Escherichia Coli* and Its Role in Development of Extra-Intestinal Infections. *Iran J Microbiol* **2010**, *2* (2), 59–72.

(10) Nataro, J. P.; Kaper, J. B. Diarrheagenic *Escherichia Coli*. *Clin Microbiol Rev* **1998**, *11* (1), 142–201. https://doi.org/10.1128/cmr.11.1.142.

(11) Sora, V. M.; Meroni, G.; Martino, P. A.; Soggiu, A.; Bonizzi, L.; Zecconi, A. Extraintestinal Pathogenic *Escherichia Coli*: Virulence Factors and Antibiotic Resistance. *Pathogens* **2021**, *10* (11), 1355. https://doi.org/10.3390/pathogens10111355.

(12) Choi, J.-K.; Yoo, J.-H. Increasing Antimicrobial Resistance of *Escherichia Coli* Makes Antimicrobial Stewardship More Important. *J Korean Med Sci* **2019**, *34* (34), e236. https://doi.org/10.3346/jkms.2019.34.e236.

(13) Aljohni, M. S.; Harun-Ur-Rashid, M.; Selim, S. Emerging Threats: Antimicrobial Resistance in Extended-Spectrum Beta-Lactamase and Carbapenem-Resistant *Escherichia Coli*. *Microbial Pathogenesis* **2025**, *200*, 107275. https://doi.org/10.1016/j.micpath.2024.107275.

(14) Raum, E.; Lietzau, S.; von Baum, H.; Marre, R.; Brenner, H. Changes in *Escherichia Coli* Resistance Patterns during and after Antibiotic Therapy: A Longitudinal Study among Outpatients in Germany. *Clinical Microbiology and Infection* **2008**, *14* (1), 41–48. https://doi.org/10.1111/j.1469-0691.2007.01841.x.

(15) Baeshen, N. A.; Baeshen, M. N.; Sheikh, A.; Bora, R. S.; Ahmed, M. M. M.; Ramadan, H. A. I.; Saini, K. S.; Redwan, E. M. Cell Factories for Insulin Production. *Microbial Cell Factories* **2014**, *13* (1), 141. https://doi.org/10.1186/s12934-014-0141-0.

(16) Blattner, F. R.; Plunkett, G.; Bloch, C. A.; Perna, N. T.; Burland, V.; Riley, M.; Collado-Vides, J.; Glasner, J. D.; Rode, C. K.; Mayhew, G. F.; Gregor, J.; Davis, N. W.; Kirkpatrick, H. A.; Goeden, M. A.; Rose, D. J.; Mau, B.; Shao, Y. The Complete Genome Sequence of *Escherichia Coli* K-12. *Science* **1997**, *277* (5331), 1453–1462. https://doi.org/10.1126/science.277.5331.1453.

(17) İncir, İ.; Kaplan, Ö. *Escherichia Coli* in the Production of Biopharmaceuticals. *Biotechnol Appl Biochem* **2025**, *72* (2), 528–541. https://doi.org/10.1002/bab.2664.

(18) Gardner, T. S.; Cantor, C. R.; Collins, J. J. Construction of a Genetic Toggle Switch in *Escherichia Coli*. *Nature* **2000**, *403* (6767), 339–342. https://doi.org/10.1038/35002131.
(19) Elowitz, M. B.; Leibler, S. A Synthetic Oscillatory Network of Transcriptional Regulators. *Nature* **2000**, *403* (6767), 335–338. https://doi.org/10.1038/35002125.
(20) Baquero, F.; Levin, B. R. Proximate and Ultimate Causes of the Bactericidal Action of Antibiotics. *Nat Rev Microbiol* **2021**, *19* (2), 123–132. https://doi.org/10.1038/s41579-020-00443-1.
(21) Klein, E. Y.; Van Boeckel, T. P.; Martinez, E. M.; Pant, S.; Gandra, S.; Levin, S. A.; Goossens, H.; Laxminarayan, R. Global Increase and Geographic Convergence in Antibiotic Consumption between 2000 and 2015. *Proceedings of the National Academy of Sciences* **2018**, *115* (15), E3463–E3470. https://doi.org/10.1073/pnas.1717295115.
(22) Abat, C.; Gautret, P.; Raoult, D. Benefits of Antibiotics Burden in Low-Income Countries. *Proceedings of the National Academy of Sciences* **2018**, *115* (35), E8109–E8110. https://doi.org/10.1073/pnas.1809354115.
(23) MACKENBACH, J. P.; LOOMAN, C. W. N. Secular Trends of Infectious Disease Mortality in the Netherlands, 1911–1978: Quantitative Estimates of Changes Coinciding with the Introduction of Antibiotics. *International Journal of Epidemiology* **1988**, *17* (3), 618–624. https://doi.org/10.1093/ije/17.3.618.
(24) Gaynes, R. The Discovery of Penicillin—New Insights After More Than 75 Years of Clinical Use. *Emerg Infect Dis* **2017**, *23* (5), 849–853. https://doi.org/10.3201/eid2305.161556.
(25) Ventola, C. L. The Antibiotic Resistance Crisis. *P T* **2015**, *40* (4), 277–283.
(26) Klastersky, J.; Aoun, M. Opportunistic Infections in Patients with Cancer. *Annals of Oncology* **2004**, *15*, iv329–iv335. https://doi.org/10.1093/annonc/mdh947.
(27) Chan, S.; Ng, S.; Chan, H. P.; Pascoe, E. M.; Playford, E. G.; Wong, G.; Chapman, J. R.; Lim, W. H.; Francis, R. S.; Isbel, N. M.; Campbell, S. B.; Hawley, C. M.; Johnson, D. W. Perioperative Antibiotics for Preventing Post-surgical Site Infections in Solid Organ Transplant Recipients. *Cochrane Database Syst Rev* **2020**, *2020* (8), CD013209. https://doi.org/10.1002/14651858.CD013209.pub2.
(28) Kohanski, M. A.; Dwyer, D. J.; Collins, J. J. How Antibiotics Kill Bacteria: From Targets to Networks. *Nat Rev Microbiol* **2010**, *8* (6), 423–435. https://doi.org/10.1038/nrmicro2333.
(29) Baran, A.; Kwiatkowska, A.; Potocki, L. Antibiotics and Bacterial Resistance—A Short Story of an Endless Arms Race. *International Journal of Molecular Sciences* **2023**, *24* (6), 5777. https://doi.org/10.3390/ijms24065777.
(30) Dalhoff, A. Selective Toxicity of Antibacterial Agents—Still a Valid Concept or Do We Miss Chances and Ignore Risks? *Infection* **2021**, *49* (1), 29–56. https://doi.org/10.1007/s15010-020-01536-y.
(31) Epand, R. M.; Walker, C.; Epand, R. F.; Magarvey, N. A. Molecular Mechanisms of Membrane Targeting Antibiotics. *Biochimica et Biophysica Acta (BBA) - Biomembranes* **2016**, *1858* (5), 980–987. https://doi.org/10.1016/j.bbamem.2015.10.018.
(32) Pancu, D. F.; Scurtu, A.; Macasoi, I. G.; Marti, D.; Mioc, M.; Soica, C.; Coricovac, D.; Horhat, D.; Poenaru, M.; Dehelean, C. Antibiotics: Conventional Therapy and Natural Compounds with Antibacterial Activity—A Pharmaco-Toxicological Screening. *Antibiotics (Basel)* **2021**, *10* (4), 401. https://doi.org/10.3390/antibiotics10040401.
(33) Timsit, J.-F.; Depuydt, P.; Kanj, S. S. When Should I Start Broad-Spectrum Antibiotics? *Intensive Care Med* **2024**, *50* (11), 1908–1911. https://doi.org/10.1007/s00134-024-07654-7.
(34) Melander, R. J.; Zurawski, D. V.; Melander, C. Narrow-Spectrum Antibacterial Agents. *Medchemcomm* **2017**, *9* (1), 12–21. https://doi.org/10.1039/c7md00528h.
(35) Hendlin, D.; Stapley, E. O.; Jackson, M.; Wallick, H.; Miller, A. K.; Wolf, F. J.; Miller, T. W.; Chaiet, L.; Kahan, F. M.; Foltz, E. L.; Woodruff, H. B.; Mata, J. M.; Hernandez, S.; Mochales, S. Phosphonomycin, a New Antibiotic Produced by Strains of *Streptomyces*. *Science* **1969**, *166* (3901), 122–123. https://doi.org/10.1126/science.166.3901.122.
(36) Silver, L. L. Fosfomycin: Mechanism and Resistance. *Cold Spring Harb Perspect Med* **2017**, *7* (2), a025262. https://doi.org/10.1101/cshperspect.a025262.

(37) Zhanel, G. G.; Walkty, A. J.; Karlowsky, J. A. Fosfomycin: A First-Line Oral Therapy for Acute Uncomplicated Cystitis. *Canadian Journal of Infectious Diseases and Medical Microbiology* **2016**, *2016* (1), 2082693. https://doi.org/10.1155/2016/2082693.
(38) Gutiérrez-Gutiérrez, B.; Rodríguez-Baño, J. Current Options for the Treatment of Infections Due to Extended-Spectrum Beta-Lactamase-Producing *Enterobacteriaceae* in Different Groups of Patients. *Clinical Microbiology and Infection* **2019**, *25* (8), 932–942. https://doi.org/10.1016/j.cmi.2019.03.030.
(39) Ruiz Ramos, J.; Salavert Lletí, M. Fosfomycin in Infections Caused by Multidrug-Resistant Gram-Negative Pathogens. *Rev Esp Quimioter* **2019**, *32* (Suppl 1), 45–54.
(40) Rubio, E. M.; Martínez, A. R.; Cruz, A. F. Fosfomycin in Antimicrobial Stewardship Programs. *Rev Esp Quimioter* **2019**, *32* (Suppl 1), 62–66.
(41) Salam, Md. A.; Al-Amin, Md. Y.; Salam, M. T.; Pawar, J. S.; Akhter, N.; Rabaan, A. A.; Alqumber, M. A. A. Antimicrobial Resistance: A Growing Serious Threat for Global Public Health. *Healthcare (Basel)* **2023**, *11* (13), 1946. https://doi.org/10.3390/healthcare11131946.
(42) Blair, J. M. A.; Webber, M. A.; Baylay, A. J.; Ogbolu, D. O.; Piddock, L. J. V. Molecular Mechanisms of Antibiotic Resistance. *Nat Rev Microbiol* **2015**, *13* (1), 42–51. https://doi.org/10.1038/nrmicro3380.
(43) Nelson, R. E.; Hyun, D.; Jezek, A.; Samore, M. H. Mortality, Length of Stay, and Healthcare Costs Associated With Multidrug-Resistant Bacterial Infections Among Elderly Hospitalized Patients in the United States. *Clinical Infectious Diseases* **2022**, *74* (6), 1070–1080. https://doi.org/10.1093/cid/ciab696.
(44) Gargate, N.; Laws, M.; Rahman, K. M. Current Economic and Regulatory Challenges in Developing Antibiotics for Gram-Negative Bacteria. *npj Antimicrob Resist* **2025**, *3* (1), 50. https://doi.org/10.1038/s44259-025-00123-1.
(45) Bhavnani, S. M.; Krause, K. M.; Ambrose, P. G. A Broken Antibiotic Market: Review of Strategies to Incentivize Drug Development. *Open Forum Infectious Diseases* **2020**, *7* (7), ofaa083. https://doi.org/10.1093/ofid/ofaa083.
(46) Anastassopoulou, C.; Ferous, S.; Petsimeri, A.; Gioula, G.; Tsakris, A. Phage-Based Therapy in Combination with Antibiotics: A Promising Alternative against Multidrug-Resistant Gram-Negative Pathogens. *Pathogens* **2024**, *13* (10), 896. https://doi.org/10.3390/pathogens13100896.
(47) Davies, J.; Davies, D. Origins and Evolution of Antibiotic Resistance. *Microbiology and Molecular Biology Reviews* **2010**, *74* (3), 417–433. https://doi.org/10.1128/mmbr.00016-10.
(48) Kolář, M.; Urbánek, K.; Látal, T. Antibiotic Selective Pressure and Development of Bacterial Resistance. *International Journal of Antimicrobial Agents* **2001**, *17* (5), 357–363. https://doi.org/10.1016/S0924-8579(01)00317-X.
(49) Larsson, D. G. J.; Flach, C.-F. Antibiotic Resistance in the Environment. *Nat Rev Microbiol* **2022**, *20* (5), 257–269. https://doi.org/10.1038/s41579-021-00649-x.
(50) Wright, G. D. Bacterial Resistance to Antibiotics: Enzymatic Degradation and Modification. *Advanced Drug Delivery Reviews* **2005**, *57* (10), 1451–1470. https://doi.org/10.1016/j.addr.2005.04.002.
(51) Van den Bergh, B.; Fauvart, M.; Michiels, J. Formation, Physiology, Ecology, Evolution and Clinical Importance of Bacterial Persisters. *FEMS Microbiology Reviews* **2017**, *41* (3), 219–251. https://doi.org/10.1093/femsre/fux001.
(52) Balaban, N. Q.; Helaine, S.; Lewis, K.; Ackermann, M.; Aldridge, B.; Andersson, D. I.; Brynildsen, M. P.; Bumann, D.; Camilli, A.; Collins, J. J.; Dehio, C.; Fortune, S.; Ghigo, J.-M.; Hardt, W.-D.; Harms, A.; Heinemann, M.; Hung, D. T.; Jenal, U.; Levin, B. R.; Michiels, J.; Storz, G.; Tan, M.-W.; Tenson, T.; Van Melderen, L.; Zinkernagel, A. Definitions and Guidelines for Research on Antibiotic Persistence. *Nat Rev Microbiol* **2019**, *17* (7), 441–448. https://doi.org/10.1038/s41579-019-0196-3.
(53) Dewachter, L.; Fauvart, M.; Michiels, J. Bacterial Heterogeneity and Antibiotic Survival: Understanding and Combatting Persistence and Heteroresistance. *Molecular Cell* **2019**, *76* (2), 255–267. https://doi.org/10.1016/j.molcel.2019.09.028.

(54) Halawa, E. M.; Fadel, M.; Al-Rabia, M. W.; Behairy, A.; Nouh, N. A.; Abdo, M.; Olga, R.; Fericean, L.; Atwa, A. M.; El-Nablaway, M.; Abdeen, A. Antibiotic Action and Resistance: Updated Review of Mechanisms, Spread, Influencing Factors, and Alternative Approaches for Combating Resistance. *Front. Pharmacol.* **2024**, *14*. https://doi.org/10.3389/fphar.2023.1305294.
(55) Reygaert, W. C. An Overview of the Antimicrobial Resistance Mechanisms of Bacteria. *AIMS Microbiol* **2018**, *4* (3), 482–501. https://doi.org/10.3934/microbiol.2018.3.482.
(56) Peterson, E.; Kaur, P. Antibiotic Resistance Mechanisms in Bacteria: Relationships Between Resistance Determinants of Antibiotic Producers, Environmental Bacteria, and Clinical Pathogens. *Front. Microbiol.* **2018**, *9*. https://doi.org/10.3389/fmicb.2018.02928.
(57) Tooke, C. L.; Hinchliffe, P.; Bragginton, E. C.; Colenso, C. K.; Hirvonen, V. H. A.; Takebayashi, Y.; Spencer, J. β-Lactamases and β-Lactamase Inhibitors in the 21st Century. *Journal of Molecular Biology* **2019**, *431* (18), 3472–3500. https://doi.org/10.1016/j.jmb.2019.04.002.
(58) Haudiquet, M.; de Sousa, J. M.; Touchon, M.; Rocha, E. P. C. Selfish, Promiscuous and Sometimes Useful: How Mobile Genetic Elements Drive Horizontal Gene Transfer in Microbial Populations. *Philosophical Transactions of the Royal Society B: Biological Sciences* **2022**, *377* (1861), 20210234. https://doi.org/10.1098/rstb.2021.0234.
(59) Tao, S.; Chen, H.; Li, N.; Wang, T.; Liang, W. The Spread of Antibiotic Resistance Genes In Vivo Model. *Canadian Journal of Infectious Diseases and Medical Microbiology* **2022**, *2022* (1), 3348695. https://doi.org/10.1155/2022/3348695.
(60) Kowalska-Krochmal, B.; Dudek-Wicher, R. The Minimum Inhibitory Concentration of Antibiotics: Methods, Interpretation, Clinical Relevance. *Pathogens* **2021**, *10* (2), 165. https://doi.org/10.3390/pathogens10020165.
(61) Andersson, D. I.; Nicoloff, H.; Hjort, K. Mechanisms and Clinical Relevance of Bacterial Heteroresistance. *Nat Rev Microbiol* **2019**, *17* (8), 479–496. https://doi.org/10.1038/s41579-019-0218-1.
(62) El-Halfawy, O. M.; Valvano, M. A. Antimicrobial Heteroresistance: An Emerging Field in Need of Clarity. *Clin Microbiol Rev* **2015**, *28* (1), 191–207. https://doi.org/10.1128/CMR.00058-14.
(63) Hernandez-Beltran, J. C. R.; Rodríguez-Beltrán, J.; Aguilar-Luviano, O. B.; Velez-Santiago, J.; Mondragón-Palomino, O.; MacLean, R. C.; Fuentes-Hernández, A.; San Millán, A.; Peña-Miller, R. Plasmid-Mediated Phenotypic Noise Leads to Transient Antibiotic Resistance in Bacteria. *Nat Commun* **2024**, *15* (1), 2610. https://doi.org/10.1038/s41467-024-45045-0.
(64) Hjort, K.; Nicoloff, H.; Andersson, D. I. Unstable Tandem Gene Amplification Generates Heteroresistance (Variation in Resistance within a Population) to Colistin in *Salmonella Enterica*. *Molecular Microbiology* **2016**, *102* (2), 274–289. https://doi.org/10.1111/mmi.13459.
(65) Band, V. I.; Weiss, D. S. Heteroresistance: A Cause of Unexplained Antibiotic Treatment Failure? *PLoS Pathog* **2019**, *15* (6), e1007726. https://doi.org/10.1371/journal.ppat.1007726.
(66) Choby, J. E.; Ozturk, T.; Abbott, C. N.; Nnabuife, C.; Colquhoun, J. M.; Satola, S. W.; Rather, P. N.; Palzkill, T.; Weiss, D. S. Copy Number Flexibility Facilitates Heteroresistance to Increasing Antibiotic Pressure and Threatens the Beta-Lactam Pipeline. *Nat Commun* **2025**, *16* (1), 5721. https://doi.org/10.1038/s41467-025-60828-9.
(67) Brauner, A.; Fridman, O.; Gefen, O.; Balaban, N. Q. Distinguishing between Resistance, Tolerance and Persistence to Antibiotic Treatment. *Nat Rev Microbiol* **2016**, *14* (5), 320–330. https://doi.org/10.1038/nrmicro.2016.34.
(68) Meredith, H. R.; Srimani, J. K.; Lee, A. J.; Lopatkin, A. J.; You, L. Collective Antibiotic Tolerance: Mechanisms, Dynamics and Intervention. *Nat Chem Biol* **2015**, *11* (3), 182–188. https://doi.org/10.1038/nchembio.1754.
(69) Kim, J.-S.; Wood, T. K. Tolerant, Growing Cells from Nutrient Shifts Are Not Persister Cells. *mBio* **2017**, *8* (2), 10.1128/mbio.00354-17. https://doi.org/10.1128/mbio.00354-17.

(70) Sulaiman, J. E.; Lam, H. Evolution of Bacterial Tolerance Under Antibiotic Treatment and Its Implications on the Development of Resistance. *Front. Microbiol.* **2021**, *12*. https://doi.org/10.3389/fmicb.2021.617412.
(71) Uruén, C.; Chopo-Escuin, G.; Tommassen, J.; Mainar-Jaime, R. C.; Arenas, J. Biofilms as Promoters of Bacterial Antibiotic Resistance and Tolerance. *Antibiotics* **2021**, *10* (1), 3. https://doi.org/10.3390/antibiotics10010003.
(72) Niu, H.; Gu, J.; Zhang, Y. Bacterial Persisters: Molecular Mechanisms and Therapeutic Development. *Sig Transduct Target Ther* **2024**, *9* (1), 174. https://doi.org/10.1038/s41392-024-01866-5.
(73) Kunnath, A. P.; Suodha Suoodh, M.; Chellappan, D. K.; Chellian, J.; Palaniveloo, K. Bacterial Persister Cells and Development of Antibiotic Resistance in Chronic Infections: An Update. *Br. J. Biomed. Sci.* **2024**, *81*, 12958. https://doi.org/10.3389/bjbs.2024.12958.
(74) Umetani, M.; Fujisawa, M.; Okura, R.; Nozoe, T.; Suenaga, S.; Nakaoka, H.; Kussell, E.; Wakamoto, Y. Observation of Persister Cell Histories Reveals Diverse Modes of Survival in Antibiotic Persistence. *eLife* **2025**, *14*, e79517. https://doi.org/10.7554/eLife.79517.
(75) Yan, J.; Bassler, B. L. Surviving as a Community: Antibiotic Tolerance and Persistence in Bacterial Biofilms. *Cell Host & Microbe* **2019**, *26* (1), 15–21. https://doi.org/10.1016/j.chom.2019.06.002.
(76) Sorek, R.; Lawrence, C. M.; Wiedenheft, B. CRISPR-Mediated Adaptive Immune Systems in Bacteria and Archaea. *Annual Review of Biochemistry* **2013**, *82* (Volume 82, 2013), 237–266. https://doi.org/10.1146/annurev-biochem-072911-172315.
(77) Jinek, M.; Chylinski, K.; Fonfara, I.; Hauer, M.; Doudna, J. A.; Charpentier, E. A Programmable Dual-RNA–Guided DNA Endonuclease in Adaptive Bacterial Immunity. *Science* **2012**, *337* (6096), 816–821. https://doi.org/10.1126/science.1225829.
(78) Barrangou, R.; Marraffini, L. A. CRISPR-Cas Systems: Prokaryotes Upgrade to Adaptive Immunity. *Molecular Cell* **2014**, *54* (2), 234–244. https://doi.org/10.1016/j.molcel.2014.03.011.
(79) Attar, N. A CRISPR Sense of Self. *Nat Rev Microbiol* **2015**, *13* (6), 329–329. https://doi.org/10.1038/nrmicro3498.
(80) Wimmer, F.; Beisel, C. L. CRISPR-Cas Systems and the Paradox of Self-Targeting Spacers. *Front. Microbiol.* **2020**, *10*. https://doi.org/10.3389/fmicb.2019.03078.
(81) Gasiunas, G.; Barrangou, R.; Horvath, P.; Siksnys, V. Cas9–crRNA Ribonucleoprotein Complex Mediates Specific DNA Cleavage for Adaptive Immunity in Bacteria. *Proceedings of the National Academy of Sciences* **2012**, *109* (39), E2579–E2586. https://doi.org/10.1073/pnas.1208507109.
(82) Swartjes, T.; Staals, R. H. J.; van der Oost, J. Editor's Cut: DNA Cleavage by CRISPR RNA-Guided Nucleases Cas9 and Cas12a. *Biochem Soc Trans* **2020**, *48* (1), 207–219. https://doi.org/10.1042/BST20190563.
(83) Barrangou, R. Diversity of CRISPR-Cas Immune Systems and Molecular Machines. *Genome Biology* **2015**, *16* (1), 247. https://doi.org/10.1186/s13059-015-0816-9.
(84) Bharathkumar, N.; Sunil, A.; Meera, P.; Aksah, S.; Kannan, M.; Saravanan, K. M.; Anand, T. CRISPR/Cas-Based Modifications for Therapeutic Applications: A Review. *Mol Biotechnol* **2022**, *64* (4), 355–372. https://doi.org/10.1007/s12033-021-00422-8.
(85) Tao, J.; Bauer, D. E.; Chiarle, R. Assessing and Advancing the Safety of CRISPR-Cas Tools: From DNA to RNA Editing. *Nat Commun* **2023**, *14* (1), 212. https://doi.org/10.1038/s41467-023-35886-6.
(86) Pickar-Oliver, A.; Gersbach, C. A. The next Generation of CRISPR–Cas Technologies and Applications. *Nat Rev Mol Cell Biol* **2019**, *20* (8), 490–507. https://doi.org/10.1038/s41580-019-0131-5.
(87) Qi, L. S.; Larson, M. H.; Gilbert, L. A.; Doudna, J. A.; Weissman, J. S.; Arkin, A. P.; Lim, W. A. Repurposing CRISPR as an RNA-Guided Platform for Sequence-Specific Control of Gene Expression. *Cell* **2013**, *152* (5), 1173–1183. https://doi.org/10.1016/j.cell.2013.02.022.
(88) Gilbert, L. A.; Larson, M. H.; Morsut, L.; Liu, Z.; Brar, G. A.; Torres, S. E.; Stern-Ginossar, N.; Brandman, O.; Whitehead, E. H.; Doudna, J. A.; Lim, W. A.; Weissman, J. S.; Qi, L.

S. CRISPR-Mediated Modular RNA-Guided Regulation of Transcription in Eukaryotes. *Cell* **2013**, *154* (2), 442–451. https://doi.org/10.1016/j.cell.2013.06.044.

(89) Widom, J. R.; Rai, V.; Rohlman, C. E.; Walter, N. G. Versatile Transcription Control Based on Reversible dCas9 Binding. *RNA* **2019**, *25* (11), 1457–1469. https://doi.org/10.1261/rna.071613.119.

(90) Karlson, C. K. S.; Mohd-Noor, S. N.; Nolte, N.; Tan, B. C. CRISPR/dCas9-Based Systems: Mechanisms and Applications in Plant Sciences. *Plants (Basel)* **2021**, *10* (10), 2055. https://doi.org/10.3390/plants10102055.

(91) Kiattisewee, C.; Karanjia, A. V.; Legut, M.; Daniloski, Z.; Koplik, S. E.; Nelson, J.; Kleinstiver, B. P.; Sanjana, N. E.; Carothers, J. M.; Zalatan, J. G. Expanding the Scope of Bacterial CRISPR Activation with PAM-Flexible dCas9 Variants. *ACS Synth. Biol.* **2022**, *11* (12), 4103–4112. https://doi.org/10.1021/acssynbio.2c00405.

(92) Byun, G.; Yang, J.; Seo, S. W. CRISPRi-Mediated Tunable Control of Gene Expression Level with Engineered Single-Guide RNA in *Escherichia Coli*. *Nucleic Acids Res* **2023**, *51* (9), 4650–4659. https://doi.org/10.1093/nar/gkad234.

(93) Li, X.; Jun, Y.; Erickstad, M. J.; Brown, S. D.; Parks, A.; Court, D. L.; Jun, S. tCRISPRi: Tunable and Reversible, One-Step Control of Gene Expression. *Sci Rep* **2016**, *6* (1), 39076. https://doi.org/10.1038/srep39076.

(94) Tian, R.; Gachechiladze, M. A.; Ludwig, C. H.; Laurie, M. T.; Hong, J. Y.; Nathaniel, D.; Prabhu, A. V.; Fernandopulle, M. S.; Patel, R.; Abshari, M.; Ward, M. E.; Kampmann, M. CRISPR Interference-Based Platform for Multimodal Genetic Screens in Human iPSC-Derived Neurons. *Neuron* **2019**, *104* (2), 239-255.e12. https://doi.org/10.1016/j.neuron.2019.07.014.

(95) Perez-Pinera, P.; Kocak, D. D.; Vockley, C. M.; Adler, A. F.; Kabadi, A. M.; Polstein, L. R.; Thakore, P. I.; Glass, K. A.; Ousterout, D. G.; Leong, K. W.; Guilak, F.; Crawford, G. E.; Reddy, T. E.; Gersbach, C. A. RNA-Guided Gene Activation by CRISPR-Cas9–Based Transcription Factors. *Nat Methods* **2013**, *10* (10), 973–976. https://doi.org/10.1038/nmeth.2600.

(96) Maeder, M. L.; Linder, S. J.; Cascio, V. M.; Fu, Y.; Ho, Q. H.; Joung, J. K. CRISPR RNA–Guided Activation of Endogenous Human Genes. *Nat Methods* **2013**, *10* (10), 977–979. https://doi.org/10.1038/nmeth.2598.

(97) Cheng, A. W.; Wang, H.; Yang, H.; Shi, L.; Katz, Y.; Theunissen, T. W.; Rangarajan, S.; Shivalila, C. S.; Dadon, D. B.; Jaenisch, R. Multiplexed Activation of Endogenous Genes by CRISPR-on, an RNA-Guided Transcriptional Activator System. *Cell Res* **2013**, *23* (10), 1163–1171. https://doi.org/10.1038/cr.2013.122.

(98) Hong, Y.; Lu, G.; Duan, J.; Liu, W.; Zhang, Y. Comparison and Optimization of CRISPR/dCas9/gRNA Genome-Labeling Systems for Live Cell Imaging. *Genome Biology* **2018**, *19* (1), 39. https://doi.org/10.1186/s13059-018-1413-5.

(99) Cai, R.; Lv, R.; Shi, X.; Yang, G.; Jin, J. CRISPR/dCas9 Tools: Epigenetic Mechanism and Application in Gene Transcriptional Regulation. *Int J Mol Sci* **2023**, *24* (19), 14865. https://doi.org/10.3390/ijms241914865.

(100) Carroll, M. S.; Giacca, M. CRISPR Activation and Interference as Investigative Tools in the Cardiovascular System. *Int J Biochem Cell Biol* **2023**, *155*, 106348. https://doi.org/10.1016/j.biocel.2022.106348.

(101) Peters, J. M.; Colavin, A.; Shi, H.; Czarny, T. L.; Larson, M. H.; Wong, S.; Hawkins, J. S.; Lu, C. H. S.; Koo, B.-M.; Marta, E.; Shiver, A. L.; Whitehead, E. H.; Weissman, J. S.; Brown, E. D.; Qi, L. S.; Huang, K. C.; Gross, C. A. A Comprehensive, CRISPR-Based Functional Analysis of Essential Genes in Bacteria. *Cell* **2016**, *165* (6), 1493–1506. https://doi.org/10.1016/j.cell.2016.05.003.

(102) Wang, T.; Guan, C.; Guo, J.; Liu, B.; Wu, Y.; Xie, Z.; Zhang, C.; Xing, X.-H. Pooled CRISPR Interference Screening Enables Genome-Scale Functional Genomics Study in Bacteria with Superior Performance. *Nat Commun* **2018**, *9* (1), 2475. https://doi.org/10.1038/s41467-018-04899-x.

(103) Giaever, G.; Nislow, C. The Yeast Deletion Collection: A Decade of Functional Genomics. *Genetics* **2014**, *197* (2), 451–465. https://doi.org/10.1534/genetics.114.161620.

(104) Baba, T.; Ara, T.; Hasegawa, M.; Takai, Y.; Okumura, Y.; Baba, M.; Datsenko, K. A.; Tomita, M.; Wanner, B. L.; Mori, H. Construction of *Escherichia Coli* K-12 in-Frame, Single-Gene Knockout Mutants: The Keio Collection. *Molecular systems biology* **2006**, *2*. https://doi.org/10.1038/msb4100050.

(105) Cain, A. K.; Barquist, L.; Goodman, A. L.; Paulsen, I. T.; Parkhill, J.; van Opijnen, T. A Decade of Advances in Transposon-Insertion Sequencing. *Nat Rev Genet* **2020**, *21* (9), 526–540. https://doi.org/10.1038/s41576-020-0244-x.

(106) Mutalik, V. K.; Novichkov, P. S.; Price, M. N.; Owens, T. K.; Callaghan, M.; Carim, S.; Deutschbauer, A. M.; Arkin, A. P. Dual-Barcoded Shotgun Expression Library Sequencing for High-Throughput Characterization of Functional Traits in Bacteria. *Nat Commun* **2019**, *10* (1), 308. https://doi.org/10.1038/s41467-018-08177-8.

(107) Tong, A. H. Y.; Evangelista, M.; Parsons, A. B.; Xu, H.; Bader, G. D.; Pagé, N.; Robinson, M.; Raghibizadeh, S.; Hogue, C. W. V.; Bussey, H.; Andrews, B.; Tyers, M.; Boone, C. Systematic Genetic Analysis with Ordered Arrays of Yeast Deletion Mutants. *Science* **2001**, *294* (5550), 2364–2368. https://doi.org/10.1126/science.1065810.

(108) Suthers, P. F.; Zomorrodi, A.; Maranas, C. D. Genome-scale Gene/Reaction Essentiality and Synthetic Lethality Analysis. *Molecular Systems Biology* **2009**, *5* (1), 301. https://doi.org/10.1038/msb.2009.56.

(109) Mateus, A.; Shah, M.; Hevler, J.; Kurzawa, N.; Bobonis, J.; Typas, A.; Savitski, M. M. Transcriptional and Post-Transcriptional Polar Effects in Bacterial Gene Deletion Libraries. *mSystems* **2021**, *6* (5), 10.1128/msystems.00813-21. https://doi.org/10.1128/msystems.00813-21.

(110) Jana, B.; Liu, X.; Dénéréaz, J.; Park, H.; Leshchiner, D.; Liu, B.; Gallay, C.; Zhu, J.; Veening, J.-W.; van Opijnen, T. CRISPRi–TnSeq Maps Genome-Wide Interactions between Essential and Non-Essential Genes in Bacteria. *Nat Microbiol* **2024**, *9* (9), 2395–2409. https://doi.org/10.1038/s41564-024-01759-x.

(111) Goodall, E. C. A.; Robinson, A.; Johnston, I. G.; Jabbari, S.; Turner, K. A.; Cunningham, A. F.; Lund, P. A.; Cole, J. A.; Henderson, I. R. The Essential Genome of *Escherichia Coli* K-12. *mBio* **2018**, *9* (1), 10.1128/mbio.02096-17. https://doi.org/10.1128/mbio.02096-17.

(112) Moriya, H. Quantitative Nature of Overexpression Experiments. *Mol Biol Cell* **2015**, *26* (22), 3932–3939. https://doi.org/10.1091/mbc.E15-07-0512.

(113) Horlbeck, M. A.; Gilbert, L. A.; Villalta, J. E.; Adamson, B.; Pak, R. A.; Chen, Y.; Fields, A. P.; Park, C. Y.; Corn, J. E.; Kampmann, M.; Weissman, J. S. Compact and Highly Active Next-Generation Libraries for CRISPR-Mediated Gene Repression and Activation. *eLife* **2016**, *5*, e19760. https://doi.org/10.7554/eLife.19760.

(114) Gilbert, L. A.; Horlbeck, M. A.; Adamson, B.; Villalta, J. E.; Chen, Y.; Whitehead, E. H.; Guimaraes, C.; Panning, B.; Ploegh, H. L.; Bassik, M. C.; Qi, L. S.; Kampmann, M.; Weissman, J. S. Genome-Scale CRISPR-Mediated Control of Gene Repression and Activation. *Cell* **2014**, *159* (3), 647–661. https://doi.org/10.1016/j.cell.2014.09.029.

(115) Sanson, K. R.; Hanna, R. E.; Hegde, M.; Donovan, K. F.; Strand, C.; Sullender, M. E.; Vaimberg, E. W.; Goodale, A.; Root, D. E.; Piccioni, F.; Doench, J. G. Optimized Libraries for CRISPR-Cas9 Genetic Screens with Multiple Modalities. *Nat Commun* **2018**, *9* (1), 5416. https://doi.org/10.1038/s41467-018-07901-8.

(116) Chidley, C.; Darnell, A. M.; Gaudio, B. L.; Lien, E. C.; Barbeau, A. M.; Vander Heiden, M. G.; Sorger, P. K. A CRISPRi/a Screening Platform to Study Cellular Nutrient Transport in Diverse Microenvironments. *Nat Cell Biol* **2024**, *26* (5), 825–838. https://doi.org/10.1038/s41556-024-01402-1.

(117) Otten, A. B. C.; Sun, B. K. Research Techniques Made Simple: CRISPR Genetic Screens. *Journal of Investigative Dermatology* **2020**, *140* (4), 723-728.e1. https://doi.org/10.1016/j.jid.2020.01.018.

(118) Meyers, S.; Demeyer, S.; Cools, J. CRISPR Screening in Hematology Research: From Bulk to Single-Cell Level. *Journal of Hematology & Oncology* **2023**, *16* (1), 107. https://doi.org/10.1186/s13045-023-01495-5.

(119) Loughran, A. J.; Narina, S.; Klein, J.; Siwak, J. F.; Connelly, J. P.; Pruett-Miller, S. M. Rapid and Robust Validation of Pooled CRISPR Knockout Screens Using CelFi. *Sci Rep* **2025**, *15* (1), 13358. https://doi.org/10.1038/s41598-025-96095-3.

(120) Torelli, F.; da Fonseca, D. M.; Butterworth, S. W.; Young, J. C.; Treeck, M. Paracrine Rescue of MYR1-Deficient *Toxoplasma Gondii* Mutants Reveals Limitations of Pooled in Vivo CRISPR Screens. *Elife* **2024**, *13*, RP102592. https://doi.org/10.7554/eLife.102592.

(121) Yin, J.-A.; Frick, L.; Scheidmann, M. C.; Liu, T.; Trevisan, C.; Dhingra, A.; Spinelli, A.; Wu, Y.; Yao, L.; Vena, D. L.; Knapp, B.; Guo, J.; De Cecco, E.; Ging, K.; Armani, A.; Oakeley, E. J.; Nigsch, F.; Jenzer, J.; Haegele, J.; Pikusa, M.; Täger, J.; Rodriguez-Nieto, S.; Bouris, V.; Ribeiro, R.; Baroni, F.; Bedi, M. S.; Berry, S.; Losa, M.; Hornemann, S.; Kampmann, M.; Pelkmans, L.; Hoepfner, D.; Heutink, P.; Aguzzi, A. Arrayed CRISPR Libraries for the Genome-Wide Activation, Deletion and Silencing of Human Protein-Coding Genes. *Nat. Biomed. Eng* **2025**, *9* (1), 127–148. https://doi.org/10.1038/s41551-024-01278-4.

(122) de Wet, T. J.; Winkler, K. R.; Mhlanga, M.; Mizrahi, V.; Warner, D. F. Arrayed CRISPRi and Quantitative Imaging Describe the Morphotypic Landscape of Essential Mycobacterial Genes. *eLife* **2020**, *9*, e60083. https://doi.org/10.7554/eLife.60083.

(123) St. Pierre, J.; Roberts, J.; Alam, M. A.; Shields, R. C. Construction of an Arrayed CRISPRi Library as a Resource for Essential Gene Function Studies in *Streptococcus Mutans*. *Microbiology Spectrum* **2023**, *12* (1), e03149-23. https://doi.org/10.1128/spectrum.03149-23.

(124) Donati, S.; Kuntz, M.; Pahl, V.; Farke, N.; Beuter, D.; Glatter, T.; Gomes-Filho, J. V.; Randau, L.; Wang, C.-Y.; Link, H. Multi-Omics Analysis of CRISPRi-Knockdowns Identifies Mechanisms That Buffer Decreases of Enzymes in *E. Coli* Metabolism. *cels* **2021**, *12* (1), 56-67.e6. https://doi.org/10.1016/j.cels.2020.10.011.

(125) Dai, X.; Shen, L. Advances and Trends in Omics Technology Development. *Front. Med.* **2022**, *9*. https://doi.org/10.3389/fmed.2022.911861.

(126) Blankenburg, M.; Haberland, L.; Elvers, H.-D.; Tannert, C.; Jandrig, B. High-Throughput Omics Technologies: Potential Tools for the Investigation of Influences of EMF on Biological Systems. *Curr Genomics* **2009**, *10* (2), 86–92. https://doi.org/10.2174/138920209787847050.

(127) Anglada-Girotto, M.; Handschin, G.; Ortmayr, K.; Campos, A. I.; Gillet, L.; Manfredi, P.; Mulholland, C.; Berney, M.; Jenal, U.; Picotti, P.; Zampieri, M. Combining CRISPRi and Metabolomics for Functional Annotation of Compound Libraries. *Nat Chem Biol* **2022**, *18* (5), 482–491. https://doi.org/10.1038/s41589-022-00970-3.

(128) Wang, Z.; Gerstein, M.; Snyder, M. RNA-Seq: A Revolutionary Tool for Transcriptomics. *Nat Rev Genet* **2009**, *10* (1), 57–63. https://doi.org/10.1038/nrg2484.

(129) Stark, R.; Grzelak, M.; Hadfield, J. RNA Sequencing: The Teenage Years. *Nat Rev Genet* **2019**, *20* (11), 631–656. https://doi.org/10.1038/s41576-019-0150-2.

(130) Han, Y.; Gao, S.; Muegge, K.; Zhang, W.; Zhou, B. Advanced Applications of RNA Sequencing and Challenges. *Bioinform Biol Insights* **2015**, *9* (Suppl 1), 29–46. https://doi.org/10.4137/BBI.S28991.

(131) Srivastava, H.; Lippincott, M. J.; Currie, J.; Canfield, R.; Lam, M. P. Y.; Lau, E. Protein Prediction Models Support Widespread Post-Transcriptional Regulation of Protein Abundance by Interacting Partners. *PLOS Computational Biology* **2022**, *18* (11), e1010702. https://doi.org/10.1371/journal.pcbi.1010702.

(132) Zhang, M.; Matyunina, L. V.; Walker, L. D.; Chen, W.; Xiao, H.; Benigno, B. B.; Wu, R.; McDonald, J. F. Evidence for the Importance of Post-Transcriptional Regulatory Changes in Ovarian Cancer Progression and the Contribution of miRNAs. *Sci Rep* **2017**, *7* (1), 8171. https://doi.org/10.1038/s41598-017-08502-z.

(133) Díez, P.; Droste, C.; Dégano, R. M.; González-Muñoz, M.; Ibarrola, N.; Pérez-Andrés, M.; Garin-Muga, A.; Segura, V.; Marko-Varga, G.; LaBaer, J.; Orfao, A.; Corrales, F. J.; De Las Rivas, J.; Fuentes, M. Integration of Proteomics and Transcriptomics Data Sets for the Analysis of a Lymphoma B-Cell Line in the Context of the Chromosome-Centric Human Proteome Project. *J. Proteome Res.* **2015**, *14* (9), 3530–3540. https://doi.org/10.1021/acs.jproteome.5b00474.

(134) Lee, J. M.; Hammarén, H. M.; Savitski, M. M.; Baek, S. H. Control of Protein Stability by Post-Translational Modifications. *Nat Commun* **2023**, *14* (1), 201. https://doi.org/10.1038/s41467-023-35795-8.

(135) Christopher, J. A.; Geladaki, A.; Dawson, C. S.; Vennard, O. L.; Lilley, K. S. Subcellular Transcriptomics and Proteomics: A Comparative Methods Review. *Molecular & Cellular Proteomics* **2022**, *21* (2), 100186. https://doi.org/10.1016/j.mcpro.2021.100186.
(136) Chandramouli, K.; Qian, P.-Y. Proteomics: Challenges, Techniques and Possibilities to Overcome Biological Sample Complexity. *Hum Genomics Proteomics* **2009**, *2009*, 239204. https://doi.org/10.4061/2009/239204.
(137) Dupree, E. J.; Jayathirtha, M.; Yorkey, H.; Mihasan, M.; Petre, B. A.; Darie, C. C. A Critical Review of Bottom-Up Proteomics: The Good, the Bad, and the Future of This Field. *Proteomes* **2020**, *8* (3), 14. https://doi.org/10.3390/proteomes8030014.
(138) Damiani, C.; Gaglio, D.; Sacco, E.; Alberghina, L.; Vanoni, M. Systems Metabolomics: From Metabolomic Snapshots to Design Principles. *Current Opinion in Biotechnology* **2020**, *63*, 190–199. https://doi.org/10.1016/j.copbio.2020.02.013.
(139) Radoš, D.; Donati, S.; Lempp, M.; Rapp, J.; Link, H. Homeostasis of the Biosynthetic *E. Coli* Metabolome. *iScience* **2022**, *25* (7). https://doi.org/10.1016/j.isci.2022.104503.
(140) Lempp, M.; Farke, N.; Kuntz, M.; Freibert, S. A.; Lill, R.; Link, H. Systematic Identification of Metabolites Controlling Gene Expression in *E. Coli*. *Nat Commun* **2019**, *10*, 4463. https://doi.org/10.1038/s41467-019-12474-1.
(141) Zampieri, M.; Zimmermann, M.; Claassen, M.; Sauer, U. Nontargeted Metabolomics Reveals the Multilevel Response to Antibiotic Perturbations. *Cell Reports* **2017**, *19* (6), 1214–1228. https://doi.org/10.1016/j.celrep.2017.04.002.
(142) Jozefczuk, S.; Klie, S.; Catchpole, G.; Szymanski, J.; Cuadros-Inostroza, A.; Steinhauser, D.; Selbig, J.; Willmitzer, L. Metabolomic and Transcriptomic Stress Response of *Escherichia Coli*. *Mol Syst Biol* **2010**, *6*, 364. https://doi.org/10.1038/msb.2010.18.
(143) Belhaj, M. R.; Lawler, N. G.; Hoffman, N. J. Metabolomics and Lipidomics: Expanding the Molecular Landscape of Exercise Biology. *Metabolites* **2021**, *11* (3), 151. https://doi.org/10.3390/metabo11030151.
(144) Fu, J.; Zhu, F.; Xu, C.; Li, Y. Metabolomics Meets Systems Immunology. *EMBO Rep* **2023**, *24* (4), e55747. https://doi.org/10.15252/embr.202255747.
(145) Metz, T. O.; Chang, C. H.; Gautam, V.; Anjum, A.; Tian, S.; Wang, F.; Colby, S. M.; Nunez, J. R.; Blumer, M. R.; Edison, A. S.; Fiehn, O.; Jones, D. P.; Li, S.; Morgan, E. T.; Patti, G. J.; Ross, D. H.; Shapiro, M. R.; Williams, A. J.; Wishart, D. S. Introducing 'Identification Probability' for Automated and Transferable Assessment of Metabolite Identification Confidence in Metabolomics and Related Studies. *bioRxiv* **2024**, 2024.07.30.605945. https://doi.org/10.1101/2024.07.30.605945.
(146) Spoto, M.; Riera Puma, J. P.; Fleming, E.; Guan, C.; Ondouah Nzutchi, Y.; Kim, D.; Oh, J. Large-Scale CRISPRi and Transcriptomics of *Staphylococcus Epidermidis* Identify Genetic Factors Implicated in Lifestyle Versatility. *mBio* **2022**, *13* (6), e0263222. https://doi.org/10.1128/mbio.02632-22.
(147) Hajnajafi, K.; Iqbal, M. A. Mass-Spectrometry Based Metabolomics: An Overview of Workflows, Strategies, Data Analysis and Applications. *Proteome Science* **2025**, *23*, 5. https://doi.org/10.1186/s12953-025-00241-8.
(148) Yuan, M.; Breitkopf, S. B.; Yang, X.; Asara, J. M. A Positive/Negative Ion–Switching, Targeted Mass Spectrometry–Based Metabolomics Platform for Bodily Fluids, Cells, and Fresh and Fixed Tissue. *Nat Protoc* **2012**, *7* (5), 872–881. https://doi.org/10.1038/nprot.2012.024.
(149) Gertsman, I.; Barshop, B. A. Promises and Pitfalls of Untargeted Metabolomics. *Journal of Inherited Metabolic Disease* **2018**, *41* (3), 355–366. https://doi.org/10.1007/s10545-017-0130-7.
(150) Fuhrer, T.; Heer, D.; Begemann, B.; Zamboni, N. High-Throughput, Accurate Mass Metabolome Profiling of Cellular Extracts by Flow Injection–Time-of-Flight Mass Spectrometry. *Anal. Chem.* **2011**, *83* (18), 7074–7080. https://doi.org/10.1021/ac201267k.
(151) Farke, N.; Schramm, T.; Verhülsdonk, A.; Rapp, J.; Link, H. Systematic Analysis of In-Source Modifications of Primary Metabolites during Flow-Injection Time-of-Flight Mass

Spectrometry. *Analytical Biochemistry* **2023**, *664*, 115036. https://doi.org/10.1016/j.ab.2023.115036.

(152) Xu, K.; Berthiller, F.; Metzler-Zebeli, B. U.; Schwartz-Zimmermann, H. E. Development and Validation of Targeted Metabolomics Methods Using Liquid Chromatography–Tandem Mass Spectrometry (LC-MS/MS) for the Quantification of 235 Plasma Metabolites. *Molecules* **2025**, *30* (3), 706. https://doi.org/10.3390/molecules30030706.

(153) Chen, S.; Kong, H.; Lu, X.; Li, Y.; Yin, P.; Zeng, Z.; Xu, G. Pseudotargeted Metabolomics Method and Its Application in Serum Biomarker Discovery for Hepatocellular Carcinoma Based on Ultra High-Performance Liquid Chromatography/Triple Quadrupole Mass Spectrometry. *Anal. Chem.* **2013**, *85* (17), 8326–8333. https://doi.org/10.1021/ac4016787.

(154) Zhang, X.; Zhu, X.; Wang, C.; Zhang, H.; Cai, Z. Non-Targeted and Targeted Metabolomics Approaches to Diagnosing Lung Cancer and Predicting Patient Prognosis. *Oncotarget* **2016**, *7* (39), 63437–63448. https://doi.org/10.18632/oncotarget.11521.

(155) Freiburghaus, K.; Largiadèr, C. R.; Stettler, C.; Fiedler, G. M.; Bally, L.; Bovet, C. Metabolomics by UHPLC–MS: Benefits Provided by Complementary Use of Q-TOF and QQQ for Pathway Profiling. *Metabolomics* **2019**, *15* (9), 120. https://doi.org/10.1007/s11306-019-1585-3.

Chapter 2: Construction and Validation of an Arrayed CRISPRi Library for the iML1515 Model

Contributions

All experimental work, data generation, figure preparation, and analysis presented in this chapter were carried out by the author (Andreas Verhülsdonk), unless stated below.

The pooled CRISPRi library design and construction was performed in Donati et al. Dr. Niklas Farke developed the custom MATLAB script used for sgRNA sequence validation. Cloning of additional or missing strains was supported by Dr. Alejandra Alverado and Felicia Troßmann. Screening and sequencing of strains was partially performed during my Master thesis.

Relevance

This chapter describes the transformation of a pooled CRISPRi library into an arrayed format serving as the basis for all subsequent experimental work. Through careful sequencing, verification, and strain selection, a high-confidence, fully arrayed library was established. This library enables single-strain resolution and reproducible gene knockdown studies, essential for the metabolic and stress-response investigations presented in Chapters 3, 4, and 6. Chapter 5 also builds upon this resource by application for refining sampling strategies.

Background

CRISPRi libraries enable scalable, genome-wide modulation of gene expression and have become central to modern bacterial genetics[1,2]. In pooled CRISPRi libraries, mixed populations containing sgRNAs that target different genes are used for high-throughput screens of gene functions under selective conditions[1,3]. However, while pooled CRISPRi libraries deliver an excellent tool for large-scale, cost-efficient screens, they do not allow insight into phenotypes past the population level[4]. Effects of individual strains like nutrient bottlenecks or lack of amino acid synthesis might be masked by those of others, and quantitative analysis can be impaired by cross-rescue effects[1,5]. The limitations of pooled libraries are especially evident when studying subtle phenotypic changes, complex cellular responses, or when reproducible validation of single gene knockdowns is required[6,7].

To overcome these limitations, pooled libraries can be transformed into arrayed formats. In arrayed libraries each strain carries a single sgRNA and is stored individually in microtiter plates. This format allows the investigation of gene functions on a single-strain basis, such as biochemical assays, growth measurements, or fluorescent microscopy[8–10]. It also enables integration with system-level methods like transcriptomics, metabolomics, or proteomics, which require well-defined, reproducible perturbation[11,12]. Arrayed libraries enable high-resolution phenotypic characterization without strain-competition effects and allow straightforward follow-up experiments[13].

This chapter describes the transformation of a pooled CRISPRi library into an arrayed format. Utilizing a previously established pooled library as a starting point, isolation of over 1,515 individual knockdown strains was achieved, including some redundancies to ensure robustness. The pooled library, developed by Stefano Donati, targets metabolic genes in *E. coli* with several sgRNAs per gene, based on the genome-scale metabolic model iML1515[11]. The resulting arrayed strain collection allowed high-resolution phenotypic analysis of defined gene knockdowns. Constructing the library required careful strain isolation, sgRNA verification, mutation identification, and large-scale organization to maintain strain identity and avoid contamination. It serves as the experimental foundation for stress-response and metabolic studies presented in Chapter 3 and Chapter 6, respectively.

Results

Isolation and Recovery of Individual CRISPRi Strains

The pooled CRISPRi library covers the *iML1515* genome-scale model with four to five sgRNA per gene[11,14]. The library was incubated for 3 hours in 5 mL LB medium and then plated in different dilutions on LB agar plates to find the best concentration for single colony formation (Figure 1A, B). Plates were incubated inverted overnight at 37°C. Dilutions of 5 x 10^5 delivered the best colony separation at high density (Figure 1C). This dilution was used to pick colonies, which were transferred to 96-deep-well plates filled with 500 µL LB medium (Figure 1D). Pipette tips were left in the deep-well plates to ensure transfer of only a single colony per well. Strains were incubated for 5 hours (h) at 37°C, 220 rpm and subsequently used for long-term glycerol stock generation (Figure 1E).

Colony picking focused on selecting regular-shaped, sufficiently large colonies spaced far enough apart to ensure single colony isolation. A total of 10,464 colonies across 109 plates were picked. Despite visible differences in cell density across isolates, all wells showed growth within 5 hours of incubation, confirmed by manual inspection rather than optical density (OD) readings or sequencing. The arrayed strains were then prepared for sequencing and analysis of sgRNA integrity.

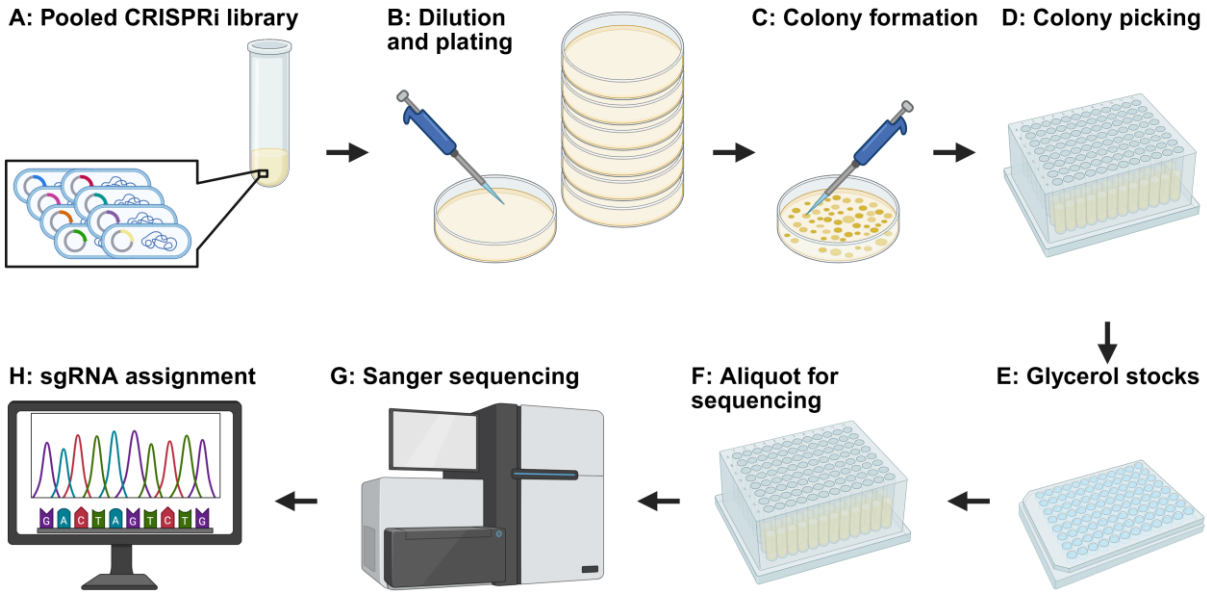

Figure 1. Workflow overview of sequencing and validation pipeline. (A) The pooled CRISPRi library was pre-incubated in LB medium. **(B)** Cells were plated in dilutions to obtain single colonies. **(C)** Colonies formed after overnight incubation at 37°C. **(D)** Individual colonies were picked and transferred to 96-deep-well plates. **(E)** Glycerol stocks for long-term storage. **(F)** An aliquot of each strain was incubated for 5 hours in LB prior to sequencing. **(G)** Sanger sequencing of single guide RNAs (sgRNAs). **(H)** Sequencing data analysis for sgRNA identification using a reference-matching pipeline.

sgRNA Identification and Quality Control

Strains were aliquoted from glycerol stocks, incubated in LB medium for 5 h, and then whole-cell samples were submitted for Sanger sequencing (Economy Run Plus, Microsynth) on a plate-by-plate basis (Figure 1F-G). The resulting sequences were compared to a database of all sgRNA sequences present in the pooled CRISPRi library, using a custom MATLAB script (Figure 1H).

Towards the end of sequencing, two plates were manually checked to evaluate the accuracy of the automated identification code. While the script correctly matched sgRNAs to the library based on fasta files, it did not consider base-level quality scores, which were provided in separate ai files. These included confidence values for each base. Reviewing these files revealed numerous false positives; sequences flagged as valid matches but contained stretches of low-confidence base calls. As a result, all sequencing results were manually reviewed.

Out of 10,416 total reads, 70% (n = 8,031) were identified as matches to expected sgRNAs, while the remaining 30% (n = 3,163) showed base substitutions, deletions, partial insertions, or were missing sgRNAs altogether, likely due to cloning failures or non-viable glycerol stocks (Figure 2A). After manual revalidation, 10% of matched sequences (n = 778) were excluded due to low confidence, resulting in 63% (n = 7,253) high-confidence strains available for downstream analysis.

Among the high confidence matches, 62.4% (n = 4,524) were unique sgRNAs, while the remaining 37.6% (n = 2,729) represented additional replicate strains (Figure 2B). Another 6.1% of the unique sgRNAs (n = 263) were discarded due to poor sequence confidence. Ultimately, a refined dataset of 4,261 unique, high confidence sgRNA strains were retained.

Each gene in the CRISPRi library was targeted by four to five sgRNAs, with sgRNA #1 located closest to the transcription start site and higher numbered sgRNA positioned progressively downstream. The distribution of sgRNA numbers was examined to ensure no bias existed in recovery rates (Figure 2C). sgRNA #1 to #4 appeared equally distributed, while sgRNA #5 occurred one-third less frequently. This discrepancy was attributed to the library design code: many genes only allowed for the design of four sgRNAs, due to their size or absence of suitable PAM sequences.

Next, the frequency of individual sgRNA occurrences was analyzed across the dataset (Figure 2D). Most sgRNAs were unique (30.6%) or appeared twice (30%), followed by triplicates (18.2%), quadruples (12%), and quintuples (4.8%). A small fraction (4.4%) appeared six or more times, with one sgRNA found in nine different strains.

In total, sequencing recovered 4,524 of the 7,184 unique sgRNAs in the pooled library, about 63% (Figure 2E, left). Despite the moderate sgRNA recovery rate, gene-level coverage was excellent: 1,467 out of 1,515 targeted genes were represented by at least one validated sgRNA, equating to 96.8% gene coverage (Figure 2E, right). This slight underrepresentation may have resulted from selection bias. Since only colonies of adequate size were picked, smaller colonies potentially affected by leaky dCas9 expression may have been overlooked.

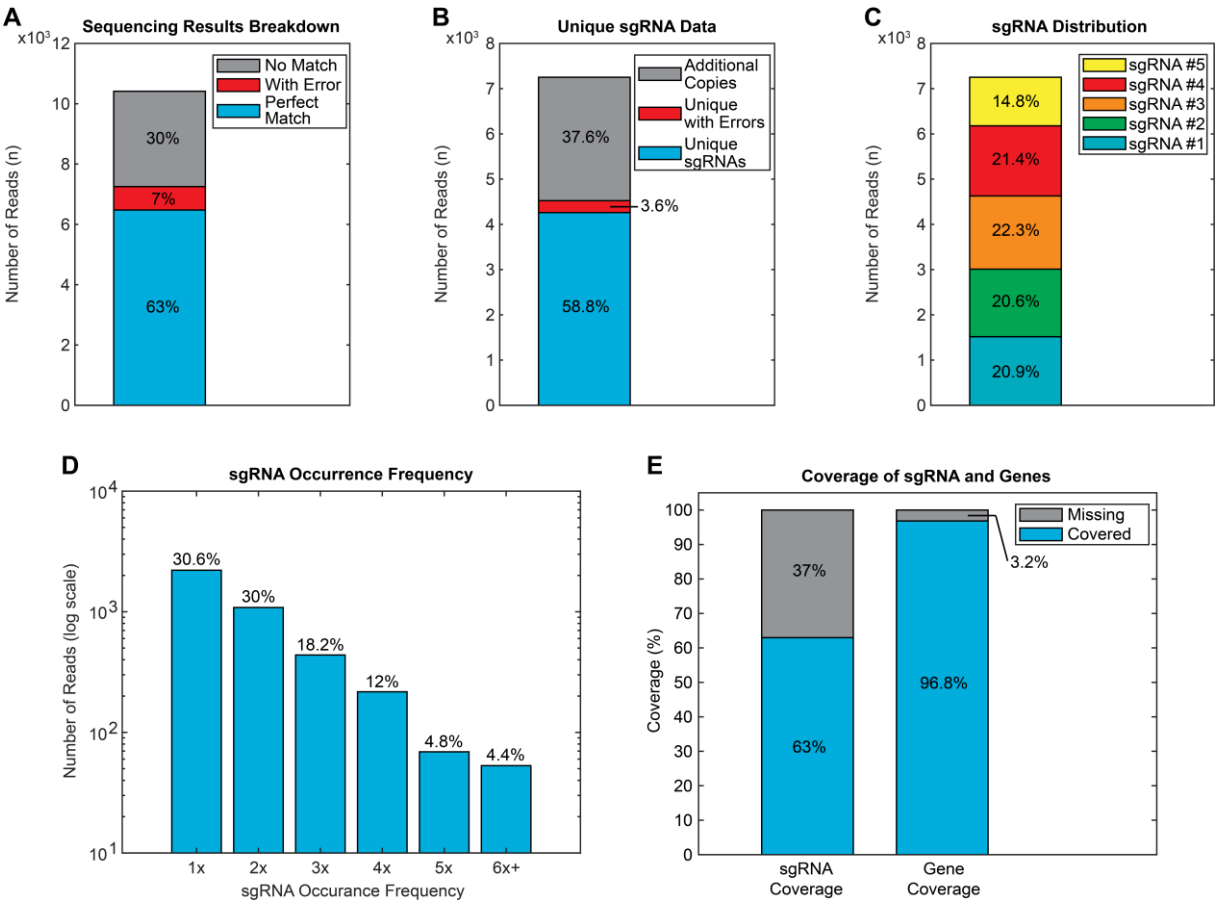

Figure 2. Summary of sequencing outcomes and single guide RNA (sgRNA) distribution in the arrayed CRISPR interference (CRISPRi) library. (A) Breakdown of total sequencing reads (n=10,416) into high confidence matches (63%, n=7,253), matches with low base quality (7%, n=778), and unmatching sequences (30%, n=3,163). **(B)** Classification of uniquely aligned sgRNA reads (n=7,253) into true unique sgRNA (58.8%, n=4,261), low confidence unique sequences (3.6%, n=263), and redundant replicates (37.6%, n=2,729). **(C)** Distribution of sgRNA positions (#1 - #5) among detected strains**. (D)** Frequency of sgRNA occurrence across strain plotted on a log scale (1x to 6x+). **(E)** sgRNA-level (n = 4,524 of 7,184) and gene-level (n = 1,467 of 1,515) coverage after validation. Gene coverage reflects representation by at least one high-confidence sgRNA.

sgRNA Selection and Library Assembly

Analysis of the reference sgRNA database showed that it only included 1,513 genes. Two small transporter subunit genes, *cydX* and *kdpF*, were missing. Upon inspection, their short sequences (114 base pair (bp) and 90 bp, respectively) limited the number of suitable PAM sites, resulting in only two potential sgRNAs per gene, which was below the design threshold of four. These sgRNAs were manually synthesized and cloned into the YY-dCas9 strain to increase genome coverage.

Previous studies have shown that sgRNAs targeting regions near the transcription start site are more effective, a finding also supported by internal work from our laboratory[11,15,16]. Therefore, for the remaining 46 underrepresented genes, sgRNA#1 was cloned by Felicia Troßmann to complete the set. For genes already represented by multiple sgRNAs, the sgRNA with the lowest number was selected for inclusion in the final library.

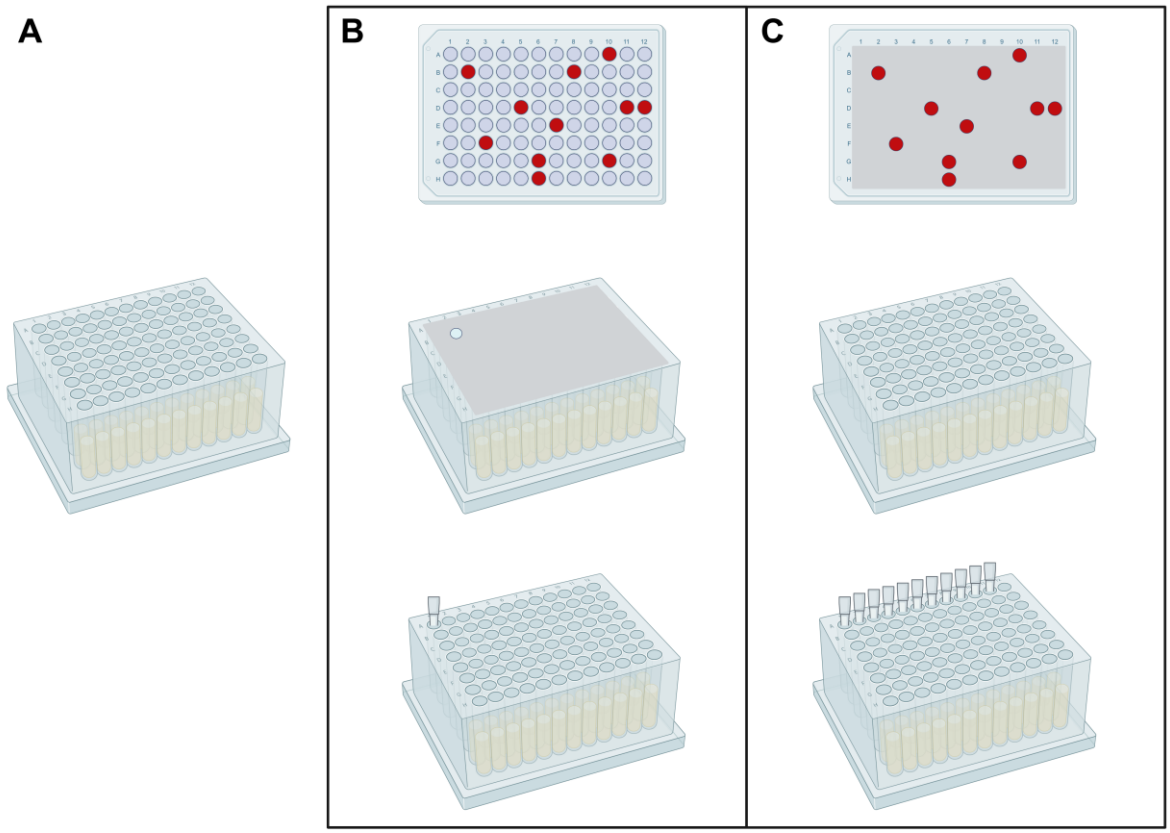

Figure 3. Workflow for validated strain transfer to the final arrayed library. (A) Original strain plates were inoculated from glycerol stocks and incubated in LB medium for 5 h. **(B)** Sterile aluminum foil was affixed to the top of each plate and punched through at inoculated positions according to the layout (top). Cultures were then transferred to a new plate (bottom), using another layout. Pipette tips were left in wells as transfer markers. **(C)** After transferring all cultures from a source plate, the punched foil was placed over the printed layout to visually confirm correct positions (top). Foils were UV-sterilized after use and stored for documentation.

Assembly of the arrayed library required a strict tracking system to ensure one strain per gene was transferred. Origin and destination wells were marked on color-coded layouts corresponding to 96-well plates. Each original library plate was fully inoculated and grown in LB for 5 hours (Figure 3A). Sterile aluminum foil was fixed over each plate (Figure 3B), and wells were punched through based on the layout. Once transfers were completed, the punched foils were aligned with printed layouts to confirm correct well identity (Figure 3C). After UV sterilization, these layouts were archived for quality assurance.

Final Library Validation

After assembly, the full library (16 plates) was re-sequenced to verify strain identities. Sixteen sgRNA errors were detected: 15 were corrected using backup replicates, and one was re-cloned. Multiple rounds of sequencing and error correction ultimately produced a fully validated, high-confidence arrayed CRISPRi library. In contrast to partially populated commercial libraries (e.g., KEIO), this library contains a defined strain in every well. Well A1 of each plate contains a control strain; the remaining 95 wells hold gene-specific knockdowns.

This library now includes knockdown strains for every gene in the iML1515 model. To validate its functional integrity, a genome-wide growth screen was performed in triplicates. Cultures were pre-grown in LB, transitioned to M9 overnight, diluted 50-fold into fresh M9 the next day, and induced with aTc for dCas9 activation following a 10-fold dilution. Growth was monitored for 24 hours.

Due to diverse growth patterns, some strains showed decreasing optical density at 600 nm (OD_{600}) over time or lacked clear exponential phases, metrics such as final OD_{600}, area under the curve (AUC), and lag time proved unreliable under these conditions. Instead, two parameters were used: growth rate (μ) and carrying capacity (K), which are less dependent on starting or ending OD.

Control strains demonstrated highly consistent growth, with μ values ranging from 0.85 to 1.1 and a median near 1 (Figure 4A, left). K values clustered tightly around 1.45 (Figure 4A, right). The Coefficient of Variation (CV) confirmed this reproducibility: K values were below 0.05 for all controls (Figure 4B), and μ values were below 0.1 in all but two strains.

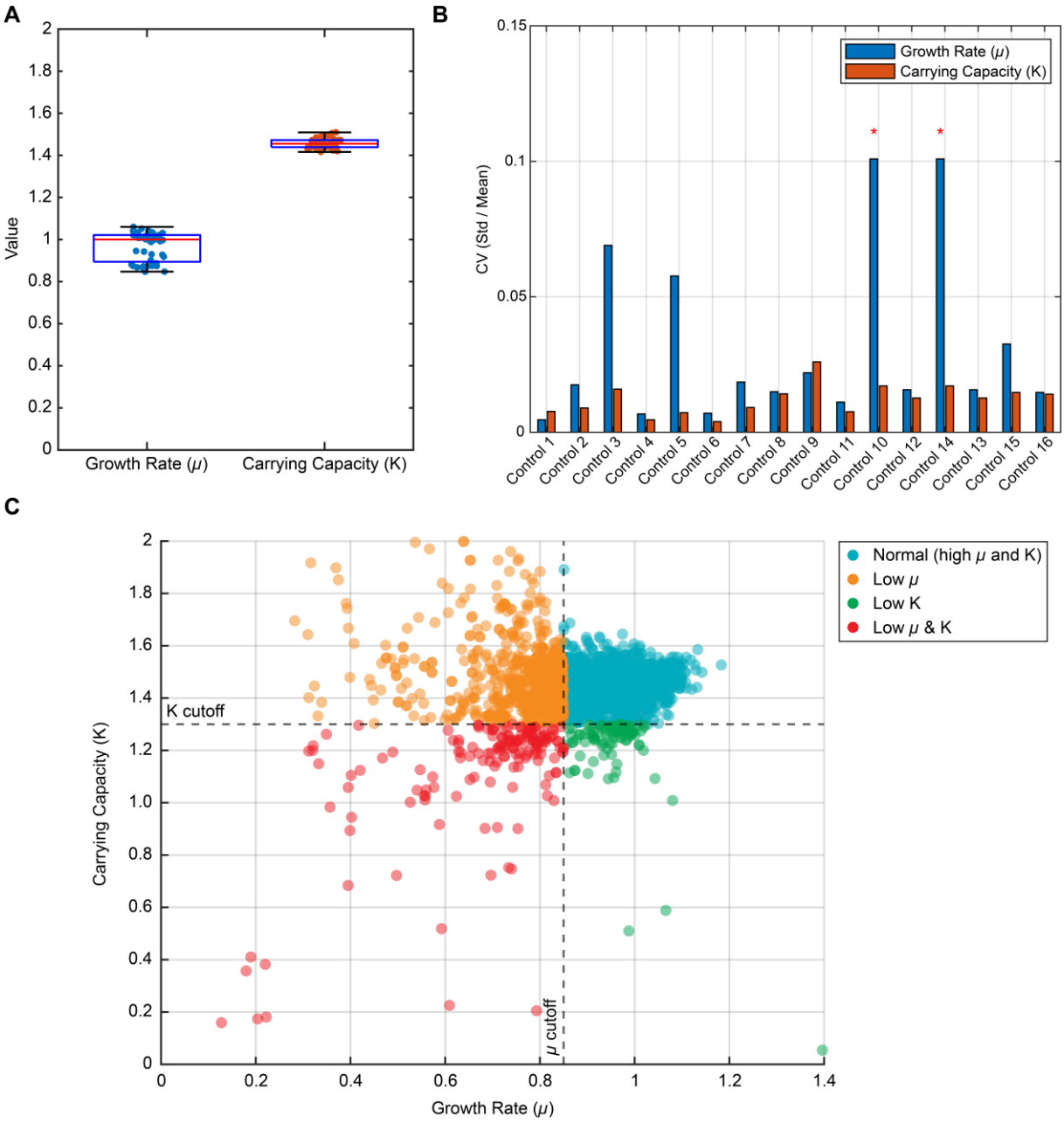

Figure 4. Growth screen analysis and classification of phenotypic responses across the arrayed CRISPR interference (CRISPRi) library. (A) Growth Rate (μ) and Carrying Capacity (K) of control strains (n =16 strains x 3 replicates). **(B)** Coefficient of Variation (CV) for μ and K across all control replicates (n=3 per control) illustrating reproducibility. Strains with CV > 0.1 are marked with asterisk (*). **(C)** Plot of carrying capacity against growth rate across all successfully fitted replicates (n=3,988). Cutoffs were set to 0.15 below the median of controls.

Phenotypic Classification of Knockdown Strains

To better understand the growth dynamics within the CRISPRi library screen, carrying capacity was plotted against the growth rate for all successfully fitted knockdown replicates (Figure 4C). In total, 3.8% of replicates (n = 172) were excluded from the μ dataset due to lack of growth or measurement artifacts, while 12.5% (n = 569) were excluded from the K dataset either due to failed model fitting or resulting in biologically implausible values exceeding K = 2. These replicates were excluded from further analysis and classified as phenotypic outliers according to the defined criteria.

For the remaining 3,988 replicates, a classification was performed using cutoffs defined as 0.15 units below the respective control medians for μ and K. Of these, 2,670 replicates (67%) exhibited both μ and K values above the respective cutoffs and were interpreted as unaffected by the knockdown, consistent with control-like growth behavior (Figure 4C, blue). A substantial fraction of replicates (n = 1,064; 27%) showed reduced growth rates (μ ≤ 0.85) but maintained normal carrying capacity, suggesting a delay in growth kinetics while still reaching typical cell densities (Figure 4C, orange). In contrast, 91 replicates (2%) exhibited normal growth rates but reduced carrying capacities, indicating cultures that initially grow at a normal rate but fail to sustain population levels, possibly due to downstream effects such as metabolic stress, resource limitations, or toxic byproduct accumulation (Figure 4C, green). Finally, 164 replicates (4%) showed impairments in both μ and K, representing strains with severe growth defects, which likely involve knockdowns of genes essential for key cellular functions such as biomass production, division, or membrane maintenance (Figure 4C, red).

These results confirm that the arrayed CRISPRi library is both genetically validated and phenotypically stable. The consistency of growth in control strains and the clear separations of knockdown phenotypes support reliability of this library for further research. Over 1,500 gene knockdowns are represented, and growth data is reproducible across replicates, providing a reliable resource for systematic analysis of gene functions in *E. coli*.

Conclusion

The transformation of the pooled CRISPRi library into an arrayed format represents an important step forward in functional metabolomics studies of *E. coli*. Over 4,200 unique knockdown strains were recovered and validated through a systematic workflow, including the joined use of colony isolation, sgRNA validation, and rigorous quality controls. The sgRNA level recovery of 63% was exceeded by 96% coverage on the gene level, indicating that the observed deficit is most probably a stochastic effect rather than dCas9 leakiness.

The development of a tracking system and sequencing validation workflow was essential for successful library assembly, allowing construction of a comprehensive library while ensuring strain reliability. Importantly, each well of the final 96-well plate format contains a functional, validated strain, representing a major improvement over partially filled commercial libraries.

The arrayed CRISPRi library allowed for precise assessment of individual gene knockdowns on cell growth. By using growth rate and carrying capacity as metrics, consistent evaluation on strain responses was determined. While most strains grew similarly to controls, over 30% showed noticeable changes. These perturbed phenotypes include slower growth, lower final cell density, or both. This highlights a widespread but highly variable response to gene knockdowns.

The CRISPRi library in arrayed format provides a reliable and versatile resource for studying gene function in *E. coli* on a single-strain level, avoiding the limitations of pooled approaches**.** In the next chapters, this resource was used to explore stress responses and metabolic pathways in more detail.

Material and Methods

Cultivation and Media

Cultivation was performed in LB medium (L3522, Sigma Aldrich) or M9 minimal medium with 5 g/l glucose as the sole carbon source. M9 medium contained (per liter): 7.52 g $Na_2HPO_4\,2H_2O$, 5 g KH_2PO_4, 1.5 g $(NH_4)_2SO_4$, 0.5 g NaCl, 10 mL trace salts solution, 2 mL 1.4 mM thiamine-HCl, 1 mL 1 M $MgSO_4$, 1 mL 0.1 M $CaCl_2$ and 0.6 mL 0.1 M $FeCl_3$. The trace salt solution (per liter) was composed of 180 mg $CoCl_2\,6H_2O$, 180 mg $ZnSO_4\,7H_2O$, 120 mg $MnSO_4\,H_2O$, 120 mg $CuCl_2\,2H_2O$. All media contained 100 µg/mL ampicillin (Amp). For dCas9 induction, 200 nM anhydrotetracycline (aTc) was added to M9 medium. LB agar plates contained 15 g/L Agar-Agar (2266.1, Roth).

Strain Cultivation and Arraying

The pooled CRISPRi library was incubated in LB for 3 h at 37°C, 220 rpm. Cultures were diluted 1:5×10⁵ and plated on 150×20 mm LB agar plates, then incubated inverted overnight at 37°C. Colonies with typical morphology and spacing were picked and transferred into 96-deep-well plates (500 µL LB/well). Tips were left in place to avoid picking twice. After 5 h of incubation at 37°C, 220 rpm, 105 µL of culture was mixed with 45 µL of 87% glycerol (glycerol:H_2O) in flat-bottom 96-well plates, sealed with adhesive aluminum foil, and stored at -80°C.

Sanger Sequencing and Data Analysis

Strains were revived in 500 µL LB and grown for 5 h at 37°C, 220 rpm before sending 50 µL for Sanger sequencing (Economy Run Plus, Microsynth). Sequencing results (fasta and ai formats) were matched to the pooled sgRNA database using a custom MATLAB script (MathWorks 2022, provided by Dr. Niklas Farke). High-confidence sequences were confirmed manually by inspecting base confidence in Benchling.

sgRNA Selection and Library Assembly

Custom MATLAB scripts were used to evaluate sgRNA coverage per gene. The sgRNA with the lowest number was preferred. Missing genes were identified by comparing to the iML1515 model. For missing targets, sgRNA #1 sequences were extracted, synthesized, and cloned into the YY-dCas9 strain. For library assembly, source and destination wells were marked on color-coded 96-well layouts.

Dr. Alejandra Alverado created a focused sub-library targeting essential genes, selecting the best-performing sgRNAs for each. Where essential genes lacked guide #1, they were cloned and added manually. This sub-library was used to replace higher-numbered sgRNAs in the main library with upstream sgRNAs wherever possible.

Strain Transfer Validation and Quality Control

Original plates were incubated in LB for 5 h at 37°C, 220 rpm. Sterile aluminum foil was affixed to the plates, and strains were transferred to new plates by puncturing the foil using the pre-annotated layout. After transfer, foils were placed over printed layouts to confirm correct punching. New plates were frozen in glycerol as described above. Used aluminum foils were UV-sterilized and archived.

Growth Screen and Parameter Analysis

Strains were grown in 96-deep-well plates for 5 h at 37°C, 220 rpm in LB and then diluted 1:100 into M9 for overnight growth at 37°C, 220 rpm. Cultures were then diluted 100-fold again and grown for 6.5 h at 37°C, 800 rpm in a plate reader (LogPhase600, Agilent), with OD readings every 10 min. Cultures were subsequently diluted 1:50 into M9 + aTc and measured for 24 h under the same conditions. OD values were converted to OD_{600}, smoothed, and used to calculate growth rate and carrying capacity using custom MATLAB scripts. Cutoffs were defined based on control strain distributions.

Bibliography

(1) Wang, T.; Guan, C.; Guo, J.; Liu, B.; Wu, Y.; Xie, Z.; Zhang, C.; Xing, X.-H. Pooled CRISPR Interference Screening Enables Genome-Scale Functional Genomics Study in Bacteria with Superior Performance. *Nat Commun* **2018**, *9* (1), 2475. https://doi.org/10.1038/s41467-018-04899-x.

(2) de Bakker, V.; Liu, X.; Bravo, A. M.; Veening, J.-W. CRISPRi-Seq for Genome-Wide Fitness Quantification in Bacteria. *Nat Protoc* **2022**, *17* (2), 252–281. https://doi.org/10.1038/s41596-021-00639-6.

(3) Bock, C.; Datlinger, P.; Chardon, F.; Coelho, M. A.; Dong, M. B.; Lawson, K. A.; Lu, T.; Maroc, L.; Norman, T. M.; Song, B.; Stanley, G.; Chen, S.; Garnett, M.; Li, W.; Moffat, J.; Qi, L. S.; Shapiro, R. S.; Shendure, J.; Weissman, J. S.; Zhuang, X. High-Content CRISPR Screening. *Nat Rev Methods Primers* **2022**, *2* (1), 8. https://doi.org/10.1038/s43586-021-00093-4.

(4) Meyers, S.; Demeyer, S.; Cools, J. CRISPR Screening in Hematology Research: From Bulk to Single-Cell Level. *Journal of Hematology & Oncology* **2023**, *16* (1), 107. https://doi.org/10.1186/s13045-023-01495-5.

(5) Torelli, F.; da Fonseca, D. M.; Butterworth, S. W.; Young, J. C.; Treeck, M. Paracrine Rescue of MYR1-Deficient *Toxoplasma Gondii* Mutants Reveals Limitations of Pooled in Vivo CRISPR Screens. *Elife* **2024**, *13*, RP102592. https://doi.org/10.7554/eLife.102592.

(6) Duan, B.; Zhou, C.; Zhu, C.; Yu, Y.; Li, G.; Zhang, S.; Zhang, C.; Ye, X.; Ma, H.; Qu, S.; Zhang, Z.; Wang, P.; Sun, S.; Liu, Q. Model-Based Understanding of Single-Cell CRISPR Screening. *Nat Commun* **2019**, *10* (1), 2233. https://doi.org/10.1038/s41467-019-10216-x.

(7) Lanning, B. R.; Vakoc, C. R. Single-Minded CRISPR Screening. *Nat Biotechnol* **2017**, *35* (4), 339–340. https://doi.org/10.1038/nbt.3849.

(8) St. Pierre, J.; Roberts, J.; Alam, M. A.; Shields, R. C. Construction of an Arrayed CRISPRi Library as a Resource for Essential Gene Function Studies in *Streptococcus Mutans*. *Microbiology Spectrum* **2023**, *12* (1), e03149-23. https://doi.org/10.1128/spectrum.03149-23.

(9) Ishikawa, K.; Soejima, S.; Nishimura, T.; Saitoh, S. Arrayed CRISPRi Library to Suppress Genes Required for *Schizosaccharomyces Pombe* Viability. *Journal of Cell Biology* **2024**, *224* (1), e202404085. https://doi.org/10.1083/jcb.202404085.

(10) Jana, B.; Liu, X.; Dénéréaz, J.; Park, H.; Leshchiner, D.; Liu, B.; Gallay, C.; Zhu, J.; Veening, J.-W.; van Opijnen, T. CRISPRi–TnSeq Maps Genome-Wide Interactions between Essential and Non-Essential Genes in Bacteria. *Nat Microbiol* **2024**, *9* (9), 2395–2409. https://doi.org/10.1038/s41564-024-01759-x.

(11) Donati, S.; Kuntz, M.; Pahl, V.; Farke, N.; Beuter, D.; Glatter, T.; Gomes-Filho, J. V.; Randau, L.; Wang, C.-Y.; Link, H. Multi-Omics Analysis of CRISPRi-Knockdowns Identifies Mechanisms That Buffer Decreases of Enzymes in *E. Coli* Metabolism. *Cell Systems* **2021**, *12* (1), 56-67.e6. https://doi.org/10.1016/j.cels.2020.10.011.

(12) Fang, L.; Hao, X.; Fan, J.; Liu, X.; Chen, Y.; Wang, L.; Huang, X.; Song, H.; Cao, Y. Genome-Scale CRISPRi Screen Identifies pcnB Repression Conferring Improved Physiology for Overproduction of Free Fatty Acids in *Escherichia Coli*. *Nat Commun* **2025**, *16* (1), 3060. https://doi.org/10.1038/s41467-025-58368-3.

(13) Yin, J.-A.; Frick, L.; Scheidmann, M. C.; Liu, T.; Trevisan, C.; Dhingra, A.; Spinelli, A.; Wu, Y.; Yao, L.; Vena, D. L.; Knapp, B.; Guo, J.; De Cecco, E.; Ging, K.; Armani, A.; Oakeley, E. J.; Nigsch, F.; Jenzer, J.; Haegele, J.; Pikusa, M.; Täger, J.; Rodriguez-Nieto, S.; Bouris, V.; Ribeiro, R.; Baroni, F.; Bedi, M. S.; Berry, S.; Losa, M.; Hornemann, S.; Kampmann, M.; Pelkmans, L.; Hoepfner, D.; Heutink, P.; Aguzzi, A. Arrayed CRISPR Libraries for the Genome-Wide Activation, Deletion and Silencing of Human Protein-Coding Genes. *Nat. Biomed. Eng* **2025**, *9* (1), 127–148. https://doi.org/10.1038/s41551-024-01278-4.

(14) Monk, J. M.; Lloyd, C. J.; Brunk, E.; Mih, N.; Sastry, A.; King, Z.; Takeuchi, R.; Nomura, W.; Zhang, Z.; Mori, H.; Feist, A. M.; Palsson, B. O. iML1515, a Knowledgebase That Computes *Escherichia Coli* Traits. *Nat Biotechnol* **2017**, *35* (10), 904–908. https://doi.org/10.1038/nbt.3956.
(15) Momen-Roknabadi, A.; Oikonomou, P.; Zegans, M.; Tavazoie, S. An Inducible CRISPR Interference Library for Genetic Interrogation of *Saccharomyces Cerevisiae* Biology. *Commun Biol* **2020**, *3*, 723. https://doi.org/10.1038/s42003-020-01452-9.
(16) Smith, J. D.; Suresh, S.; Schlecht, U.; Wu, M.; Wagih, O.; Peltz, G.; Davis, R. W.; Steinmetz, L. M.; Parts, L.; St.Onge, R. P. Quantitative CRISPR Interference Screens in Yeast Identify Chemical-Genetic Interactions and New Rules for Guide RNA Design. *Genome Biology* **2016**, *17* (1), 45. https://doi.org/10.1186/s13059-016-0900-9.

Chapter 3: Lower Abundance of ATPase and Pyruvate Kinase Reduces Susceptibility of *E. coli* to Fosfomycin

Contributions

This chapter contains a manuscript submitted on 2025.07.14 to ACS infectious diseases with the title “CRISPRi identifies metabolic genes that reduce susceptibility of *E. coli* to fosfomycin“ and is currently under revision (as of August 2025). Author contributions are listed on the table below.

Author	Author position	Scientific ideas %	Data generation %	Analysis & interpretation %	Paper writing %
Andreas Verhülsdonk	1	80	95	80	50
Amelie Stadelmann	2	0	4	0	0
Johanna Rapp	3	0	1	0	0
Hannes Link	4	20	0	20	50
Title of paper:		CRISPRi identifies metabolic genes that reduce susceptibility of *E. coli* to Fosfomycin			
Status of publication process		Submitted to ACS infectious diseases			

Relevance

This chapter investigates how gene knockdowns influence antibiotic stress responses in *E. coli*. Using the arrayed CRISPRi library established in Chapter 2, strains were screened against Fosfomycin at concentrations well above the minimal inhibitory concentration (MIC), enabling the identification of tolerant, resistant, and heteroresistant phenotypes. This work represents the first major application of the library, complemented by the metabolomics screen presented in Chapter 6.

CRISPR interference identifies metabolic genes that reduce susceptibility of *E. coli* to fosfomycin

Andreas Verhülsdonk[1,2,3], Amelie Stadelmann[1,2,3], Johanna Rapp[1,2,3], Daniel Straub[3,4], Hannes Link[1,2,3]

[1]Interfaculty Institute of Microbiology and Infection Medicine, University of Tübingen, 72076 Tübingen, Germany

[2]Cluster of Excellence "Controlling Microbes to Fight Infections", University of Tübingen, 72076 Tübingen, Germany

[3]M3 Research Center, University of Tübingen, Otfried-Müller-Str. 37, 72076 Tübingen, Germany

[4]Quantitative Biology Center (QBiC), University of Tübingen, Otfried-Müller-Str. 37, 72076 Tübingen, Germany

Corresponding author: hannes.link@uni-tuebingen.de

Abstract

The phosphonic antibiotic fosfomycin is a bacterial cell wall synthesis inhibitor that targets MurA, the first enzyme in the peptidoglycan pathway. Transporter loss or enzymatic inactivation confers resistance to fosfomycin, but whether the metabolic state of a bacterium influences the efficacy of this antibiotic has not been characterized. Here, we used an *Escherichia coli* CRISPR interference library targeting 1,515 metabolic genes to identify metabolic activities that influence fosfomycin susceptibility. We discovered that knockdowns of ATP synthase and pyruvate kinase genes led to a regrowth phenotype, whereby cells resumed growth after an initial phase of killing. By following up on this phenotype with resistance and time-kill assays, as well as repeated treatment cycles, we found evidence that a heteroresistant population may promote evolution of major fosfomycin resistance. Metabolome analysis showed accumulation of the MurA substrate phosphoenolpyruvate in regrowing cells, which may prevent fosfomycin binding to MurA. Transcriptome analysis provided further insight into the mechanism of cell regrowth, such as upregulation of genes encoding cell envelope stress response regulators like *cpxP*. These results suggest that the metabolic state can modulate fosfomycin efficacy and contribute to resistance evolution.

Introduction

Escherichia coli is a bacterial pathogen that causes urinary tract infections (UTIs), bloodstream infections, and intra-abdominal infections[1]. Because *E. coli* strains are developing resistances against various antibiotics, fosfomycin has become clinically relevant again although it is on the WHO reserve and watch group[2]. Fosfomycin is a phosphonic acid-derived antibiotic that inhibits bacterial cell wall synthesis by targeting the enzyme UDP-N-acetylglucosamine enolpyruvyl transferase (MurA). MurA catalyzes the first commitment step in peptidoglycan synthesis and converts UDP-*N*-acetyl-α-D-glucosamine and phosphoenolpyruvate (PEP) to UDP-*N*-acetyl-α-D-glucosamine-enolpyruvate. Fosfomycin is a structural analog of PEP and covalently binds at the MurA active site.

Although fosfomycin is highly effective in killing bacterial cells, *E. coli* can evolve resistance against fosfomycin by mutations that affect the GlpT and UhpT transporters, which are required for drug uptake, as well as through the acquisition of plasmids encoding fosfomycin-modifying enzymes like the glutathione S-transferase FosA, which enzymatically inactivate the antibiotic[2–5]. In addition to such canonical resistance mechanisms, recent studies suggest that bacteria can evade killing of antibiotics like fosfomycin without acquiring resistance mutations[6]. For example, bacteria can enter a state of *persistence*, which is characterized by the presence of a cell subpopulation that is tolerant to the antibiotic and therefore can survive antibiotic exposure and recover after the treatment[7,8]. A similar phenomenon called *heteroresistance* describes the emergence of a cell subpopulation that is able to grow in the presence of antibiotics[7,9]. The resulting resistant population reverts to its original sensitive state over the next generations once the antibiotic is removed[7,9]. Persistence and heteroresistance can contribute to treatment failure and even promote the development of canonical resistance such as mutations in the drug target[10,11].

Reduced metabolic activities can also decrease the efficacy of antibiotics[12]. In case of fosfomycin, mutations in genes that are involved in the synthesis of the regulatory metabolite cyclic AMP (cAMP) like *ptsI* or *cyaA* can decrease the concentration of cAMP, which in turn decreases the expression of GlpT and UhpT, thus reducing fosfomycin uptake[3,13]. In *Staphylococcus aureus*, the concentration of PEP is thought to influence the efficacy of fosfomycin[14], although evidence for changes in PEP levels is missing. Mutations in UhpA, a direct regulator of the UhpT transporter, also increase fosfomycin survival rates[15]. Moreover, recent studies have shown that fosfomycin also relies on outer membrane porins OmpF, OmpC and LamB to enter the cell, and mutations in these genes confer fosfomycin resistance[4]. Furthermore, phosphonate degradation enzymes and phosphate transporters, identified via high-density transposon mutagenesis, are suspected to modulate the transport systems by affecting intracellular phosphate levels[16].

Here we sought to systematically identify metabolic activities that change the susceptibility of *E. coli* to fosfomycin. Therefore, we measured growth of a metabolism-wide CRISPR interference (CRISPRi) library[17] during fosfomycin treatment. The library comprises 1,515 *E. coli* strains each with a knockdown of a single metabolic gene in the iML1515 metabolic model of *E. coli*[18]. Using this large-scale functional genomics approach, we identified genes that influence susceptibility of *E. coli* to fosfomycin. We then followed up on top hits from this screen, which are CRISPRi strains that target ATP synthetase (*atpH*) and pyruvate kinases (*pykF* and *pykA*), and found evidence that heteroresistance causes a shift in fosfomycin susceptibility that promotes evolution of major resistance mechanisms.

Results

We screened an *E. coli* CRISPRi library[17] against fosfomycin which targets each metabolic gene in the metabolic model iML1515[18]. The CRISPRi strains have an anhydrotetracycline (aTc)-inducible dCas9 on the genome and a sgRNA on a plasmid, which enables dynamic knockdowns of all metabolism-related genes (Figure 1A). For the screen, we arrayed 1,515 CRISPRi strains on 96-well plates, each targeting one of the 1,515 genes in iML1515.

First, we used a control strain with a non-targeting sgRNA to determine the minimal inhibitory concentration (MIC) against fosfomycin in liquid broth assays (Supplementary Figure 1). At a fosfomycin concentration of 76 µg/mL the control strain showed no growth over a period of 24 h and we used this concentration of fosfomycin as the MIC in this study. For the CRISPRi screen, we added 304 µg/mL (4X MIC) fosfomycin 6.5 h after induction of dCas9 (Figure 1A). After the addition of fosfomycin the optical density at 600 nm (OD_{600}) of the control strain culture increased for almost 1 h followed by an OD_{600} decrease, presumably due to cell lysis (Figure 1B). We systematically assigned the strains to four categories by scoring OD time profiles. Category 1 included 1477 strains that exhibited a response similar to the control upon fosfomycin treatment, suggesting that the knockdown did not affect their susceptibility to fosfomycin. Category 2 consisted of 16 strains with a markedly longer cell lysis phase indicating that the knockdown influenced bactericidal activity of fosfomycin (Figure 1C). Category 3 included 15 strains that responded like the control during the first cultivation phase but re-grew at later time points (>9 h, Figure 1D). Finally, category 4 consisted of 7 strains that showed no reduction in OD, and they slowly grew during the 24-hours (Figure 1E), thus indicating low-level resistance against fosfomycin.

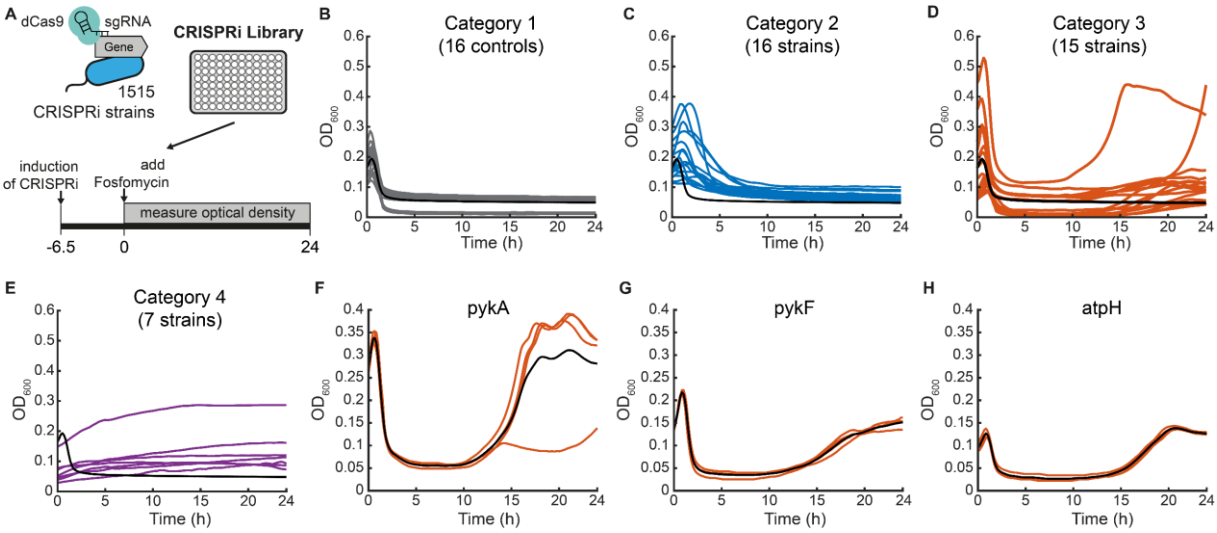

Figure 1. A CRISPRi screen identifies metabolic genes that influence the response of *E. coli* to fosfomycin. (**A)** Schematic of the CRISPRi library antibiotics screen. The library containing 1515 CRISPRi strains was induced with aTc for 6.5 h and subsequently cultivated for another 24 h in medium containing 304 µg/mL fosfomycin (n=2). **(B)** Response of controls (n=16) to addition of fosfomycin at t=0. **(C)** Strains in category 2 (16 strains) have an OD_{600} decrease phase at least 2x longer than controls (black line, n = 16) and were categorized as reduced killing phenotypes. **(D)** Strains in category 3 (15 strains) grew like controls in the first phase (<9 h) and showed OD_{600} increases in later phases (>9 h). **(E)** Strains in category 4 showed increases in OD_{600}. **(F)** Validation of the regrowth phenotype in the pykA strain (n = 4). The black line is the mean. **(G)** Same as (F) for the pykF strain (n = 4). **(H)** same as (F) for the atpH strain (n=4). Note that the black line in B-E shows the same mean of controls (n=16) as a reference.

To confirm the phenotypes of all 38 strains from category 2-4, we repeated the experiment. The list of 38 strains for validation was extended by strains not detected in the initial screen for the remaining ATP synthase genes (3) and the pyruvate kinase 1 gene (*pykF*) since the strongest re-growth phenotype was the pyruvate kinase 2 (*pykA*) knockdown (Supplementary Table 1). The growth pattern of all strains was confirmed, except the knockdown of the gene encoding the glycine betaine ABC transporter membrane subunit YehY, which grew like the control in all four replicates (Supplementary Figure 2).

Next, we focused on the 15 strains that regrew after the initial phase, which we will refer to as re-growth phenotype. The pykA and pykF strains both showed the re-growth phenotype (Figure 1 F, G). The difference in the intensity of the regrowth phenotype is probably due to the different activity of pyruvate kinases 1 and 2 under different levels of oxygen supply[19]. All ATP synthase knockdown strains showed the re-growth phenotype, which means that decreasing the abundance of a subunit of the ATP synthase or associated proteins (AtpI) led to the regrowth phenotype (Figure 1H, Supplementary Figure 2).

To assess if the CRISPRi strains with regrowth phenotype had MIC increases relative to the control strain, we measured MICs of all 15 strains using agar dilution assays[20] (Supplementary Figure 3). No tangible MIC changes were observed, except for the waaF, lpxL and pykF strains. The waaF and lpxL strains showed bloated colonies at 76 µg/mL, consistent with the reported increase in biofilm formation upon deletion of *waaF*[21]. Biofilm formation also increases when lipopolysaccharide synthesis is perturbed, which can explain the phenotype of the lpxL strain[21]. Thus, the only strain that showed a markedly higher MIC was the pykF strain, which grew at 2X higher fosfomycin levels than the control strain. This is consistent with recent studies that have shown that mutations in *pykF* increase fosfomycin survival rates in uropathogenic *E. coli*[22].

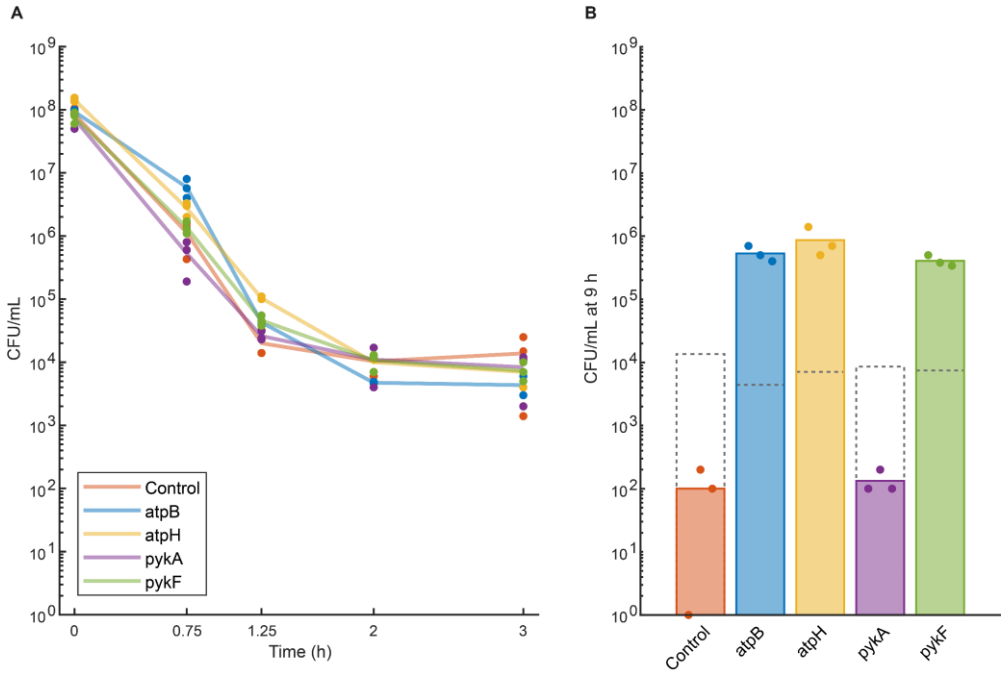

Figure 2. The pykF, atpH and atpB strain increase colony forming units after initial killing. (A) Time kill assay with CRISPRi strains (control, atpB, atpH, pykF, pykA). Strains were incubated for 9 hours in minimal glucose medium containing aTc and 304 µg/mL fosfomycin (n=3). Before treatment, all strains reached exponential growth at OD_{600} >0.25. Lines indicate mean of n=3 replicates, and dots individual replicates. Live cells per mL were determined by counting colony forming units. **(B)** Live cells per mL after 9 hours treatment. Dashed lines are the means of the 3 h timepoint.

Next, we focused on the killing activity of fosfomycin in the CRISPRi strains and measured colony forming units (CFUs) of the atpH strain, atpB strain, pykF strain, pykA strain and the control strain after various times of fosfomycin treatment (Figure 2). During the first 3 h of fosfomycin treatment the killing activity was almost identical in all strains, and CFUs decreased by 90-95% (Figure 2A). Killing during this phase is consistent with the results of the CRISPRi screen, where strains with a re-growth phenotype responded similar to the control strain in the initial phase of treatment. However, after 9 h treatment we observed an increase in CFUs for the pykF, atpH, and atpB strains, whereas the pykA and control strain showed hardly any CFUs (Figure 2B). Thus, the regrowth phenotype of the pykF, atpH and atpB strains is an active increase in cell number, which could be due to a subpopulation that is resistant to fosfomycin (heteroresistance).

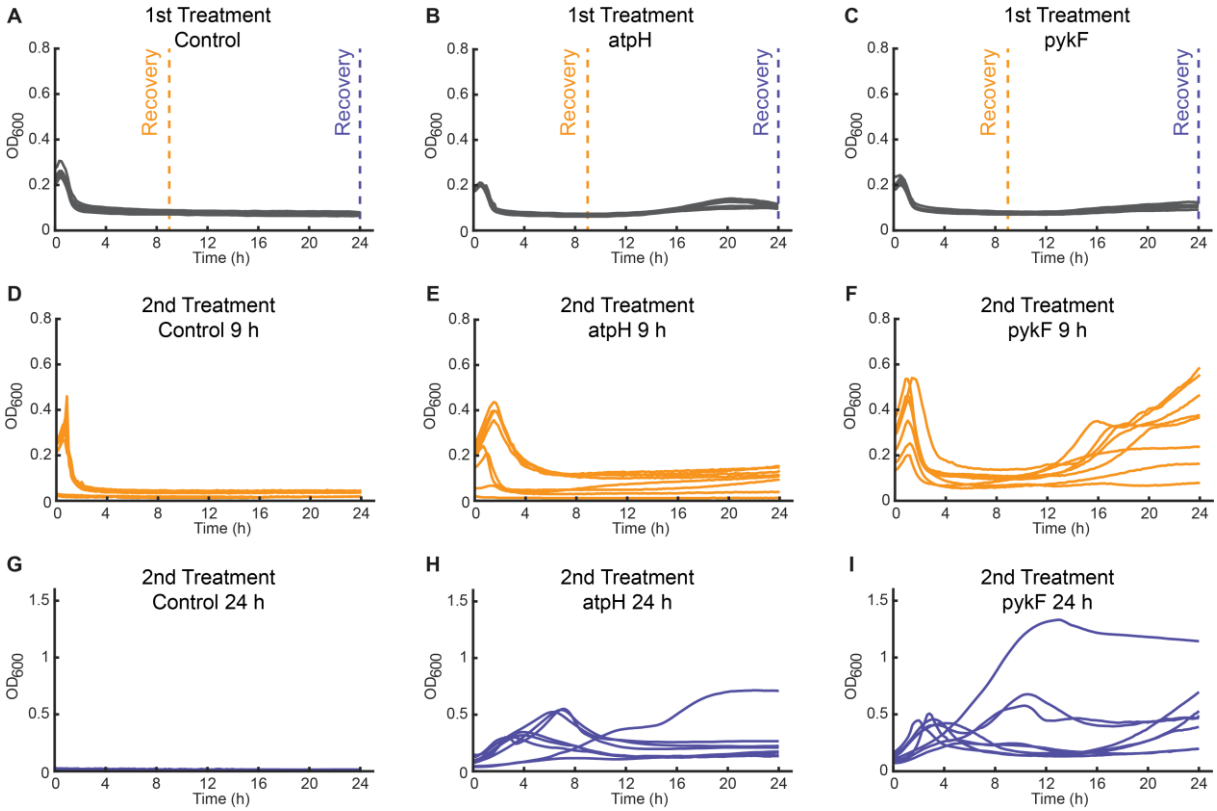

Figure 3. Response of the control strain, the pykF strain and the atpH strain to repeated fosfomycin treatment. (A-C) The control strain (A), atpH strain (B), and pykF strain (C) were treated with 304 µg/mL fosfomycin (n=8). Cells were collected after 9 h (orange line) and 24 h (blue line) and recovered in drug-free rich LB medium for 24 h. **(D-F)** Cells recovered after 9 h were subjected to the same fosfomycin treatment. D: 9h-control, E: 9h-atpH and F: 9h-pykF. **(G-I)** Cells recovered after 24 h were subjected to the same fosfomycin treatment. G: 24h-control, H: 24h-atpH and I: 24h-pykF. Lines in each graph represent different replicates.

To determine if the regrowth phenotype is due to reversible heteroresistance or due to permanent mutations, we exposed the control strain, atpH strain and pykF strain to repeated cycles of fosfomycin treatment (Figure 3A-C). Therefore, these strains were treated with fosfomycin and recovered after 9 and 24 hours to again be treated with fosfomycin for 24h. The control strain did not recover after 24 hours treatment, but 4 out of the 8 replicate cultures could recover after 9 hours (Figure 3D, G). In case of the pykF strain, all replicate cultures recovered after 9 hours, and they were susceptible to fosfomycin (Figure 3F). However, their regrowth phenotype was more pronounced than after the initial treatment (Figure 3C). Importantly, after the initial treatment of 24 h, some replicates showed fast growth in the presence in fosfomycin (Figure 3I), which suggests that they had acquired permanent resistant mutations. The atpH strain showed a similar behavior to the pykF strain (Figure 3B,E,H). This progressive shift toward resistance suggests that in the pykF and atpH strains, a fraction of resistant cells can withstand the 4X MIC of fosfomycin and this promotes the development of antibiotic resistance mutations.

Next, we sought to understand the mechanisms by which *pykF* and *atpH* knockdowns reduce susceptibility to fosfomycin. We hypothesized that CRISPRi knockdowns of *pykF* reduce the susceptibility to fosfomycin by increasing the concentration of the pyruvate kinase substrate PEP. PEP is the co-substrate of MurA and at high levels, it may compete with fosfomycin for binding to MurA[23]. To measure PEP, we collected samples for LC-MS/MS analysis from the control strain, the atpH strain and the pykF strain before fosfomycin treatment and from cells that had recovered after 9 hours of fosfomycin treatment. PEP levels were similar before treatment in all strains (Figure 4A). However, after 9 hours of fosfomycin treatment we observed an increase in PEP levels in the pykF strain (4.2-fold), as well as in the atpH strain (1.7-fold). The latter had the lowest ATP levels of all three strains, a perturbation that might indirectly lead to higher PEP levels (Figure 4B-D).

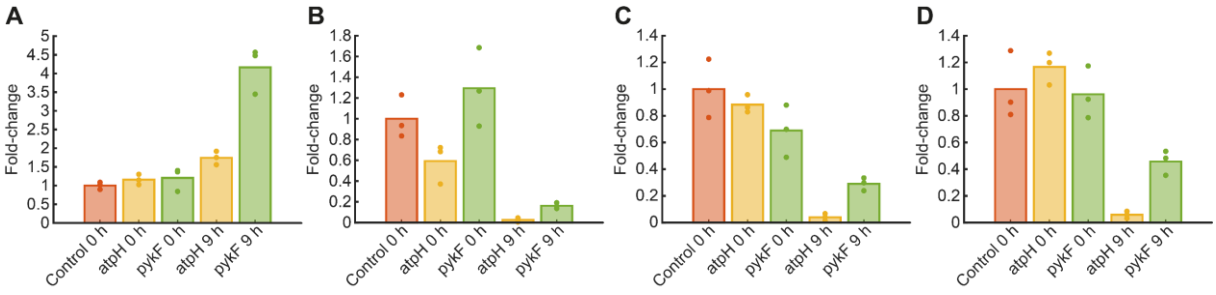

Figure 4. Phosphoenolpyruvate increases in fosfomycin-treated CRISPRi strains. Strains were incubated for 3 hours to OD_{600} >0.25 in aTc-containing minimal medium before fosfomycin treatment. Metabolites were measured after 0 and 9 hours of fosfomycin treatment (304 µg/mL). Bars are the mean fold-change relative to the control, and dots indicate fold-changes of replicates (n = 3). Intensities were normalized to OD_{600}. Fold-changes relative to the control strain are shown for phosphoenolpyruvate (**A**), adenosine monophosphate (**B**), adenosine diphosphate (**C**), and adenosine triphosphate (**D**).

To gain further insight into the cellular response of fosfomycin surviving cells, we analyzed the transcriptome of the surviving pykF and atpH strains after 9 h of treatment. As a reference we measured the untreated control, pykF and atpH strains (Figure 5). Before treatment, the atpH strain showed significant decreases in all ATP synthase gene transcripts that are downstream of atpH, showing that CRISPRi is effective and impacts all downstream genes of atpH (Figure 5A). Also, the pykF strain showed strong decreases of pykF transcripts (Figure 5C). Notably, CpxP increased significantly in the untreated atpH strain. CpxP activates the CpxAB two-component system, which represses the expression of GlpT and UhpT (the main fosfomycin importers) and this may contribute to the survival advantage of the atpH strain[24]. CpxP levels were also 3-fold higher in the untreated pykF strain, but they remained below our cut-off (log_2 FC>2, Figure 5C). After 9 hours of fosfomycin treatment, the atpH strain showed a broad transcriptional response with many genes above the cut-off (log_2 FC>2, Figure 5B). ATP synthase genes remained decreased, while CpxP expression increased even further. Similarly, the pykF strain also increased CpxP levels 9 hours after fosfomycin treatment. In both strains, the transcript levels of the pyruvate:H^+ symporter BtsT increased (Figure 5B). BtsT is generally activated under nutrient-limited conditions to facilitate pyruvate transport[25]. Given the similarity of PEP and fosfomycin, BtsT activity may influence the intracellular concentration of the drug. BtsT transcript levels were also strongly increased in the pykF strain after 9 h of fosfomycin treatment (Figure 5D). MetR, a transcriptional activator of the methionine biosynthesis pathway, was also increased in the 9 h samples of the pykF strain and the atpH strain (Figure 5B, D). While enhanced methionine synthesis has not been directly linked to fosfomycin, it may support sulfur metabolism or redox homeostasis, thus indirectly enhancing survival[26].

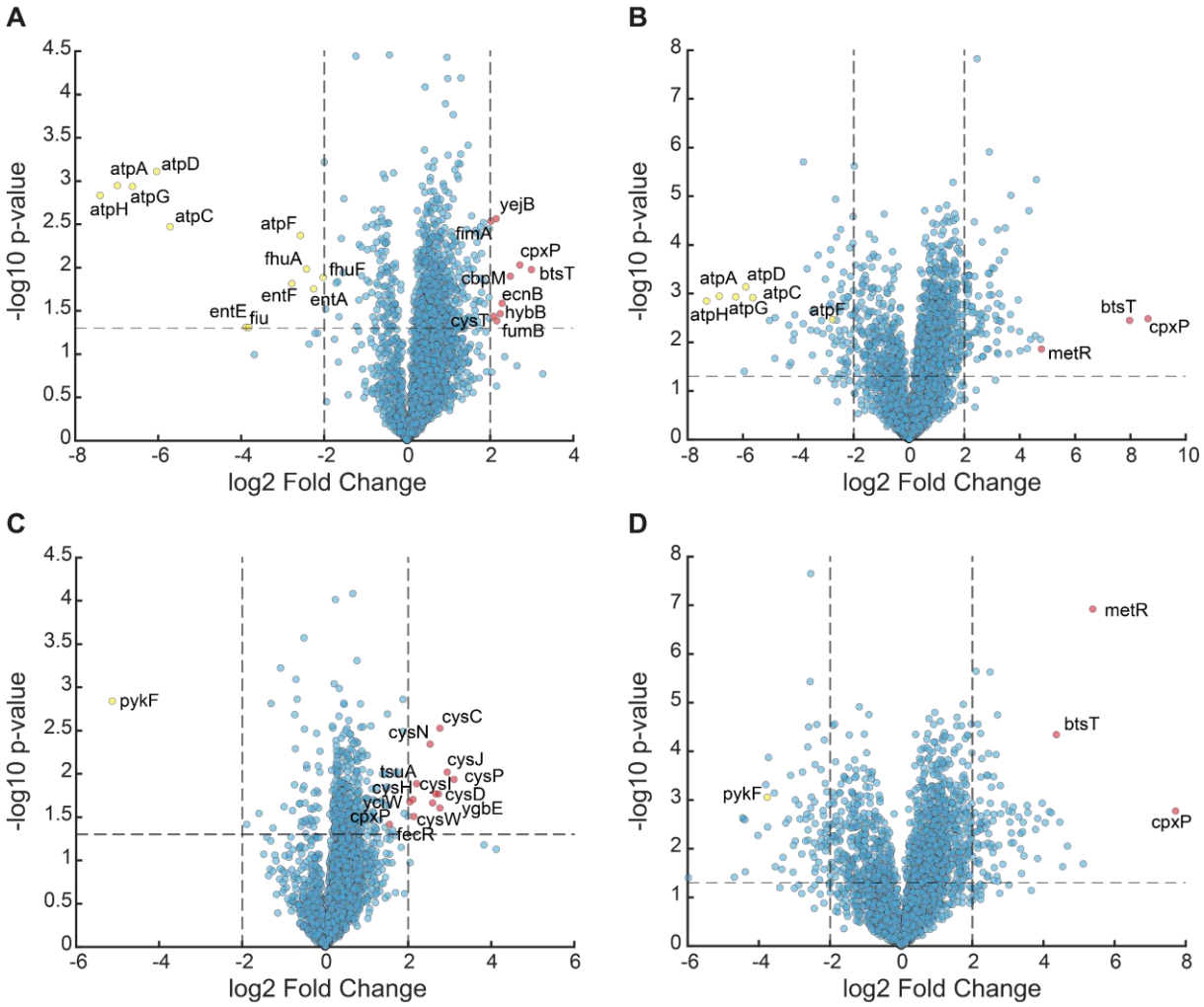

Figure 5. Transcriptome of the pykF strain and the atpH strain with and without fosfomycin. Strains were incubated for 3 hours to OD_{600} >0.25 in aTc-containing minimal medium before fosfomycin treatment. RNA sequencing was performed after 0 and 9 hours of fosfomycin treatment (304 µg/mL). Fold-changes were calculated relative to the mean of the control strain. **(A)** Transcript levels of the atpH strain and **(B)** pykF strain before fosfomycin treatment. **(C)** Transcript levels of the atpH strain and **(D)** pykF strain after 9 hours of fosfomycin treatment.

In summary, our study identified metabolic genes that reduce the susceptibility of *E. coli* to fosfomycin by promoting regrowth after 9 h of exposure to fosfomycin (at 4X MIC). If this phenotype is due to a heteroresistant subpopulation or if all cells recover remains to be elucidated. Here, we obtained first evidence that this regrowth phenotype is transient because recovering cells after 9 h were eventually killed when re-exposed to fosfomycin. However, after a 24 h recovery, several cultures showed growth in the presence of fosfomycin, suggesting that the regrowth phenotype promotes the evolution of major resistance. Metabolite data provided first evidence that the concentration of PEP might play a role in this phenotype because PEP levels were 4-fold increased in cells that regrew after 9 h of treatment. Also, the transcriptome indicated that the response to cell envelope stress and changes in pyruvate transporter levels may undermine the efficacy of fosfomycin.

Methods and Protocols

Strains

Reagent or Resource	Source	Identifier
CRISPRi library in YYdCas9: BW25993 CRISPRipgRNA intC::tetR-dcas9-aadA lacY::ypet-cat	Donati et al. 2021	N/A
YYdCas9: BW25993 intC::tetR-dcas9-aadA lacY::ypet-cat (BW25993 *intC::tetR-dcas9-aadA lacY::ypet-cat araB::T7 RNAP-tetA* Δ*araB)*	Lawson et al., 2017	N/A

Media

Cultivation was performed in LB medium (L3522, Sigma Aldrich) or M9 minimal medium with 5 g/l glucose as the sole carbon source. M9 medium contained (per liter) 7.52 g $Na_2HPO_4\,2H_2O$, 5 g KH_2PO_4, 1.5 g $(NH_4)_2SO_4$, 0.5 g NaCl, 10 mL trace salts solution, 2 mL 1.4 mM thiamine-HCl, 1 mL 1 M $MgSO_4$, 1 mL 0.1 M $CaCl_2$ and 0.6 mL 0.1 M $FeCl_3$. The trace salt solution was composed of (per liter) 180 mg $CoCl_2\,6H_2O$, 180 mg $ZnSO_4\,7H_2O$, 120 mg $MnSO_4\,H_2O$, 120 mg $CuCl_2\,2H_2O$. Both media contained 100 µg/mL ampicillin (Amp). For dCas9 expression, aTc was added to M9 medium (200 nM). Fosfomycin was added at concentrations of 304 µg/mL unless stated otherwise.

Screening of Antibiotic Phenotypes of the CRISPRi Library

Using a replicator system (Deutz-System, Kuhner) strains were transferred from flat-bottom 96-well plate glycerol stocks to 96-deep-well plates containing LB medium and incubated for 5 h at 37°C, 220 rpm. LB culture was diluted in M9 medium in 96-deep-well plates and incubated at 37°C, 220 rpm for 16 h. Cultures were diluted 150-fold in fresh M9 containing aTc and incubated at 800 rpm, 37°C in a plate reader (LogPhase600, Agilent) for 6.5 h. Cultures were 2-fold diluted in M9 containing aTc and 8x MIC fosfomycin (608 µg/mL). Plates were incubated in a plate reader at 800 rpm, 37°C for 24 h.

Generation of Growth Curves and Determination of Phenotypes

Growth data was extracted from plate reader and loaded into MATLAB (R2024b), OD values were converted to OD_{600}, and values smoothed. Growth data was plotted for all 24 h. Phenotype determination was performed by comparing OD_{600} at timepoints 0, 4, 12 and 24 h. Each strain had to reach an OD_{600} of at least 0.05 within 24 h to be further considered for phenotypes. Strains were characterized as tolerant category when OD_{600} at 4 h was 1.5x higher than OD_{600} at 24 h. OD_{600} increase category required OD_{600} at 12 h to be lower than at 24 h, and resistant category strains had to have increased OD_{600} values over all four time points.

Agar Dilution Assays

Strains were inoculated in LB medium and incubated at 220 rpm, 37°C for 5 h. Subsequently, 100 µL LB culture was transferred to 10 mL M9 medium in shake flasks and incubated at 37°C, 220 rpm for 16 h. OD_{600} was measured, cultures normalized to OD_{600} 0.05, and incubated for 3 h in shake flasks at 37°C, 220 rpm. Cultures were then diluted back to OD_{600} 0.1, serial diluted four times, and all dilutions were spotted onto M9 agar plates containing exponentially increasing fosfomycin concentrations. After 36 h, pictures were taken.

Regrowth of Fosfomycin Treated Strains

Strains were inoculated in LB medium and incubated at 220 rpm, 37°C for 5 h. Subsequently, cultures were diluted in M9 medium in a 96-deep-well plate and incubated at 37°C, 220 rpm for 16 h. OD_{600} was measured, cultures normalized to OD_{600} 0.05 in M9 containing aTc and incubated in a plate reader for ~6 h at 37°C, 220 rpm, until OD_{600} of >0.5 was reached. Cultures were diluted 2-fold in flat-bottom plates filled with M9 containing aTc and 8x MIC fosfomycin (608 µg/mL). Plates were incubated in a plate reader at 37°C, 800 rpm for 24 h. After 9 h, cultures were diluted 200-fold in fresh LB medium, and after 24 h incubation, cultures were diluted again 200-fold in fresh LB medium. LB cultures were incubated for 24 h, and glycerol stocks were created. Glycerol stocks were inoculated in LB medium and incubated at 220 rpm, 37°C for 5 h. Subsequently, LB cultures were diluted 50-fold in M9 medium in a 96-deep-well plate and incubated at 37°C, 220 rpm overnight. OD_{600} was measured, cultures normalized to OD_{600} 0.05 in M9 containing aTc and incubated in a plate reader for ~6 h at 37°C, 800 rpm, until OD_{600} 0.5 was reached for most strains. Then, cultures were diluted 2-fold in two flat-bottom plates filled with M9 containing aTc and 8x MIC fosfomycin (608 µg/mL). Plates were incubated in a plate reader at 37°C, 800 rpm for 24 h.

Time-Kill Assay

Strains were inoculated in LB medium and incubated at 220 rpm, 37°C for 5 h. Subsequently, LB cultures were diluted 100-fold in M9 medium and incubated at 37°C, 220 rpm for 16 h. OD_{600} was determined, cultures were started at OD_{600} 0.05, and incubated for ~3 h at 37°C, 220 rpm, until OD_{600} 0.25 was reached. Then, fosfomycin (304 µg/mL) was added and shake flasks incubated for an additional 24 h at 37°C, 220 rpm. At timepoints 0 h, 0.75 h, 1.25 h, 2 h, 3 h, and 9 h, aliquots were removed, a six-instance serial dilution prepared, and spotted on M9 plates containing Amp. After 36 h, pictures were taken, colonies at the dilution with the best resolution were counted, and live cells per milliliter were calculated.

Metabolomics atpH, pykF and Control Strain

CRISPRi strains were inoculated in LB medium and incubated at 220 rpm, 37°C for 5 h. Subsequently, cultures were diluted 100-fold in M9 medium in shake flasks and incubated at 37°, 220 rpm for 16 h. Cultures were diluted back to a starting OD_{600} 0.05 in M9 medium containing aTc in shake flasks and grown for 3 h, until OD_{600} 0.25 when 304 µg/mL fosfomycin was added. Cultures were then incubated at 37°C, 220 rpm for 9 h. Right before fosfomycin addition and after 9 h treatment, cultures were sampled by centrifugation at 4°C, 2,000g for 2 min, supernatant removed, and pellets quenched in ice-cold AcN:MeOH:H_2O (40:40:20). Samples were incubated for 16 h at -20°C, centrifuged at 17,000 rpm, -9°C for 5 min, supernatant transferred to fresh reaction tubes and stored on -80°C until measurement.

Targeted Metabolomics

Metabolite quantification was carried out using an Agilent 6495 triple quadrupole mass spectrometer (Agilent Technologies), coupled to an Agilent 1290 Infinity II UHPLC system. Metabolite extracts were mixed in a 1:1 ratio with uniformly ^{13}C-labeled *E. coli* K-12 internal standard prior to analysis. Chromatographic separation was performed at 10°C with an injection volume of 3 µL. Depending on ionization conditions, either an Acquity BEH Amide column (30 × 2.1 mm, 1.7 µm) for acidic mode or an iHILIC-Fusion(P) column (50 × 2.1 mm, 5 µm) for basic mode was used.

Mobile phase A consisted of either water with 10 mM ammonium formate and 0.1% formic acid (v/v) for acidic conditions, or water with 10 mM ammonium carbonate and 0.2% ammonium hydroxide for basic conditions. Mobile phase B was acetonitrile with 0.1% formic acid (v/v) under acidic conditions, or plain acetonitrile under basic conditions. The LC gradient for both modes: 0 min, 90% B; 1.3 min, 40% B; 1.5 min, 40% B; 1.7 min, 90% B; 2.0 min, 90% B. Quantification was based on the ratio of ^{12}C to ^{13}C peaks.

Transcriptomics of the atpH, pykF and Control Strain

Strains were inoculated in LB medium and incubated at 220 rpm, 37°C for 5 h. Subsequently, cultures were diluted 100-fold in M9 medium in shake flasks and incubated at 37°C, 220 rpm overnight. OD_{600} of overnight cultures was measured, cultures normalized to OD_{600} 0.05 and incubated for 3 h in shake flasks at 37°C, 220 rpm till OD_{600} 0.25 was reached. Fosfomycin was added to a final concentration of 4x MIC (304 µg/mL), and immediately, 2 mL of each culture was removed and centrifuged for 5 min at 5330 rpm, 37°C. The supernatant was removed, dry pellets were shock-frozen in liquid nitrogen and stored at -80°C. The remaining cultures were incubated for 9 h at 37°C, 220 rpm. 2x 50 mL per strain were centrifuged at 5330 rpm, 37°C for 5 min, supernatant was removed, dry pellets shock-frozen in liquid nitrogen and stored at -80°C. RNA extraction, sequencing library preparation and NGS sequencing were performed at the Institute for Medical Microbiology and Hygiene (MGM) of the University of Tübingen. Total RNA was quantified using the Qubit RNA Broad Range Assay Kit (Thermo Fisher), and RNA quality was assessed with the Agilent 2100 BioAnalyzer in combination with the RNA 6000 Pico Kit (Agilent Technologies, #5067-1513). RNA was of good quality with RIN between 6.4 and 9.6. For library preparation, the Illumina Stranded Total RNA Prep kit was employed, incorporating rRNA depletion with the Ribo-Zero Plus Microbiome Kit (Illumina). In brief, 100 ng of total RNA per sample was processed to remove ribosomal RNA, followed by synthesis of cDNA libraries, ligation of adapters, and PCR amplification. The resulting libraries were quantified using the Qubit 1x dsDNA High Sensitivity Assay Kit (Thermo Fisher), and fragment size distribution was analyzed using the High Sensitivity DNA Kit on the Agilent BioAnalyzer. Libraries were then pooled and sequenced on an Illumina MiSeq platform using the MiSeq Reagent Kit v3 (150 cycles), yielding 874,147 to 1,759,004 single-end reads per sample (17,720,891 reads in total). Data processing, including quality control, mapping, and quantification, was done using nf-core/rnaseq v3.18.0 (https://nf-co.re/rnaseq, https://doi.org/10.5281/zenodo.14537300) of the nf-core collection of workflows[27]. nf-core/rnaseq was executed with Nextflow v24.04.4[28] and singularity v3.8.7[29]. The read quality was assessed with FastQC v0.12.1 and led to the removal of around <1% base pairs per sample due to adapter contamination and trimming of low-quality regions with Trim Galore! v0.6.10. rRNA sequences were removed (1.1% to 16% per sample; average: 2.7%) with SortMeRNA v4.3.7[30]. More than 97% reads were aligned with STAR v2.6.1d to *E. coli* BW25113 (NCBI RefSeq GCF_000750555.1-RS_2024_06_01) with 4522 genes. Transcripts were quantified by Salmon v1.10.3[31] to Transcripts per million (TPM). TPM values were used to calculate log2 fold-changes relative to the mean of the control strain. Genes with zero TPM in any sample were excluded. P-values were calculated with a two-sided Welch t-test assuming unequal variances.

Bibliography

(1) Khalil, I. A.; Troeger, C.; Blacker, B. F.; Rao, P. C.; Brown, A.; Atherly, D. E.; Brewer, T. G.; Engmann, C. M.; Houpt, E. R.; Kang, G.; Kotloff, K. L.; Levine, M. M.; Luby, S. P.; MacLennan, C. A.; Pan, W. K.; Pavlinac, P. B.; Platts-Mills, J. A.; Qadri, F.; Riddle, M. S.; Ryan, E. T.; Shoultz, D. A.; Steele, A. D.; Walson, J. L.; Sanders, J. W.; Mokdad, A. H.; Murray, C. J. L.; Hay, S. I.; Reiner, R. C. Morbidity and Mortality Due to *Shigella* and Enterotoxigenic *Escherichia Coli* Diarrhoea: The Global Burden of Disease Study 1990–2016. *The Lancet Infectious Diseases* **2018**, *18* (11), 1229–1240. https://doi.org/10.1016/S1473-3099(18)30475-4.

(2) Falagas, M. E.; Vouloumanou, E. K.; Samonis, G.; Vardakas, K. Z. Fosfomycin. *Clinical Microbiology Reviews* **2016**, *29* (2), 321–347. https://doi.org/10.1128/cmr.00068-15.

(3) Silver, L. L. Fosfomycin: Mechanism and Resistance. *Cold Spring Harb Perspect Med* **2017**, *7* (2), a025262. https://doi.org/10.1101/cshperspect.a025262.

(4) Bianchi, M.; Winterhalter, M.; Harbig, T. A.; Hörömpöli, D.; Ghai, I.; Nieselt, K.; Brötz-Oesterhelt, H.; Mayer, C.; Borisova-Mayer, M. Fosfomycin Uptake in *Escherichia Coli* Is Mediated by the Outer-Membrane Porins OmpF, OmpC, and LamB. *ACS Infect. Dis.* **2024**, *10* (1), 127–137. https://doi.org/10.1021/acsinfecdis.3c00367.

(5) Monte, D. F. M.; Doi, Y.; Lincopan, N. High Prevalence and Global Distribution of Fosfomycin Resistance Genes in *Salmonella Serovars*. *The Lancet Microbe* **2023**, *4* (12), e968. https://doi.org/10.1016/S2666-5247(23)00261-6.

(6) Dörr, T. Understanding Tolerance to Cell Wall–Active Antibiotics. *Annals of the New York Academy of Sciences* **2021**, *1496* (1), 35–58. https://doi.org/10.1111/nyas.14541.

(7) Dewachter, L.; Fauvart, M.; Michiels, J. Bacterial Heterogeneity and Antibiotic Survival: Understanding and Combatting Persistence and Heteroresistance. *Molecular Cell* **2019**, *76* (2), 255–267. https://doi.org/10.1016/j.molcel.2019.09.028.

(8) Bollen, C.; Louwagie, E.; Verstraeten, N.; Michiels, J.; Ruelens, P. Environmental, Mechanistic and Evolutionary Landscape of Antibiotic Persistence. *EMBO reports* **2023**, *24* (8), e57309. https://doi.org/10.15252/embr.202357309.

(9) Band, V. I.; Weiss, D. S. Heteroresistance to Beta-Lactam Antibiotics May Often Be a Stage in the Progression to Antibiotic Resistance. *PLoS Biol* **2021**, *19* (7), e3001346. https://doi.org/10.1371/journal.pbio.3001346.

(10) Levin-Reisman, I.; Ronin, I.; Gefen, O.; Braniss, I.; Shoresh, N.; Balaban, N. Q. Antibiotic Tolerance Facilitates the Evolution of Resistance. *Science* **2017**, *355* (6327), 826–830. https://doi.org/10.1126/science.aaj2191.

(11) Bakkeren, E.; Diard, M.; Hardt, W.-D. Evolutionary Causes and Consequences of Bacterial Antibiotic Persistence. *Nat Rev Microbiol* **2020**, *18* (9), 479–490. https://doi.org/10.1038/s41579-020-0378-z.

(12) Stokes, J. M.; Lopatkin, A. J.; Lobritz, M. A.; Collins, J. J. Bacterial Metabolism and Antibiotic Efficacy. *Cell Metabolism* **2019**, *30* (2), 251–259. https://doi.org/10.1016/j.cmet.2019.06.009.

(13) Ohkoshi, Y.; Sato, T.; Suzuki, Y.; Yamamoto, S.; Shiraishi, T.; Ogasawara, N.; Yokota, S. Mechanism of Reduced Susceptibility to Fosfomycin in *Escherichia Coli* Clinical Isolates. *Biomed Res Int* **2017**, *2017*, 5470241. https://doi.org/10.1155/2017/5470241.

(14) Petek, M.; Baebler, Š.; Kuzman, D.; Rotter, A.; Podlesek, Z.; Gruden, K.; Ravnikar, M.; Urleb, U. Revealing Fosfomycin Primary Effect on *Staphylococcus Aureus* Transcriptome: Modulation of Cell Envelope Biosynthesis and Phosphoenolpyruvate Induced Starvation. *BMC Microbiology* **2010**, *10* (1), 159. https://doi.org/10.1186/1471-2180-10-159.

(15) Nilsson, A. I.; Berg, O. G.; Aspevall, O.; Kahlmeter, G.; Andersson, D. I. Biological Costs and Mechanisms of Fosfomycin Resistance in *Escherichia Coli*. *Antimicrob Agents Chemother* **2003**, *47* (9), 2850–2858. https://doi.org/10.1128/AAC.47.9.2850-2858.2003.

(16) Turner, A. K.; Yasir, M.; Bastkowski, S.; Telatin, A.; Page, A. J.; Charles, I. G.; Webber, M. A. A Genome-Wide Analysis of *Escherichia Coli* Responses to Fosfomycin Using TraDIS-Xpress Reveals Novel Roles for Phosphonate Degradation and Phosphate

Transport Systems. *J Antimicrob Chemother* **2020**, *75* (11), 3144–3151. https://doi.org/10.1093/jac/dkaa296.

(17) Donati, S.; Kuntz, M.; Pahl, V.; Farke, N.; Beuter, D.; Glatter, T.; Gomes-Filho, J. V.; Randau, L.; Wang, C.-Y.; Link, H. Multi-Omics Analysis of CRISPRi-Knockdowns Identifies Mechanisms That Buffer Decreases of Enzymes in *E. Coli* Metabolism. *cels* **2021**, *12* (1), 56-67.e6. https://doi.org/10.1016/j.cels.2020.10.011.

(18) Monk, J. M.; Lloyd, C. J.; Brunk, E.; Mih, N.; Sastry, A.; King, Z.; Takeuchi, R.; Nomura, W.; Zhang, Z.; Mori, H.; Feist, A. M.; Palsson, B. O. iML1515, a Knowledgebase That Computes *Escherichia Coli* Traits. *Nat Biotechnol* **2017**, *35* (10), 904–908. https://doi.org/10.1038/nbt.3956.

(19) Zhao, C.; Lin, Z.; Dong, H.; Zhang, Y.; Li, Y. Reexamination of the Physiological Role of PykA in *Escherichia Coli* Revealed That It Negatively Regulates the Intracellular ATP Levels under Anaerobic Conditions. *Appl Environ Microbiol* **2017**, *83* (11), e00316-17. https://doi.org/10.1128/AEM.00316-17.

(20) Wiegand, I.; Hilpert, K.; Hancock, R. E. W. Agar and Broth Dilution Methods to Determine the Minimal Inhibitory Concentration (MIC) of Antimicrobial Substances. *Nat Protoc* **2008**, *3* (2), 163–175. https://doi.org/10.1038/nprot.2007.521.

(21) Nakao, R.; Ramstedt, M.; Wai, S. N.; Uhlin, B. E. Enhanced Biofilm Formation by *Escherichia Coli* LPS Mutants Defective in Hep Biosynthesis. *PLoS One* **2012**, *7* (12), e51241. https://doi.org/10.1371/journal.pone.0051241.

(22) Bermudez, T. A.; Brannon, J. R.; Dudipala, N.; Reasoner, S.; Morales, G.; Wiebe, M.; Cecala, M.; DaCosta, M.; Beebout, C.; Amir, O.; Hadjifrangiskou, M. Raising the Alarm: Fosfomycin Resistance Associated with Non-Susceptible Inner Colonies Imparts No Fitness Cost to the Primary Bacterial Uropathogen. *Antimicrob Agents Chemother 68* (1), e00803-23. https://doi.org/10.1128/aac.00803-23.

(23) Skarzynski, T.; Mistry, A.; Wonacott, A.; Hutchinson, S. E.; Kelly, V. A.; Duncan, K. Structure of UDP-*N*-Acetylglucosamine Enolpyruvyl Transferase, an Enzyme Essential for the Synthesis of Bacterial Peptidoglycan, Complexed with Substrate UDP-*N*-Acetylglucosamine and the Drug Fosfomycin. *Structure* **1996**, *4* (12), 1465–1474. https://doi.org/10.1016/S0969-2126(96)00153-0.

(24) Brand, C.; Newton-Foot, M.; Grobbelaar, M.; Whitelaw, A. Antibiotic-Induced Stress Responses in Gram-Negative Bacteria and Their Role in Antibiotic Resistance. *Journal of Antimicrobial Chemotherapy* **2025**, *80* (5), 1165–1184. https://doi.org/10.1093/jac/dkaf068.

(25) Kristoficova, I.; Vilhena, C.; Behr, S.; Jung, K. BtsT, a Novel and Specific Pyruvate/H+ Symporter in *Escherichia Coli*. *J Bacteriol* **2018**, *200* (2), e00599-17. https://doi.org/10.1128/JB.00599-17.

(26) Martínez, Y.; Li, X.; Liu, G.; Bin, P.; Yan, W.; Más, D.; Valdivié, M.; Hu, C.-A. A.; Ren, W.; Yin, Y. The Role of Methionine on Metabolism, Oxidative Stress, and Diseases. *Amino Acids* **2017**, *49* (12), 2091–2098. https://doi.org/10.1007/s00726-017-2494-2.

(27) Ewels, P. A.; Peltzer, A.; Fillinger, S.; Patel, H.; Alneberg, J.; Wilm, A.; Garcia, M. U.; Di Tommaso, P.; Nahnsen, S. The Nf-Core Framework for Community-Curated Bioinformatics Pipelines. *Nat Biotechnol* **2020**, *38* (3), 276–278. https://doi.org/10.1038/s41587-020-0439-x.

(28) Di Tommaso, P.; Chatzou, M.; Floden, E. W.; Barja, P. P.; Palumbo, E.; Notredame, C. Nextflow Enables Reproducible Computational Workflows. *Nat Biotechnol* **2017**, *35* (4), 316–319. https://doi.org/10.1038/nbt.3820.

(29) Kurtzer, G. M.; Sochat, V.; Bauer, M. W. Singularity: Scientific Containers for Mobility of Compute. *PLoS One* **2017**, *12* (5), e0177459. https://doi.org/10.1371/journal.pone.0177459.

(30) Kopylova, E.; Noé, L.; Touzet, H. SortMeRNA: Fast and Accurate Filtering of Ribosomal RNAs in Metatranscriptomic Data. *Bioinformatics* **2012**, *28* (24), 3211–3217. https://doi.org/10.1093/bioinformatics/bts611.

(31) Patro, R.; Duggal, G.; Love, M. I.; Irizarry, R. A.; Kingsford, C. Salmon Provides Fast and Bias-Aware Quantification of Transcript Expression. *Nat Methods* **2017**, *14* (4), 417–419. https://doi.org/10.1038/nmeth.4197.

Supplementary Figures

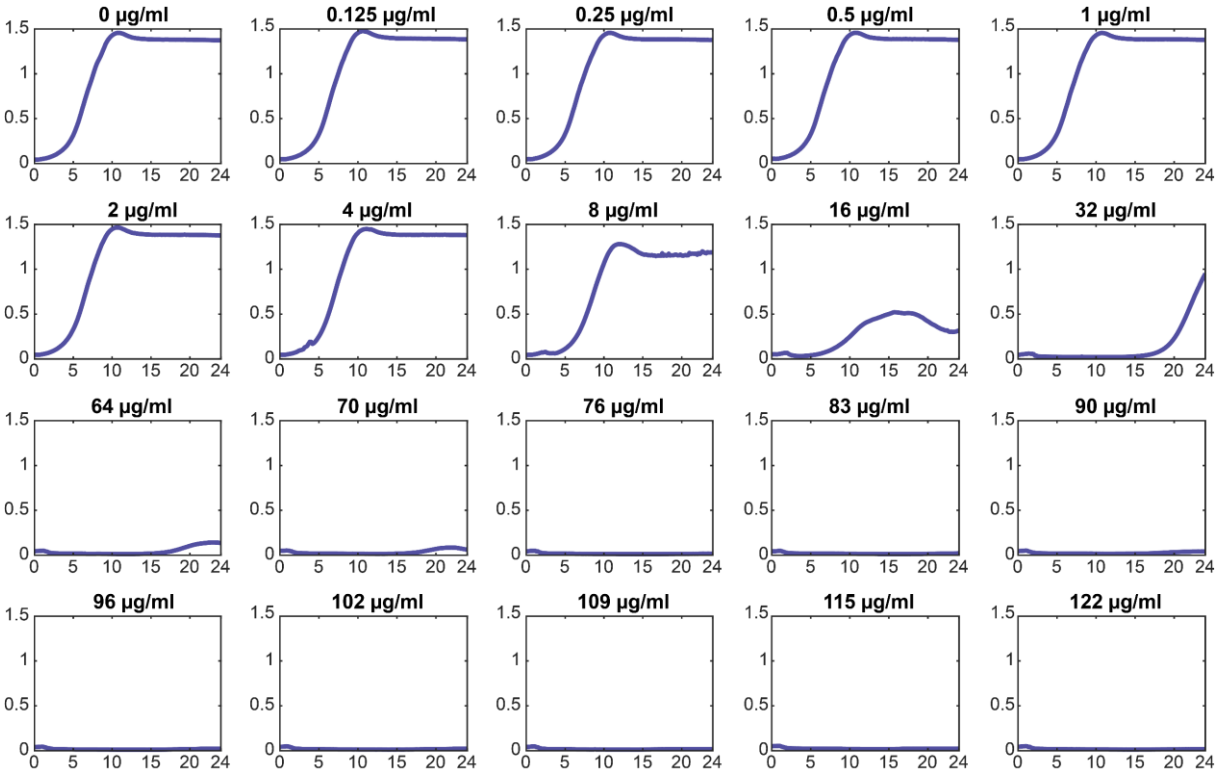

Supplementary Figure 1. Fosfomycin MIC determination. The control strain was incubated for 24 hours in aTc induced minimal glucose medium under increasing Fosfomycin concentrations (n=8). The first concentration displaying no growth over 24 hours at 76 µg/mL determined the MIC.

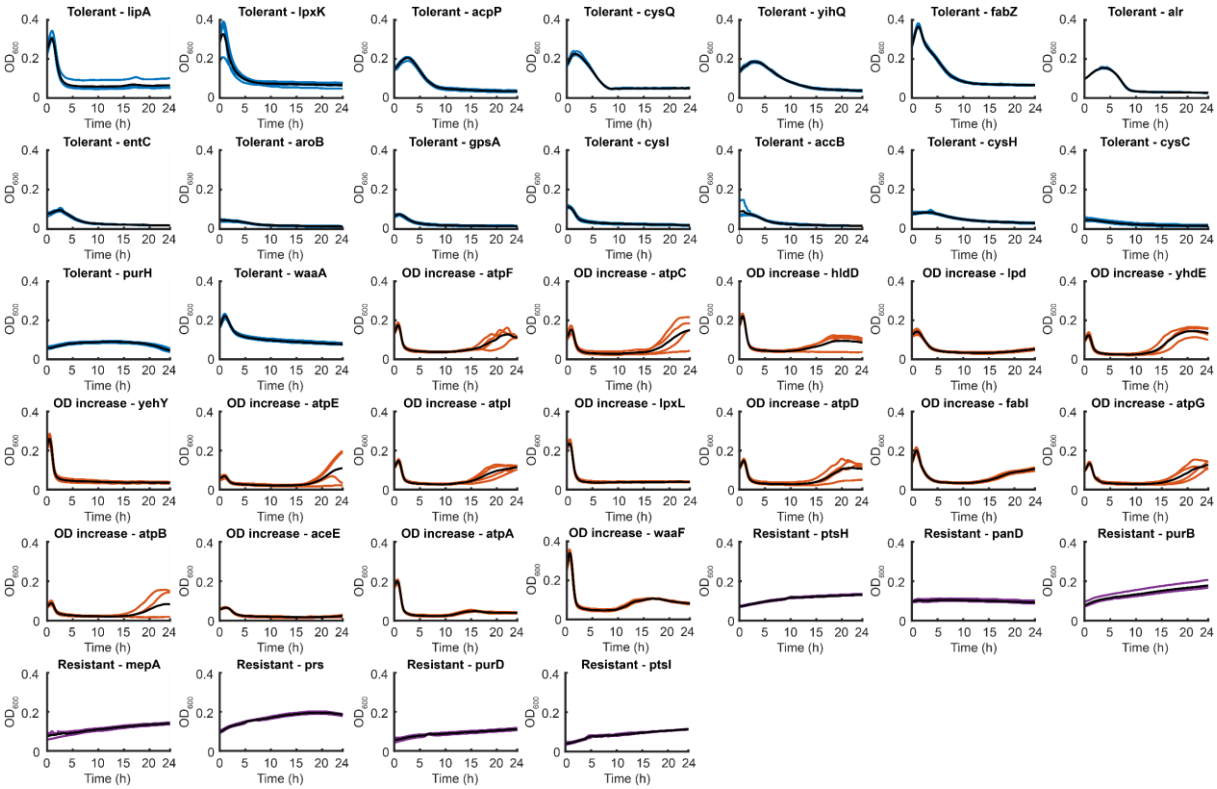

Supplementary Figure 2. Phenotype validations under fosfomycin treatment. Strains were incubated for 6.5 hours in aTc induced minimal glucose medium and subsequently for 24 h in aTc induced minimal glucose medium containing 304 µg/mL fosfomycin (n=4). Black lines in each graph indicate mean of all replicates. Colors refer to determined phenotypes in the initial screen: Tolerant (blue), OD increase (orange), and resistant (purple).

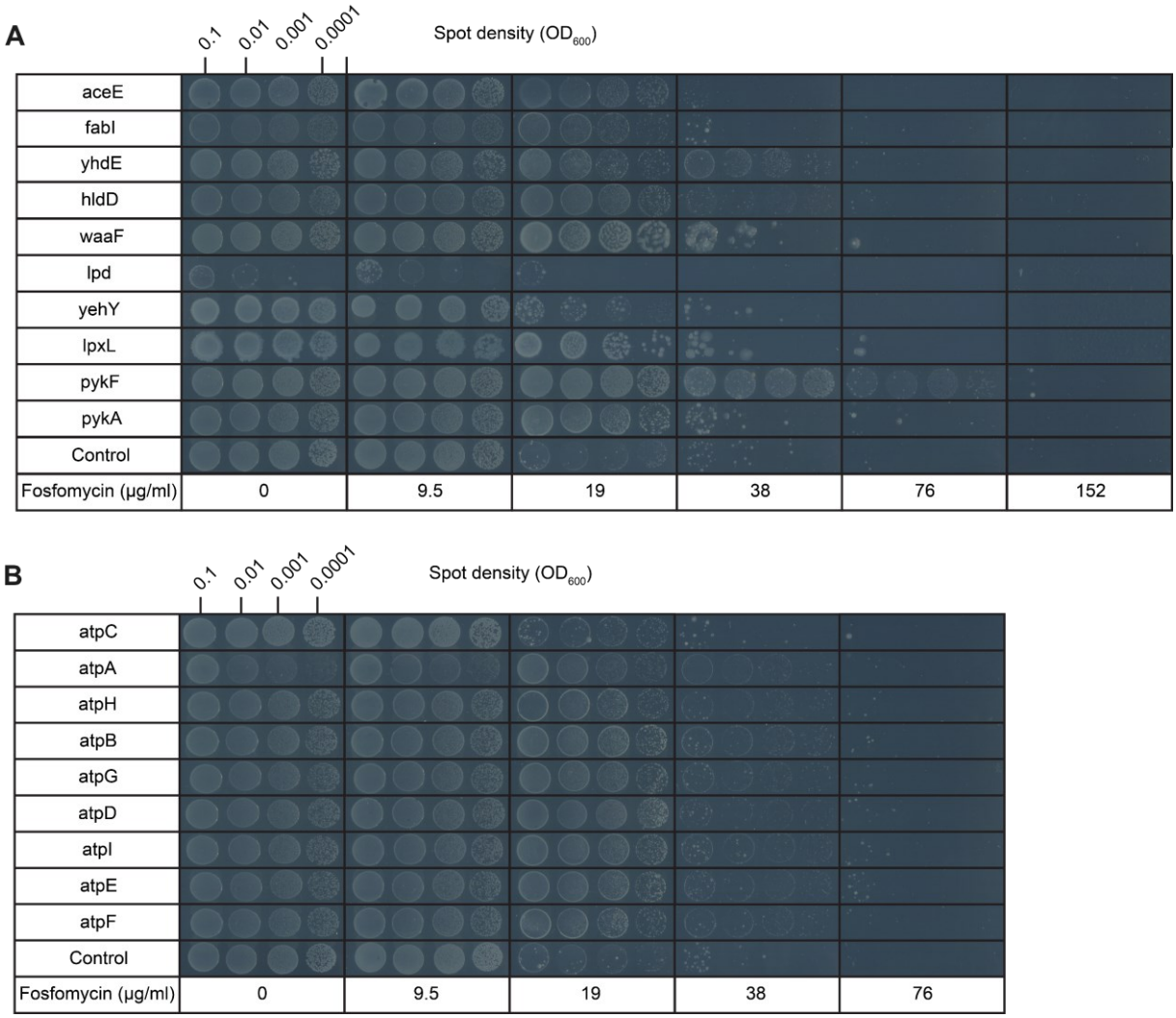

Supplementary Figure 3. Agar dilution assays of OD increase phenotype strains. (A) OD increase phenotype strains outside the ATP synthase pathway. **(B)** OD increase phenotype strains within the ATP synthase pathway.

Chapter 4: CRISPRi Library Antibiotic Stress Screen with Ciprofloxacin, Gentamicin, Rifampicin, and Meropenem.

Contributions

All work and data analysis were performed by the author (Andreas Verhülsdonk), unless stated in the following text. MIC determination and growth data collection were supported by my student at the time, Amelie Stadelmann.

Relevance

This chapter complements the fosfomycin stress screen described in Chapter 3 by extending the CRISPRi-based antibiotic screening to four additional compounds: ciprofloxacin, gentamicin, rifampicin, and meropenem. It also builds on the arrayed CRISPRi library created in Chapter 2. These antibiotics, each with distinct cellular targets and mechanisms of action, were tested alongside fosfomycin. While the most striking and informative phenotypes were observed under fosfomycin exposure, the datasets presented here provide a broader view of gene perturbation effects under antibiotic stress. Although some results, particularly for bactericidal antibiotics, were less conclusive, the data provides a basis for more targeted analyses and follow-up experiments.

Background

To broaden the scope of the antibiotic susceptibility screens, additional screens were performed using four more antibiotics, each with distinct mechanisms of action, cellular targets, and antibiotic classes. These screens were exploratory in nature and were not followed by downstream validation experiments yet, so the results presented here reflect preliminary findings.

The first antibiotic, **ciprofloxacin (Cip)**, is a fluoroquinolone antibiotic of the second generation introduced in the 1980s[1]. It targets the *E. coli* topoisomerase IV (ParC/ParE) and DNA gyrase (GyrA/GyrB), which are essential for DNA supercoiling and replication[2]. Sensitivity to ciprofloxacin can be influenced by pathways involved in cell-wall biosynthesis; for example, knockdowns in the lipid core biosynthesis may enhance susceptibility[3]. Resistance is commonly achieved through target-site mutations or upregulation of efflux systems[4].

The second antibiotic, **gentamicin (Genta)**, is an aminoglycoside antibiotic first introduced in the 1960s, originally derived from *Micromonospora* species[5]. It binds to the 30S ribosomal subunit, resulting in truncated protein products, mistranslations, and increased production of reactive oxygen species (ROS)[6]. Knockdowns in the tricarboxylic acid (TCA) cycle may reduce susceptibility, as aerobic respiration promotes ROS formation[7]. In addition, since gentamicin uptake depends on the proton motive force (PMF), disruptions in PMF generation can impair antibiotic entry[8]. Resistance mechanisms include enzymatic inactivation, uptake reduction, and 16S rRNA methylation[9,10].

The third antibiotic, **rifampicin (Rif)**, belongs to the rifamycin class and was first introduced in 1967, primarily for the treatment of tuberculosis and other mycobacterial infections[14,15]. It binds to the β-subunit of RNA polymerase (*rpoB*), inhibiting the initiation of transcription[16]. Knockdowns in nucleoside triphosphate (NTP) biosynthesis or components of the stringent response, such as *relA* or *spoT*, may influence rifampicin tolerance[17]. Resistance typically results from point mutations in *rpoB* that preserve polymerase function while preventing drug binding; efflux pump overexpression can also contribute[18,19].

The fourth antibiotic, **meropenem (Mero)**, is a broad-spectrum carbapenem antibiotic introduced in the mid-1990s for the treatment of severe infections[11]. It inhibits several penicillin-binding proteins (PBP), thereby blocking peptidoglycan cross-linking and compromising the bacterial cell wall[12]. Sensitivity may increase in knockdowns affecting cell envelope biogenesis, central carbon metabolism, or cell wall stress response pathways[12]. Resistance can arise through the acquisition of carbapenemase genes or via porin modifications that reduce uptake[13].

The antibiotics differ in both their modes of action and their effects on cellular phenotypes. Gentamicin and meropenem are bacteriolytic, leading to cell lysis and release of intracellular contents, while ciprofloxacin and rifampicin do not cause cell disintegration[20]. Since the screens were performed in liquid broth, distinguishing between tolerance and susceptibility can be challenging. For example, tolerance determination was particularly difficult for gentamicin and meropenem, similar to what was observed with fosfomycin. This can likely explain the absence of clearly identifiable tolerant phenotypes in these cases.

This chapter summarizes the CRISPRi knockdown screen results for ciprofloxacin, gentamicin, rifampicin, and meropenem. For each antibiotic, observed phenotypes were outlined and the most notable hits highlighted, either top-ranking knockdowns or, where appropriate, all hits based on detectable effects. While these screens were not analyzed in detail, they still illustrate the complexity of high-throughput antibiotic screening and some of the practical limitations encountered during analysis. Finally, a comparative analysis across all antibiotics is presented to highlight knockdowns identified in multiple screens. Despite these limitations, the results point to several candidate knockdowns worth investigating in follow-up studies.

Results

MICs for the four additional antibiotics were determined using the same protocol as in the fosfomycin screen. Control strains were initially cultured in LB medium, then transferred to M9 medium, and finally grown in M9 medium supplemented with aTc until an average OD_{600} of 0.5 was reached. Strains were then exposed to exponentially increasing concentrations of the respective antibiotics. To refine the MIC values, a second round of MIC determination was performed using concentration ranges between the initially estimated MIC and the next lower dilution step. The following concentrations, corresponding to four times the determined MIC values, were used in subsequent experiments: ciprofloxacin (60 ng/mL), gentamicin (1.2 µg/mL), meropenem (4.8 µg/mL), and rifampicin (80 µg/mL).

For all antibiotic screens, strains were cultured following the same three-step protocol: initial growth in LB medium, followed by transfer to M9 medium, and final induction in M9 medium containing aTc until control cultures reached an OD_{600} of 0.5. Cultures were then diluted 1:1 in fresh aTc-induced M9 medium containing 8× MIC of the respective antibiotic. Growth was monitored over 24 hours using a LogPhase600 plate reader (Agilent).

Detailed phenotype definitions and growth analysis procedures are described in the Materials and Methods section.

Ciprofloxacin

Variation in growth dynamics made phenotype determination challenging in this screen. Initially, we tried to use metrics normally used for phenotype determination. Area under the curve (AUC) values for each replicate were calculated, normalized (AUC_{norm}) to control averages, and plotted (replicate 1 vs. replicate 2) to identify resistant strains (Figure 1A). Strains were considered resistant if their normalized MIC was ≥1.5× that of the control and if replicates were within 1.5× of each other. This yielded 60 candidate strains.

To identify tolerant strains, we calculated the minimum OD_{600} and early growth rate for each knockdown. Tolerant strains were defined as those with slower OD_{600} reductions compared to controls. Strains outside ±2 standard deviations from control averages were considered tolerant (Figure 1B), unless poor replicate alignment excluded them. This approach flagged 81 strains as potentially tolerant.

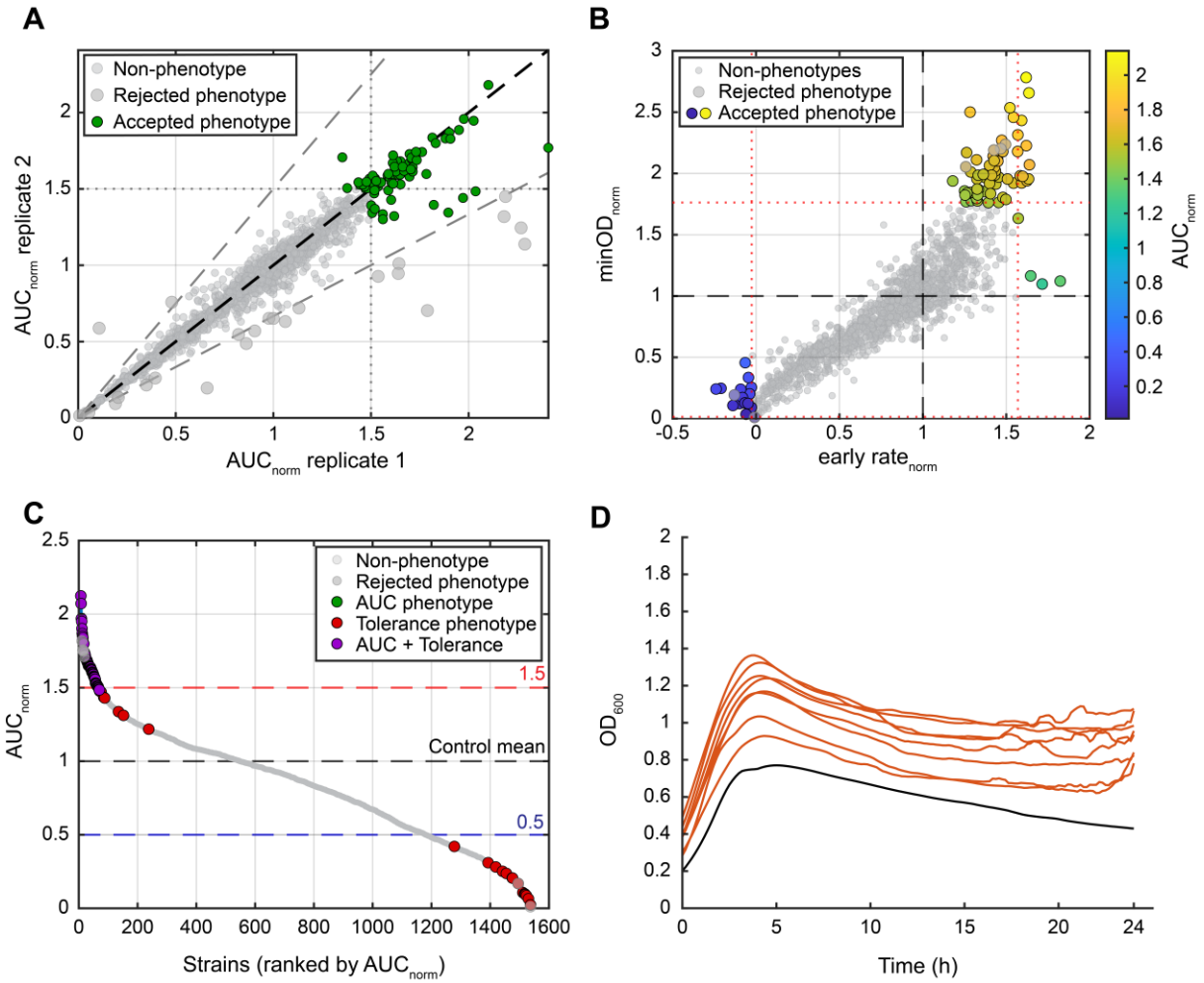

Figure 1. Summary of ciprofloxacin knockdown screen results. (A) Scatter plot comparing normalized area under the curve (AUC_{norm}) values between biological replicates. Green dots indicate strains with reproducible resistance phenotypes (AUC_{norm} > 1.5 in both replicates), while grey dots outside the 1.5-fold range were rejected. The black diagonal line represents a 1:1 ratio; dashed grey lines represent ±1.5-fold thresholds. **(B)** Tolerance phenotyping based on normalized minimal optical density ($minOD_{norm}$) and early growth rate ($earlyRate_{norm}$). Each point is colored by normalized AUC (see color bar). Accepted tolerance phenotypes (high $minOD_{norm}$ and/or high $earlyRate_{norm}$) appear in color, while rejected phenotypes (outside cutoffs) are marked with dark grey circles. Non-phenotypical strains are shown as light grey circles. Vertical and horizontal red dotted lines indicate ±2 SD cutoffs. **(C)** Strains ranked by average normalized AUC. Light grey circles show non-phenotypes; green dots are accepted resistant phenotypes (AUC_{norm} > 1.5), red dots are tolerance phenotypes, and purple dots possess both resistance and tolerance. Dark grey dots mark rejected strains. Horizontal dashed lines at AUC_{norm} = 1.5 (red) and 0.5 (blue) show the thresholds. **(D)** Regrowth phenotypes under ciprofloxacin exposure. Orange lines show mean optical density at 600 nm (OD_{600}) trajectories of knockdown strains (n = 8 x 2); black lines represent the means of all controls (n = 16 × 2).

All resistant and tolerant candidates were pooled, and AUC values were plotted (Figure 1C), resulting in 83 unique knockdowns: 58 of which appeared in both categories, 2 only from replicate agreement, and 23 only from the tolerance screen. This high overlap highlighted a key issue: this phenotype classification is highly sensitive to experimental noise, especially when OD_{600} values vary at start points due to knockdown-induced growth defects. As a result, each antibiotic required tailored parameters to define phenotypes.

Resistance was defined by increased OD_{600} at five distinct timepoints over the 24-hour period. Tolerance was assigned to strains whose OD_{600} decline persisted at least 50% longer than controls. A regrowth phenotype was defined by late-stage OD_{600} increases, while susceptibility was assessed by time-to-peak OD_{600}: strains reaching their peak in ≤75% of the control time were marked as susceptible. Detailed parameters per antibiotic are listed in the Material and Methods section.

Ciprofloxacin exposure allowed limited initial growth (~3 hours) followed by an OD_{600} decline, likely due to high drug concentration and cell lysis (Figure 1D, black line). Even with adjusted parameters, no strong resistance or tolerance phenotypes were found—only 8 strains showed late-stage regrowth (orange lines). Of these, 3 (*yadF*, *emrE*, *sbp*) exhibited regrowth in only one replicate, suggesting possible escape mutations.

Several transporter-related genes (*nikA*, *yddG*, *fepA*) were enriched in the regrowth phenotype category, though no published data supports their role in ciprofloxacin response (Table 1). Two standouts include the SMR efflux pump *EmrE*, and *betB*, encoding a ferric enterobactin dehydrogenase. Knockdown of *fepA*, which mediates enterobactin-ciprofloxacin conjugate uptake, was hypothesized to reduce ciprofloxacin entry, which may explain the phenotype[21,22].

Table 1. Regrowth phenotype knocked down genes under ciprofloxacin.

Gene	Function	Known Cip Effects
rutC	Pyrimidine catabolism enzyme	No data found
yadF	β-carbonic anhydrase	No data found
nikA	Nickel ABC transporter component	No data found
sbp	Sulfate/thiosulfate binding protein	No data found
yddG	Aromatic amino acid export transporter	No data found
emrE	SMR efflux pump	Possible modest effect, but no direct study
betB	Betaine-aldehyde dehydrogenase	No data found
fepA	Ferric-enterobactin outer membrane receptor	No direct data found

Gentamicin

Control strains initially grew for ~2 hours, followed by an OD_{600} decline and a secondary slow phase leading to a final plateau (Figure 2A-B, black lines). Applying adjusted parameters revealed both resistance and regrowth phenotypes.

Twelve knockdowns showed sustained growth over 24 hours and were classified as resistant (Figure 2A, purple lines; Table 2). Several knockdowns belonged to functionally related pathways. For example, *dxs* and *dxr* (MEP pathway) impair aminoglycoside uptake via reduced proton motive force[23,24]. Knockdowns of *ubiE* and *ubiG* disrupt ubiquinone synthesis or aerobic respiration, again reducing PMF[25]. Mutants of *lpxB* impair outer membrane integrity, paradoxically reducing hydrophilic aminoglycoside uptake[26]. Additional PMF-related hits include *hemH* and *pgsA*[27,28].

Additional noteworthy knockdowns include components of polyamine transport (e.g., *potD*, *potA*) and *dauA*, a C4-dicarboxylate transporter (Figure 2A, yellow dashed lines). These knockdowns may have impacted membrane potential; however, direct involvement in gentamicin resistance remains speculative[29]. Currently, there is no evidence in the literature linking these genes to antibiotic resistance, the robust growth of *potA* and *potD* knockdowns suggests they could be interesting targets for follow-up experiments.

Table 2. Resistant phenotypes under gentamicin treatment.

Gene	Function	Known Genta Effects of Knockdown
dauA	C4-dicarboxylate transporter	No direct data found
dxr	MEP pathway enzyme	Reduces PMF uptake
dxs	MEP pathway enzyme	Reduces PMF uptake
fepC	Siderophore uptake ABC ATPase subunit	No data found
hemH	Heme biosynthesis enzyme	Reduces PMF uptake
lpxB	LPS biosynthesis	Reduces PMF uptake
pgsA	Phospholipid synthesis enzyme	Reduces PMF uptake
potA	Polyamine ABC transporter	No data found
potD	Polyamine ABC transporter	No data found
ubiE	Ubiquinone biosynthesis methyltransferase	Reduces PMF uptake
ubiG	Ubiquinone methyltransferase	Reduces PMF uptake

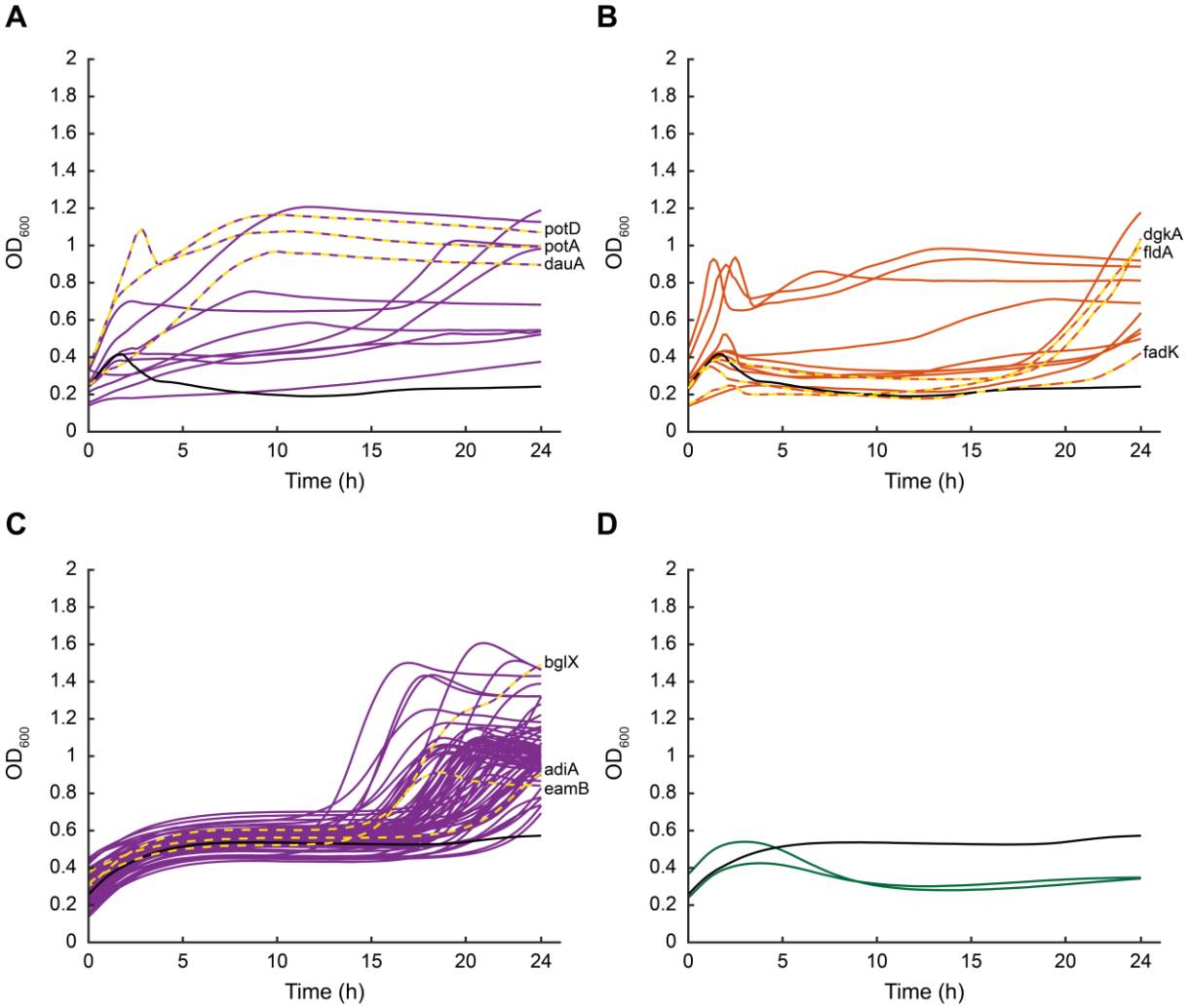

Figure 2. Summary of phenotypes detected in gentamicin and rifampicin screens. In all panels, black lines represent the mean optical density at 600 nm (OD_{600}) trajectories of control strains (n = 16 × 2) under the corresponding antibiotic condition, yellow dashed lines noteworthy strains for further investigation **(A)** Resistant phenotypes under gentamicin exposure. Purple lines represent knockdown strains mean (n = 12 x 2). **(B)** Regrowth phenotypes under gentamicin exposure. Orange lines show mean OD_{600} trajectories of knockdown strains (n = 12 x 2). **(C)** Resistant phenotypes under rifampicin exposure. Purple lines represent knockdown strains mean (n = 73 x 2). **(D)** Susceptible phenotypes under rifampicin exposure. Green lines represent knockdown strains means (n = 2 x 2).

Twelve regrowth phenotypes were identified (Figure 2B, orange lines; Table 3), with one strain showing the effect in only one replicate. Several knockdowns (*hemD*, *hemF*, *ispA*, *ubiA*, *ubiF*, *ubiH*) fall within the same PMF-linked pathways as the resistant strains. *cyoA*, part of the cytochrome bo3 oxidase, also reduces PMF when disrupted[30].

The gene *iscS*, encoding a cysteine desulfurase required for Fe-S cluster assembly, is another notable hit. Disruption likely impaired respiration similarly to *ryhB*, an iron-regulatory RNA previously linked to gentamicin response[31].

For *dgkA*, *fadK*, and *fldA*, no direct links to gentamicin resistance have been reported in the literature. However, their involvement in phospholipid recycling, fatty acid metabolism, and electron transport, respectively, makes them intriguing candidates for further study (Figure 2B, yellow dashed lines)[32–34]. Notably, only *dgkA* consistently exhibited the phenotype across both replicates, underscoring that additional validation is required.

One strain classified as resistant showed a notable OD_{600} decrease after several hours (Figure 2A, purple lines), a pattern also observed in three of the strongest regrowth phenotypes (Figure 2B, orange lines). This observation may reflect either the emergence of resistant subpopulations or the influence of technical artifacts. Altered cell morphology was previously observed to cause accumulation in the center of the well during shaking. When the pellet reaches a critical size, it can suddenly disperse, leading to sharp changes in OD_{600} readings. These factors complicate the interpretation of these four strains, and they could plausibly be classified as either resistant or regrowth phenotypes.

Table 3. Regrowth phenotypes under gentamicin treatment.

Gene	Function	Known Genta Effects of Knockdown
cyoA	Cytochrome *bo*$_3$ oxidase subunit 2	Reduces PMF uptake
dgkA	Diacylglycerol kinase	No data found
fadK	Anaerobic fatty acid kinase	No data found
fldA	Flavodoxin-A electron carrier	No data found
hemD	Heme biosynthesis enzyme	Reduces PMF uptake
hemF	Heme biosynthesis enzyme	Reduces PMF uptake
iscS	Cysteine desulfurase	No direct data found
ispA	Isoprenoid precursor enzyme	Reduces PMF uptake
ubiA	Ubiquinone prenyltransferase	Reduces PMF uptake
ubiF	Ubiquinone hydroxylase	Reduces PMF uptake
ubiH	Ubiquinone hydroxylase	Reduces PMF uptake

Rifampicin

Rifampicin caused gradual OD_{600} reduction over the first 6–7 hours, followed by a stable plateau (Figure 2C, black line). Minor late-stage increases were traced to a single outlier in the control group. Both resistance and susceptibility phenotypes were identified in this screen.

In total, 73 strains were flagged as resistant based on their continued OD_{600} increase and higher final OD_{600} compared to controls (Figure 2C, purple lines). However, only 23 of these were consistent across both replicates, emphasizing the need for further validation. Given the number of hits and the complexity of rifampicin's mechanism, here on knockdowns within functional categories previously associated with rifampicin resistance were focused,

specifically, energy metabolism, cell envelope biosynthesis, stress response pathways, and iron acquisition[35,36] (Table 4).

Knockdowns of NADH dehydrogenase I subunits (*nuoF*, *nuoM*) and ATP synthase subunits (*atpC*, *atpG*) likely reduced metabolic activity and PMF, diminishing rifampicin uptake[36]. Iron acquisition genes (*entA*, *feoB*) affect respiration, while capsular polysaccharide (*cpsB*, *cpsG*, *wzxE*) and LPS core (*waaR*) knockdowns may have triggered envelope stress, leading to activation of the Rcs system[37,38]. Disulfide bond formation genes (*dsbA*, *dsbC*, *dsbD*) also induced stress pathways upon disruption[39].

Of the remaining 58 phenotypic knockdown strains, three genes (*adiA*, *bglX*, *eamB*) stood out due to their lack of known association with rifampicin resistance, making them intriguing candidates for follow-up analysis (Figure 2C, yellow dashed lines). *AdiA* is part of the arginine-dependent acid resistance system[40]; its knockdown may lead to reduced pH and/or energy levels, potentially disrupting nitrogen flux and membrane charge. *BglX* is predicted to be involved in periplasmic glycan hydrolysis, though its physiological role remains poorly characterized, with no reported phenotypes upon deletion or overexpression[41,42]. Knockdown of *bglX* could affect periplasmic osmolarity and envelop tension, prevent accumulation of toxic intermediates, or activate stress response pathways. *EamB*, a cysteine/O-acetylserine exporter, may influence sulfur signaling and thiol redox balance when depleted[43]. Its absence could also result in ROS accumulation or triggering compensatory stress responses that paradoxically enhance antibiotic tolerance.

Two strains showed a consistent susceptible phenotype across both replicates (Figure 2D, green lines). These were knockdowns of *nrdA* and *nrdB*, the large and small subunits of ribonucleotide reductase (RNR). Although no direct association with rifampicin has been reported, the impairment of DNA replication likely synergizes with rifampicin inhibiting RNA polymerase[44], suggesting that combining rifampicin with DNA replication inhibitors may enhance treatment efficacy.

Table 4. Selected phenotypes under rifampicin treatment, grouped by functional category. Displayed knockdowns were selected from the broader set of resistant strains based on involvement in pathways known to influence rifampicin susceptibility. Groupings include genes linked to energy metabolism, envelope stress responses, iron homeostasis, and redox regulation, as supported by CRISPRi, Tn-Seq, or other functional genomic studies.

Gene	Functional group	Known Rif Effects of Knockdown
nuoF, nuoM, atpC, atpG	Aerobic respiration/ATP synthesis	No direct data found
entA. feoB	Iron/siderophore metabolism	Respiration reduction
cpsB, cpsG, waaR, wzxE	Cell envelope structure	No direct data found
dsbA, dsbC, dsb	Periplasmic stress response	No direct data found
nrdA, nrdB	Ribonucleotide reductase subunit	No direct data found

Meropenem

Meropenem produced the broadest range of phenotypes after fosfomycin, with a total of 127 knockdowns identified. Growth dynamics of control strains under meropenem exposure were characterized by a short initial growth phase lasting approximately one hour, followed by a pronounced and sustained decline in OD_{600} over the next several hours (Figure 3, black lines). After around five hours, cultures reached a plateau that persisted for the remainder of the 24-hour period.

Six knockdowns demonstrated continuous growth over the full time course in both replicates and were classified as resistant (Figure 3A, purple lines; Table 5). Several of these genes are supported by prior studies indicating mechanisms of β-lactam resistance. For example, knockdowns affecting lipopolysaccharide (LPS) assembly, such as *waaA*, have been associated with increased tolerance to meropenem through stress signaling and delayed lysis responses[12]. Similarly, knockdowns of genes involved in purine biosynthesis, including *purD* and *prs*, reduce β-lactam sensitivity by weakening target engagement[45]. Related genes upstream in the purine biosynthetic pathway, such as *panB*, *folE*, and *gltX*, likely reduce metabolic flux through this pathway and further impair purine production[46]. Notably, *gltX* knockdown has also been associated with impaired protein synthesis and reduced biomass accumulation, features that have been linked to bacterial persistence[47]. In addition, knockdown of the TCA cycle enzyme *icd* likely induced metabolic stress and redox imbalance, creating conditions conducive to slow growth and increased antibiotic survival[46]. Similarly, reduction of CysU, a component of the sulfur uptake pathway, may activate starvation-induced stress responses that enhance survival under meropenem pressure[48].

Table 5. Resistant phenotypes found under Meropenem treatment.

Gene	Function	Known Mero Effects of Knockdown
cysU	Sulfate import	No direct data found
folE	Folate biosynthesis	No direct data found
gltX	Glutamate-tRNA ligase	Metabolic slowdown
icd	Isocitrate dehydrogenase (TCA cycle)	No direct data found
panB	Pantothenate synthesis	No direct data found
prs	Phosphoribosyl synthase	Reduced sensitivity
purD	Purine biosynthesis	Reduced sensitivity
waaA	LPS core assembly enzyme	Increases tolerance

The screen also identified 102 knockdowns classified as regrowth phenotypes, 16 of which showed the phenotype in only one of the two replicates (Figure 3B, orange lines; Table 6). Due to the high number of hits, it was not feasible to analyze all strains in depth. Therefore, analysis focused on knockdowns in functional groups previously linked to β-lactam tolerance and resistance[12].

The first group includes genes associated with central metabolic processes (Table 6). These knockdowns were likely to reduce the rate of cellular growth and ATP production, thereby lowering the rate of cell wall synthesis, one of the primary targets of meropenem, and mitigating lytic pressure[47,49–51]. A second group consists of genes involved in the biosynthesis and maintenance of the cell envelope. Disruption of these genes is expected to activate envelope stress responses (ESRs), including the RpoE, Rcs, and CpxRA systems, which promote survival by limiting autolysis and slowing cellular activity[12,37]. Another group comprises components of the respiratory chain, particularly NADH dehydrogenase I subunits such as *nuoJ*, *nuoK*, and *nuoM*. Their knockdown impairs PMF generation and reduces ATP output, slowing metabolic rates and indirectly limiting cell wall synthesis[12,52].

Table 6. Functionally grouped knockdowns exhibiting regrowth phenotypes under meropenem treatment. Genes were grouped based on shared biological functions or pathway membership, as inferred from existing literature and functional annotations. Groupings reflect pathways previously associated with altered antibiotic susceptibility, including metabolism, cell envelope biogenesis, respiration, stress responses, and transport systems.

Genes	Functional group	Known Mero Effects of Knockdown
fadA, fadI, pykA, ptsG, glgP, glgX, otsA, pepD, uxuA, fdoH, poxB	Metabolism linked knockdowns	Slow cellular growth and ATP production
waaL, wzzE, wecD, wecG, lpxM, wcaJ	LPS or capsule biosynthesis	Slow cellular growth and reduced autolysis
nuoJ, nuoK, nuoM	Respiration and PMF	Low energy state and cell-wall synthesis
fhuC, fhuD, livF, livG, btuC, pitA, putP, gltL/D, ansB, appA, potG, dppF, dppD	Transport & uptake systems	Growth and cell-wall synthesis reduction
sodA, ahpF, msrB, fldB	Management of ROS	ROS induced stress responses
acrB, acrF, emtA	Efflux systems	Lowered PMF, slowed growth, envelope stress response

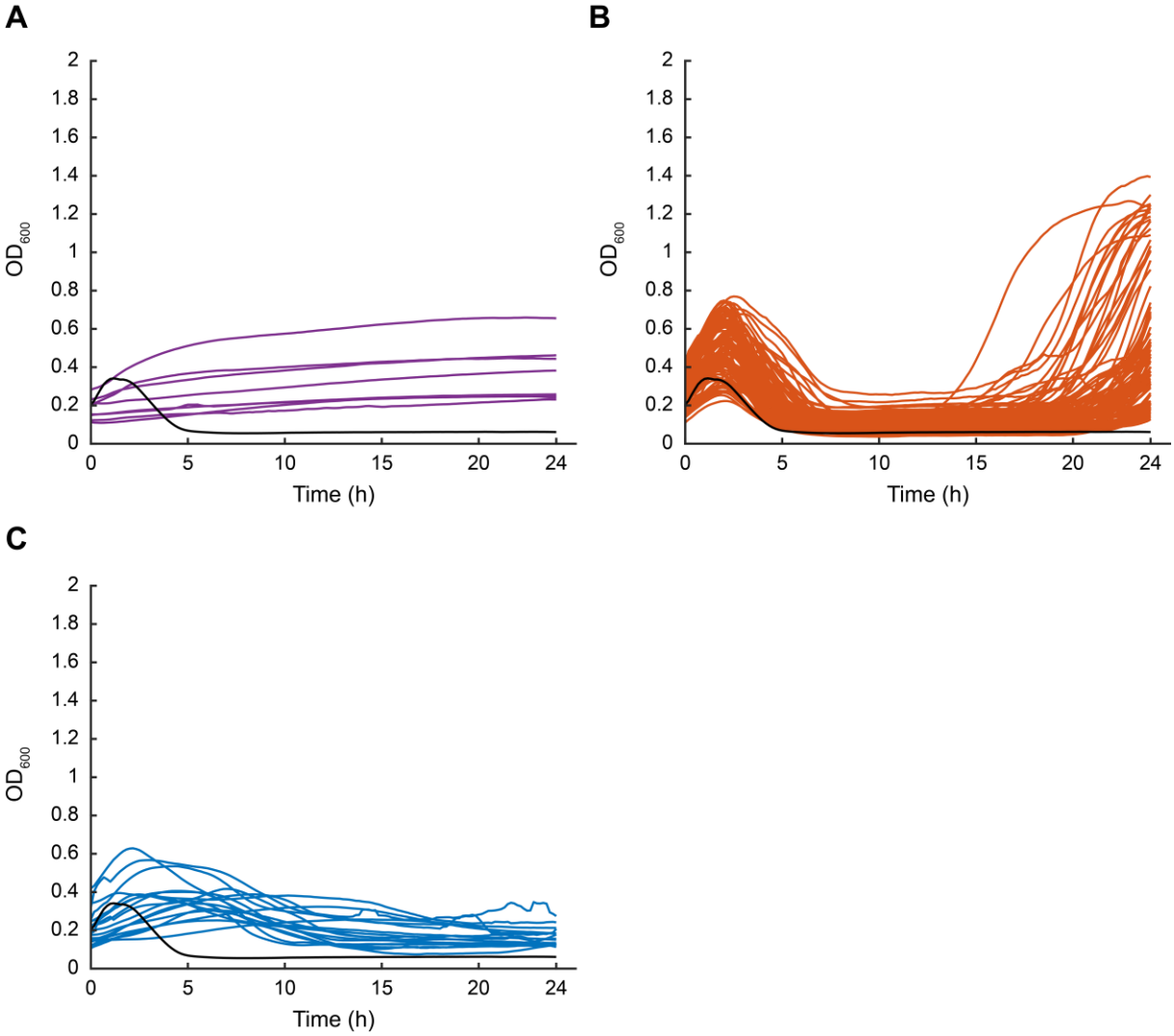

Figure 3. Summary of phenotypes detected in the meropenem screen. In all panels, black lines represent the mean optical density at 600 nm (OD_{600}) trajectories of control strains (n = 16 × 2) under meropenem exposure **(A)** Resistant phenotypes are shown in purple; lines represent knockdown strains mean (n = 8 x 2). **(B)** Regrowth phenotypes are shown in orange; lines show mean OD_{600} trajectories of knockdown strains (n = 102 × 2). **(C)** Tolerant phenotypes are shown in blue; lines show mean OD_{600} trajectories of knockdown strains (n = 17 × 2).

Further candidate genes are part of transport and uptake pathways. Knockdowns in this category may impair nutrient uptake and trigger starvation responses, consistent with slow growth and enhanced tolerance[35,53]. Another group includes genes involved in ROS management and redox homeostasis. These knockdowns may increase ROS levels, potentially activating SOS or OxyR stress responses[54]. Finally, the screen identified several transport and efflux system components whose knockdown, while seemingly counterintuitive, may reduce PMF and lead to activation of envelope or metabolic stress pathways. These changes slow cellular activity and may increase bacterial survival under meropenem treatment[55,56].

Although a relatively high number of regrowth phenotypes were observed, interpretation of regrowth phenotypes is complicated by the short half-life of meropenem at 37°C[57,58]. Thus, reduced antibiotic activity at later time points could explain many of these phenotypes. This limits the ability to confidently identify candidates, warranting further investigation.

In addition to resistant and regrowth phenotypes, the screen identified 17 strains with reproducible tolerance phenotypes in both replicates (Figure 3C, blue lines; Table 7). As with regrowth strains, the analysis focused on functional gene groups. The first group includes genes involved in nucleotide and cofactor biosynthesis, whose knockdown likely slows cell growth and division while activating nutrient stress responses. These knockdowns may have reduced metabolic flux, contributing to tolerance against meropenem-induced lysis[12,47]. The second group consists of transport-related genes such as *msbA*, *tonB*, and *mscL*. Disruption of these genes may reduce PMF and trigger ESR activation, once again leading to slower growth and increased survival[12,59,60]. A third group includes genes involved in central energy regulation, including *pgi* and *fabH*. These knockdowns are predicted to reduce energy production and fatty acid biosynthesis, slowing cell wall synthesis and introducing transient tolerance[61,62]. Finally, knockdown of *trxA*, encoding thioredoxin, may activate multiple stress regulons and contribute to a persistence-like behavior[63,64].

These results indicate that knockdown responses vary strongly by antibiotic and are compared across antibiotics in the next section.

Table 7. Functionally categorized tolerant phenotypes identified under meropenem exposure. Knockdowns were organized into categories based on their involvement in related metabolic, transport, or regulatory functions. Groupings were derived from known cellular pathways and published studies linking these genes to stress adaptation or antibiotic tolerance mechanisms.

Genes	Functional group	Known Mero Effects of Knockdown
purA, purN, pyrH, nadD, ribF, folD, folK, argH, coaE, metA	Nucleotide and cofactor biosynthesis	Reduced growth, cell division, and metabolic flux + stress responses
msbA, tonB, mscL	Transport systems	Envelope stress response, reduced PMF
pgi, fabH	Energy regulation	Slow metabolism, low energy production and envelope biosynthesis
trxA	Redox hemostasis	Stress regulon activation

Global Analysis of All Screened Antibiotics

Despite limited overlap between individual screens, five knockdowns were identified in both the meropenem regrowth and rifampicin resistance screens (Table 8). Given the relatively large number of total hits in these conditions (n = 102 and n = 73, respectively), the overlap may reflect the large number of responsive strains in these screens, rather than a direct functional link. Although some overlap may be expected by chance, the consistent phenotypes of delayed OD_{600} recovery under meropenem and rifampicin suggest shared survival mechanisms, such as membrane stress resistance or reduced metabolic activity.

Among the five overlapping hits, a recurring theme emerged around impaired metabolic and energetic functions. The genes *atpG* and *nuoM* encode components of the bacterial respiratory chain and ATP synthase complex, both central to PMF generation and energy production[65,66]. Their knockdown likely leads to reduced cellular respiration and ATP synthesis; a condition associated with increased tolerance to bactericidal antibiotics[7,67]. Although the gene *ghxQ*, is poorly characterized, its product is thought to function in purine salvage, potentially impacting nucleotide balance and energy homeostasis[68]. The identification of *lacZ* and *sgbU* in this context could suggest links to sugar metabolism or nutrient uptake, but direct evidence for such a role, particularly for the poorly characterized *sgbU,* is currently lacking[69]. These findings support the idea that reduced metabolic activity can promote survival under different antibiotic stresses, even across drugs with distinct modes of action.

A similar pattern is observed for *prs* and *purD*, which exhibited resistance phenotypes in both the fosfomycin and meropenem screens. Both genes are involved in purine biosynthesis, and their disruption is expected to reduce nucleotide availability and overall metabolic flux[70]. This reduced-growth, stress-adapted state likely lowers antibiotic target engagement, especially for antibiotics that rely on active cell wall synthesis, such as β-lactams and fosfomycin.

Knockdown of *aceE*, which encodes a component of the pyruvate dehydrogenase complex, was associated with regrowth phenotypes under both fosfomycin and gentamicin. As *aceE* links glycolysis to the TCA cycle, its disruption impairs energy generation and biosynthetic precursor supply[71]. This metabolic deceleration may delay antibiotic killing and facilitate regrowth after transient inhibition, representing a potential tolerance mechanism shared across antibiotic classes.

Finally, *waaA*, whose product is a key enzyme in LPS core biosynthesis, was associated with resistance to meropenem and tolerance to fosfomycin. Loss of *WaaA* function alters outer membrane structure and likely activates envelope stress responses that buffer against antibiotic-induced damage[72]. The appearance of *waaA* knockdown across two bactericidal antibiotics suggests that envelope remodeling and stress pathway activation contribute broadly to survival under bactericidal antibiotics in *E. coli*.

Table 8. Genes affected by several antibiotics during exposure.

Genes	Function	Phenotypes identified in Screen
aceE	Pyruvate dehydrogenase component	Regrowth in Fosfo and Genta
atpG	ATP synthase subunit	Regrowth Fosfo and resistant Rif
ghxQ	Guanin/hypoxanthine transporter	Regrowth Mero and resistant Rif
lacZ	Beta-galactosidase	Regrowth Mero and resistant Rif
nuoM	NADH dehydrogenase subunit	Regrowth Mero and resistant Rif
prs	Phosphoribosyl pyrophosphate synthase	Resistant Fosfo and Mero
purD	Phosphoribosylamine-glycine ligase	Resistant Fosfo and Mero
sgbU	Putative sugar transporter	Regrowth Mero and resistant Rif
waaA	LPS biosynthesis transferase	Resistant Mero and tolerant Fosfo

Discussion

This chapter extended the fosfomycin CRISPRi screen by evaluating gene knockdown effects under four additional antibiotics, each targeting distinct cellular processes: ciprofloxacin, gentamicin, rifampicin, and meropenem. For the global analysis, phenotype data from the fosfomycin screen (Chapter 3) was included to enable cross-antibiotic comparisons.

While the screen enabled a broad survey of gene-drug interactions, several practical limitations affected phenotype resolution. Notably, replicate inconsistencies limit confidence in many ciprofloxacin and rifampicin phenotypes, particularly those classified as resistant or exhibiting regrowth. Such discrepancies may stem from random mutations arising in a single replicate under antibiotic selective pressure, or from a loss of antibiotic potency over time[57,73]. Additionally, the detection of susceptible phenotypes proved challenging in most conditions, with only rifampicin yielding consistent susceptibility calls across replicates. These limitations reflect both biological variability and technical constraints of OD-based liquid culture screens, particularly under conditions that induce rapid cell lysis or growth arrest.

Beyond technical considerations, the number and diversity of phenotypes varied notably between antibiotics, offering insights into both their relative efficacy and how adaptable cells are under each condition. Ciprofloxacin, for instance, yielded almost no interpretable phenotypes under the tested concentration, consistent with its highly potent, bactericidal activity that rapidly eliminates cells and leaves little opportunity for genetic buffering, recovery, or delayed growth. In contrast, meropenem and fosfomycin supported a broader spectrum of resistant, tolerant, and regrowth phenotypes. This broader range of phenotypes may reflect slower killing dynamics and greater reliance on stress responses, which expose protective knockdowns. These differences show that parallel screening is useful for distinguishing antibiotic-specific responses from broader survival mechanisms.

In data interpretation, it is important to consider potential escape mechanisms that may confound phenotype classification over extended treatment periods. For instance, antibiotic degradation or instability over 24 hours could reduce selective pressure and permit regrowth in strains not truly resistant. This is particularly relevant for β-lactams such as meropenem, which are susceptible to hydrolysis and chemical breakdown in aqueous media[74,75]. Additionally, certain strains may escape killing not by genuine resistance, but through indirect effects such as altered permeability, induction of efflux systems, or shifts in growth phase that reduce target engagement[76,77]. Such physiological adaptations, while not necessarily genetically stable, can contribute to transient survival and complicate interpretation of regrowth or tolerance phenotypes. Even when phenotypes reproduce across replicates, follow-up validation with time-resolved assays is needed to separate true genetic tolerance from passive escape effects.

Some phenotypic ambiguities may also stem from experimental artifacts related to OD measurement. For example, several gentamicin-exposed strains showed abrupt OD_{600} changes that may result from sedimented cell aggregates redistributing during shaking, rather than true regrowth or resistance. Because similar OD_{600} changes can result from altered cell morphology or pellet dispersal, these cases should be interpreted carefully and confirmed with additional evidence.

Across antibiotics, a recurring pattern emerged in which knockdowns disrupting energy metabolism or nucleotide biosynthesis, such as *atpG*, *nuoM*, *prs*, and *purD*, were linked to increased resistance or tolerance. These perturbations likely reduce antibiotic target engagement through metabolic slowdown, which can reduce susceptibility to bactericidal antibiotics.

Similarly, genes involved in membrane architecture and stress response activation were repeatedly associated with increased survival. For instance, *waaA*, involved in LPS core biosynthesis, emerged across multiple screens, reinforcing the idea that envelope remodeling contributes to stress adaptation.

In addition to these common patterns, several antibiotic-specific hits warrant closer examination. Under gentamicin exposure, knockdowns of *potA*, *potD*, and *dgkA*, genes involved in polyamine transport, dicarboxylate exchange, and lipid metabolism, exhibited robust phenotypes despite no prior links to aminoglycoside resistance. Their influence on membrane potential and redox state suggests novel routes to survival beyond canonical PMF disruption.

The rifampicin screen similarly revealed intriguing candidates. AdiA, part of the arginine-dependent acid resistance system, may alter intracellular pH and energy balance; BglX, though poorly characterized, could affect periplasmic structure and osmotic regulation; and EamB may disrupt sulfur signaling and thiol redox homeostasis. These findings suggest that envelope integrity and redox balance may contribute to rifampicin tolerance, though this has not been reported previously.

Unlike the other antibiotics, rifampicin yielded reproducible susceptibility phenotypes. Knockdowns of *nrdA* and *nrdB*, which impair DNA synthesis, likely synergize with rifampicin's transcriptional inhibition, suggesting that combining rifampicin with DNA synthesis inhibitors could be an effective strategy for combinatory therapies.

Taken together, these results highlight both the strengths and limitations of CRISPRi-based phenotyping under antibiotic stress. The identified knockdowns serve as starting points for mechanistic studies, including detailed investigations of the molecular pathways underlying resistance and tolerance. Functional validation of these hits could clarify the contributions of specific genes to antibiotic uptake, metabolism, and stress response, while system-level analyses may reveal interactions that govern susceptibility. Collectively, these follow-up studies provide a basis for developing combination treatment approaches and antibiotic design in *E. coli* and related species.

Material & Methods

MIC Determination

MICs for ciprofloxacin, gentamicin, rifampicin, and meropenem were determined as described in Chapter 3. The resulting MIC values were: 15 ng/mL for ciprofloxacin; 0.3 µg/mL for gentamicin; 1.2 µg/mL for meropenem; and 20 µg/mL for rifampicin.

Antibiotics Screening

CRISPRi library screening under antibiotic stress was carried out using the same protocol described in Chapter 3.

Phenotype Determination

Optical density growth data from all screens were imported into MATLAB (R2024b, MathWorks), converted to OD_{600} values, and smoothed using the built-in smooth function with default settings (moving average).

AUC was calculated for each strain and replicate, as well as for the controls. AUC values for each strain were then normalized to the average control AUC. Strains were considered potential resistant phenotypes if their normalized AUC exceeded 1.5× the control average and both replicates fell within 1.5× of each other.

Due to diverse growth patterns caused by antibiotic treatment, tolerance, resistance, and regrowth criteria had to be adjusted for each antibiotic individually, as shown in the following section.

Ciprofloxacin

For ciprofloxacin, phenotypes were determined based on growth changes at defined timepoints:

Tolerance: OD_{600} values were extracted at 4 h (the time of peak growth in control strains) and again at 6 h. The difference between these timepoints was calculated and normalized to the control difference. Strains with normalized values ≥1.5× those of the control average were classified as tolerant.

Resistance: Strains were classified as resistant if they exhibited a continuous increase in OD_{600} across five timepoints: 0 h, 4 h, 6 h, 12 h, and 24 h.

Regrowth: Regrowth phenotypes were assigned to strains with 24 h OD_{600} that was ≥1.3× higher than at 12 h.

Gentamicin

For gentamicin, phenotype classification was based on early growth dynamics and final OD_{600}:

Tolerance: Tolerant strains were defined by an OD_{600} ratio (4 h / 2 h) ≥1.5× that of controls.

Resistance: Strains were considered resistant if they displayed sustained OD_{600} increases across five timepoints (0 h, 2 h, 4 h, 12 h, 24 h) and reached 24 h OD_{600} ≥2× the control average.

Regrowth: Regrowth was assigned to strains that either (i) reached 24 h OD_{600} ≥1.5× their value at 12 h OD_{600}, or (ii) reached 24 h OD_{600} >0.6 but without showing continuous growth across the resistance-defining timepoints (i.e., did not meet resistance criteria).

Rifampicin

Rifampicin phenotypes were identified based on delayed decline and regrowth behavior:

Tolerance: Strains were classified as tolerant if their OD_{600} decline occurred ≥2 h later than in controls (i.e., after 7 h instead of 5 h).

Resistance: Resistance was assigned to strains with a 24 h OD_{600} ≥1.5× its 12 h value and a minimum 24 h OD_{600} ≥0.5.

Regrowth: A resistant regrowth phenotype was assigned when OD_{600} declined between 7 h and 12 h but subsequently increased by 24 h to exceed the 7 h value.

Meropenem

Phenotype assignments under meropenem exposure were based on delayed growth and 24 h OD_{600} values:

Tolerance: Strains were classified as tolerant if their OD_{600} at 8 h was ≥1.5× their 24 h OD_{600}, provided the starting and 24 h OD_{600} were both ≥0.1 to exclude non-growing strains.

Resistance: Resistance was defined as a consistent increase in OD_{600} across five timepoints (0 h, 1.5 h, 4 h, 12 h, 24 h), and 24 h OD_{600}≥2× the average of controls to exclude non-growing strains.

Regrowth: Strains were considered regrowth phenotypes if (i) the 2 h OD_{600} was ≥2.5× higher than at 12 h OD_{600}, (ii) the 24 h OD_{600} was ≥1.3× higher than at 12 h OD_{600}, and (iii) the 24 h OD_{600} was ≥2× the control average. These specific rules were required to separate these phenotypes from resistant and tolerant phenotypes.

Susceptibility Criteria (All Antibiotics)

For all antibiotics, susceptibility was defined as reaching maximal OD_{600} reduction in 75% or less of the time required by controls.

Bibliography

(1) Sanders, C. C. Ciprofloxacin: In Vitro Activity, Mechanism of Action, and Resistance. *Rev Infect Dis* **1988**, *10* (3), 516–527. https://doi.org/10.1093/clinids/10.3.516.

(2) Collins, J. A.; Oviatt, A. A.; Chan, P. F.; Osheroff, N. Target-Mediated Fluoroquinolone Resistance in *Neisseria Gonorrhoeae*: Actions of Ciprofloxacin against Gyrase and Topoisomerase IV. *ACS Infect. Dis.* **2024**, *10* (4), 1351–1360. https://doi.org/10.1021/acsinfecdis.4c00041.

(3) *Determination of Antibiotic Hypersensitivity among 4,000 Single-Gene-Knockout Mutants of Escherichia coli | Journal of Bacteriology*. https://journals.asm.org/doi/10.1128/jb.01982-07 (accessed 2025-07-26).

(4) Tewawong, N.; Kowaboot, S.; Lektrakul, W.; Supcharoengoon, U.; Watanagul, N.; Pitaksajjakul, P. Mechanisms of Fluoroquinolone Resistance among *Escherichia Coli* Isolates from Urinary Tract Infections in Thailand. *PLOS ONE* **2025**, *20* (5), e0325175. https://doi.org/10.1371/journal.pone.0325175.

(5) Weinstein, M. J.; Luedemann, G. M.; Oden, E. M.; Wagman, G. H.; Rosselet, J. P.; Marquez, J. A.; Coniglio, C. T.; Charney, W.; Herzog, H. L.; Black, J. Gentamicin,1 a New Antibiotic Complex from Micromonospora. *J. Med. Chem.* **1963**, *6* (4), 463–464. https://doi.org/10.1021/jm00340a034.

(6) Kohanski, M. A.; Dwyer, D. J.; Wierzbowski, J.; Cottarel, G.; Collins, J. J. Mistranslation of Membrane Proteins and Two-Component System Activation Trigger Antibiotic-Mediated Cell Death. *Cell* **2008**, *135* (4), 679–690. https://doi.org/10.1016/j.cell.2008.09.038.

(7) Shiraliyev, R.; Orman, M. A. Metabolic Disruption Impairs Ribosomal Protein Levels, Resulting in Enhanced Aminoglycoside Tolerance. *eLife* **2024**, *13*, RP94903. https://doi.org/10.7554/eLife.94903.

(8) Cm, W.; Am, W.; S, F.; Lg, H.; Gk, R.; M, S. Proton Motive Force Underpins Respiration-Mediated Potentiation of Aminoglycoside Lethality in Pathogenic *Escherichia Coli*. *Archives of microbiology* **2022**, *204* (1). https://doi.org/10.1007/s00203-021-02710-y.

(9) Hu, X.; Xu, B.; Yang, Y.; Liu, D.; Yang, M.; Wang, J.; Shen, H.; Zhou, X.; Ma, X. A High Throughput Multiplex PCR Assay for Simultaneous Detection of Seven Aminoglycoside-Resistance Genes in *Enterobacteriaceae*. *BMC Microbiology* **2013**, *13* (1), 58. https://doi.org/10.1186/1471-2180-13-58.

(10) Garneau-Tsodikova, S.; Labby, K. J. Mechanisms of Resistance to Aminoglycoside Antibiotics: Overview and Perspectives. *Med. Chem. Commun.* **2016**, *7* (1), 11–27. https://doi.org/10.1039/C5MD00344J.

(11) Linden, P. Safety Profile of Meropenem. *Drug-Safety* **2007**, *30* (8), 657–668. https://doi.org/10.2165/00002018-200730080-00002.

(12) Thomson, N. M.; Turner, A. K.; Yasir, M.; Bastkowski, S.; Lott, M.; Webber, M. A.; Charles, I. G. A Whole-Genome Assay Identifies Four Principal Gene Functions That Confer Tolerance of Meropenem Stress upon *Escherichia Coli*. *Front. Antibiot.* **2022**, *1*. https://doi.org/10.3389/frabi.2022.957942.

(13) Kim, H.-R.; Eom, Y.-B. Synergistic Activity of Equol and Meropenem against Carbapenem-Resistant *Escherichia Coli*. *Antibiotics* **2021**, *10* (2), 161. https://doi.org/10.3390/antibiotics10020161.

(14) Molodtsov, V.; Scharf, N. T.; Stefan, M. A.; Garcia, G. A.; Murakami, K. S. Structural Basis for Rifamycin Resistance of Bacterial RNA Polymerase by the Three Most Clinically Important RpoB Mutations Found in *Mycobacterium Tuberculosis*. *Molecular Microbiology* **2017**, *103* (6), 1034–1045. https://doi.org/10.1111/mmi.13606.

(15) Murray, J. F.; Schraufnagel, D. E.; Hopewell, P. C. Treatment of Tuberculosis. A Historical Perspective. *Annals ATS* **2015**, *12* (12), 1749–1759. https://doi.org/10.1513/AnnalsATS.201509-632PS.

(16) Mosaei, H.; Zenkin, N. Inhibition of RNA Polymerase by Rifampicin and Rifamycin-Like Molecules. *EcoSal Plus* **2020**, *9* (1), 10.1128/ecosalplus.ESP-0017–2019. https://doi.org/10.1128/ecosalplus.esp-0017-2019.

(17) Brown, D. R.; Barton, G.; Pan, Z.; Buck, M.; Wigneshweraraj, S. Nitrogen Stress Response and Stringent Response Are Coupled in *Escherichia Coli*. *Nat Commun* **2014**, *5* (1), 4115. https://doi.org/10.1038/ncomms5115.
(18) Narang, A.; Garima, K.; Porwal, S.; Bhandekar, A.; Shrivastava, K.; Giri, A.; Sharma, N. K.; Bose, M.; Varma-Basil, M. Potential Impact of Efflux Pump Genes in Mediating Rifampicin Resistance in Clinical Isolates of *Mycobacterium Tuberculosis* from India. *PLOS ONE* **2019**, *14* (9), e0223163. https://doi.org/10.1371/journal.pone.0223163.
(19) Jin, D. J.; Gross, C. A. Mapping and Sequencing of Mutations in the *Escherichia Coli rpoB* Gene That Lead to Rifampicin Resistance. *Journal of Molecular Biology* **1988**, *202* (1), 45–58. https://doi.org/10.1016/0022-2836(88)90517-7.
(20) Baquero, F.; Levin, B. R. Proximate and Ultimate Causes of the Bactericidal Action of Antibiotics. *Nat Rev Microbiol* **2021**, *19* (2), 123–132. https://doi.org/10.1038/s41579-020-00443-1.
(21) Tj, B.; Me, W.; Ma, M. Mutations in the *Escherichia Coli* Receptor FepA Reveal Residues Involved in Ligand Binding and Transport. *Molecular microbiology* **2001**, *41* (3). https://doi.org/10.1046/j.1365-2958.2001.02473.x.
(22) Sargun, A.; Gerner, R. R.; Raffatellu, M.; Nolan, E. M. Harnessing Iron Acquisition Machinery to Target *Enterobacteriaceae*. *The Journal of Infectious Diseases* **2021**, *223* (Supplement_3), S307–S313. https://doi.org/10.1093/infdis/jiaa440.
(23) Paul, E.; Ghai, I.; Hörömpöli, D.; Brötz-Oesterhelt, H.; Winterhalter, M.; Bafna, J. A. Uptake of Aminoglycosides through Outer Membrane Porins in *Escherichia Coli*. bioRxiv September 5, 2022, p 2022.09.05.506620. https://doi.org/10.1101/2022.09.05.506620.
(24) Brown, A. C.; Parish, T. Dxr Is Essential in *Mycobacterium Tuberculosis* and Fosmidomycin Resistance Is Due to a Lack of Uptake. *BMC Microbiology* **2008**, *8* (1), 78. https://doi.org/10.1186/1471-2180-8-78.
(25) Webster, C. M.; Shepherd, M. A Mini-Review: Environmental and Metabolic Factors Affecting Aminoglycoside Efficacy. *World J Microbiol Biotechnol* **2022**, *39* (1), 7. https://doi.org/10.1007/s11274-022-03445-8.
(26) Parab, L.; Dherbey, J. R.; Rivera, N.; Schwarz, M.; Gallie, J.; Bertels, F. Chloramphenicol and Gentamicin Reduce the Evolution of Resistance to Phage ΦX174 by Suppressing a Subset of E. Coli LPS Mutants. *PLOS Biology* **2025**, *23* (1), e3002952. https://doi.org/10.1371/journal.pbio.3002952.
(27) CRISPRi Screening Reveals E. Coli's Anaerobic-like Respiratory Adaptations to Gentamicin: Membrane Depolarization by CpxR. *mSystems* **2025**, *10* (7). https://doi.org/10.1128/msystems.00353-25.
(28) Benarroch, J. M.; Asally, M. The Microbiologist's Guide to Membrane Potential Dynamics. *Trends in Microbiology* **2020**, *28* (4), 304–314. https://doi.org/10.1016/j.tim.2019.12.008.
(29) Sugiyama, S.; Vassylyev, D. G.; Matsushima, M.; Kashiwagi, K.; Igarashi, K.; Morikawa, K. Crystal Structure of PotD, the Primary Receptor of the Polyamine Transport System in *Escherichia Coli*(∗). *Journal of Biological Chemistry* **1996**, *271* (16), 9519–9525. https://doi.org/10.1074/jbc.271.16.9519.
(30) Ibacache-Quiroga, C.; Oliveros, J. C.; Couce, A.; Blázquez, J. Parallel Evolution of High-Level Aminoglycoside Resistance in *Escherichia Coli* Under Low and High Mutation Supply Rates. *Front. Microbiol.* **2018**, *9*. https://doi.org/10.3389/fmicb.2018.00427.
(31) Chareyre, S.; Barras, F.; Mandin, P. A Small RNA Controls Bacterial Sensitivity to Gentamicin during Iron Starvation. *PLOS Genetics* **2019**, *15* (4), e1008078. https://doi.org/10.1371/journal.pgen.1008078.
(32) Wahl, A.; My, L.; Dumoulin, R.; Sturgis, J. N.; Bouveret, E. Antagonistic Regulation of dgkA and plsB Genes of Phospholipid Synthesis by Multiple Stress Responses in *Escherichia Coli*. *Molecular Microbiology* **2011**, *80* (5), 1260–1275. https://doi.org/10.1111/j.1365-2958.2011.07641.x.
(33) Morgan-Kiss, R. M.; Cronan, J. E. The *Escherichia Coli fadK* (*ydiD*) Gene Encodes an Anerobically Regulated Short Chain Acyl-CoA Synthetase*. *Journal of Biological Chemistry* **2004**, *279* (36), 37324–37333. https://doi.org/10.1074/jbc.M405233200.
(34) Bakkes, P. J.; Biemann, S.; Bokel, A.; Eickholt, M.; Girhard, M.; Urlacher, V. B. Design and Improvement of Artificial Redox Modules by Molecular Fusion of Flavodoxin and

Flavodoxin Reductase from *Escherichia Coli*. *Sci Rep* **2015**, *5* (1), 12158. https://doi.org/10.1038/srep12158.

(35) Choe, D.; Lee, E.; Kim, K.; Hwang, S.; Jeong, K. J.; Palsson, B. O.; Cho, B.-K.; Cho, S. Rapid Identification of Key Antibiotic Resistance Genes in *E. Coli* Using High-Resolution Genome-Scale CRISPRi Screening. *iScience* **2025**, *28* (5), 112435. https://doi.org/10.1016/j.isci.2025.112435.

(36) Wang, Y.; Fu, H.; Shi, X.-J.; Zhao, G.-P.; Lyu, L.-D. Genome-Wide Screen Reveals Cellular Functions That Counteract Rifampicin Lethality in *Escherichia Coli*. *Microbiology Spectrum* **2023**, *12* (1), e02895-23. https://doi.org/10.1128/spectrum.02895-23.

(37) Meng, J.; Young, G.; Chen, J. The Rcs System in *Enterobacteriaceae*: Envelope Stress Responses and Virulence Regulation. *Front. Microbiol.* **2021**, *12*. https://doi.org/10.3389/fmicb.2021.627104.

(38) Bury-Moné, S.; Nomane, Y.; Reymond, N.; Barbet, R.; Jacquet, E.; Imbeaud, S.; Jacq, A.; Bouloc, P. Global Analysis of Extracytoplasmic Stress Signaling in *Escherichia Coli*. *PLOS Genetics* **2009**, *5* (9), e1000651. https://doi.org/10.1371/journal.pgen.1000651.

(39) Vertommen, D.; Depuydt, M.; Pan, J.; Leverrier, P.; Knoops, L.; Szikora, J.-P.; Messens, J.; Bardwell, J. C. A.; Collet, J.-F. The Disulphide Isomerase DsbC Cooperates with the Oxidase DsbA in a DsbD-Independent Manner. *Molecular Microbiology* **2008**, *67* (2), 336–349. https://doi.org/10.1111/j.1365-2958.2007.06030.x.

(40) Giles, T. N.; Graham, D. E. Characterization of an Acid-Dependent Arginine Decarboxylase Enzyme from *Chlamydophila Pneumoniae*. *Journal of Bacteriology* **2007**, *189* (20), 7376–7383. https://doi.org/10.1128/jb.00772-07.

(41) Ngo, L.; Weimer, J.; Sui, L.; Pickens, T.; Stourman, N. V. Periplasmic β-Glucosidase BglX from *E. Coli* Demonstrates Greater Activity towards Galactose-Containing Substrates. *Int J Biochem Mol Biol* **2023**, *14* (4), 76–86.

(42) Yang, M.; Luoh, S.-M.; Goddard, A.; Reilly, D.; Henzel, W.; Bass, S. The bglX Gene Located at 47.8 Min on the *Escherichia Coli* Chromosome Encodes a Periplasmic β-Glucosidase. *Microbiology* **1996**, *142* (7), 1659–1665. https://doi.org/10.1099/13500872-142-7-1659.

(43) Franke, I.; Resch, A.; Daßler, T.; Maier, T.; Böck, A. YfiK from *Escherichia Coli* Promotes Export of O-Acetylserine and Cysteine. *J Bacteriol* **2003**, *185* (4), 1161–1166. https://doi.org/10.1128/JB.185.4.1161-1166.2003.

(44) Campion, C.; Charbon, G.; Thomsen, T. T.; Nielsen, P. E.; Løbner-Olesen, A. Antisense Inhibition of the *Escherichia Coli* NrdAB Aerobic Ribonucleotide Reductase Is Bactericidal Due to Induction of DNA Strand Breaks. *Journal of Antimicrobial Chemotherapy* **2021**, *76* (11), 2802–2814. https://doi.org/10.1093/jac/dkab305.

(45) Lubrano, P.; Smollich, F.; Schramm, T.; Lorenz, E.; Alvarado, A.; Eigenmann, S. C.; Stadelmann, A.; Thavapalan, S.; Waffenschmidt, N.; Glatter, T.; Hoffmann, N.; Müller, J.; Peter, S.; Drescher, K.; Link, H. Metabolic Mutations Reduce Antibiotic Susceptibility of *E. Coli* by Pathway-Specific Bottlenecks. *Molecular Systems Biology* **2025**, *21* (3), 274–293. https://doi.org/10.1038/s44320-024-00084-z.

(46) Seregina, T. A.; Petrushanko, I. Y.; Zaripov, P. I.; Shakulov, R. S.; A. Sklyarova, S.; Mitkevich, V. A.; Makarov, A. A.; Mironov, A. S. Activation of Purine Biosynthesis Suppresses the Sensitivity of *E. Coli* gmhA Mutant to Antibiotics. *International Journal of Molecular Sciences* **2023**, *24* (22), 16070. https://doi.org/10.3390/ijms242216070.

(47) Niu, H.; Gu, J.; Zhang, Y. Bacterial Persisters: Molecular Mechanisms and Therapeutic Development. *Sig Transduct Target Ther* **2024**, *9* (1), 174. https://doi.org/10.1038/s41392-024-01866-5.

(48) Sivapragasam, S.; Grove, A. The Link between Purine Metabolism and Production of Antibiotics in *Streptomyces*. *Antibiotics* **2019**, *8* (2), 76. https://doi.org/10.3390/antibiotics8020076.

(49) Westblade, L. F.; Errington, J.; Dörr, T. Antibiotic Tolerance. *PLOS Pathogens* **2020**, *16* (10), e1008892. https://doi.org/10.1371/journal.ppat.1008892.

(50) Ye, D.; Li, X.; Zhao, L.; Liu, S.; Jia, X.; Wang, Z.; Du, J.; Ge, L.; Shen, J.; Xia, X. Oxidized Glutathione Reverts Carbapenem Resistance in blaNDM-1-Carrying *Escherichia Coli*.

EMBO Molecular Medicine **2024**, *16* (5), 1051–1062. https://doi.org/10.1038/s44321-024-00061-x.

(51) Dörr, T. Understanding Tolerance to Cell Wall–Active Antibiotics. *Annals of the New York Academy of Sciences* **2021**, *1496* (1), 35–58. https://doi.org/10.1111/nyas.14541.

(52) El Khoury, J. Y.; Zamarreño Beas, J.; Huguenot, A.; Py, B.; Barras, F. Bioenergetic State of *Escherichia Coli* Controls Aminoglycoside Susceptibility. *mBio* **2023**, *14* (1), e0330222. https://doi.org/10.1128/mbio.03302-22.

(53) Poole, K. Bacterial Stress Responses as Determinants of Antimicrobial Resistance. *Journal of Antimicrobial Chemotherapy* **2012**, *67* (9), 2069–2089. https://doi.org/10.1093/jac/dks196.

(54) Wu, Y.; Vulić, M.; Keren, I.; Lewis, K. Role of Oxidative Stress in Persister Tolerance. *Antimicrobial Agents and Chemotherapy* **2012**, *56* (9), 4922–4926. https://doi.org/10.1128/aac.00921-12.

(55) Yu, X.; Liu, M.; Liu, P.; Hao, Z.; Zhao, L.; Zhao, X. Increased Expression of AbcA Efflux Pump Accelerated Resistance Development from Tolerance to Resistance Against Oxacillin in *Staphylococcus Aureus*. *Microorganisms* **2025**, *13* (5), 1140. https://doi.org/10.3390/microorganisms13051140.

(56) Brand, C.; Newton-Foot, M.; Grobbelaar, M.; Whitelaw, A. Antibiotic-Induced Stress Responses in Gram-Negative Bacteria and Their Role in Antibiotic Resistance. *Journal of Antimicrobial Chemotherapy* **2025**, *80* (5), 1165–1184. https://doi.org/10.1093/jac/dkaf068.

(57) Fawaz, S.; Barton, S.; Whitney, L.; Swinden, J.; Nabhani-Gebara, S. Stability of Meropenem After Reconstitution for Administration by Prolonged Infusion. *Hosp Pharm* **2019**, *54* (3), 190–196. https://doi.org/10.1177/0018578718779009.

(58) Liebchen, U.; Rakete, S.; Vogeser, M.; Arend, F. M.; Kinast, C.; Scharf, C.; Zoller, M.; Schönermarck, U.; Paal, M. The Role of Non-Enzymatic Degradation of Meropenem—Insights from the Bottle to the Body. *Antibiotics* **2021**, *10* (6), 715. https://doi.org/10.3390/antibiotics10060715.

(59) *Disrupting Gram-Negative Bacterial Outer Membrane Biosynthesis through Inhibition of the Lipopolysaccharide Transporter MsbA | Antimicrobial Agents and Chemotherapy*. https://journals.asm.org/doi/10.1128/aac.01142-18 (accessed 2025-07-26).

(60) *Overcoming Iron Deficiency of an Escherichia coli tonB Mutant by Increasing Outer Membrane Permeability | Journal of Bacteriology*. https://journals.asm.org/doi/10.1128/jb.00340-19 (accessed 2025-07-26).

(61) Charusanti, P.; Conrad, T. M.; Knight, E. M.; Venkataraman, K.; Fong, N. L.; Xie, B.; Gao, Y.; Palsson, B. Ø. Genetic Basis of Growth Adaptation of *Escherichia Coli* after Deletion of Pgi, a Major Metabolic Gene. *PLOS Genetics* **2010**, *6* (11), e1001186. https://doi.org/10.1371/journal.pgen.1001186.

(62) *Antibiotic tolerance due to restriction of cAMP-Crp regulation by mannitol, a non-glucose-family PTS carbon source | mSphere*. https://journals.asm.org/doi/10.1128/msphere.00772-24 (accessed 2025-07-26).

(63) Möller, M. C.; Hederstedt, L. Extracytoplasmic Processes Impaired by Inactivation of trxA (Thioredoxin Gene) in *Bacillus Subtilis*. *Journal of Bacteriology* **2008**, *190* (13), 4660–4665. https://doi.org/10.1128/jb.00252-08.

(64) Cheng, C.; Dong, Z.; Han, X.; Wang, H.; Jiang, L.; Sun, J.; Yang, Y.; Ma, T.; Shao, C.; Wang, X.; Chen, Z.; Fang, W.; Freitag, N. E.; Huang, H.; Song, H. Thioredoxin A Is Essential for Motility and Contributes to Host Infection of *Listeria Monocytogenes* via Redox Interactions. *Front. Cell. Infect. Microbiol.* **2017**, *7*. https://doi.org/10.3389/fcimb.2017.00287.

(65) G, U.; J, B. Alternative Respiratory Pathways of *Escherichia Coli*: Energetics and Transcriptional Regulation in Response to Electron Acceptors. *Biochimica et biophysica acta* **1997**, *1320* (3). https://doi.org/10.1016/s0005-2728(97)00034-0.

(66) Sielaff, H.; Duncan, T. M.; Börsch, M. The Regulatory Subunit ε in *Escherichia Coli* FOF1-ATP Synthase. *Biochimica et Biophysica Acta (BBA) - Bioenergetics* **2018**, *1859* (9), 775–788. https://doi.org/10.1016/j.bbabio.2018.06.013.

(67) Van den Bergh, B.; Schramke, H.; Michiels, J. E.; Kimkes, T. E. P.; Radzikowski, J. L.; Schimpf, J.; Vedelaar, S. R.; Burschel, S.; Dewachter, L.; Lončar, N.; Schmidt, A.; Meijer, T.; Fauvart, M.; Friedrich, T.; Michiels, J.; Heinemann, M. Mutations in Respiratory Complex I Promote Antibiotic Persistence through Alterations in Intracellular Acidity and Protein Synthesis. *Nat Commun* **2022**, *13* (1), 546. https://doi.org/10.1038/s41467-022-28141-x.

(68) Papakostas, K.; Botou, M.; Frillingos, S. Functional Identification of the Hypoxanthine/Guanine Transporters YjcD and YgfQ and the Adenine Transporters PurP and YicO of *Escherichia Coli* K-12*. *Journal of Biological Chemistry* **2013**, *288* (52), 36827–36840. https://doi.org/10.1074/jbc.M113.523340.

(69) Yew, W. S.; Gerlt, J. A. Utilization of L-Ascorbate by *Escherichia Coli* K-12: Assignments of Functions to Products of the Yjf-Sga and Yia-Sgb Operons. *Journal of Bacteriology* **2002**, *184* (1), 302–306. https://doi.org/10.1128/jb.184.1.302-306.2002.

(70) Abdelwahed, E. K.; Hussein, N. A.; Moustafa, A.; Moneib, N. A.; Aziz, R. K. Gene Networks and Pathways Involved in *Escherichia Coli* Response to Multiple Stressors. *Microorganisms* **2022**, *10* (9), 1793. https://doi.org/10.3390/microorganisms10091793.

(71) Schutte, K. M.; Fisher, D. J.; Burdick, M. D.; Mehrad, B.; Mathers, A. J.; Mann, B. J.; Nakamoto, R. K.; Hughes, M. A. *Escherichia Coli* Pyruvate Dehydrogenase Complex Is an Important Component of CXCL10-Mediated Antimicrobial Activity. *Infection and Immunity* **2015**, *84* (1), 320–328. https://doi.org/10.1128/iai.00552-15.

(72) Klein, G.; Lindner, B.; Brabetz, W.; Brade, H.; Raina, S. *Escherichia Coli* K-12 Suppressor-Free Mutants Lacking Early Glycosyltransferases and Late Acyltransferases. *Journal of Biological Chemistry* **2009**, *284* (23), 15369–15389. https://doi.org/10.1074/jbc.M900490200.

(73) Pal, A.; Ghosh, D.; Thakur, P.; Nagpal, P.; Irulappan, M.; Maruthan, K.; Mukherjee, S.; Patil, N. G.; Dutta, T.; Veeraraghavan, B.; Vivekanandan, P. Clinically Relevant Mutations in Regulatory Regions of Metabolic Genes Facilitate Early Adaptation to Ciprofloxacin in *Escherichia Coli*. *Nucleic Acids Res* **2024**, *52* (17), 10385–10399. https://doi.org/10.1093/nar/gkae719.

(74) de Souza Barbosa, F.; Capra Pezzi, L.; Tsao, M.; Dias Macedo, S. M.; de Oliveira, T. F.; Schapoval, E. E. S.; Mendez, A. S. L. Stability in Clinical Use and Stress Testing of Meropenem Antibiotic by Direct Infusion ESI-Q-TOF: Quantitative Method and Identification of Degradation Products. *Journal of Pharmaceutical and Biomedical Analysis* **2020**, *179*, 112973. https://doi.org/10.1016/j.jpba.2019.112973.

(75) Takasu, Y.; Yoshida, M.; Tange, M.; Asahara, K.; Uchida, T. Prediction of the Stability of Meropenem in Intravenous Mixtures. *Chemical and Pharmaceutical Bulletin* **2015**, *63* (4), 248–254. https://doi.org/10.1248/cpb.c14-00516.

(76) Li, X.-Z.; Plésiat, P.; Nikaido, H. The Challenge of Efflux-Mediated Antibiotic Resistance in Gram-Negative Bacteria. *Clinical Microbiology Reviews* **2015**, *28* (2), 337–418. https://doi.org/10.1128/cmr.00117-14.

(77) Boldrin, F.; Provvedi, R.; Cioetto Mazzabò, L.; Segafreddo, G.; Manganelli, R. Tolerance and Persistence to Drugs: A Main Challenge in the Fight Against *Mycobacterium Tuberculosis*. *Front. Microbiol.* **2020**, *11*. https://doi.org/10.3389/fmicb.2020.01924.

Chapter 5: Developing a High-Throughput Metabolome Sampling Method

Contributions

All experimental and analytical work was performed by the author (Andreas Verhülsdonk), unless stated below.

Application of high-throughput filter sampling methods was supported by Dr. Alejandra Alvarado and Felicia Troßmann. Metabolite MS analysis was carried out by Dr. Niklas Farke and Dr. Johanna Rapp. This chapter contains a new image of reanalyzed and revised data from my master thesis (Figure 2).

Relevance

This chapter forms the methodological link between the arrayed CRISPRi library introduced in Chapter 2 and the metabolic screen presented in Chapter 6. It details the development, testing, and optimization of the high-throughput sampling method used in the Chapter 6 screen. Stepwise improvements and practical considerations are described, making this a key foundation for the metabolomics workflow applied later in this dissertation.

Background

Metabolomics profiles small-molecule metabolites in biological systems and is widely applied to studies of cellular physiology, disease mechanisms, and metabolic engineering[1–4]. Accurate and reproducible sampling is critical for quality and interpretability of metabolomics data, since it must capture the metabolic state of cells under near in-vivo conditions[5–8]. Because metabolites change rapidly and are sensitive to environmental shifts, sampling must quench metabolism quickly and prevent degradation[9,10].

In our laboratory, established low-throughput protocols for metabolome sampling have been routinely applied to microbial cultures, focusing on quenching and extraction efficiency, reproducibility, and compatibility with LC-MS and FI-TOF MS[11–15]. These methods involve manual filtration and centrifugation as well as rapid cooling and extraction of intracellular metabolites in cold organic solvents. While these approaches have proven reliable and robust for small- to medium-scale experiments, they are limited in throughput and scalability, particularly when large numbers of samples or experimental conditions must be processed in parallel.

To address this limitation and enable a complete metabolic analysis of the iML1515 metabolic model, a high-throughput metabolome sampling pipeline designed to increase processing speed, reduce variability, and support experiments at larger scale was developed[16]. The new workflow integrates rapid quenching and extraction procedures with compatibility for 96-well plate formats. Throughout this work, different methods were developed and systematically compared to the performance of the high-throughput method in terms of metabolite coverage, quantitative reproducibility, and sample integrity. This chapter outlines the motivation for developing the method, the design of the high-throughput pipeline, and the experiments used for benchmarking and validation.

Results

Established Metabolite Sampling Methods

Two metabolite sampling methods were previously established and extensively validated in our laboratory.

The first method, named **filter sampling**, involves growing bacterial cultures in a minimal glucose medium in shake flasks. Cultures are harvested during the exponential phase, typically at an OD_{600} of ~0.5. Simultaneously, a vacuum filter flask with glass frit, 0.45 µm PVDF filters, and pipette tips are pre-warmed to 37°C to minimize temperature-induced perturbations during sampling (Figure 1A). A 2 mL aliquot of culture is vacuum-filtered through a PVDF membrane, which is then immediately transferred into a flask containing 1 mL of quenching solution (AcN/MeOH/H_2O, 40:40:20) pre-cooled to -20°C. The sample is incubated at -20°C overnight, centrifuged at 13,000 rpm for 10 minutes at -9°C, and the supernatant is harvested for metabolite analysis.

The second method, called **whole cell broth sampling**, follows the same cultivation protocol but omits the filtration step. Instead, cultures are diluted 1:5 in cold (-20°C) quenching solution (AcN/MeOH, 50:50) and incubated at -20°C overnight (Figure 1B). While this method is simpler, faster, and more robust, it results in extracts of lower analytical quality. Since the extraction solvent in this case includes the culture medium itself, large quantities of salts are introduced into the sample. The consequences are reduced signal intensities, elevated background noise, formation of salt adducts and increased risk of instrument contamination[17-19].

High-Throughput Filter Sampling

Our analytical platform, FI-TOF MS, provides broad m/z coverage (50–1700) but lower precision than targeted MS methods. Under these conditions, reduced sensitivity and salt contamination are particularly problematic. Furthermore, salt accumulation on the MS nebulizer increases with sample throughput and progressively degrades measurement quality.

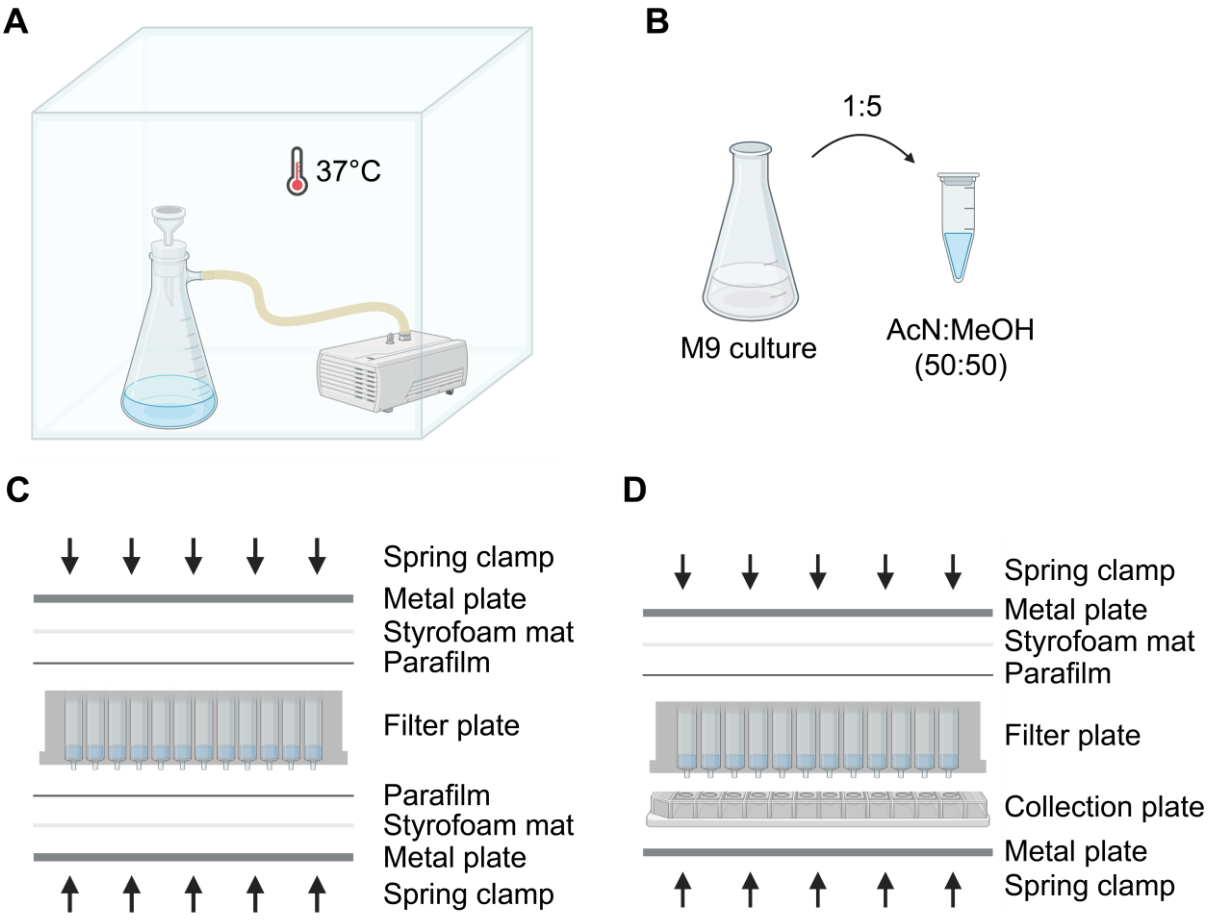

Figure 1. Established low-throughput and development of a high-throughput sampling method. These images show the central differences between sampling methods. **(A)** Overview of the primary method of filter sampling, where pump and bacterial cultures are kept inside a temperate chamber especially designed for this approach. **(B)** The second method whole cell broth sampling without filtering. **(C, D)** Key differences to improve high-throughput filter sampling performed in this dissertation. **(C)** Sampling setup in initial screening trial and **(D)** optimized final setup.

The filter-based method yields high-quality extracts with minimal contamination but is too labor-intensive for processing large numbers of samples. To address this problem, the filter method was adapted to a high-throughput and scalable format using 96-well plates. A custom vacuum chamber was constructed to accommodate standard 96-well filter plates. Initial tests were conducted using Merck polyvinylidene fluoride (PVDF) 96-well filter plates (Merck Millipore, MVHVN4525), which use the same 0.45 µm membrane material as in the low-throughput protocol.

In the first high-throughput trial, 500 µL of culture at OD_{600} ~0.5 was added to each well, vacuum filtered, and quenched with 200 µL of extraction solution. The filter plate was then sealed on both sides: first with a layer of parafilm, followed by a Styrofoam mat and a metal plate, and finally clamped with four spring clamps to ensure uniform pressure (Figure 1C). The entire assembly was incubated overnight at -20 °C. After incubation, the plate was disassembled, and the extracts were collected by vacuum filtration into a v-bottom 96-well collection plate.

Several issues were encountered during the initial high-throughput sampling trials. The first involved the time delay between culture filtration and the addition of quenching solution. In the low-throughput protocol, this interval is kept below 5 seconds to minimize metabolic changes. However, during early 96-well trials this delay exceeded 15 seconds, primarily due to the inability to use a 96-channel pipette concurrently with vacuum filtration. This issue was resolved by enlisting a second researcher to divide tasks: one person performed medium removal while the other added the quenching solution. This intervention reduced the delay to under 5 seconds.

Additional problems arose during the incubation setup. The industrial-grade spring clamps used were unwieldy, making it difficult to secure the sampling construct quickly. As a result, the transfer time to the -20°C freezer exceeded one minute, significantly longer than the 5-second benchmark in the original protocol. With the assistance of a second researcher, the setup was streamlined, and the transfer time was reduced to approximately 10 seconds.

Post-incubation, two more challenges became apparent. First, the quenching solution occasionally leaked through the filters, and a portion adhered to the parafilm seal, leading to inconsistent sample recovery. Second, during extract filtration droplets often misaligned, hitting the well rims or spilling into neighboring wells, hindering subsequent heat sealing and risking cross-contamination.

These issues were addressed by replacing the bottom parafilm seal with a 96-well flat-bottom plate, allowing any leaking liquid to be collected directly (Figure 1D). In addition, reducing distances between collection plates and filter plates increased the likelihood of accurate droplet capture. Bringing the collection plate into closer contact with the filter plate inside the vacuum chamber further improved alignment and collection accuracy. As a second improvement, the post-incubation filtration was replaced with centrifugation for 5 min at -9°C, 4,000 rpm. In this setup, the filter and collection plates were stacked directly on top of each other, improving recovery and alignment.

Despite these improvements, chemical compatibility of the 96-well filter plates remained a concern. While the filter material itself is resistant to acetonitrile, the filter membranes are adhered by an industrial adhesive. Manufacturer documentation indicated that the adhesive can react with acetonitrile, leading to leakage and possible MS contamination[20]. Additionally, PVDF membranes show limited resistance to methanol, risking damage during overnight incubations[20]. To address this, a screening experiment was conducted to test alternative filter plates and extraction solvents with varying chemical stability and extraction performance (Figure 2).

In addition to the Merck PVDF plates used in earlier experiments, chosen for their similarity to the low-throughput approach, two alternative filter plate types were tested: Pall Supor (Pall Corporation, PN 8039) and water wettable Polytetrafluoroethylene (wwPTFE; Pall Corporation, PN 8584). These plates were selected due to their significantly higher resistance to organic solvents[21]. To evaluate extraction and quenching efficiency, five additional solutions were tested: distilled water at 21°C & 80°C, ethanol & methanol at -20°C, and a Methanol/distilled water mixture (80:20) at -20°C (Figure 2). These were tested alongside the previously used acetonitrile/methanol/distilled water mixture (40:40:20). Apart from the trial solvent 21°C H_2O, the selection of solvents was based on their prior use in metabolite harvesting protocols and the different chemical interactions with filter materials[11,22–26]. Whole-cell broth extracts were prepared to serve as a reference for evaluating extraction quality.

To assess the quality of each plate-solvent combination, the concentrations of glutamate and adenosine triphosphate (ATP) were measured across twelve replicates and compared. ATP depletes rapidly under oxidative stress, making it a reliable marker of degradation during prolonged handling[27,28]. Similarly, glutamate participates in stress-response pathways such as nitrogen metabolism and nutrient sensing, and its levels fluctuate under extended handling[29-31].

The glutamate and ATP measurements from whole-cell broth extracts exhibited a common issue: high variability in signal intensity across all extraction solutions except 80°C H_2O, likely due to measurement inaccuracies caused by salt interference (Figure 2G-H). In contrast, replicates obtained from all filter plate conditions showed narrower intensity distributions, highlighting how salt removal improved measurement consistency (Figure 2A-F).

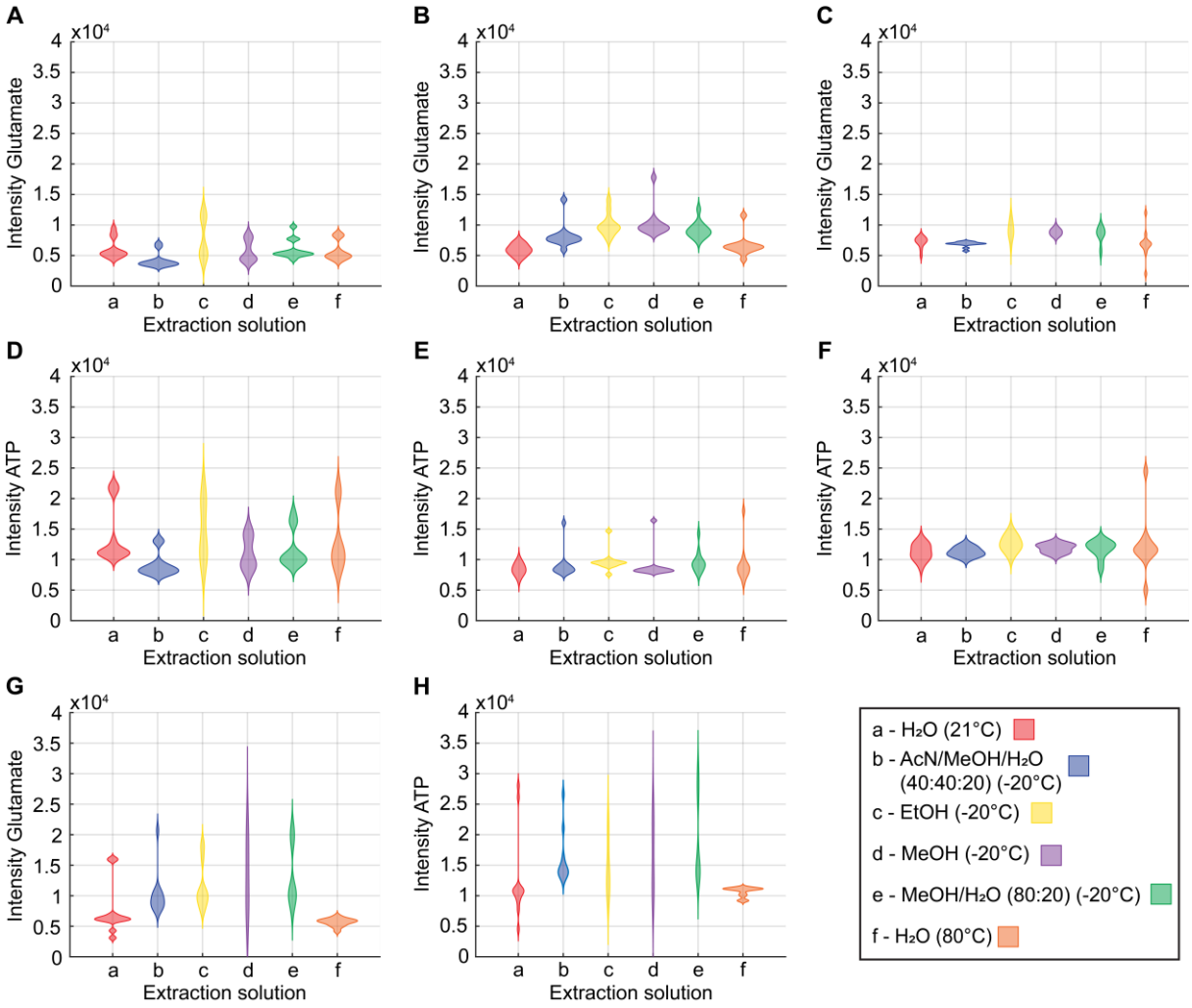

Figure 2. Filter material and solvent affect sample quality. Metabolites were measured following extraction with different solutions and filtration through various filter plates. Glutamate intensities were measured after filtration using **(A)** Merck PVDF, **(B)** Pall Supor, and **(C)** Pall water wettable PTFE (wwPTFE) filter plates. ATP intensities after filtration with **(D)** Merck PVDF, **(E)** Pall Supor, and **(F)** Pall wwPTFE filter plates. High-throughput whole cell broth sampling was performed as a reference for **(G)** glutamate and **(H)** ATP.

The Merck PVDF plates displayed distinct intensity clustering for each extraction solution, showing two distinct intensity groups per metabolite (Figure 2A, D). This is likely due to the adhesive used in the filter plates, which is sensitive to both organic solvents and temperature[20]. Either the adhesive partially dissolved and interfered with the extracts directly, or the quenching solution may have bypassed the cell-containing filter layer too quickly, leading to inconsistent exposure times. Because of these issues, Merck PVDF plates were excluded from further use in this study.

Pall Supor plates showed lower intra-condition variability than the PVDF plates, though outliers were still present in all extraction conditions except 21 °C H_2O (Figure 2B, E). While Supor plates are marketed as chemically robust, organic solvents and elevated temperatures still impaired extraction quality[32]. Although Supor plates performed better than PVDF plates overall, they yielded lower metabolite concentrations across all extraction conditions for ATP (Figure 2E).

Pall wwPTFE plates showed the most consistent results, with low replicate variance in most conditions, except for boiling water (80°C) for both metabolites (Figure 2C, F). In particular, the AcN/MeOH/H_2O and methanol-only conditions produced tightly clustered intensity values, reflecting good extraction reproducibility. Since wwPTFE plates performed well and were compatible with the earlier protocol, the combination with AcN/MeOH/H_2O (40:40:20) extraction solution was selected as the optimal method for high-throughput filter sampling in later experiments.

High-Throughput Centrifugation Sampling

While the sampling method became more reliable and yielded acceptable quality results, two issues remained unresolved.

First, although a collection plate was already integrated into the incubation setup and centrifugation was employed to equalize volumes, inconsistencies in the amount of extraction solution passing through the filters prior to centrifugation made it impossible to determine whether cells had been correctly incubated or were merely exposed to the chemicals for a short period.

Second, the sampling process required the assistance of a second trained scientist, due to its complexity and the need for precise execution of multiple steps. However, requiring a second person is impractical for routine use and adds considerable labor.

To address these limitations, based on observations from the filter-based method, we adapted metabolite sampling protocols developed for *Saccharomyces cerevisiae* and *E. coli*[33–35]. Although these protocols used different extraction media, which were also tested in our filter-based system, they all relied on centrifugation for cell harvesting, followed by quenching and metabolite extraction.

In the centrifugation-based approach, all steps were carried out within a single 96-deep-well plate. Cultures (275 µL, aTc-induced, grown in minimal glucose medium) were incubated for 5 hours and then 25 µL were removed and diluted for OD measurements. The remaining cultures were centrifuged at 3,750 rpm for 5 min at 0°C. After centrifugation, the supernatant was removed, and 125 µL of a quenching solution (acetonitrile/methanol/water, 40:40:20) was added. Plates were sealed within an incubation construct and incubated for 60 min at -20°C (Figure 3A). Afterwards, the plates were centrifuged again for 5 min at 3,750 rpm and 0°C, and the resulting supernatants were collected for metabolite analysis.

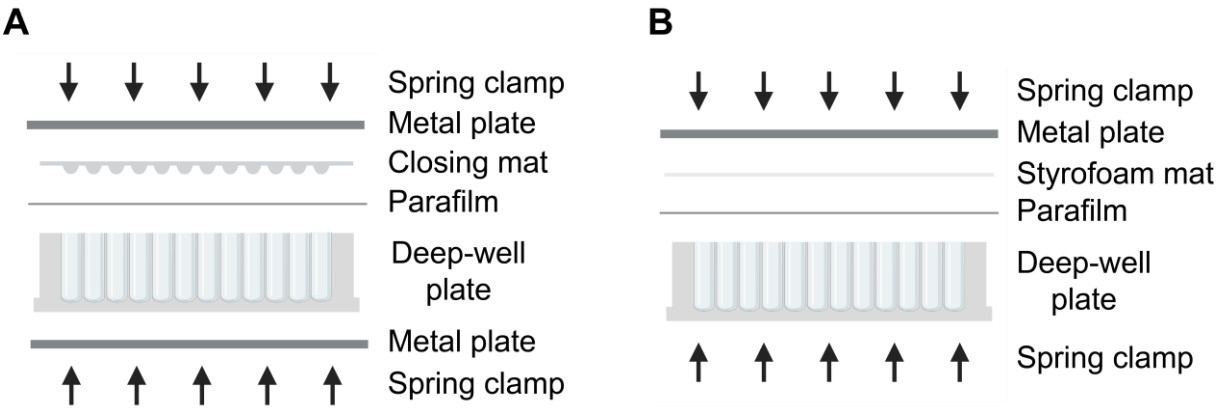

Figure 3. Evolution of experimental high-throughput centrifugation sampling. These images show the incubation construct used in the metabolite harvesting method. **(A)** Setup of initial centrifugation-based high-throughput sampling. **(B)** Setup of final, optimized centrifugation-based sampling protocol.

During initial trials, several issues were identified. To enhance pellet integrity, we tested centrifugation durations necessary for forming solid pellets from cultures at OD_{600} 0.5 at 3,350 rpm. These pellets needed to remain stable when the plate was inverted and firmly tapped onto a stack of sterile cleaning paper to remove residual medium. While solid pellets formed after 2 minutes, approximately 20% of cells remained suspended in the supernatant. After 3 minutes, no cells remained in suspension. Centrifugation was set to 2 minutes as a compromise between pellet stability and speed.

To compensate for cell loss, we increased the dilution factor of the medium in the quenching solution from 2:1 to 5:1 by increasing culture volume to 1.05 mL and quenching volume to 200 µL. Additionally, incubation time was extended to 6.5 hours to harvest cells at higher density, which typically resulted in OD_{600} values between 0.5 and 0.8.

To further improve centrifugation efficiency, we maintained the temperature at 37 °C during the first centrifugation step. Since both the plate and its contents were initially at 37 °C, two minutes was insufficient to significantly cool the sample and slow metabolic activity. To avoid adding stress from temperature shifts on top of oxygen and nutrient depletion, the plate was kept at 37 °C until quenching.

To streamline transfer to –20 °C for incubation, we modified the incubation construct. The previously used sealing mat, which was time-consuming to apply, was replaced by a soft Styrofoam mat that quickly and effectively pressed parafilm into each well (Figure 3B). The second metal plate was also removed, reducing assembly time to well below 10 seconds.

This protocol was applied in a metabolite screen of the entire CRISPRi library generated in Chapter 2, referred to in the following as the n=1 screen. To ensure comparable final OD_{600} values across strains, each of which was affected differently by gene knockdown, every strain was incubated in quintuplicates at four different initial OD_{600}s: 0.025, 0.05, 0.1, and 0.25. From these, the replicate with a final OD_{600} closest to the target range of 0.5-0.8 was selected for mass spectrometry analysis.

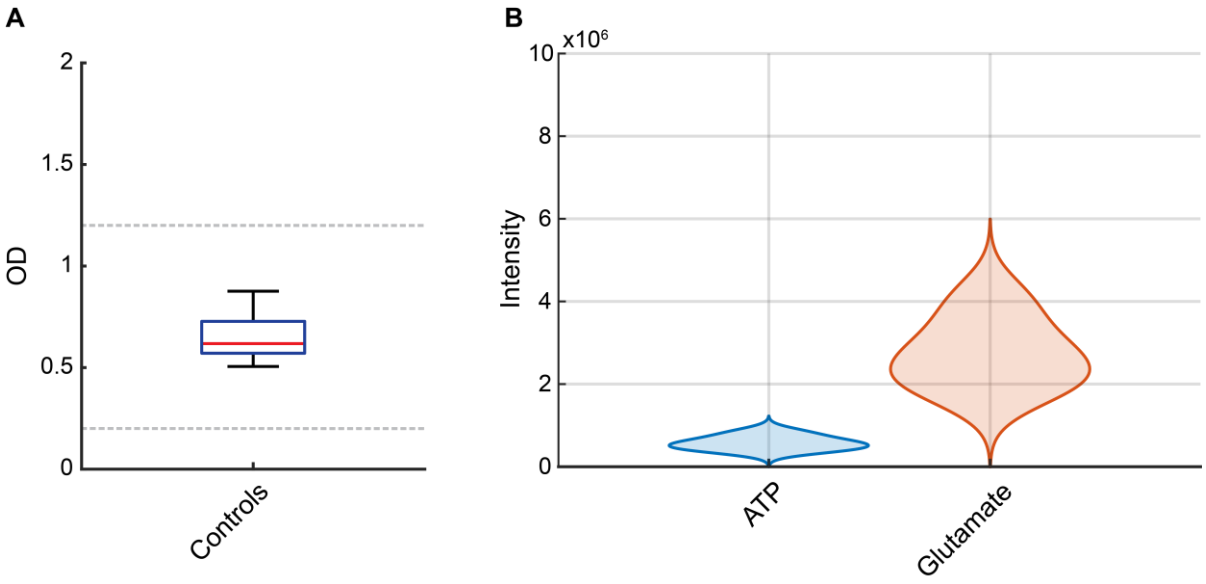

Figure 4. Centrifugation sampling control data of the n=1 screen. (A) Optical density at 600 nm (OD_{600}) range of control strains used in this screen. Blue box contains middle 50% of values, whiskers the smallest and largest non-outlier values, the red line the median, and grey dashed lines the acceptable OD_{600} range. **(B)** Violin plots of ATP and glutamate concentrations across controls. Graphics reflect data of 12 controls normalized to OD_{600} 0.5 for higher comparability to filter sampling.

Control strain data was extracted to compare to high-throughput filter sampling methods. While in the filtration screen culture from a single flask at OD_{600} 0.5 was sampled simultaneously, the centrifugation method required cultures at similar end ODs for comparability. OD_{600} data for 12 controls has shown little variance and value placement in the very center of the acceptable OD_{600} range (Figure 4A). Data from the extraction method with the best performance, -20°C AcN/MeOH/H_2O on Pall wwPTFE plates, was used as a benchmark for quality (Figure 2C, F). Metabolite data from the screen was normalized to OD_{600} 0.5 to allow comparison across strains (Figure 4B). It must be mentioned that in the filtration method 500 µL culture were quenched in 250 µL AcN/MeOH/H_2O, while the concentrations in the centrifugation protocol were 1,000 µL and 200 µL, respectively. The 100-fold higher ATP concentrations measured in the centrifugation method, as well as a >500-fold increase in glutamate concentration, indicated much higher sensitivity of the centrifugation method (Figure 2C, F, Figure 4B).

Specifically, the increased ATP concentrations indicate a better metabolite sample quality, since prolonged sample handling causes ATP depletion[5]. The low spread of ATP intensities also attests to this hypothesis, since a low variance indicates cells were handled and harvested at simultaneous timeframes across several experiments, as only one control replicate was sampled per day, the low variance suggests consistent handling across experiments (Figure 4B). In combination, these results indicate low ATP variance at elevated intensity levels.

The spread of glutamate on the other hand had greatly increased (Figure 4B). An increase in glutamate is correlated to prolonged sample handling at unfavorable temperatures, which may reflect glutamate accumulation during the 2-minute centrifugation at 37 °C, when pellets were formed.

High-Throughput, Multi-Replicate Centrifugation Sampling

While the initial protocol yielded promising results, the lack of replicates limited the statistical reliability of the results. Additional replicate measurements of different starting OD_{600}s were not possible, as too few strains had sufficient replicates within the target range of final OD_{600}s. We therefore revised the sampling method with two main goals: (1) to achieve similar final OD_{600}s across strain replicates, minimizing extract waste and allowing comparability with only two cultures per plate; and (2) to maintain metabolite extract quality and yield comparable to the n=1 screen.

As a reference point, the protocol from the n=1 screen was repeated using two replicates per condition, starting at an OD_{600} of 0.05 with a single CRISPRi library plate (Figure 5A). This yielded considerable OD_{600} variation, with some replicates growing to more than twice the OD_{600} of their counterparts, resulting in a poor correlation (r = 0.24). To address this, two key changes were introduced. First, we limited the glucose concentration in the overnight cultures to 1.75 g/L, which led to more consistent OD_{600} values by the end of overnight incubation. Second, we delayed aTc induction by two hours while keeping incubation times constant, shortening the induction phase to 4.5 hours, as knockdowns strongly affect growth rates. These adjustments substantially improved replicate correlation (r = 0.94) with only two OD_{600} range outliers (Figure 5B).

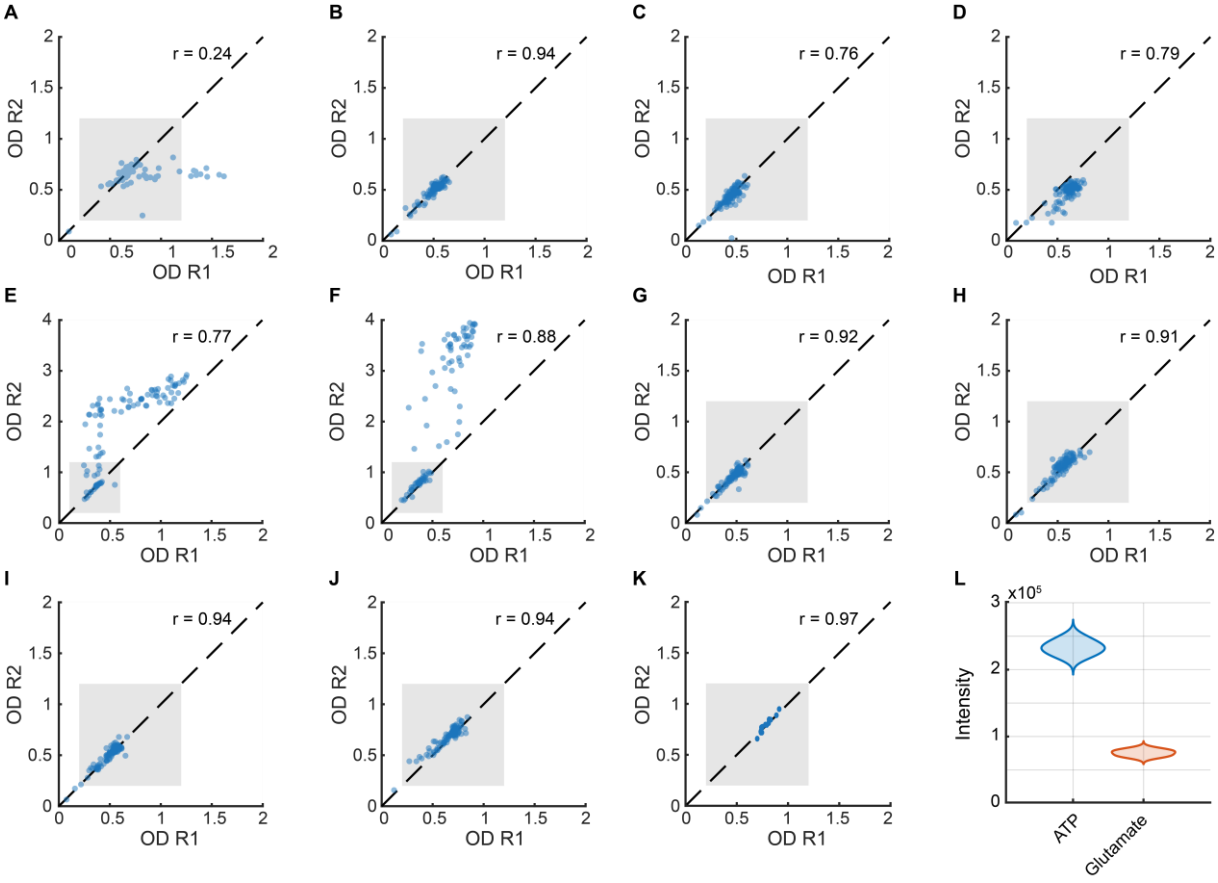

Figure 5. Comparison of replicate optical density (OD) across multiple experimental conditions to optimize culture reproducibility for metabolite sampling. (A-K) Each subplot shows the correlation of sample OD at 600 nm (OD_{600}) between R1 and R2 under varying experimental parameters. Data includes Pearson correlation coefficient (r) while shaded areas indicate desired OD_{600} range. **(A)** Sampling identical to the n=1 screen for two replicates. **(B)** First sampling approach with improved overnight culture ODs and reduced induction time. **(C)** Change of induction time to 6.5 h at start OD_{600} 0.04 and **(D)** 0.05. **(E)** Increased start OD_{600} to 0.1 and change of LB culture incubation time to 5 h and **(F)** 7 h. **(G-J)** Test of a new OD_{600} determination method and culture splitting at start OD_{600} 0.05 **(G)** and 0.1 **(H)** and without splitting at start OD_{600} 0.05 **(I)** and 0.1 **(J)**. **(K, L)** Data of 12 controls in duplicates measured in the final screen. **(K)** Correlation of control duplicate OD_{600}s. **(L)** Violin plots of ATP and glutamate metabolite concentrations normalized to OD_{600} 0.5.

We then analyzed metabolite extracts from this improved setup, focusing on 16 knockdown strains causing metabolite accumulations, as identified in the n=1 screen (Figure 6A). These knockdowns were implicated in 38 metabolic features, of which 22 showed accumulations detectable in positive ionization mode above an intensity >5,000. However, while OD_{600} reproducibility improved in the adjusted protocol, metabolite accumulation dropped substantially. Only 7 and 6 metabolite signals were strongly elevated in replicates R1 and R2, respectively, with another 5 and 6 showing increases that remained below our detection threshold (intensity $<10^4$) (Figure 6B-C). These results indicated the need for further protocol optimization to improve metabolite recovery while maintaining OD_{600} consistency.

We hypothesized that the shortened induction period might prevent strains from reaching metabolic bottlenecks, as demonstrated in previous publications[11]. Additionally, to dilute the highly concentrated aTc, 10% of culture were replaced by M9 diluted aTc, reducing the cell content of each well. Thus, the aTc induction time was reverted to 6.5 hours. From this point forward, metabolite extracts were only analyzed from experiments with the best OD_{600} correlation to reduce unnecessary measurements.

We next tested varying starting OD_{600}s (0.04, 0.05, 0.06) under 6.5-hour aTc induction (Figure 5C-D). The OD_{600} 0.06 data was excluded because replicate variation was too high for reliable analysis. While starting OD_{600} had minimal effect on final OD_{600} or correlation, the improved LB incubation substantially raised replicate agreement from $r = 0.24$ to >0.75 (Figure 5B, D). Metabolite profiles at OD_{600} 0.04 varied between replicates: one showed improved accumulation, while the other resembled previous suboptimal results (Figure 6D-E). At OD_{600} 0.05, accumulation improved for both replicates, nearly matching the n=1 screen, although a few metabolites remained below the threshold (Figure 6F-G).

Based on these results, we aimed to retain high metabolite recovery while improving OD_{600} consistency. We tested whether glucose limitation in the main culture had an effect on optical density, but no improvement was detected (data not shown). Indeed, allowing cultures to exit exponential growth resulted in closer OD_{600} convergence (data not shown). Next, we tested whether a higher starting OD_{600} (0.1) combined with extended LB pre-culture incubation from 5 to 7 hours would enhance extraction performance (Figure 5E-F). The higher starting OD_{600} led to overgrowth beyond the desired range, while increased LB incubation slightly improved correlation. Metabolite detection was also reduced: fewer features passed the intensity threshold, and signal intensities were generally lower (Figure 6H–K).

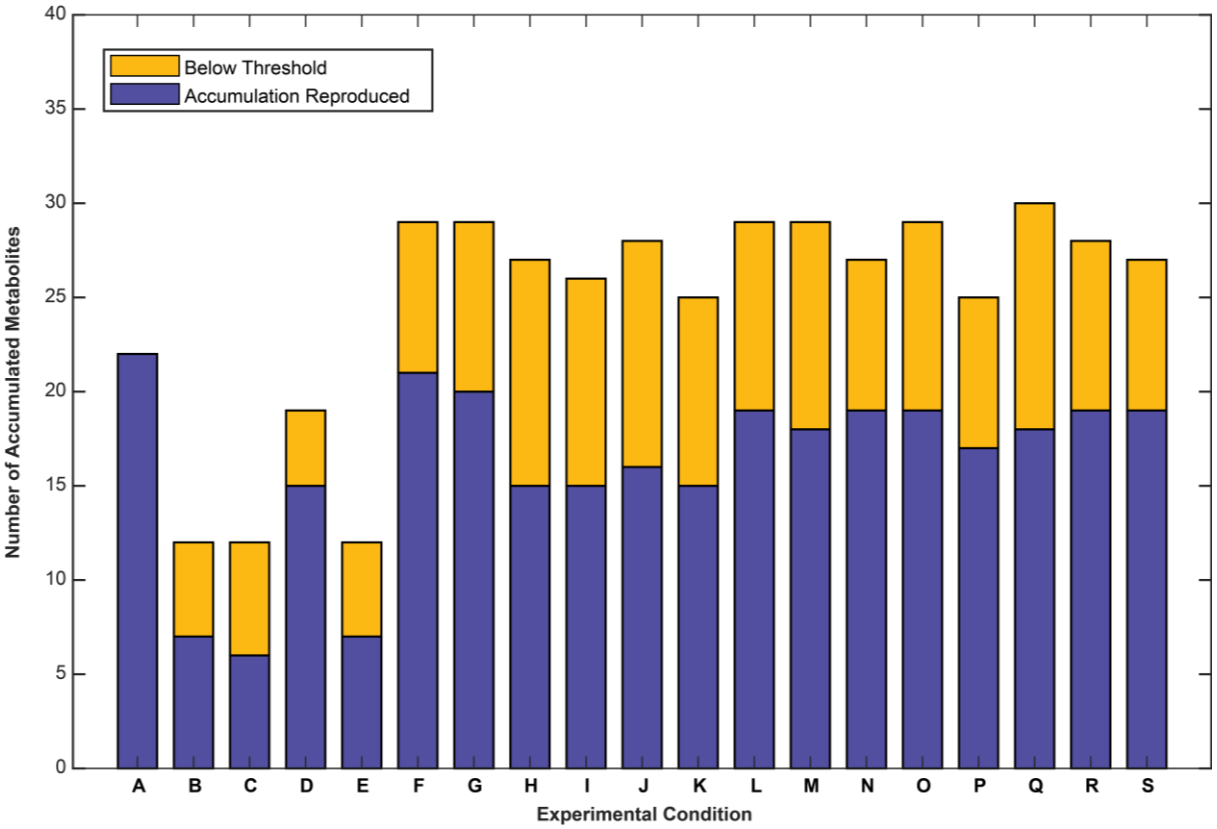

Figure 6. Accumulation of metabolites across experimental conditions. This graph shows the accumulations of 40 annotatable metabolites concentrations across a single plate of the n=1 screen in positive ionization mode, found within 16 strains. These strains have shown metabolite accumulations above an intensity of 10,000 (blue), which served as the cutoff, and above 5,000 (yellow). **(A)** Accumulations in the initial n=1 screen used as benchmark. (**B-S)** Metabolite accumulations of two replicates across experimental conditions. **(B,C)** Results of the optical density at 600 nm (OD_{600}) streamlined protocol. **(D,E)** Increase of induction time to 6.5 h at start OD_{600} 0.04 and **(F,G)** 0.05. **(H,I)** Comparison of LB culture induction time of 7 and **(J,K)** 5 hours. **(L,M)** Evaluation LB pre-culture split effect performed at starting OD_{600} 0.05 and **(N,O)** 0.1 and without splitting at starting OD_{600} **(P,Q)** 0.05 and **(R,S)** 0.1.

These unexpected results prompted a detailed review of the protocol. We realized that our method of calculating starting OD_{600} was flawed: Initially, cultures were shaken for 5 minutes, and OD_{600} was measured every minute over a total of six readings, from which the mean was calculated. However, for several strains, the OD_{600} steadily decreased during these measurements which biased the calculated mean and distorted the starting OD_{600} values. These effects might be caused by uneven distribution or cell settling. To address this issue, we revised the protocol: cultures were shaken continuously for 5 minutes, followed by a 3-minute period in which OD_{600} was measured intermittently. We introduced this change after observing that OD_{600} values stabilized within 5 minutes across all wells and no further decrease was detected. This adjustment led to mean OD_{600} values that more accurately reflected actual culture density and improved consistency across experiments.

We then compared starting OD_{600}s of 0.05 and 0.1 and evaluated whether splitting a single LB culture into two deep-well plates after two hours of incubation, versus using two independently inoculated LB cultures, would impact replicate correlation (Figure 5G-J). This comparison aimed to determine whether splitting cultures partway through growth introduces variability in final OD_{600}. The results showed nearly identical OD_{600} correlation between the two approaches at OD_{600} 0.05, with r = 0.92 for independently grown replicates and r = 0.91 for the split-culture method (Figure 5G, J). At OD_{600} 0.1, using a single shared LB culture throughout the entire incubation slightly improved the correlation to r = 0.94 (Figure 5I, K), and almost all strains reached final OD_{600}s within the desired range. Metabolite profiles were highly consistent across all conditions, with slightly better signal stability observed at OD_{600} 0.1 (Figure 6L-S). Based on these results, we concluded that using a single overnight LB culture split into two plates after incubation, combined with a starting OD_{600} of 0.1, was the most consistent setup for reproducible metabolite measurements.

Finally, we investigated why some metabolite accumulations observed on the n=1 screen were still not reproducible. For instance, the *ynfF* and *ndk* knockdowns each showed accumulation of three metabolites on the n=1 screen, but only one was detected under the current n=2 conditions. We traced this discrepancy to the fact that these strains grew slower upon induction and, in the n=1 screen, had started at OD_{600} 0.25 and reached a much higher final OD_{600}, nearly four times greater than in the revised setup. As a result, we concluded that the optimized conditions were suitable for most strains, but slow-growing knockdowns still required dedicated handling. These strains were pooled on a dedicated plate and incubated at a higher starting OD_{600} (0.25) to ensure adequate metabolite accumulation.

The results for controls of the screen of Chapter 6 were extracted to compare the screen quality to that of previous high-throughput sampling methods (Figure 4, Figure 5K, L). The data shows that both methods produce sampling OD_{600}s within the desired range. While it is complex to compare n=1 and n=2 results for OD_{600} correlation, the r=0.97 value for the controls of the final n=2 screen indicates improved comparability (Figure 4A, Figure 5K). Also, a change in metabolite variance and intensities was observed, where both ATP and glutamate were lower in the final n=2 screen (Figure 3L). While this is welcome for glutamate, which suggests improved sample handling, a 2-fold decrease in ATP was detected. Potential explanation for this phenomenon like quenching inefficiency or ATP instability were not feasible since changes in the protocol affecting these factors were not made, so the reason for this remains elusive. Overall, the spread across the 12x2 control samples is heavily reduced, showing that methodological adjustments have improved data quality.

Conclusion

In this chapter, a series of high-throughput sampling protocols for microbial metabolomics were developed and optimized, adapting previously established low-throughput methods into scalable formats. Initial high-throughput filter-based approaches yielded acceptable data but had limitations including high labor demands, low robustness, increased waste production, and limited signal strength (Figure 2). Specifically, across all tested extraction conditions most metabolite signals were barely above our established laboratory intensity threshold of 10^4, making them unsuitable for reliable downstream analysis (Figure 2).

To overcome these limitations, a high-throughput centrifugation-based protocol inspired by approaches developed in other laboratories was designed[36,37]. After applying several modifications, this method strongly improved metabolite recovery. This was especially true for ATP and glutamate, which showed improved recovery and lower variance in the initial n=1 screen (Figure 5). Moreover, the data generated from this protocol formed the basis of the second manuscript (Chapter 6), showing the importance of having a reliable, high-throughput sampling method for large-scale metabolomics. However, the lack of replicates limited statistical significance and led to inefficient resource use, as many samples fell outside the acceptable OD_{600} range and had to be discarded.

To address these shortcomings, a refined workflow was developed: high-throughput, multi-replicate centrifugation sampling. This approach enabled the generation of reproducible metabolite profiles with high comparability between replicates and across strains (Figure 6). By carefully optimizing culture conditions, induction timing, and OD_{600} matching, the method reduced labor and waste while maintaining detection of most annotated metabolites found in the initial screen. Though some low-abundance metabolites dropped below the 10^4 detection threshold, the method preserved overall data quality and reproducibility.

While the n=2 screen was the most effective balance we could achieve between metabolite detection, throughput, and statistical reliability, some limitations remain. Specifically, certain metabolite accumulations seen in the original screen were not reproducible under optimized conditions, especially for slow-growing knockdowns. These may require dedicated handling, such as higher starting OD_{600}s or extended incubation. Additionally, the drop in ATP signal intensity in the final screen, though still above threshold and of lower variance, remains unexplained and should be examined further.

To further improve metabolite coverage while preserving replicate quality, a hybrid approach could be applied: performing the screen across four different starting OD_{600}s, as in the n=1 screen, and selecting the best matching replicate pairs for analysis. Although this would increase labor and waste, it could yield the most comprehensive metabolomic dataset using the high-throughput framework. The finalized n=2 protocol allows a full-library screen to be completed within a week, assuming proper preparation, making it practical for routine high-throughput applications.

More broadly, the final protocol developed here provides a reproducible and scalable sampling strategy with relatively low complexity. While optimized for *E. coli* and CRISPRi-based screens, its principles are broadly applicable to other microbial metabolomics workflows. Future improvements could include integrating automation to further improve throughput.

Material and Methods

Cultivation and Media

Media preparation and strain cultivation were performed as stated in Chapter 2.

Cultures

Unless stated otherwise, the same cultivation protocol was used for all sampling methods described below. Glycerol stocks of strains were inoculated in LB medium and incubated for 5 h at 220 rpm, 37°C. Cultures were then diluted hundred-fold in M9 medium and incubated for 16 h at 220 rpm, 37°C.

Filter Sampling

M9 cultures were normalized to OD_{600} 0.05 in M9 medium containing aTc in shake flasks. Cultures were incubated at 220 rpm, 37°C till an OD_{600} of >0.5 was detected in the hourly measurements. Meanwhile, a heating chamber was set to 37°C and filled with all consumables and equipment required for sampling. Additionally, sampling flasks containing 1 mL AcN/MeOH/H_2O (40:40:20), in the following referred to as quenching solution, were pre-chilled to -20°C. 2 mL culture were filtered through a PVDF membrane filter (Merk Milipore, HVWG04700), which was immediately transferred to the sampling flask and incubated at -20°C for 30 min. Filters were washed with the quenching solution in the sampling flask, 700 µL extract transferred to fresh pre-chilled 1.5 mL reaction tubes, and centrifuged for 5 min at 17,000 rpm, -9°C. 500 µL supernatant were transferred to a fresh, pre-chilled 1.5 mL reaction tube and stored at -80°C until measurement.

Whole Cell Broth Sampling

M9 cultures were normalized to OD_{600} 0.05 in M9 medium containing aTc in shake flasks. Cultures were incubated at 220 rpm, 37°C till an OD_{600} of >0.5 was reached in the hourly measurements. Meanwhile, 1.5 mL sampling tubes containing 400 µL AcN/MeOH (50:50) were pre-chilled to -20°C. 100 µL culture were added to prepared tubes and immediately incubated at -20°C for 30 min. Extracts were centrifuged for 10 min at 17,000 rpm, -9°C. 400 µL supernatant were transferred to a fresh pre-chilled 1.5 mL reaction tube and stored at -80°C until measurement.

Initial Try of High-Throughput Filter Sampling

M9 cultures were normalized to OD_{600} 0.05 in 1 mL M9 medium containing aTc in 96-deep-well plates and incubated at 37°C, 220 rpm until the control reached OD_{600} 0.5. 500 µL were transferred to a PVDF filter plate (Merck) and medium was removed via vacuum. 200 µL of quenching solution pre-chilled to -20°C were added to each well and filter quickly washed by pipetting. Filter plates were sealed on both sides with layers of parafilm, Styrofoam, and metal

plates, held together by spring clamps, and incubated at -20°C for 30 min. The filter plate was unpacked, placed on the vacuum device, and extracts were pulled into a v-bottom 96-well collection plate which was heat-sealed and subsequently stored at -80°C until measurement.

Optimized High-Throughput Filter Sampling

M9 cultures were normalized to OD_{600} 0.05 in 500 µL M9 medium containing aTc in 96-deep-well plates and incubated at 37°C, 220 rpm until the control reached OD_{600} 0.5. 250 µL were transferred to a wwPTFE filter plate (Pall Corporation) and medium was removed via vacuum. 125 µL pre-chilled quenching solution were added to each well and quickly washed by pipetting. Filter plates were sealed on top with parafilm, Styrofoam, and a metal plate, and at the bottom with a 96-well collection plate, Styrofoam, and another metal plate. The assembly was secured by spring clamps and incubated at -20°C for 60 min. The filter and collection plates were kept stacked and centrifuged for 5 min at 9°C, 4,000 rpm for extraction. The collection plate was heat-sealed and subsequently stored at -80°C until measurement.

Initial Try of High-Throughput Centrifuge Sampling

M9 cultures were diluted to OD_{600} 0.05 in 275 µL aTc-induced M9 medium in a 96-deep-well plate and incubated for 5 h at 37°C, 220 rpm. 25 µL were diluted six-fold for OD measurement in a plate reader (Epoch, BioTek; 5 min shaking with 6 intermittent reads). Remaining cultures were centrifuged for 5 min at 0°C, 3,750 rpm in the 96-deep-well plate. Supernatants were removed and 125 µL pre-chilled quenching solution added to each well. The plate was sealed with parafilm and a closing mat on top, followed by metal plates on both sides, held together by spring clamps. The assembly was incubated for 60 min at -20°C and subsequently centrifuged again for 5 min at 3,750 rpm, 0°C. 100 µL supernatant were transferred to a collection plate, heat sealed and stored at -80°C until measurement.

Optimized High-Throughput Centrifuge Sampling

M9 cultures were diluted to OD_{600} 0.025, 0.05, 0.1, and 0.2 in 1,050 µL aTc induced M9 medium in four 96-deep-well plate and incubated for 6.5 h at 37°C, 220 rpm. For each plate, 50 µL were diluted threefold for OD measurement in a plate reader (Infinite, Tecan; 5 min shaking with 6 intermittent reads). Remaining cultures were centrifuged for 2 min at 37°C, 3,350 rpm. Supernatants were discarded and 200 µL pre-chilled quenching solution added to each well. Plates were sealed with parafilm and Styrofoam on top, metal plates on both sides, and secured with spring clamps. The assembly was incubated for 16 h at -20°C and then centrifuged for 5 min at 4,000 rpm, -9°C. 150 µL of supernatant were transferred to a collection plate, heat sealed and stored at -80°C until measurement.

OD Optimized High-Throughput, Multi-Replicate Centrifuge Sampling

For multi-replicate optimization, 16 h M9 cultures contained only 1.75 g/L Glucose. 150 µL overnight culture were transferred to a 96-well flat-bottom plate. OD_{600} was measured using a plate reader (Infinite, Tecan, 5 min shaking with 6 intermittent reads), and the mean OD_{600} across all strains calculated. M9 cultures were diluted to OD_{600} 0.05 in 1,050 µL M9 medium in two 96-deep-well plate and incubated for 6.5 h at 37°C, 220 rpm. After 2 h aTc was added. For each plate 50 µL were diluted threefold for OD measurement in a plate reader (Infinite, Tecan). Cultures were centrifuged for 2 min at 37°C, 3,350 rpm, supernatant discarded, and 200 µL pre-chilled quenching solution added. Plates were sealed with parafilm and Styrofoam on top, followed by metal plates on both sides, secured with spring clamps. The assembly was incubated for 16 h at -20°C and subsequently centrifuged for 5 min at 4,000 rpm, -9°C. 150 µL supernatant were transferred to a collection plate, heat sealed and stored at -80°C until measurement.

Final Optimized High-Throughput, Multi-Replicate Centrifuge Sampling

16 h M9 cultures contained only 1.75 g/L Glucose. 150 µL overnight culture were transferred to a 96-well flat-bottom plate. OD_{600} was measured using a plate reader (Infinite, Tecan, 5 min shaking followed by 3 min shaking with 3 intermittent reads), and the mean OD_{600} across all strains calculated. M9 cultures were diluted to OD_{600} 0.1 in 1,050 µL M9 medium in two 96-deep-well plate and incubated for 6.5 h at 37°C, 220 rpm. For each plate 50 µL were diluted threefold for OD measurement in a plate reader (Infinite, Tecan). Cultures were centrifuged for 2 min at 37°C, 3,350 rpm, supernatant discarded, and 200 µL pre-chilled quenching solution added. Plates were sealed with parafilm and Styrofoam on top, followed by metal plates on both sides, secured with spring clamps. The assembly was incubated for 16 h at -20°C and subsequently centrifuged for 5 min at 4,000 rpm, -9°C. 150 µL supernatant were transferred to a collection plate, heat sealed and stored at -80°C until measurement.

Targeted Metabolomics

Targeted metabolomics were performed as described in Chapter 3.

Untargeted Metabolomics

Untargeted metabolomics was performed by direct infusion of metabolite extracts into an Agilent 6546 quadrupole time-of-flight mass spectrometer (Q-TOF MS; Agilent Technologies). Electrospray ionization was conducted in both positive and negative modes. The mobile phase (60:40 isopropanol:water) was buffered with 10 mM ammonium carbonate and 0.04% (v/v) ammonium hydroxide and used for both modes at a flow rate of 0.15 mL/min.

Mass calibration was performed using 2-propanol and HP-921 (negative mode), and purine with HP-921 (positive mode). Spectra were acquired in profile mode from m/z 50–1700 at 1.4 spectra/s for 0.5 min using a 10 GHz resolving power.

Data was converted to mzXML and processed using custom MATLAB scripts. Monoisotopic masses were annotated against the iML1515 model within a ±3 mDa tolerance, considering $[M–H]^-$ (negative) and $[M+H]^+$ (positive) ion forms[16].

Annotations were merged, with positive-mode annotations prioritized if present in both modes. For the n=2 screen discussed in Chapter 6, only metabolites annotated in both replicates were retained. Peak intensities were normalized to the mean across all 3000+ isolates to calculate fold-change values.

Bibliography

(1) Wishart, D. S. Metabolomics for Investigating Physiological and Pathophysiological Processes. *Physiological Reviews* **2019**, *99* (4), 1819–1875. https://doi.org/10.1152/physrev.00035.2018.

(2) Peng, B.; Li, H.; Peng, X.-X. Functional Metabolomics: From Biomarker Discovery to Metabolome Reprogramming. *Protein Cell* **2015**, *6* (9), 628–637. https://doi.org/10.1007/s13238-015-0185-x.

(3) Newgard, C. B. Metabolomics and Metabolic Diseases: Where Do We Stand? *Cell Metabolism* **2017**, *25* (1), 43–56. https://doi.org/10.1016/j.cmet.2016.09.018.

(4) Fernie, A. R.; Trethewey, R. N.; Krotzky, A. J.; Willmitzer, L. Metabolite Profiling: From Diagnostics to Systems Biology. *Nat Rev Mol Cell Biol* **2004**, *5* (9), 763–769. https://doi.org/10.1038/nrm1451.

(5) Lu, W.; Su, X.; Klein, M. S.; Lewis, I. A.; Fiehn, O.; Rabinowitz, J. D. Metabolite Measurement: Pitfalls to Avoid and Practices to Follow. *Annual Review of Biochemistry* **2017**, *86* (Volume 86, 2017), 277–304. https://doi.org/10.1146/annurev-biochem-061516-044952.

(6) Álvarez-Sánchez, B.; Priego-Capote, F.; Luque de Castro, M. D. Metabolomics Analysis I. Selection of Biological Samples and Practical Aspects Preceding Sample Preparation. *TrAC Trends in Analytical Chemistry* **2010**, *29* (2), 111–119. https://doi.org/10.1016/j.trac.2009.12.003.

(7) Prasad Maharjan, R.; Ferenci, T. Global Metabolite Analysis: The Influence of Extraction Methodology on Metabolome Profiles of *Escherichia Coli*. *Analytical Biochemistry* **2003**, *313* (1), 145–154. https://doi.org/10.1016/S0003-2697(02)00536-5.

(8) Schaub, J.; Schiesling, C.; Reuss, M.; Dauner, M. Integrated Sampling Procedure for Metabolome Analysis. *Biotechnology Progress* **2006**, *22* (5), 1434–1442. https://doi.org/10.1021/bp050381q.

(9) Canelas, A. B.; Ras, C.; ten Pierick, A.; van Dam, J. C.; Heijnen, J. J.; van Gulik, W. M. Leakage-Free Rapid Quenching Technique for Yeast Metabolomics. *Metabolomics* **2008**, *4* (3), 226–239. https://doi.org/10.1007/s11306-008-0116-4.

(10) Sake, C. L.; Newman, D. M.; Boyle, N. R. Evaluation of Quenching Methods for Metabolite Recovery in Photoautotrophic *Synechococcus Sp*. PCC 7002. *Biotechnology Progress* **2020**, *36* (5), e3015. https://doi.org/10.1002/btpr.3015.

(11) Donati, S.; Kuntz, M.; Pahl, V.; Farke, N.; Beuter, D.; Glatter, T.; Gomes-Filho, J. V.; Randau, L.; Wang, C.-Y.; Link, H. Multi-Omics Analysis of CRISPRi-Knockdowns Identifies Mechanisms That Buffer Decreases of Enzymes in *E. Coli* Metabolism. *cels* **2021**, *12* (1), 56-67.e6. https://doi.org/10.1016/j.cels.2020.10.011.

(12) Radoš, D.; Donati, S.; Lempp, M.; Rapp, J.; Link, H. Homeostasis of the Biosynthetic *E. Coli* Metabolome. *iScience* **2022**, *25* (7), 104503. https://doi.org/10.1016/j.isci.2022.104503.

(13) Wang, C.-Y.; Lempp, M.; Farke, N.; Donati, S.; Glatter, T.; Link, H. Metabolome and Proteome Analyses Reveal Transcriptional Misregulation in Glycolysis of Engineered *E. Coli*. *Nat Commun* **2021**, *12* (1), 4929. https://doi.org/10.1038/s41467-021-25142-0.

(14) Lempp, M.; Farke, N.; Kuntz, M.; Freibert, S. A.; Lill, R.; Link, H. Systematic Identification of Metabolites Controlling Gene Expression in *E. Coli*. *Nat Commun* **2019**, *10*, 4463. https://doi.org/10.1038/s41467-019-12474-1.

(15) Sander, T.; Wang, C. Y.; Glatter, T.; Link, H. CRISPRi-Based Downregulation of Transcriptional Feedback Improves Growth and Metabolism of Arginine Overproducing *E. Coli*. *ACS Synth. Biol.* **2019**, *8* (9), 1983–1990. https://doi.org/10.1021/acssynbio.9b00183.

(16) Monk, J. M.; Lloyd, C. J.; Brunk, E.; Mih, N.; Sastry, A.; King, Z.; Takeuchi, R.; Nomura, W.; Zhang, Z.; Mori, H.; Feist, A. M.; Palsson, B. O. iML1515, a Knowledgebase That Computes *Escherichia Coli* Traits. *Nat Biotechnol* **2017**, *35* (10), 904–908. https://doi.org/10.1038/nbt.3956.

(17) Rakusanova, S.; Cajka, T. Tips and Tricks for LC–MS-Based Metabolomics and Lipidomics Analysis. *TrAC Trends in Analytical Chemistry* **2024**, *180*, 117940. https://doi.org/10.1016/j.trac.2024.117940.
(18) Sacks, J. S.; Heal, K. R.; Boysen, A. K.; Carlson, L. T.; Ingalls, A. E. Quantification of Dissolved Metabolites in Environmental Samples through Cation-Exchange Solid-Phase Extraction Paired with Liquid Chromatography–Mass Spectrometry. *Limnology and Oceanography: Methods* **2022**, *20* (11), 683–700. https://doi.org/10.1002/lom3.10513.
(19) Johnson, W. M.; Kido Soule, M. C.; Kujawinski, E. B. Extraction Efficiency and Quantification of Dissolved Metabolites in Targeted Marine Metabolomics. *Limnology and Oceanography: Methods* **2017**, *15* (4), 417–428. https://doi.org/10.1002/lom3.10181.
(20) MilliporeSigma, M. Kg. Milipore Chemical Compatibility of Filter Components, 2023. https://www.sigmaaldrich.com/deepweb/assets/sigmaaldrich/marketing/global/documents/137/321/chemical-compatibility-data-sheet-ds2523en-mk.pdf (accessed 2025-07-10).
(21) Fisher Scientific, P. C. Pall AcroPrep Filter Plates, 2021. https://www.fishersci.de/content/dam/fishersci/en_EU/lifescience/16419_NEW_Minisite/Molecular_Biology/Pall_AcroPrep_Filter_Plates.pdf (accessed 2025-07-14).
(22) Steinmann, A.; Schullehner, K.; Kohl, A.; Dickmeis, C.; Finger, M.; Hubmann, G.; Jach, G.; Commandeur, U.; Girhard, M.; Urlacher, V. B.; Lütz, S. A Targeted Metabolomics Method for Extra- and Intracellular Metabolite Quantification Covering the Complete Monolignol and Lignan Synthesis Pathway. *Metabolic Engineering Communications* **2022**, *15*, e00205. https://doi.org/10.1016/j.mec.2022.e00205.
(23) Fuchs, A.; Tripet, B. P.; Ammons, M. C. B.; Copié, V. Optimization of Metabolite Extraction Protocols for the Identification and Profiling of Small Molecule Metabolites from Planktonic and Biofilm Pseudomonas Aeruginosa Cultures. *Curr Metabolomics* **2016**, *4* (2), 141–147. https://doi.org/10.2174/2213235x04666151126203043.
(24) de Jonge, L. P.; Douma, R. D.; Heijnen, J. J.; van Gulik, W. M. Optimization of Cold Methanol Quenching for Quantitative Metabolomics of Penicillium Chrysogenum. *Metabolomics* **2012**, *8* (4), 727–735. https://doi.org/10.1007/s11306-011-0367-3.
(25) Ye, D.; Li, X.; Wang, C.; Liu, S.; Zhao, L.; Du, J.; Xu, J.; Li, J.; Tian, L.; Xia, X. Improved Sample Preparation for Untargeted Metabolomics Profiling of *Escherichia Coli*. *Microbiology Spectrum* **2021**, *9* (2), e00625-21. https://doi.org/10.1128/Spectrum.00625-21.
(26) Chen, M.; Li, A.; Sun, M.; Feng, Z.; Meng, X.; Wang, Y. Optimization of the Quenching Method for Metabolomics Analysis of Lactobacillus Bulgaricus. *J. Zhejiang Univ. Sci. B* **2014**, *15* (4), 333–342. https://doi.org/10.1631/jzus.B1300149.
(27) Tiwari, B. S.; Belenghi, B.; Levine, A. Oxidative Stress Increased Respiration and Generation of Reactive Oxygen Species, Resulting in ATP Depletion, Opening of Mitochondrial Permeability Transition, and Programmed Cell Death. *Plant Physiol* **2002**, *128* (4), 1271–1281. https://doi.org/10.1104/pp.010999.
(28) Ha, H. C.; Snyder, S. H. Poly(ADP-Ribose) Polymerase Is a Mediator of Necrotic Cell Death by ATP Depletion. *Proceedings of the National Academy of Sciences* **1999**, *96* (24), 13978–13982. https://doi.org/10.1073/pnas.96.24.13978.
(29) Fomenko, M. V.; Yanshole, L. V.; Tsentalovich, Y. P. Stability of Metabolomic Content during Sample Preparation: Blood and Brain Tissues. *Metabolites* **2022**, *12* (9), 811. https://doi.org/10.3390/metabo12090811.
(30) An, Z.; Shi, C.; Li, P.; Liu, L. Stability of Amino Acids and Related Amines in Human Serum under Different Preprocessing and Pre-Storage Conditions Based on iTRAQ®-LC-MS/MS. *Biology Open* **2021**, *10* (2). https://doi.org/10.1242/bio.055020.
(31) Breier, M.; Wahl, S.; Prehn, C.; Fugmann, M.; Ferrari, U.; Weise, M.; Banning, F.; Seissler, J.; Grallert, H.; Adamski, J.; Lechner, A. Targeted Metabolomics Identifies Reliable and Stable Metabolites in Human Serum and Plasma Samples. *PLOS ONE* **2014**, *9* (2), e89728. https://doi.org/10.1371/journal.pone.0089728.
(32) Pall Membrane Technology Center, P. T. IMSMEN - Supor® Membrane, 2027. https://www.pall.com/content/dam/pall/chemicals-polymers/literature-library/non-gated/IMSMEN_Supor.pdf (accessed 2025-07-10).

(33) Ewald, J. C.; Heux, S.; Zamboni, N. High-Throughput Quantitative Metabolomics: Workflow for Cultivation, Quenching, and Analysis of Yeast in a Multiwell Format. *Anal. Chem.* **2009**, *81* (9), 3623–3629. https://doi.org/10.1021/ac900002u.
(34) Mülleder, M.; Calvani, E.; Alam, M. T.; Wang, R. K.; Eckerstorfer, F.; Zelezniak, A.; Ralser, M. Functional Metabolomics Describes the Yeast Biosynthetic Regulome. *Cell* **2016**, *167* (2), 553-565.e12. https://doi.org/10.1016/j.cell.2016.09.007.
(35) Fuhrer, T.; Zampieri, M.; Sévin, D. C.; Sauer, U.; Zamboni, N. Genomewide Landscape of Gene–Metabolome Associations in *Escherichia Coli*. *Molecular Systems Biology* **2017**, *13* (1), 907. https://doi.org/10.15252/msb.20167150.
(36) Gruber, C. H.; Noor, E.; Buffing, M. F.; Sauer, U. Systematic Identification of Allosteric Effectors in *Escherichia Coli* Metabolism. *Proceedings of the National Academy of Sciences* **2025**, *122* (10), e2423767122. https://doi.org/10.1073/pnas.2423767122.
(37) Schastnaya, E.; Raguz Nakic, Z.; Gruber, C. H.; Doubleday, P. F.; Krishnan, A.; Johns, N. I.; Park, J.; Wang, H. H.; Sauer, U. Extensive Regulation of Enzyme Activity by Phosphorylation in *Escherichia Coli*. *Nat Commun* **2021**, *12* (1), 5650. https://doi.org/10.1038/s41467-021-25988-4.

Chapter 6: The Metabolome Response to Genome-Wide Perturbations in the *E. coli* Metabolic Network

Contributions

This chapter contains a manuscript submitted to Cell systems on 2025.08.19 with the title: “Metabolite accumulation in CRISPRi strains identifies principles of metabolic robustness and targets for engineering“. The manuscript is currently under revision (as of August 2025). Author contributions are listed below.

Author	Author position	Scientific ideas %	Data generation %	Analysis & interpretation %	Paper writing %
Johanna Rapp	1	45	5	75	70
Andreas Verhülsdonk	2	10	90	5	5
Anton Garcke	3	0	<5	<5	0
Amelie Stadelmann	4	0	<5	0	0
Niklas Farke	5	0	0	<5	0
Felicia Troßmann	6	0	<5	0	0
Hannes Link	7	45	0	15	25
Title of paper:		Metabolite accumulation in CRISPRi strains identifies principles of metabolic robustness and targets for engineering			
Status of publication process		Re-submission to Cell systems			

Relevance

This chapter presents a functional metabolome screen based on the CRISPRi library introduced in Chapter 2 and the sample preparation protocol developed in Chapter 5. The screen investigates how genome-wide gene perturbations affect global metabolite levels in *E. coli* and identifies metabolite accumulation patterns that reveal both regulatory and robust principles in central metabolism.

The dataset enabled the annotation of MS2 spectra for over 100 previously unmeasured metabolites and revealed cases of substrate-level buffering, product inhibition, and metabolic crosstalk. Furthermore, the study identified biosynthetic intermediates that accumulate due to enzyme knockdowns and can be leveraged for strain optimization, such as the increase in farnesyl pyrophosphate (FPP) upon *ispB* knockdown, which enhanced carotenoid production in a synthetic pathway.

Together, this work expands the measurable *E. coli* metabolome, provides new insight into metabolic regulation, and offers a valuable resource for metabolic engineering. It complements the antibiotic stress phenotyping presented in Chapter 3 and Chapter 4.

Metabolite Accumulation in CRISPRi Strains Identifies Principles of Metabolic Robustness and Targets for Engineering

Johanna Rapp[1,2,3,8]*, Andreas Verhülsdonk[1,2,3,8], Anton Garcke[1,2], Amelie Stadelmann[1,2,3], Niklas Farke[1,2], Felicia Troßmann[1,2,3], Thales Kronenberger[4,5,6], Alejandra Alvarado[1,2], Daniel Petras[7], Hannes Link[1,2,3,9]*

[1]Interfaculty Institute of Microbiology and Infection Medicine, University of Tübingen, 72076 Tübingen, Germany

[2]Cluster of Excellence "Controlling Microbes to Fight Infections", University of Tübingen, 72076 Tübingen, Germany

[3]M3 Research Center, University of Tübingen, Otfried-Müller-Str. 37, 72076 Tübingen, Germany

[4] German Center for Infection Research (DZIF), partner-site Tübingen, 72076 Tübingen, Germany.

[5] Institute of Medical Microbiology and Hygiene, Interfaculty Institute of Microbiology and Infection Medicine (IMIT), University of Tübingen, Elfriede-Aulhorn-Str. 6, 72076 Tübingen, Germany.

[6] School of Pharmacy, Faculty of Health Sciences, University of Eastern Finland, Kuopio 70211, Finland.

[7] Department of Biochemistry, University of California, Riverside, 169 Aberdeen Dr., Riverside, CA 92507, USA

[8] equally contributed

[9] Lead contact

* Corresponding authors: hannes.link@uni-tuebingen.de, johanna.rapp@uni-tuebingen.de

Abstract

Metabolite concentration changes can have broad consequences on the function and robustness of metabolic networks. Here, we measured the metabolome response of 1,515 CRISPR interference (CRISPRi) *E. coli* strains targeting all genes in the *i*ML1515 metabolic model. Metabolites that are hardly measurable in *E. coli* accumulated in specific CRISPRi strains, indicating that they are normally maintained at low levels. We confirmed metabolite accumulation using LC-MS/MS and generated putative reference spectra for 102 metabolites for which no MS^2 data had previously been available. We show that minimal metabolite pools confer robustness by i) enabling substrate level buffering of enzyme decreases, ii) preventing competitive inhibition, and iii) suppressing side reactions. However, minimal metabolite pools also limit flux through engineered pathways. For example, low levels of farnesyl diphosphate (frdp) constrained a synthetic carotenoid pathway, and we show that the knockdown of octaprenyl diphosphate synthase (*ispB*) increased frdp levels and carotenoid production. These results provide a map of metabolic engineering targets, expand the measurable metabolome, and reveal principles of metabolic robustness.

Introduction

Intracellular metabolite levels influence enzyme activity and therefore metabolic flux. For example, the concentration of substrate metabolites determines reaction rates via Michaelis–Menten kinetics[1]. Many other metabolites function as allosteric regulators or competitive inhibitors of enzymes[2,3]. Therefore, the size of metabolite pools has an important function in the metabolic network. However, despite the large body of theories like Metabolic Control Analysis[4], we still lack a systematic understanding of how metabolite levels are maintained in the cell and how they respond to perturbations.

Quantitative metabolomics data showed that the *Escherichia coli* metabolome is dominated by a few highly abundant metabolites and that the ten most abundant metabolites account for 77% of the total molar concentration across 101 metabolites[5]. This suggests that most metabolites are present in low abundance, presumably because low metabolite levels can enhance the specificity of metabolic reactions by favoring enzymes with high affinity. Additionally, low metabolite levels may mitigate the self-inhibitory nature of metabolic networks[6] and reduce toxicity, especially in the case of biosynthetic intermediates[7]. The importance of maintaining low levels of biosynthetic intermediates is further evidenced by metabolic engineering approaches, which make marked efforts to prevent the accumulation of pathway intermediates due to their negative effects on the host[8].

Therefore, a hypothesis is that bacteria benefit from maintaining metabolites at low concentrations. However, this hypothesis has been difficult to test directly, because metabolomics methods do not cover all metabolites in primary metabolism. For example, the *E. coli* metabolic model *i*ML1515 has 1025 distinct metabolites[9], but targeted metabolomics analysis of the *E. coli* and *Bacillus subtilis* metabolome captured only 35-101 metabolites[10–12]. Although untargeted LC-MS methods can detect a much larger number of putative metabolites in bacterial metabolite extracts[13], systematic peak annotation could only assign about 200-300 unique metabolites to these data[14,15]. This incomplete coverage of the metabolome could support the hypothesis of minimal metabolite pools but may also result from technical limitations. These technical limitations include: i) limited ionization efficiencies, ii) biases towards polar or non-polar metabolites during the extraction step, iii) suboptimal chromatographic methods, and iv) metabolite instability or side reactions during sample preparation.

So far, only a few studies have systematically investigated how metabolite levels change upon genetic perturbations. A study in yeast demonstrated that intracellular concentrations of substrate metabolites are inversely related to the in vivo capacity of their corresponding enzymes, suggesting a tradeoff between enzyme abundance and substrate levels[16]. A study with the *E. coli* KEIO knockout collection measured metabolome changes across 3807 gene deletion strains and showed that single-gene deletions often result in broad and sometimes unanticipated metabolite changes[17]. However, such studies with gene deletions are restricted to non-essential genes and exclude many enzymes in major *de novo* biosynthesis pathways that produce essential amino acids, nucleotides, and other biomass building blocks.

In this study, we constructed a sorted CRISPR interference (CRISPRi) library that targets all 1,515 genes included in the genome-scale model *i*ML1515 of *E. coli*. We profiled the metabolome of each strain using high-throughput flow injection mass spectrometry (FI-MS) and found specific and reproducible accumulation of metabolites. To confirm and structurally characterize the accumulating metabolites, we performed high-throughput targeted LC-MS/MS. By following up on selected CRISPRi strains we show that minimal metabolite pools provide several robustness benefits. In the AroC strain, the substrate accumulated before growth was impaired, thus indicating a substrate-buffering mechanism, in which substrate levels increase to compensate for reduced enzyme activity. In the MetE strain, high metabolite levels led to side reactions that formed non-canonical metabolites that are not covered by the *i*ML1515 model. In the AroB strain, accumulation of the substrate metabolite led to regulatory crosstalk between chorismate biosynthesis and peptidoglycan recycling. Finally, accumulation of farnesyl diphosphate in the IspB strain improved a synthetic metabolic pathway, demonstrating that our data is a resource for metabolic engineering.

Results

Metabolome Screening of a Metabolism-Wide CRISPRi Library

We created an arrayed CRISPRi library that targets all 1,515 genes in the *i*ML1515 genome-scale model of *E. coli* metabolism (Figure 1A, Table S1). The 1,515 CRISPRi strains were derived from a pooled CRISPRi library[18], by sorting single strains into 96-well plates and sequencing their single guide RNA (sgRNA). The CRISPRi strains have an anhydrotetracycline (aTc)-inducible dCas9 on the genome and a sgRNA on a plasmid, which enables dynamic knockdowns of all metabolism-related genes. Out of 1,515 CRISPRi strains, 489 CRISPRi strains showed growth defects in minimal glucose medium, whereas 1,026 CRISPRi strains showed no tangible growth defect (Figure S1, Table S2). In 162 of the 489 strains with a growth defect, essential genes were targeted by CRISPRi. The other 46 essential genes in our library did not show a growth defect, which is consistent with other CRISPRi screens in *E. coli*[19–21] and probably due to overcapacities of enzymes and other buffering mechanisms[18].

To measure the metabolome of the 1,515 CRISPRi strains, we cultured them on minimal glucose medium in 96-well plates and collected samples by a fast centrifugation method. Each CRISPRi strain was sampled twice from two independent plates to test reproducibility. Out of 1,515 CRISPRi strains, 17 did not reach the required OD_{600} range at the time of sampling (6.5 hours after induction) and were not further analyzed. The remaining 1,498 strains had sampling OD_{600}s between 0.2 and 1.2 and sampling OD_{600}s were consistent across the two replicates (Figure S2, Table S3). Additionally, we collected metabolome samples from 15 replicates of a control strain carrying a non-targeting sgRNA. This strain was distributed across the cultivation plates.

Next, we used FI-MS[22,23] to screen the 3,026 metabolite extracts (1,498 CRISPRi strains and 15 control strains, each in biological duplicates). Each extract was injected twice to measure MS^1 mass spectra in both positive and negative ionization mode. We calculated fold changes of *m/z* features that could be annotated to one of the 802 isobaric metabolites in the *E. coli* *i*ML1515 model (Table S4). Log_2-fold changes were reproducible between the two biological replicates (Figure 1B and Supplementary Datafile 1), with only 37 strains showing a mean relative error greater than 40% between replicates, and 99% of the variability between biological replicates being smaller than a log_2-fold change of 1.7 (Supplementary Datafile 1). Therefore, we defined differential metabolites as annotated *m/z* features with log_2-fold changes >2 or <-2 in both replicates (Figure 1B). In total, 411 strains had at least one increasing metabolite (log_2-fold change >2 in both replicates, Table S5). 395 strains had at least one decreasing metabolite feature (log_2-fold change <-2 in both replicates). These responses were highly specific, because on average only 3% of differential metabolites were shared between any two strains (mean Jaccard similarity = 0.03, Figure S3).

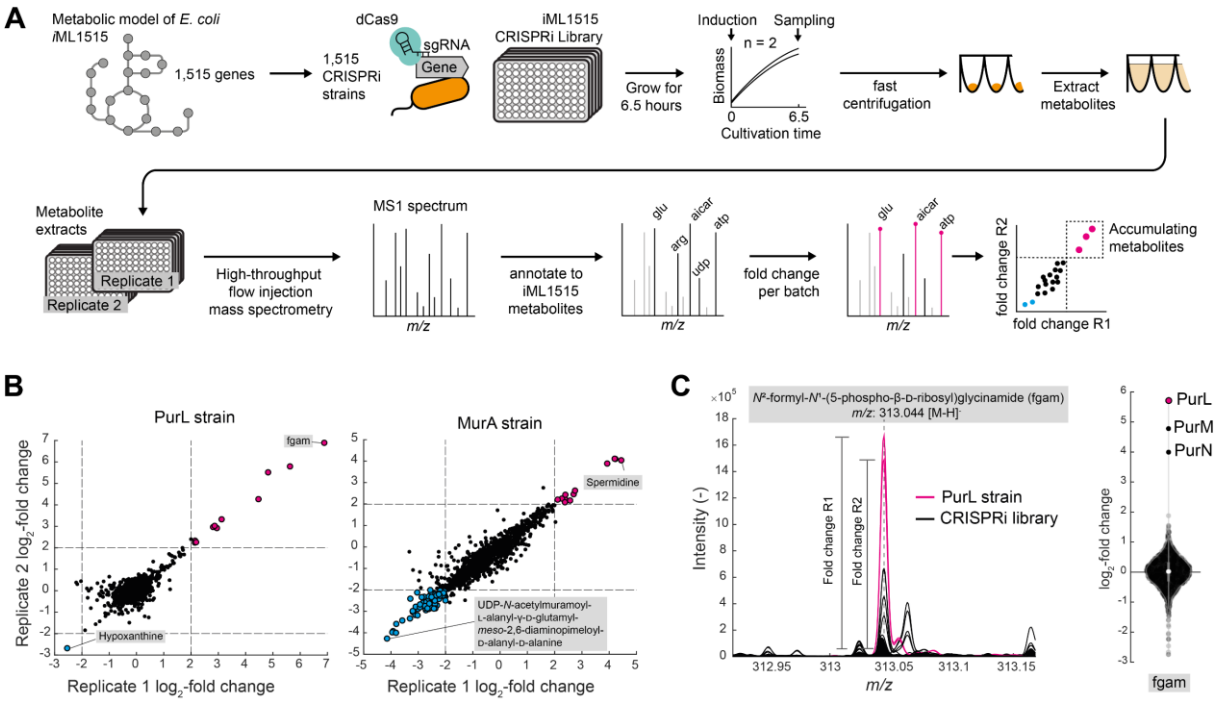

Figure 1. Metabolome profiling of a CRISPRi library that targets all 1,515 genes in the *i*ML1515 genome-scale metabolic model of *E. coli*. (A) CRISPRi strains were constructed for all 1,515 genes in the *i*ML1515 genome-scale metabolic model. The CRISPR interference system in our study consisted of an *E. coli* strain (YYdCas9) that has an inducible dCas9 integrated into the genome[41], and a single guide RNA on a plasmid[42]. The library was sorted into 16 different 96-well plates and samples for metabolomics were collected by fast centrifugation in n=2 replicates per CRISPRi strain. The metabolite extracts were analyzed by flow injection mass spectrometry (FI-MS). *m/z* features were annotated to 802 isobaric metabolites in the *i*ML1515 model. Annotated *m/z* features with $\log_2$-fold change > 2 in both replicates were considered as accumulating metabolites. **(B)** Log_2-fold changes of all annotated *m/z* features in the two replicates of the PurL strain and the MurA strain. Features with $\log_2$-fold changes >2 and <-2 in both replicates are shown in red and blue respectively. **(C)** MS^1 spectra of 3026 metabolite extracts. Shown is a window around the mass feature that was annotated to N^2-Formyl-N^1-(5-phospho-D-ribosyl)glycinamide (fgam). MS^1 spectra of extracts of the PurL strain are shown in purple. The violin plot shows the distribution of fgam across 1,513 CRISPRi strains (mean of n=2 replicates for each strain). Log_2-fold changes were calculated from the intensities of the *m/z* features in MS^1 spectra, normalized to the median per sample batch.

Several strains showed an accumulation of metabolites directly upstream of the CRISPRi-target enzyme. For example, the knockdown of phosphoribosylformylglycinamide synthetase (*purL*) showed increases in the *m/z* feature that matched N²-formyl-N¹-(5-phospho-β-D-ribosyl)glycinamide (fgam), which is a direct substrate metabolite of PurL (Figure 1C). Other strains had distal metabolite changes that occurred in pathways unrelated to the targeted reaction. For example, the MurA strain had increased levels of spermidine (Figure 1B), which is a polyamine that alleviates oxidative stress in *E. coli*[24]. The strongest decrease in the MurA strain was the end product of the respective pathway (UDP-*N*-acetylmuramoyl-pentapeptide biosynthesis), indicating an effective knockdown of MurA. Thus, FI-MS captured reproducible and strain-specific metabolome responses to CRISPRi perturbations, including both local effects (e.g. accumulation of substrates of the targeted enzyme) and distal changes in unrelated metabolic pathways (Table S5).

Targeted LC-MS/MS Confirms Metabolite Accumulation and Captures Fragmentation Spectra of 175 Unique Metabolites

The FI-MS screen identified metabolite accumulation in 1,385 strain–metabolite pairs (log_2-fold change > 2 in both replicates, Figure 2A, Table S5). This covered 411 unique CRISPRi strains and 319 unique metabolite features (Figure 2A). Fifty-three of the accumulations were probably due to operon structure, because the accumulating metabolite was a reactant of an enzyme encoded downstream of the target gene, resulting in 1,322 cases of metabolite accumulations (Figure 2A, Table S5).

We selected 1,256 strain–metabolite pairs with the strongest accumulation for targeted LC-MS/MS analysis at three collision energies (10, 20 and 40 keV) (Figure 2B). These data confirmed metabolite increase in 85% of the tested pairs (log_2-fold change >1 of the maximum intensity in extracted ion chromatograms) (Figure 2C, Table S6). The remaining cases were either false positives from the FI-MS screen, or the metabolites were not resolved by the liquid chromatographic (LC) method. The LC method was based on Hydrophilic Interaction Liquid Chromatography (HILIC), which primarily captures polar metabolites. Nevertheless, LC-MS/MS analysis confirmed also increases in less polar metabolites like 1-hexadecanoyl-*sn*-glycerol 3-phosphate (1hdecg3p), but these compounds eluted at early retention times (Figure S4).

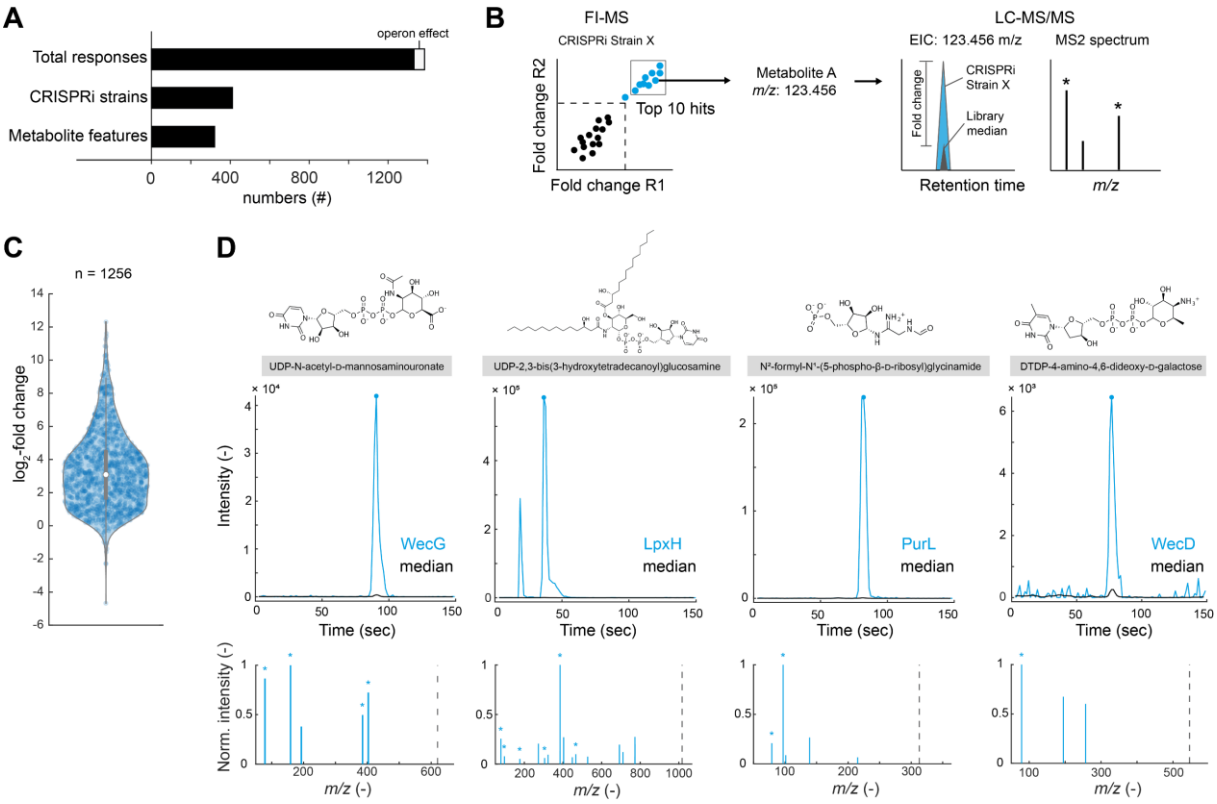

Figure 2. Targeted LC-MS/MS confirms accumulation of metabolites and provides MS² reference spectra. (A) Number of accumulations (log_2-fold change > 2 in both replicates) in FI-MS screen. 1,385 strain–metabolite pairs showed an accumulation. These cases included 411 unique CRISPRi strains and 319 unique metabolite features. 53 accumulating metabolites are reactants of an enzyme encoded downstream of the CRISPRi target gene (indicated in white, operon effect). **(B)** A maximum of 10 accumulating metabolites per strain from the FI-MS screen were used for targeted LC-MS/MS analysis to confirm accumulation. Fold changes of the peak height in the extracted ion chromatogram (EIC) compared to the median peak height of the whole library were used to quantify the accumulation of the respective metabolite in the CRISPRi strain. Experimental MS^2 spectra were compared to predicted fragments from CFM-ID 4.0 (indicated with *). **(C)** Log_2-fold changes for 1256 strain–metabolite pairs determined by targeted LC-MS/MS. **(D)** EIC of *m/z* features annotated as UDP-*N*-acetyl-D-mannosaminouronate (uacmamu, $[M-H]^-$), UDP-2,3-bis(3-hydroxytetradecanoyl)glucosamine (u23ga, $[M-H]^-$), N^2-formyl-N^1-(5-phospho-β-D-ribosyl)glycinamide (fgam, $[M-H]^-$), and DTDP-4-amino-4,6-dideoxy-D-galactose (dtdp4addg, $[M-H]^-$). Dot in EIC indicates where MS^2 spectrum was extracted. MS^2 spectra are shown at different collision energies (uacmamu: 40 keV, u23ga: 40 keV, fgam: 10 keV and dtdp4addg: 40 keV). Fragment ions predicted by CMF-ID are indicated with *. Dashed line shows mass of parent ion.

Next, we inspected the MS^2 spectra of accumulating metabolites and if fragments matched *in silico* predictions from CFM-ID 4.0[25]. Therefore, we selected LC-MS/MS data with a precursor intensity >5000, a log_2-fold change >1, high precursor purity in MS^1 spectra and at least one fragment in the MS^2 spectra (Table S6). Out of 1,256 measurements, 569 fulfilled these criteria, and 84% of them had at least one predicted fragment (Table S6). From 569 LC-MS/MS measurements, we obtained MS^2 spectra of 174 unique metabolites, for 102 of which no experimental spectrum is available in the ECMDB database[26,27]. Moreover, 75 of these metabolites are not commercially available from Sigma-Aldrich or Biosynth. Examples of such metabolites that previously lacked MS^2 data are UDP-*N*-acetyl-D-mannosaminouronate, UDP-2,3-bis(3-hydroxytetradecanoyl)glucosamine, N^2-formyl-N^1-(5-phospho-β-D-ribosyl) glycinamide and dTDP-4-amino-4,6-dideoxy-D-galactose (Figure 2D). MS^2 spectra at three collision energies, SMILES codes of predicted fragments and retention times are integrated into a .MGF file, which can be used as putative reference spectra (e.g. for spectral library search in mzMine, Supplementary Datafile 2).

CRISPRi enforces substrate accumulation as a potential buffering mechanism

To better understand which parts of the metabolic network responded to CRISPRi knockdowns, we grouped metabolites and CRISPRi target genes into 465 EcoCyc pathways (Table S11). Out of 1,332 metabolite accumulations detected by FI-MS, 182 (14%) were metabolites that are within the same pathways as the target gene (Figure 3A), which is a significant enrichment (*p*-value < 0.0001, hypergeometric test, Figure S6A).

In total, 110 accumulations are direct reactants of the enzyme targeted by CRISPRi (Figure 3A), which is also a significant enrichment (*p*-value < 0.0001, hypergeometric test, Figure S6B). Reactants had on average significantly higher log_2-fold changes compared to all other accumulating metabolites (Figure 3B). This local response of reactants is exemplified by the chorismate biosynthesis pathway. Knockdowns of AroB, AroD, AroE and AroA accumulated their direct substrate metabolites, but not upstream metabolites (Figure 3C). Only the AroC strain accumulated its substrate (5-*O*-(1-carboxyvinyl)-3-phosphoshikimate, 3psme) and one upstream metabolite (shikimate-5-phosphate, skm5p). We excluded the AroK strain from this analysis because it responded like the AroB strain due to the *aroK-aroB* operon structure and the polarity of CRISPRi. The AroD strain accumulated a downstream metabolite 3-dehydroshikimate (3dhsk), but this was due to in-source fragmentation (H_2O loss) of the AroD substrate 3-dehydroquinate (3dhq) (Figure S7).

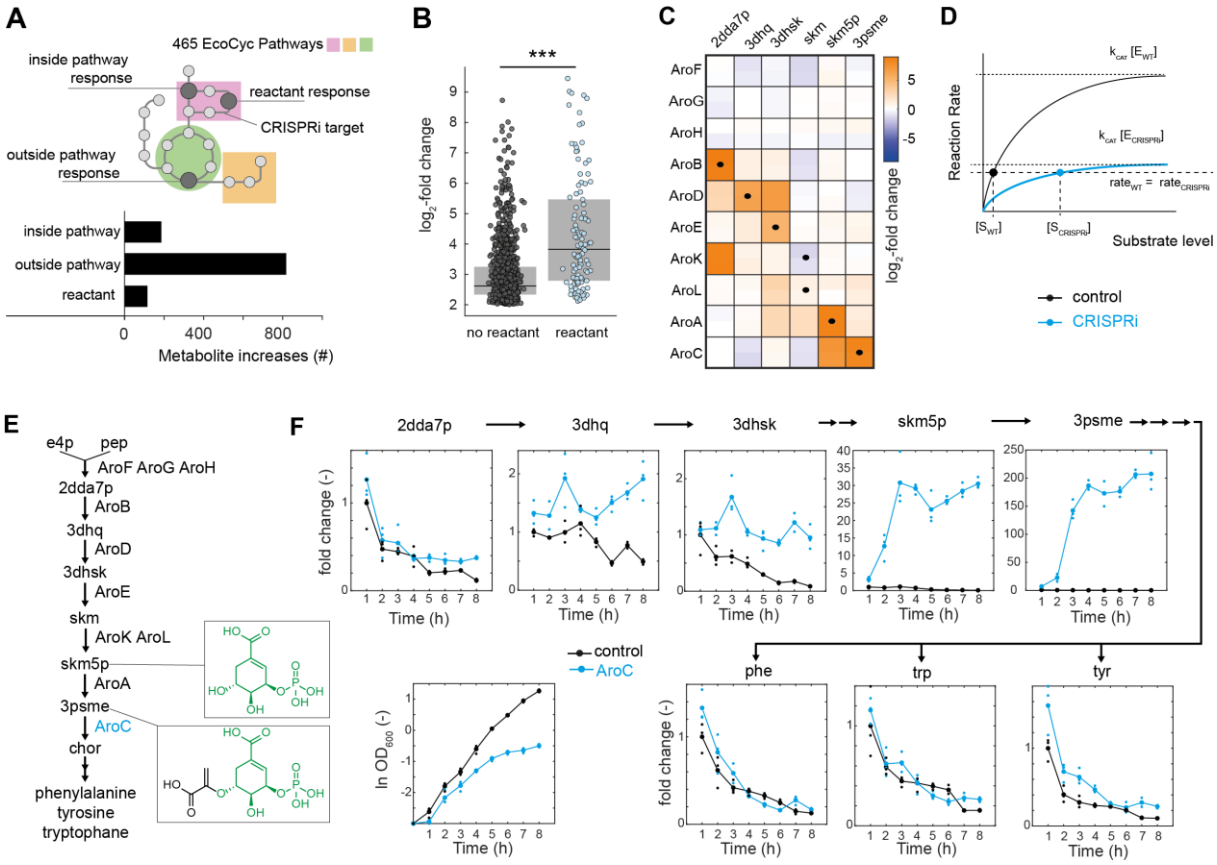

Figure 3. Substrate accumulation is a buffering mechanism of knockdowns in the chorismate pathway. (A) Number of accumulating *m/z* features in the FI-MS screen that are annotated as reactants of the CRISPRi target gene (according to *i*ML1515 model) and accumulations inside and outside the pathway targeted by CRISPRi. Subpathways from the EcoCyc database were used for the classification of metabolites (Table S12). Note that not all *i*ML1515 genes are connected to EcoCyc subpathways and are therefore not considered. **(B)** Boxplots show log_2-fold changes of all accumulating metabolites detected by FI-MS. The blue group are 110 strain-metabolites pairs, in which the accumulating metabolite is a reactant of the enzyme that is targeted by CRISPRi in the respective strain. The grey group are the remaining 1,212 strain-metabolites pairs. *** *p*-value <0.001 in *t*-test. **(C)** Log_2-fold changes of *m/z* features that are annotated to metabolites in chorismate pathway (negative mode of the FI-MS screen). Only strains targeting enzymes in the chorismate pathway are shown. Black dots indicate metabolites that are substrates of the enzyme targeted in the respective strain. Two replicates are shown per box. **(D)** Schematic of a Michaelis-Menten relationship between substrate level and reaction rate. Black is the relationship at wild-type enzyme-levels (E_{WT}). Blue is the relationship when enzyme levels decrease in a CRISPRi strain ($E_{CRISPRi}$). **(E)** Metabolites and enzymes in the chorismate pathway. **(F)** Time-course of intermediates in the chorismate pathway after induction of CRISPRi (at t = 0 h). Metabolites were measured with targeted LC-MS/MS. Intensities were normalized to OD_{600} at the time of sampling and normalized to the mean of the control strain at t = 1 h. Big dots are the mean of n = 3 replicates that are shown as smaller dots. Black is the control strain and blue the aroC strain.

We hypothesized that substrate accumulation functions as a buffering mechanism, because by increasing substrate concentrations the remaining enzyme pool operates closer to saturation (closer to v_{max}, Figure 3D). This, in turn, compensates for the lower enzyme level. If this mechanism is active, substrate accumulation should occur during the early phase of the knockdown, when growth is not yet impaired. In contrast, passive accumulation due to a bottleneck in the pathway should appear later. To test this, we examined how metabolites respond dynamically to the *aroC* knockdown. Chorismate biosynthesis intermediates were measured during an 8-hour period after CRISPRi induction with targeted LC-MS/MS^{28} and MS^2 spectra from our screen (Table S6). Consistent with the substrate buffering hypothesis, 3psme increased during the first 4 hours, when growth was not yet impaired (Figure 3F). After 4 hours, growth decreased, and 3psme accumulation stopped. Skm5p showed a similar accumulation to 3psme, thus indicating that 3psme inhibits AroA due to structural similarities with skm5p (Figure 3E). Together, these results support a buffering model, where decreasing enzyme levels immediately lead to substrate accumulation, which in turn maintains metabolic flux by operating the enzyme closer to v_{max} (Figure 3D).

In conclusion, we found that accumulation of substrate metabolites was a relatively frequent response to CRISPRi of enzymes. For the *aroC* knockdown, we show that this accumulation occurs rapidly and before growth defects, consistent with an active substrate buffering mechanism. However, most strains in our library did not show reactant accumulation, and we only demonstrate the buffering model for the AroC strain. Therefore, it remains to be tested whether this mechanism applies more broadly, and why substrates do not accumulate in other CRISPRi strains.

Crosstalk between chorismate biosynthesis and peptidoglycan recycling through 2dda7p accumulation

Having established that CRISPRi knockdowns in the chorismate pathway enforces a local accumulation of substrates (Figure 3C), we wondered if these responses lead to crosstalk with other pathways. For example, 2-dehydro-3-deoxy-arabino-heptulosonate 7-phosphate (2dda7p, the substrate of AroB) was the strongest accumulated metabolite in the AroB strain (Figure 4A). LC-MS/MS data confirmed a strong 2dda7p accumulation in the AroB strain (Figure S8A). 2dda7p also accumulated in the AroK strain due to the *aroK-aroB* operon structure and the polarity of CRISPRi. Apart from 2dda7p, in the AroB strain, we observed an accumulation of 17 unique metabolites, which participate in different pathways (Figure 4A). One of these metabolites is an intermediate in the peptidoglycan recycling pathway, *N*-acetylmuramate 6-phosphate (acmum6p), which showed a 6-fold increase in the AroB strain and accumulated even more (18-fold) in the MurQ strain, where it is the direct substrate metabolite (Figure 4B). Other metabolites in the peptidoglycan recycling pathway accumulated

in the respective CRISPRi strain (anhgm in NagZ strain, anhm in Anmk strain), demonstrating that this pathway is active (Figure 4B). Accumulation of acmum6p in the MurQ and AroB strain was confirmed by LC-MS/MS (Figure S8B), and we sought to identify the mechanism of acmum6p accumulation in the AroB strain.

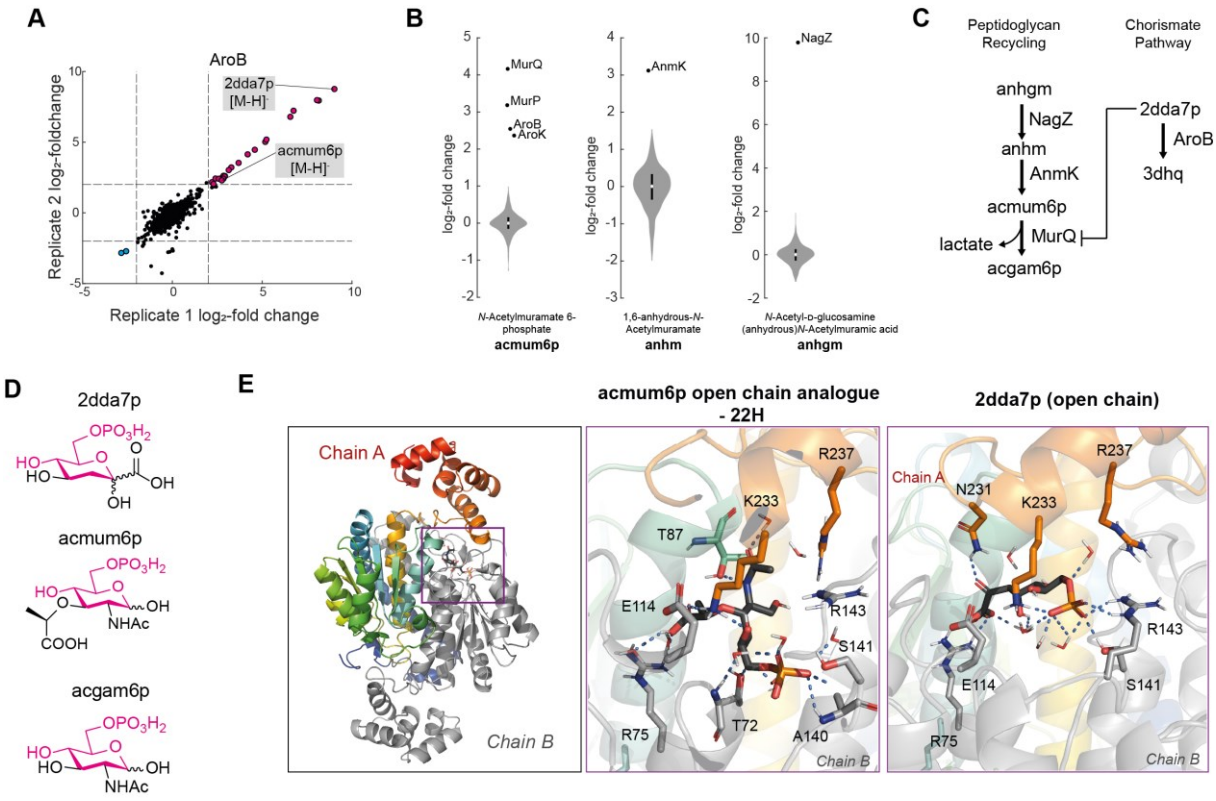

Figure 4. 2dda7p accumulation leads to regulatory crosstalk between chorismate biosynthesis and peptidoglycan recycling. (A) Log_2-fold changes of all annotated *m/z* features in the two replicates of the AroB strain. Features with log_2-fold changes >2 and <-2 in both replicates are shown in red and blue respectively. *N*-acetylmuramate 6-phosphate (acmum6p) and 2-dehydro-3-deoxy-arabino-heptulosonate-7-phosphate (2dda7p) are indicated. **(B)** Response of intermediates in peptidoglycan recycling to CRISPRi knockdowns. Log_2-fold changes were calculated from the intensities of the *m/z* features normalized to the median per sample batch. The violin plots show the distribution of acmum6p, anhm and anhgm across 1,513 CRISPRi strains (mean of n= 2 replicates for each strain). CRISPRi strains with log_2-fold change > 2 are indicated. **(C)** Peptidoglycan recycling pathway and a putative interaction with 2-dehydro-3-deoxy-arabino-heptulosonate-7-phosphate (2dda7p) in the chorismate pathway. **(D)** Structures of 2-dehydro-3-deoxy-arabino-heptulosonate 7-phosphate (2dda7p) and the MurQ substrate *N*-acetylmuramate 6-phosphate (acmum6p) and product *N*-acetyl-D-glucosamine 6-phosphate (acgam6p). **(E)** Overview of the original dimeric *E. coli* MurQ (*Ec*MurQ) model structure displaying its two chains (black box). Molecular docking showed that acmum6p and 2dda7p can bind in their closed 6-ring confirmation to MurQ, but binding of the linear structure is better (Supplemental Datafile 3). Proposed binding mode for acmum6p open chain analogue 22H[30,43] (left purple box) and 2dda7p (right purple box) retrieved relevant simulation frames as determined from hierarchical clustering of the trajectory (5x200 ns). Polar interactions are shown as dashed lines.

We hypothesized that 2dda7p inhibits MurQ (Figure 4C). In solvent, 2dda7p exists in its closed 6-ring (pyranose) conformation[29] and structurally resembles MurQ reactants (Figure 4D). To verify that 2dda7p binds to MurQ, we performed molecular docking experiments (Figure 4E, Supplementary Datafile 3). The MurQ substrate acmum6p and 2dda7p can bind in their closed 6-ring confirmation, but the binding is weak (Supplementary Datafile 3). As ring opening of the monosaccharide species is the first step of the MurQ catalyzed reaction[30], we also examined binding of the open chain structures. Indeed, open chain 2dda7p and the open chain analogue of acmum6p strongly bind to MurQ. This supports our hypothesis that 2dda7p binds to MurQ and acts as a competitive inhibitor. This would explain acmum6p accumulation in the AroB strain, although AroB is not directly connected to peptidoglycan recycling. Off-target effects of the AroB sgRNA are unlikely, given that AroK shows the same phenotype and is targeted by a different sgRNA.

In summary, 2dda7p increases in the AroB strain and probably buffers the knockdown. However, increases of 2dda7p cause regulatory crosstalk by inhibiting MurQ. This reveals a novel interaction between aromatic amino acid biosynthesis and peptidoglycan recycling. Notably, flux balance analysis with *i*ML1515 predicts that peptidoglycan recycling is inactive during exponential growth on glucose in minimal medium. Our data, however, indicates that this pathway is active and sensitive to perturbations by CRISPRi (Figure 4B), which is consistent with previous studies[31]. Similarly, in 15 other strains that target inactive genes, we found an accumulation of reactants, such as the TreF strain (trehalose degradation), the GloB strain (methylglyoxal degradation) and the UgpQ strain (glycerol phosphodiester degradation, Figure S9).

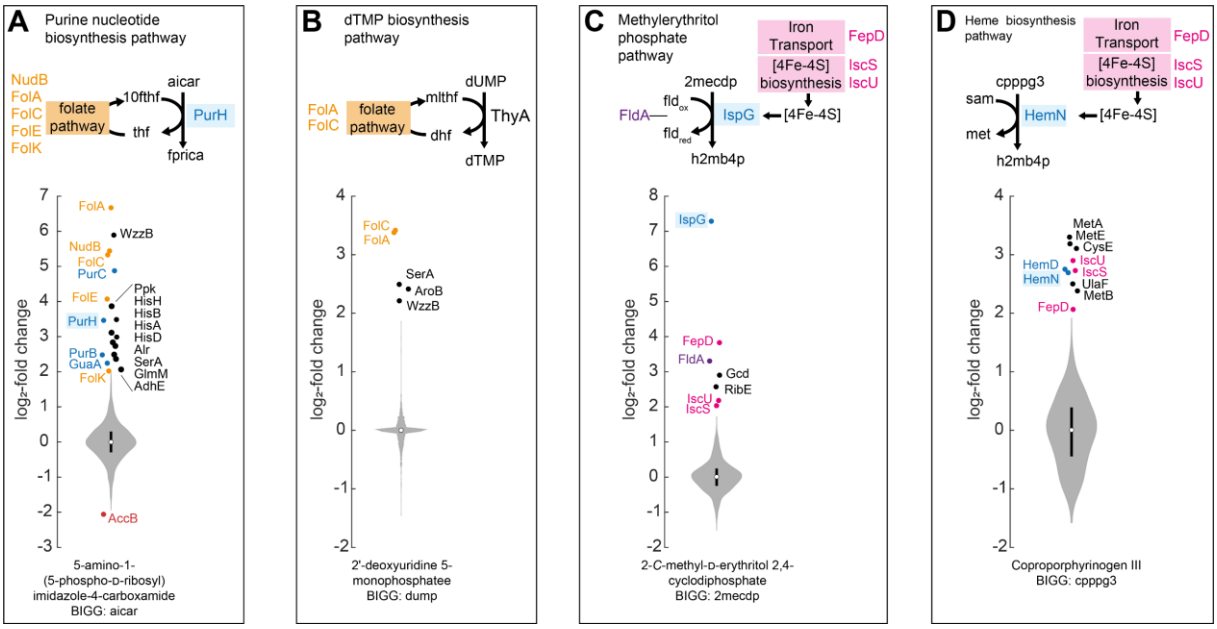

Figure 5. CRISPRi identifies the most sensitive folate-, SAM-, and Fe-S-dependent reactions. (A) Response of aicar to CRISPRi knockdowns. Log_2-fold changes were calculated from the intensities of the *m/z* features normalized to the median per sample batch. The violin plot shows the distribution of aicar across 1,513 CRISPRi strains (mean of n= 2 replicates for each strain). CRISPRi strains with log_2-fold change > 2 are shown as dots and name of the target gene. **(B)** Same as A, for dump. **(C)** Same as A, for 2mecdp. **(D)** Same as A, for cpppg3.

Cofactor Dependencies and Stoichiometric Coupling Trigger Responses in Distal Pathways

Many metabolites accumulated outside the pathway targeted by CRISPRi (Figure 3A). Such distal metabolite-gene interactions are common[17] and expected, given the interconnected structure of cellular metabolism. For example, cofactor dependencies explain why knockdowns in folate biosynthesis, especially the FolA and FolC strain, caused accumulation of 5-amino-1-(5-phospho-D-ribosyl)imidazole-4-carboxamide (aicar, Figure 5A) and deoxyuridine-phosphate (dUMP, Figure 5B). Aicar is the substrate of PurH, which requires 10-formyl-tetrahydrofolate, and dUMP is the substrate of ThyA, which depends on 5,10-methylene-tetrahydrofolate. Another class of cofactor sensitive enzymes consisted of iron–sulfur (Fe–S) cluster enzymes. In the MEP pathway, IspG and IspH both require Fe–S clusters. The IspG substrate 2C-methyl-D-erythritol 2,4-cyclodiphosphate (2mecdp) accumulated in the IspG strain (Figure 5C), but also in knockdowns of *fepD* (iron uptake) and *iscS*/*iscU* (Fe-S cluster assembly). This suggests that availability of Fe-S clusters limits IspG activity in the FepD, IcsS and IcsU strain, which leads to 2mecdp accumulation even when *ispG* itself is not targeted. Similarly, the substrate metabolite of HemN in heme biosynthesis, coproporphyrinogen III (cpppg3), accumulated in the HemN strain but also in the strains that perturb Fe-S cluster biosynthesis (FepD, IscU and IscS strain, Figure 5D). The co-substrate of HemN is *S*-adenosylmethionine (SAM), which is derived from methionine and cysteine, and therefore

perturbations in these pathways (MetA, MetE, MetB and CysE strain) led to cpppg3 accumulation. This reveals a sensitive stoichiometric coupling between methionine and cysteine biosynthesis and heme metabolism, where perturbations in methionine biosynthesis propagate to SAM dependent reactions such as heme biosynthesis. Thus, our data can functionally identify the most sensitive Fe-S cluster enzymes, SAM-dependent reactions, or folate-dependent steps.

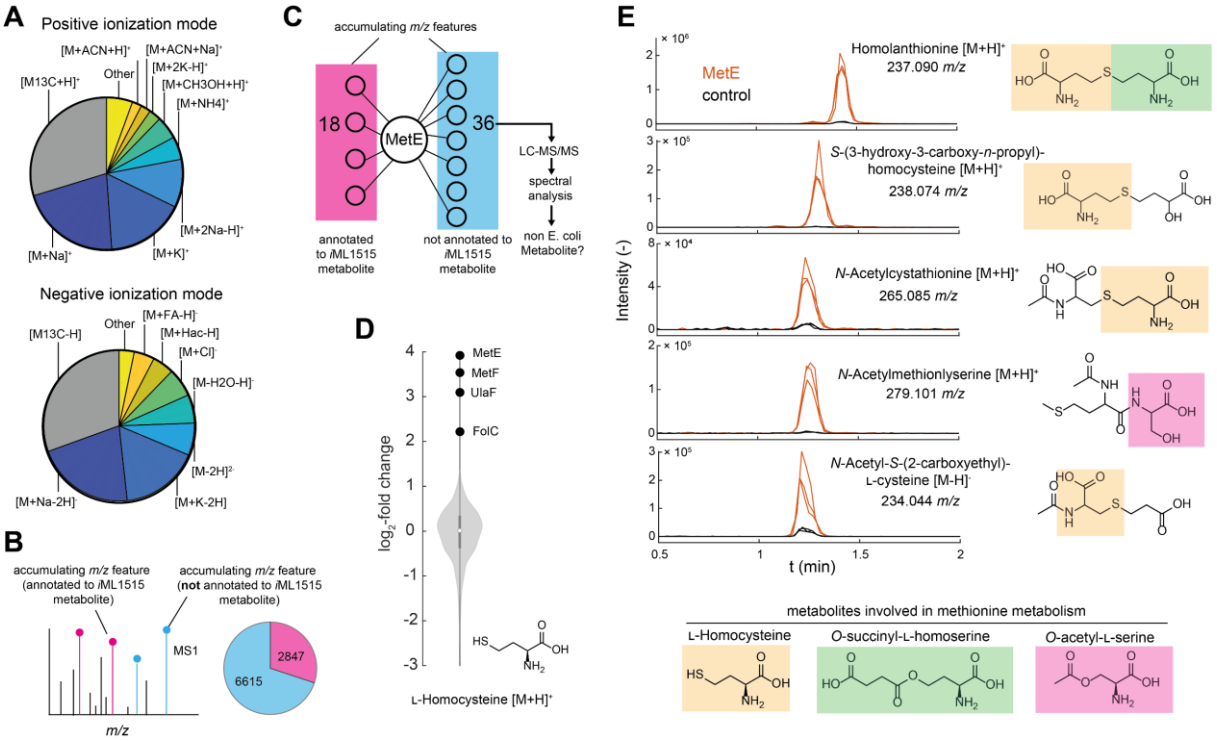

Figure 6. CRISPRi strains accumulate metabolites that are outside the *i*ML1515 model. (A) Frequency of adducts and isotopes. For all *i*ML1515 metabolites that accumulated in protonated form (positive mode) or deprotonated form (negative mode), it was assessed whether their adducts or isotopes also accumulate (*m/z* feature with $\log_2$-fold change >2). The proportion of cases where this occurs is shown as a pie chart. **(B)** 2,847 accumulating *m/z* features (across all CRISPRi strains) could be annotated to an *i*ML1515 metabolite either (de-)protonated or as an adduct or isotope shown in (A). 6,615 accumulating *m/z* features were not annotated. **(C)** Non-annotated *m/z* features in the MetE strain were analyzed by targeted LC-MS/MS. **(D)** Response of homocysteine to CRISPRi knockdowns. Log_2-fold changes were calculated from the intensities of the m/z features normalized to the median per sample batch. The violin plots show the distribution across 1,513 CRISPRi strains (mean of n= 2 replicates for each strain). CRISPRi strains with $\log_2$-fold change > 2 are indicated. **(E)** Non-annotated *m/z* features in the MetE strain and the control strain were analyzed with targeted LC-MS/MS analysis (n = 3 replicates). MS^2 spectra were analyzed with SIRIUS (Table S8). Extracted ion chromatograms (EIC) of SIRIUS predicted metabolites are shown for the MetE strain (orange) and the control strain (black).

Non-Canonical *E. coli* Metabolites Accumulate in CRISPRi Strains

So far, we focused only on accumulating *m/z* features that are annotated to *i*ML1515 metabolites. To identify *m/z* features that may originate from non-canonical *E. coli* metabolites, we first identified all *m/z* features with $\log_2$-fold change >2 in both replicates. This analysis identified 9462 cases in which *m/z* features accumulated in a CRISPRi strain (Table S7). Next, we removed features that can be annotated to *i*ML1515 metabolites and their most frequent adducts, neutral losses or ^{13}C isotopes (Figure 6A). This filtering step resulted in 6615 cases in which unannotated *m/z* features accumulate in a CRISPRi strain (Figure 6B, Table S7). Therefore, it seems likely that CRISPRi perturbations enforce increases in metabolites that are outside the *i*ML1515 model.

Next, we sought to identify the unannotated *m/z* features in the MetE strain. The MetE strain had 36 accumulating *m/z* features that could not be annotated to *i*ML1515 metabolites or their adducts, neutral losses and isotopes (Figure 6C, Table S7). To confirm accumulation and identify these *m/z* features, we used targeted LC-MS/MS. Structural prediction with SIRIUS resulted in annotations of 11 *m/z* features, including homolanthionine, *S*-(3-hydroxy-3-carboxy-n-propyl)homocysteine, *N*-acetylcystathionine, *N*-acetylmethionylserine and *N*-acetyl-*S*-(2-carboxyethyl)-L-cysteine (Figure 6 E, Table S8). None of these compounds are included in *i*ML1515 model, nor in the EcoCyc or ECMDB database, demonstrating that the MetE strain accumulates metabolites that are outside the canonical *E. coli* metabolic network.

To better understand the origin of the non-canonical *E. coli* metabolites in the MetE strain, we inspected intermediates in methionine metabolism (Figure S10A). LC-MS/MS data confirmed accumulation of known intermediates: L-homocysteine, *O*-acetyl-L-serine, and *O*-succinyl-L-homoserine (Figure S10B, Table S8). Many of the newly identified, unannotated metabolites (Figure 6E) contain substructures derived from these intermediates, suggesting they are metabolic side products formed because of accumulating methionine intermediates. For example, homolanthionine is probably produced from L-homocysteine and *O*-succinyl-L-homoserine through a promiscuous reaction of MetB (Figure S10C), which has been described in the literature[32]. The distinct retention times of methionine intermediates and the newly identified metabolites exclude artefacts from in-source fragmentation (Table S8).

These findings suggest that an excess of metabolites involved in methionine metabolism can drive spontaneous or enzyme catalyzed side reactions, resulting in the formation of metabolites outside the known *E. coli* metabolic network. This, in turn, implies that *E. coli* must maintain low concentrations of biosynthetic intermediates to suppress such unwanted side reactions.

Accumulation of Farnesyl Diphosphate in the IspB Strain Improves a Synthetic Carotenoid Pathway

Several of the accumulating metabolites identified in our screen are direct precursors of engineered biosynthetic pathways, which shows the potential of our dataset to identify metabolic engineering targets for strain optimization. An example is farnesyl diphosphate (frdp), an intermediate in isoprenoid biosynthesis and a precursor for many bioproducts, including carotenoids[33] (Figure 7A). FI-MS indicated that frdp accumulated in the IspB knockdown, which was confirmed by targeted LC-MS/MS (Figure 7B). To test whether this accumulation improves bioproduct formation in metabolically engineered strains, we introduced a synthetic carotenoid biosynthesis pathway into the IspB and control strains (Figure 7C). Carotenoid biosynthesis uses the endogenous methylerythritol phosphate (MEP) pathway of *E. coli* for frdp production. Frdp is then converted into carotenoids by heterologous carotenoid biosynthesis enzymes from *Pantoea ananatis* (*crtE*, *crtB*, *crtI*, *crtY* and *crtW*), which we expressed from a plasmid (Figure 7C). The IspB strain produced almost 4-fold more carotenoids than the control, showing that higher frdp availability improves production of carotenoids in this strain (Figure 7C). This shows, in turn, that while providing robustness of endogenous metabolism, minimal metabolites pools are a barrier to channel flux into synthetic pathways. Our metabolome data in the *i*ML1515 CRISPRi library provides a map of knockdowns that can overcome this barrier.

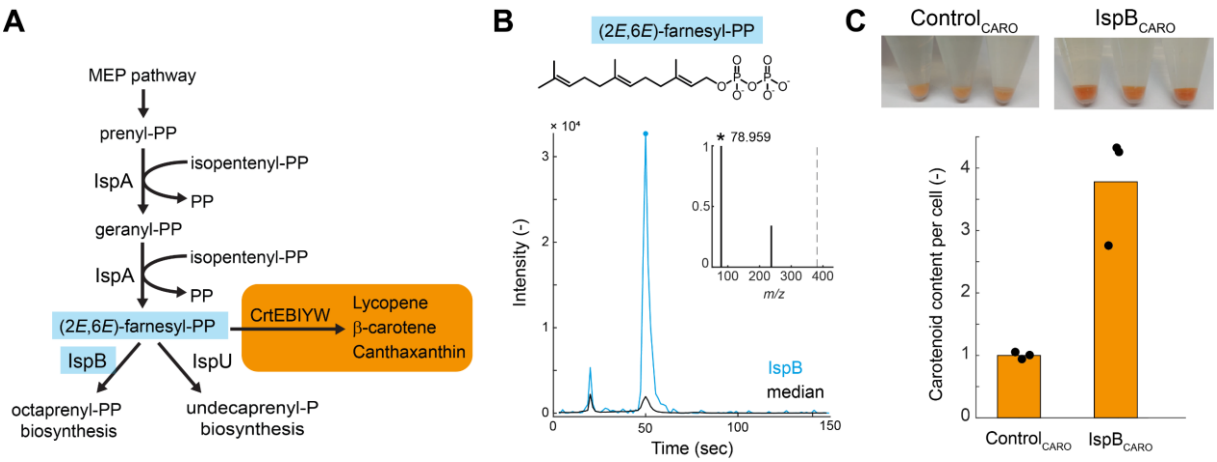

Figure 7. Accumulation of farnesyl-diphosphate in the IspB strain improves a synthetic carotenoid production pathway. (A) Enzymes and metabolites in the methylerythritol phosphate (MEP) pathway in *E. coli*. A synthetic carotenoid biosynthesis pathway from *Pantoea ananatis* (*crtE*, *crtB*, *crtI*, *crtY* and *crtW*) is shown in orange. **(B)** Targeted LC-MS/MS analysis of (2*E*,6*E*)-farnesyl diphosphate. Extracted ion chromatogram (EIC) of the 381.1237 *m/z* feature annotated as (2*E*,6*E*)-farnesyl diphosphate (frdp, $[M-H]^-$) and MS^2 spectra at collision energy 40 keV. Fragment ions predicted by CMF-ID are indicated with *. The dashed line shows the exact mass of the precursor ion. **(C)** Carotenoid production in the control strain and the IspB strain. Both strains express the operon *crtEBIYZ* from a plasmid. Pictures show cell pellets of three replicates per strain after 24 hours of cultivation. Bar plot shows carotenoid content measured by absorbance at 470 nm (dots are n= 3 replicates). Data was normalized to the mean of the control strain.

Discussion

Metabolic networks consist of several hundred metabolites and enzymes, whose concentrations are intimately interconnected. Although computational methods like metabolic control analysis provide theories of how changes in enzyme levels propagate through the metabolic network, the predictions of these methods are limited, especially at the level of metabolite pools. Metabolite pools are highly sensitive and dynamic, and current metabolic models fail to predict their response at a metabolism-wide scale. In this study, we used a metabolism-wide CRISPRi library to systematically perturb *E. coli* metabolism and measured metabolome responses with high-throughput mass spectrometry. Despite technical challenges, especially the risk of metabolite changes during sampling, our fast centrifugation method in 96-well plates and analysis by FI-MS captured robust and reproducible metabolome responses.

A relatively frequent metabolome response to CRISPRi was the local accumulation of reactants. On average, reactants accumulated more strongly than unrelated metabolites (Figure 3B), which supports the idea that reactant accumulation reflects direct functional links between enzymes and metabolites. This suggests that metabolome responses to CRISPRi perturbations may help to infer enzyme-substrate relationships and could be used to generate functional hypotheses for uncharacterized genes. This could be relevant in the context of annotating gene function in microbes that are less well characterized than *E. coli*, including the human microbiome[34].

However, despite the strong accumulation of reactants in many CRISPRi strains (Figure 3B), most strains (462) targeting genes that are active under our conditions showed no reactant accumulation. This does not imply an absence of metabolic response but rather reflects a combination of biological and technical factors. In some cases, metabolite changes remained below our 4-fold cutoff. For example, the PapC strain showed a 2-fold increase of its substrate metabolite 4-aminodeoxychorismate in both replicates (Table S4). In other cases, isoenzymes probably compensated for the knockdown, such as the ArgF and ArgI strains that are the only knockdowns in the arginine pathway without reactant increases (Figure S11). Operon structure can further prevent the accumulation of reactants. For example, responses in histidine biosynthesis are probably limited because the second reaction is catalyzed by an enzyme encoded by the last gene in the histidine operon (*hisI*). Technical limitations may also contribute, such as efficiency of CRISPRi, poor ionization efficiency of the metabolite or our extraction protocol that is biased towards polar metabolites. Finally, there could be regulatory interactions or other buffering mechanisms that prevent an accumulation of reactants in the first place.

For the AroC strain, we show that substrate accumulation is fast and occurs before fitness defects. This indicates that substrate accumulation is not a passive consequence of metabolic bottlenecks but an active compensatory response. Thus, a simple model is that decreases of enzyme levels are accompanied by increases of substrates such that the decreasing enzyme operates closer to saturation and can therefore maintain flux. This substrate buffering aligns with classical Michaelis-Menten kinetics, because enzymes operating below their K_m can significantly increase reaction rates by substrate increase. Whether all accumulating substrates in our dataset are an active buffering mechanism remains to be elucidated.

Our data also supports the hypothesis that minimal metabolite pools provide metabolic robustness by preventing product inhibition and competitive inhibition by structurally similar metabolites, which is especially important in organism without compartmentalization[6]. This inhibitory nature of metabolism has been postulated before based on interactions in databases[6] and here the metabolome supports this hypothesis. For example, in the AroB knockdown, the accumulation of its substrate 2dda7p led to inhibition of MurQ, revealing a previously unrecognized regulatory link between chorismate biosynthesis and peptidoglycan recycling. Such effects are only possible when metabolites are structurally similar and present at concentrations high enough to interfere with other enzymes. Our data provides first evidence that this is generally avoided under physiological conditions. Further, we observed that product inhibition is probably the reason for the accumulation of multiple upstream metabolites, e.g. skm5p and 3pmse in the AroC strain. Since biosynthetic pathways proceed through small structural modifications, downstream metabolites are often structurally similar to their precursors. Our data provides a systematic map of such competitive inhibitory effects.

Another consequence of high metabolite levels is the production of non-canonical metabolites through side reactions. Across all CRISPRi strains, we observed an accumulation of hundreds of *m/z* features that did not match known *E. coli* metabolites. We show for the MetE strain that structural predictions and MS^2 data can identify these compounds and that they are derivatives of the accumulating intermediates in methionine biosynthesis (Figure 7). These findings suggest that high metabolite levels can drive spontaneous or promiscuous side reactions, resulting in a chemical diversity that is beyond current metabolic reconstructions. Future studies could use such data to identify enzyme promiscuity and to expand genome-scale metabolic networks. However, since our CRISPRi library is based on genes in *i*ML1515, novel reactions can currently only be linked to existing model genes. The physiological relevance of these non-canonical metabolites or their effect on *E. coli* remains unclear, but their presence demonstrates the selective pressure to maintain low metabolite levels to avoid such side effects.

In addition to revealing such kinetic information and principles of robustness, our approach expands the number of metabolites for which experimental MS^2 spectra are available. We obtained fragmentation spectra and retention times for 175 metabolites, including 102 for which no experimental MS^2 spectrum was available in the ECMDB database. We have the highest confidence in MS^2 spectra of metabolites that are known substrates of the targeted enzymes, but we report all metabolites that passed quality control (Table S6, Supplementary Datafile 2). Because not all metabolites are available as pure standards our approach of obtaining MS^2 spectra from CRISPRi strains can improve metabolite annotations and or molecular networking[35].

Finally, we demonstrated that metabolite accumulation in CRISPRi strains can identify metabolic engineering targets. For example, knockdown of *ispB* led to accumulation of farnesyl diphosphate (frdp), a precursor for carotenoid biosynthesis. Introduction of a heterologous carotenoid pathway into the IspB strain resulted in a 4-fold increase in carotenoid production. This example illustrates how our dataset can guide the selection of metabolic engineering targets.

In conclusion, metabolome profiling of genome-scale CRISPRi libraries is not yet a routine approach, mainly because of the experimental challenge of arraying, sampling and measuring many samples. Our combination of high-throughput sampling and FI-MS allowed us to scale up this process efficiently, making screens with thousands of CRISPRi strains feasible. Future efforts could further increase throughput by mass spectrometry readable barcodes[36,37], automated culturomics[38] or MALDI imaging of colony arrays[39]. Equally important will be advances in data analysis, because even linking genes to metabolites and inferring distal interactions was a challenge in our study. Combining kinetic modeling with machine learning[40] may help to infer kinetic information and regulatory interactions from complex metabolite signatures and to predict the functionally most relevant changes in engineered microbes.

Supplementary Figures

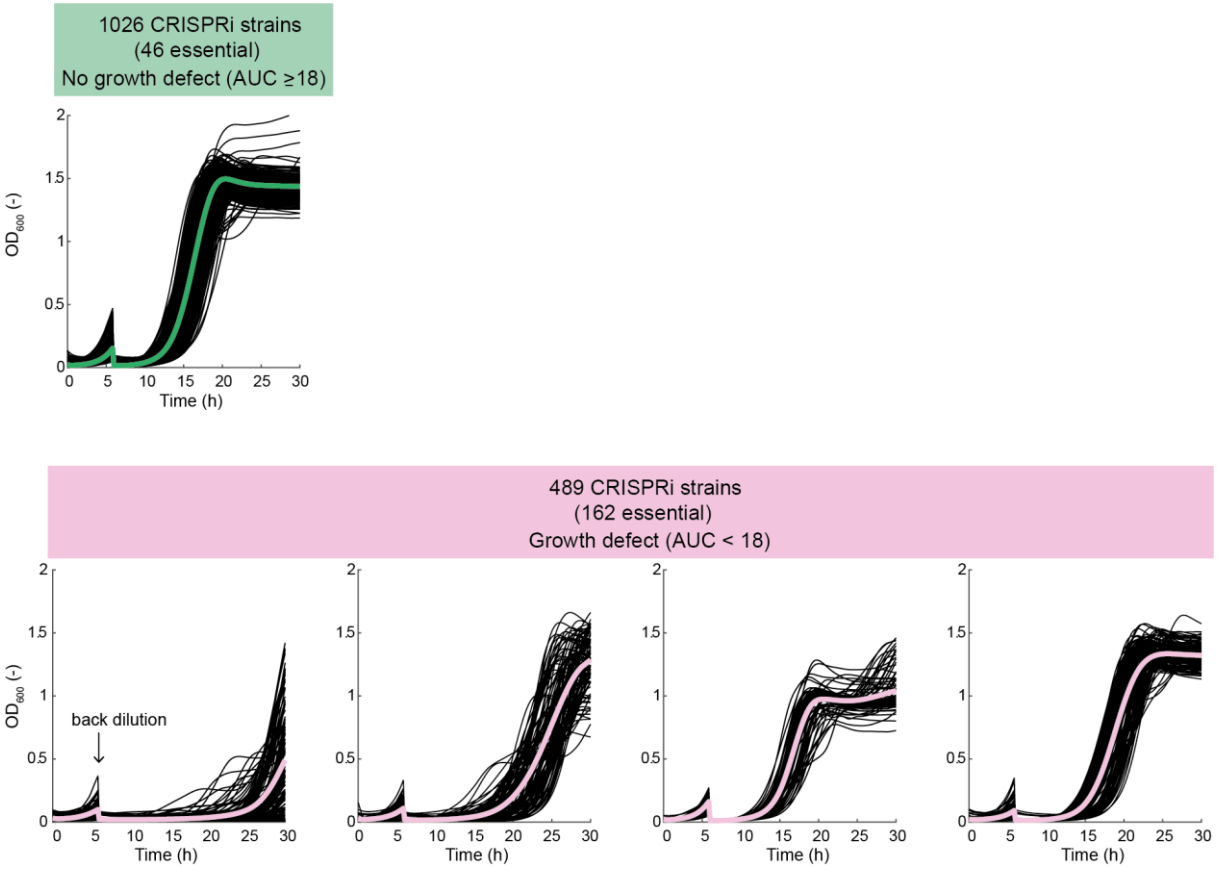

Figure S1. Growth of CRISPRi strains. Growth curves of all strains in the library were determined in plate readers. dCas9 expression was induced at t = 0 h by addition of aTc. Growth curves show means from n=3 cultures cultivated in minimal glucose medium in a plate reader. The cultures were back diluted into fresh medium at t = 6 h. The area under the curve (AUC) was used to classify CRISPRi strains with and without growth defect (AUC cutoff of 18). K-means clustering (k=4) was used to group CRISPRi strains with growth defects to improve visualization of growth patterns.

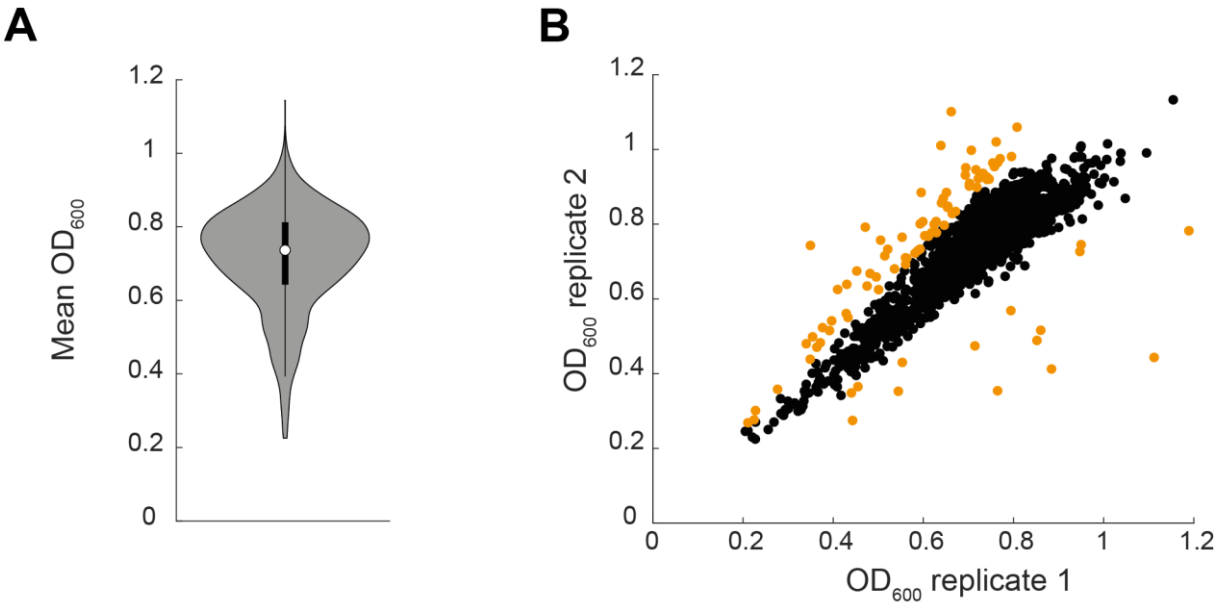

Figure S2. Sampling ODs of CRISPRi strains. Sampling ODs of 1498 CRISPRi strains and 15 control strains cultivated in n = 2 replicates. 17 CRISPRi strains of the library did not reach the required OD_{600} range at the time of sampling (6.5 hours after induction) and are not shown. **(A)** Mean sampling OD_{600} of 1,513 strains. **(B)** Optical density of replicate 1 and replicate 2 at the time of sampling. 89 strains have more than 20% error between replicates and are shown in orange.

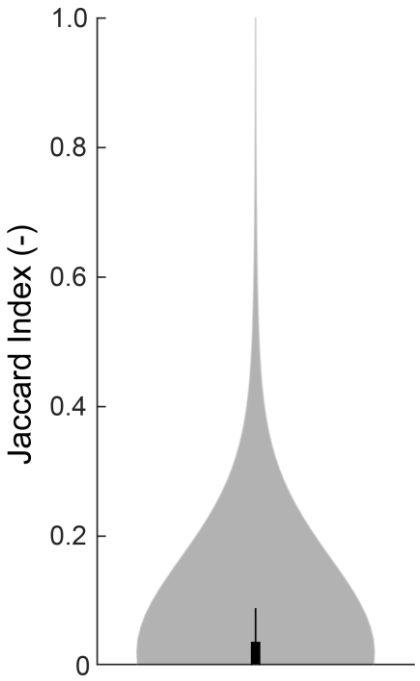

Figure S3. Similarity of metabolome responses in CRISPRi strains. Pairwise Jaccard indices were calculated based on the sets of differential metabolites in each CRISPRi strain (log_2-fold change >2 or <-2).

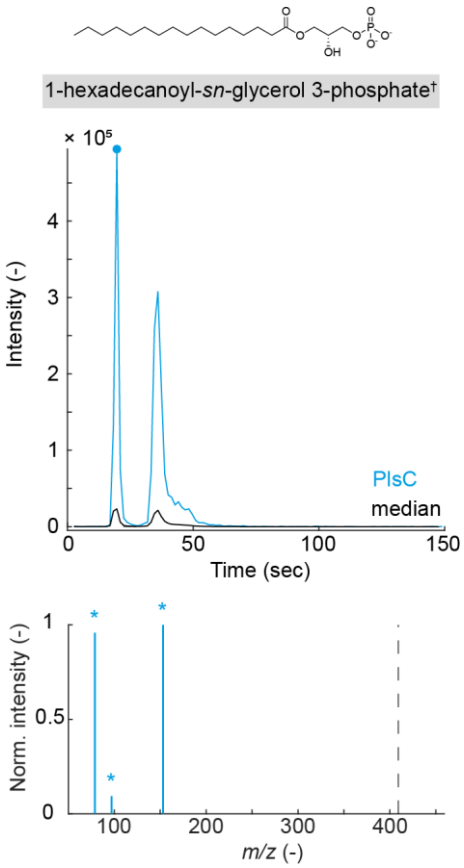

Figure S4. Accumulation of a non-polar metabolite in the plsC strain. Targeted LC-MS/MS analysis of 1-hexadecanoyl-*sn*-glycerol 3-phosphate (1hdecg3p) in the plsC strain. Extracted ion chromatograms (EIC) of *m/z* feature 409.236 annotated as 1-hexadecanoyl-*sn*-glycerol 3-phosphate ($[M-H]^-$). Blue: plsC strain, black: median EIC of all other strains. MS^2 spectrum is shown for a collision energy of 40 keV. Fragment ions predicted by CMF-ID are indicated with *. The dashed line shows the precursor ion mass. The dot in the EIC indicates where the MS^2 spectrum was extracted. †Note that 1hdecg3p has an isobaric metabolite: 2-hexadecanoyl-*sn*-glycerol 3-phosphate (2hdecg3p)).

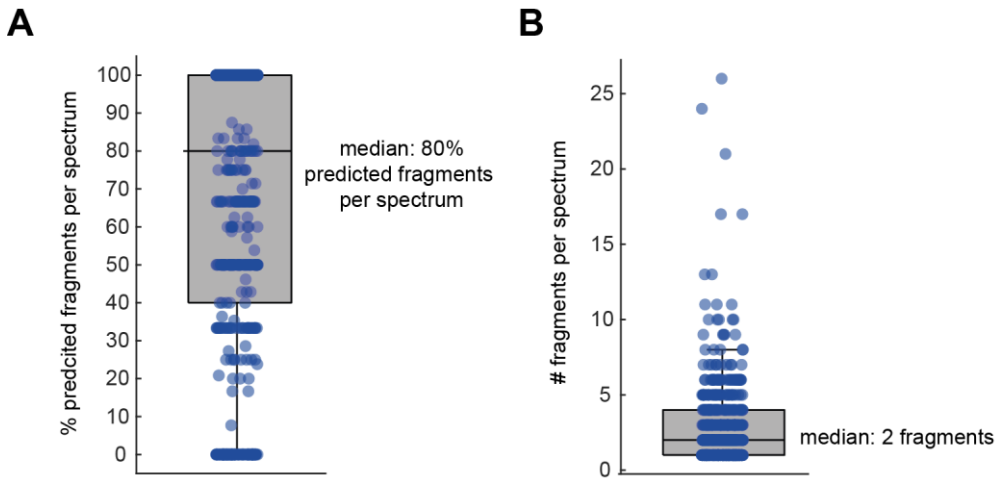

Figure S5. Analysis of MS^2 fragments in targeted LC-MS/MS measurements. Out of 1,256 targeted LC-MS/MS measurements, 569 satisfied the following criteria: precursor intensity >5000 and log_2-fold change >1, high precursor purity in MS^1 spectra and at least one fragment in the MS^2 spectra. MS^2 fragments were compared with *in silico* predictions from CFM-ID 4.0[25]**. (A)** Fraction of predicted fragments in a MS^2 spectra. As measurement was performed at three different collision energies, the collision energy with highest percentage of predicted fragments is shown. **(B)** Number of fragments in MS^2 spectra. Results for the collision energy with highest number of fragments are shown.

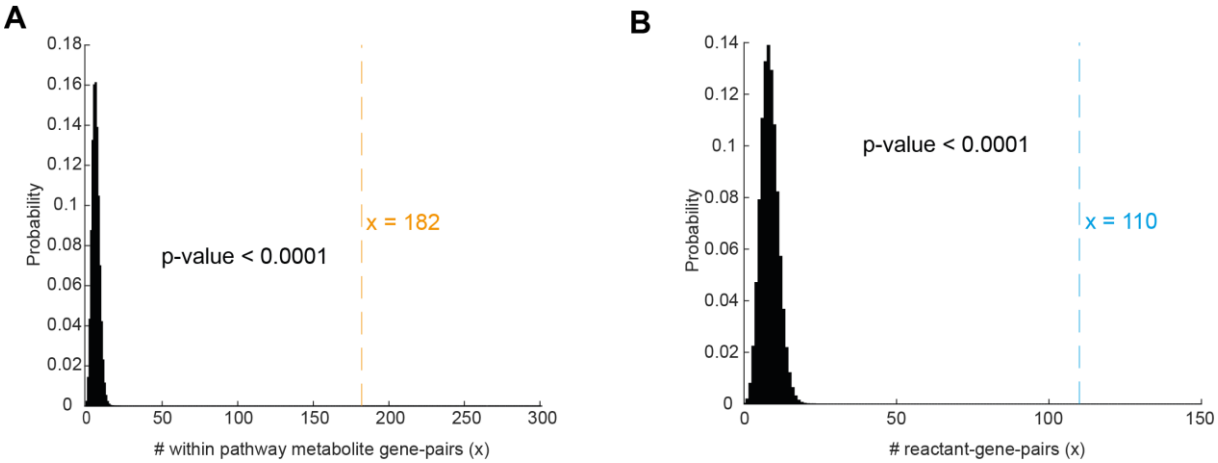

Figure S6. Enrichment analysis of accumulations in CRISPRi strains.

Black bars show the hypergeometric probability density function:

$$y = f(x \mid \mathrm{M}, \mathrm{K}, \mathrm{N}) = \frac{\binom{K}{x}\binom{M-K}{N-x}}{\binom{M}{N}}$$

(A) Enrichment of within pathway responses. M = 701750 (total number of metabolite-gene pairs: 875 genes x 802 metabolites), K= 4246 (number of all metabolite-gene pairs in EcoCyc pathways: all possible items), N = 996 (number of measurements) and x = 182 (observed "within pathway" accumulations; dashed blue line). Strains that are not included in the pathway lists from EcoCyc (Table S11) are not included in the analysis. *p*-value shows the probability to randomly pick 182 "within pathway metabolite-gene pairs". **(B)** Enrichment of reactant responses. M = 1213426 (total number of metabolite-gene pairs; 1513 genes x 802 metabolites), K= 7683 (number of all reactant-gene pairs in population), N = 1322 (number of measurements) and x = 110 (observed reactant-gene pairs; show in blue). *p*-value shows the probability to randomly pick 110 reactant-gene pairs.

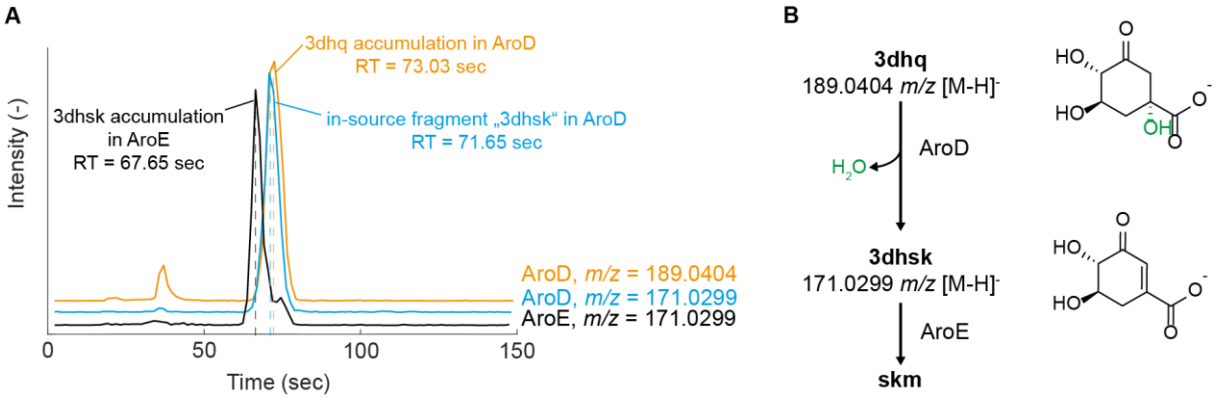

Figure S7. In-source fragmentation of 3-dehydroquinate (3dhq) confirmed by targeted LC-MS/MS measurement. (A) Extracted ion chromatogram (EIC) of *m/z* features 189.040 and 171.0299 in the AroD CRISPRi strain (orange and blue). EIC of *m/z* feature 171.0299 in the AroE CRISPRi strain (black). All metabolites are annotated in their single deprotonated form $[M-H]^-$. *m/z* feature 171.0299 in AroD is an in-source fragment of the accumulating 3-dehydroquinate (3dhq) (H_2O loss; the same as in the physiological reaction), but not 3-dehydroshikimate (3dhsk). 3dhsk accumulating in the AroE CRISPRi strain has another retention time than the in-source fragment in AroD strain. 3dhq accumulation in AroD and 3dhsk accumulation in AroE was further verified by MS^2 fragments, which matches predicted MS^2 fragments (Table S6). Dot in EIC indicates where MS^2 were extracted. **(B)** Metabolites involved in AroD and AroE catalyzed reactions.

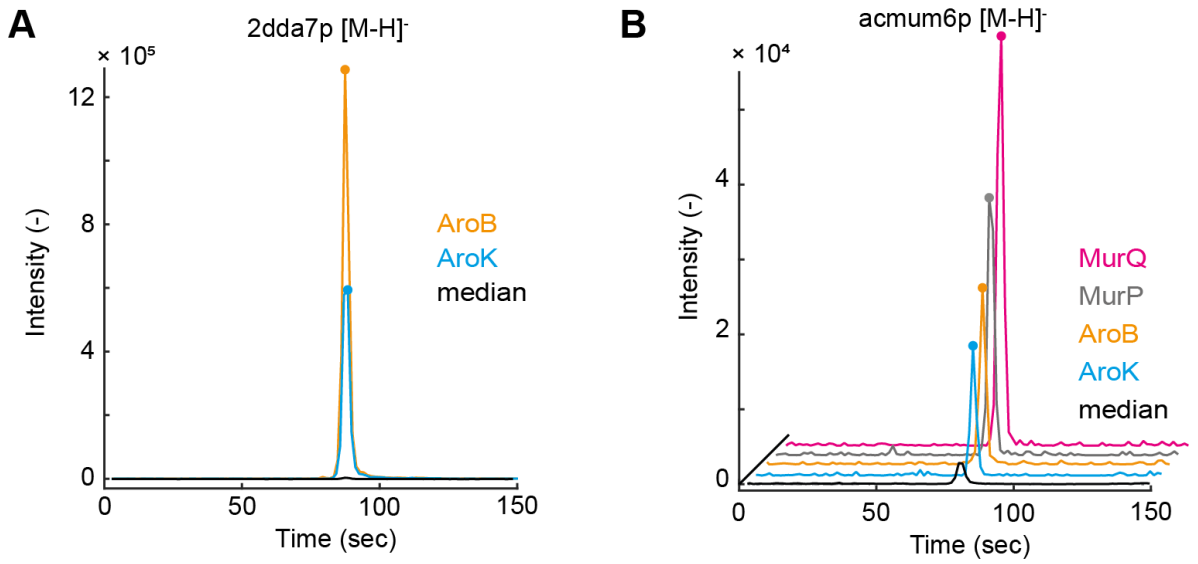

Figure S8. LC-MS/MS analysis of 2dda7p and acmum6p. (A) EIC of *m/z* feature 287.017 annotated as 2dda7p ([M-H]$^-$). 2dda7p accumulation is verified by MS^2 fragments, which matches predicted MS^2 fragments (Table S6). **(B)** The AroB, AroK, MurP and MurQ strain accumulate acmum6p. Figure shows results of targeted LC-MS/MS experiment. EIC of *m/z* feature 372.070 annotated as acmum6p ([M-H]$^-$). Acmum6p accumulation is verified by MS^2 fragments, which matches predicted MS^2 fragments (Table S6).

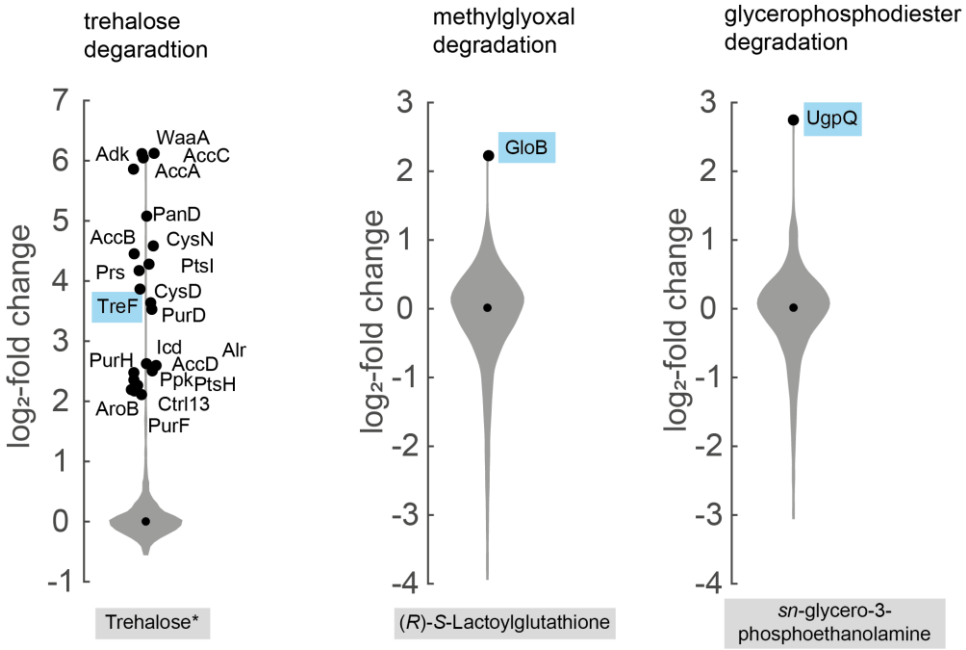

Figure S9. CRISPRi reveals active pathways, which were assigned as non-active by flux balance analysis (FBA). Examples of metabolite accumulation in CRISPRi strains targeting a gene that was assigned as inactive by FBA. Violin plots show mean log$_2$-fold change (2 replicates of each strain) of FI-MS data. Metabolite accumulation in the blue labelled strains was confirmed by LC-MS/MS data (Table S6). *Note that trehalose has isobaric metabolites: cellobiose, lactose, maltose, melibiose, sucrose.

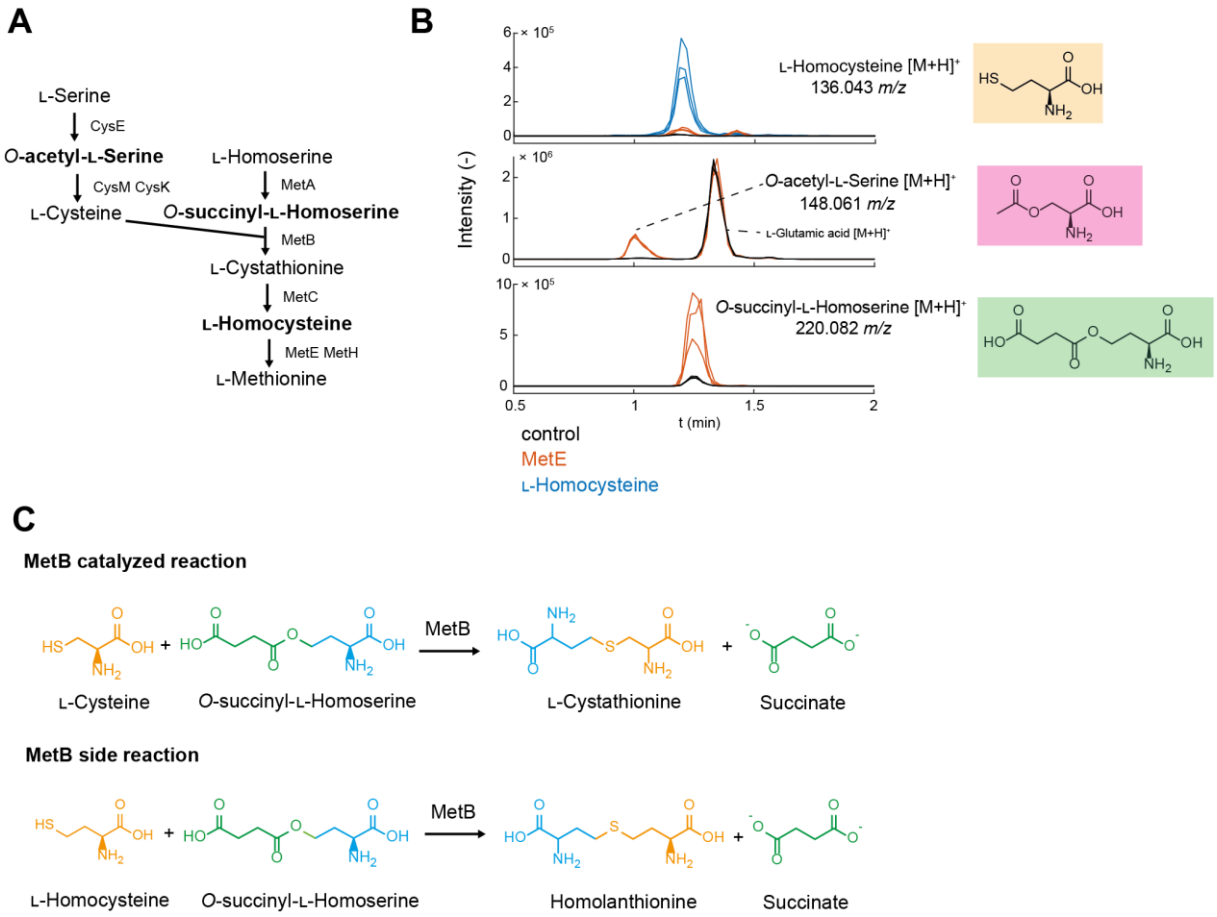

Figure S10. Accumulation of compounds related to methionine metabolism in the MetE CRISPRi strain. (A) Methionine metabolism in *E. coli*. Main enzymes and metabolites are shown. **(B)** Accumulation of selected metabolites associated with methionine metabolism in MetE. Chromatograms show EICs of respective *m/z* features of three replicates (black: control, orange: MetE, blue: L-Homocysteine standard, 10 µM in matrix). Accumulation of L-homocysteine (fold change: 5.15, compared to control), *O*-acetyl-L-serine (fold change: 26.68) and *O*-succinyl-L-homoserine (fold change: 8.6) were verified via targeted LC-MS/MS and SIRIUS predictions. L-Homocysteine accumulation was further confirmed with an authentic standard. **(C)** Reactions catalyzed by MetB. In the methionine biosynthesis, MetB catalyzes the reaction of L-cysteine and *O*-succinyl-L-homoserine to L-cystathionine and succinate. When high L-homocysteine levels are present, MetB can use L-homocysteine as a substrate leading to homolanthionine formation. In *Corynebacterium glutamicum* the k_m-value of MetB for L-homocysteine is more than 2-times higher than for L-cysteine[32].

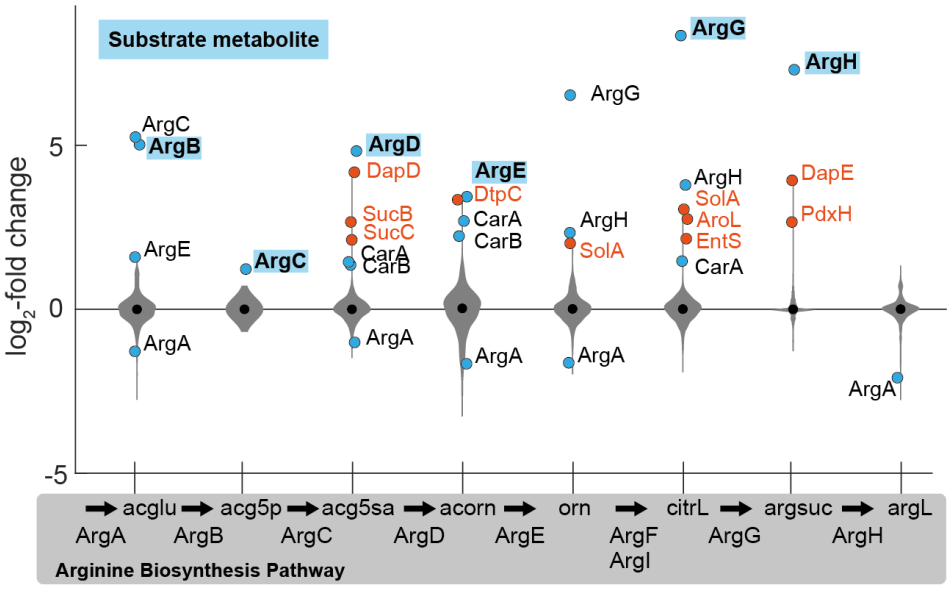

Figure S11. Response of metabolites in arginine biosynthesis to CRISPRi. Log_2-fold changes were calculated from the intensities of the *m/z* features normalized to the median per sample batch. The violin plots show the distribution of the intermediates across 1,513 CRISPRi strains (mean of n= 2 replicates for each strain). CRISPRi strains with log_2-fold change > 2 are indicated.

Material and Methods

Strains and Culture

E. coli YYdCas9 strain[41] was the wild-type strain used in this study. All strains in this study derive from the YYdCas9 strain and are listed in the Key Resources Table.

Media

Cultivations were performed with LB medium or M9 minimal medium with glucose as the sole carbon source (5 $g*L^{-1}$). M9 medium contained (per liter): 7.52 g Na_2HPO_4 $2*H_2O$, 5 g KH_2PO_4, 1.5 g $(NH_4)2_SO_4$, 0.5 g NaCl. The following components were sterilized separately and then added (per liter of final medium): 1 mL 0.1 M $CaCl_2$, 1 mL 1 M $MgSO_4$, 0.6 mL 0.1 M $FeCl_3$, 2 mL 1.4 mM thiamine-HCl and 10 mL trace salts solution. The trace salts solution contained (per liter): 180 mg $ZnSO_4$ $7*H_2O$, 120 mg $CuCl_2$ $2*H_2O$, 120 mg $MnSO_4*H_2O$, 180 mg $CoCl_2*6$ H_2O. LB, LB agar, and M9 media contained 100 $\mu g*mL^{-1}$ ampicillin (Amp). Anhydrotetracycline (aTc) was added to a final concentration of 200 nM to induce expression of the dCas9 protein in the YYdCas9 strain.

Construction of the Sorted CRISPRi Library

500 µL of a pooled CRISPRi library[18] glycerol stock was transferred into 50 mL LB medium in a 500 mL shake flask. The medium was diluted to achieve a start OD_{600} of 0.05. After three hours, the OD_{600} was measured and $1:5x10^5$ dilutions were prepared. 100 µL aliquots of the dilutions were spread on LB agar plates and incubated at 37 °C overnight. Single colonies were picked and transferred to 96-deep-well plates containing 500 µL LB medium. Plates were closed using breathe-easy foil (Diversified Biotech) and incubated for 5 h at 37 °C, 220 rotations per minute (rpm). 45 µL of 87 % glycerol were added to each well of 96-well flat-bottom plates and combined with 105 µL culture. These glycerol cryo-stock plates were closed by adhesive metal foil and stored at -80 °C. Strains were transferred from glycerol cryo-stocks to 96-deep-well plates containing 500 µL LB medium by a replicator (Deutz-System, KUHNER), closed using breathe-easy foil and incubated for 5 h at 37 °C 220 rpm. 50 µl of each plate culture were transferred to 96-well plates and sent for sequencing (Seqlab, Microsynth). Custom MATLAB scripts were used to match sequencing reads to library members.

For inclusion in the final library, the sgRNA closest to the start codon (ATG) was chosen for each gene. Missing sgRNAs were constructed individually. Strains were then transferred to 16 different 96-deep-well plates containing 500 µL of LB medium. Position A1 of each 96-deep-well plate contains the control strain. Plates were closed using breathe-easy foil and incubated for 5 h at 37 °C, 220 rpm. 45 µl of 87 % glycerol were added to each well of 96-well flat-bottom plates and combined with 105 µl of culture. These glycerol cryo-stock plates of the final library were closed by adhesive metal foil and stored at -80 °C.

Growth Analysis of Arrayed Library

Strains were transferred to 96-deep-well plates containing 500 µL LB medium by a replicator, closed using breathe-easy foil, and incubated for 5 h at 37 °C, 220 rpm. 5 µL LB pre-cultures were diluted in 495 µL M9 medium in 96-deep-well plates, closed using breathe-easy foil and incubated overnight at 37 °C with shaking at 220 rpm. M9 pre-cultures were diluted 150-fold in M9 in 96-well flat-bottom plates, which were then closed using breathe-easy foil. OD_{600} was measured every 10 min for 6 h at 37 °C, with shaking at 800 rpm, in a plate reader (LogPhase600, BioTek). Subsequently, cultures were diluted 1:50 in M9 with the inducer aTc. Plates were closed using breathe-easy foil and OD_{600} was measured every 10 min for 24 h at 37 °C and 800 rpm. Data was analyzed with custom MATLAB scripts to obtain the area under the curve using the *trapz.m* function.

Metabolome Sampling

Overnight cultures were prepared in M9 with 1.75 % glucose. 150 µL overnight culture were transferred to a 96-well flat-bottom plate. OD_{600} was measured using a plate reader (Infinite, Tecan, 5 min shaking followed by 3 min shaking with 3 intermittent reads) and the mean OD_{600} across all strains was calculated. M9 cultures were diluted to OD_{600} 0.1 in 1,050 µL M9 medium in 96-deep-well plates and incubated for 6.5 h at 37 °C, 220 rpm. For each plate 50 µL were diluted 3-fold for OD measurement in a plate reader (Infinite, Tecan). Cultures were centrifuged for 2 min at 37 °C, 3,350 rpm, supernatant was discarded, and 200 µL pre-chilled (-20 °C) 40%:40%:20% (v/v/v) methanol-acetonitrile-water extraction solution was added. Plates were sealed, incubated for 16 h at -20 °C, and subsequently centrifuged for 5 min at 4,000 rpm, -9 °C. 150 µL supernatant were transferred to a collection plate, heat sealed and stored at -80 °C until measurement.

Metabolome Screening with Flow Injection Mass Spectrometry

Samples were analyzed with FI-MS on an Agilent 6546 quadrupole time-of-flight mass spectrometer (Agilent Technologies). Electrospray ionization was performed in positive and negative ionization modes. The mobile phase consisted of 60%:40% (v/v) 2-propanol (Rotisolv ≥99.95%, Ultra LC-MS, Roth) and water buffered with 10 mM ammoniumcarbonate ($(NH_4)_2CO_3$, Sigma Aldrich) and 0.04% (v/v) ammonium hydroxide (Honeywell/Fluka TraceSELECT Ultra, 20-22%) for both ionization modes. The flow rate was 0.15 $mL*min^{-1}$. Online mass axis correction was performed with 2-propanol (from mobile phase) and HP-921 (formate adduct) in negative ionization mode and purine and HP-921 in positive ionization mode. Mass spectra were recorded in profile mode from 50 to 1700 *m/z* with a frequency of 1.4 $spectra*sec^{-1}$ for 0.5 min using 10 Ghz resolving power. Source temperature was set to 225 °C, with 11 $L*min^{-1}$ drying gas and a nebulizer pressure of 20 psi. Sheat gas Temperature was 350 °C with a flow of 10 $L*min^{-1}$. Capillary voltage was 3500 V, Noozle voltage 2000 V. Fragmentor, skimmer, and octupole voltages were set to 120 V, 65 V, and 650 V, respectively, and were based on previous studies[22].

Processing of Data from Flow Injection Mass Spectrometry

Raw files were converted into .mzXML-files by MSConvert (Version 3.0.21335-05cc7bd, [44], Settings: 64-bit, Write index, TPP compatibility). Further data processing was performed using custom MATLAB scripts (Version R2023b, The Mathworks, Inc., USA). The spectra were resampled to $2x10^6$ data points to align *m/z* values of all samples. The 32 spectra with the highest signal in the total ion count were summed up to obtain one MS^1 spectrum per measurement.

For annotation to *i*ML1515 metabolites, the *findpeaks.m* function was used to pick *m/z* features in MS^1 spectra with a peak height and prominence cutoff of 5000. Peaks were annotated to *i*ML1515 metabolites with a mass tolerance of 0.003 Da. Because FI-MS analysis cannot distinguish compounds with the same mass, all isobaric metabolites were merged resulting in 802 metabolites with unique monoisotopic masses (**Table S9**). Metabolites with a monoisotopic mass below 1000 Da were annotated in their single protonated form ($[M+H]^+$) or their deprotonated form ($[M-H]^-$). In addition, metabolites >1000 Da were additionally annotated in multiple charged states: $[M+2H]^{2+}$, $[M+3H]^{3+}$ and $[M-2H]^{2-}$, $[M-3H]^{3-}$. The intensity of the annotated *m/z* features was used to calculate fold changes relative to the median on a per batch basis (**Table S4**). Samples with missing *m/z* features were baseline imputed if at least one sample of the batch had an *m/z* feature with a peak height and prominence of at least 5000. Metabolites with log_2-fold changes >2 in both replicates were considered as

accumulating (**Table S5**). For metabolites that accumulated in negative and positive ionization mode, the polarity with the higher peak intensity was selected for further analysis.

For global analysis of all *m/z* features, the *findpeaks.m* function was used to pick *m/z* features with a peak height and prominence cutoff of 10,000. Hierarchical clustering based on Euclidean distances of *m/z* features was used for binning. For *m/z* features within a single bin, a centroid *m/z* value was calculated from averaging individual *m/z* values. The intensity of the centroided *m/z* features was used to calculate fold changes relative to the mean on a per batch basis. Centroided *m/z* features with $\log_2$-fold changes >2 in both replicates were considered as accumulating. Accumulating *m/z* features that could not be annotated to *i*ML1515 metabolites (as $[M-H]^-$, $[M^{13}C-H]^-$, $[M+Na-2H]^-$, $[M+K-2H]^-$, $[M-2H]^{2-}$, $[M-H_2O-H]^-$, $[M+Cl]^-$, $[M+Hac-H]^-$, $[M+FA-H]^-$, $[M+H]^+$, $[M^{13}C+H]^+$, $[M+Na]^+$, $[M+K]^+$, $[M+2Na-H]^+$, $[M+NH_4]^+$, $[M+CH_3OH+H]^+$, $[M+2K-H]^+$, $[M+ACN+Na]^+$, $[M+ACN+H]^+$) were considered as non-annotated metabolites that are outside the *i*ML1515 model (Table S7).

E. coli Metabolic Pathways and Reactants

Reactants (substrate or product) of all genes were extracted from the gene-protein-reaction associations from the *i*ML1515 model[9] (Table S10). Pathways of *E. coli* K-12 substr. MG1655 were extracted from the EcoCyc database (www.ecocyc.org, as of March 17, 2025)[45,46] with a customized MATLAB script (Table S11). Reactants of *i*ML1515 model were added to the genes of the pathway list from EcoCyc (Table S12).

Targeted LC-MS/MS Measurements

Accumulating metabolites in CRISPRi extracts were measured with targeted LC-MS/MS. A maximum of 10 metabolites were measured per strain (those with highest mean fold change). As precursor ion, the mass of the (de-)protonated molecule was used. Samples were analyzed with liquid chromatography time-of-flight mass spectrometry on an Agilent 6546 quadrupole time of flight (QTOF) mass spectrometer equipped with an electrospray ionization source coupled to an Agilent 1290 Infinity II Bio UHPLC. Chromatographic separation was achieved with a SeQuant® ZIC®-pHILIC column (5 µm, polymeric, 50x2.1 mm, Merck) in basic conditions with mobile phase A: H_2O + 10 mM ammoniumcarbonate (99.999%, Sigma-Aldrich) + 0.04% ammonium hydroxide (Honeywell/Fluka TraceSELECT Ultra, 20-22%) and mobile phase B: acetonitrile. The flow rate was 0.4 mL*min^{-1} and the gradient was 0 min: 10% A, 1.30 min: 60% A, 1.50 min: 60% A, 1.70 min: 10% A, 2.00 min: 10% A, 2.50 min: 10% A. 5 µL of the sample was injected. Online mass axis correction was performed with purine (119.0363/121.0509, negative/positive) and HP-921 (966.0007/922.0098, negative/positive). MS^1 and MS^2 spectra were recorded in profile mode from 50 to 1700 *m/z* with a frequency of 1.4 spectra*sec^{-1}. One MS^1 scan alternates with three MS^2 scans, where the target ion was isolated with an isolation width of 1.3 *m/z* (narrow). Fragmentation was performed at three different collision energies (10 eV, 20 eV, 40 eV) with nitrogen as collision gas. Ion source settings are the same as described for the FI-MS method.

Raw files were converted into .mzXML-files by MSConvert (Version 3.0.21335-05cc7bd[44], Settings: 64-bit, Write index, TPP compatibility). Further data processing was performed using MATLAB version R2023a (The Mathworks, Inc., USA). MS^1 scans were extracted from the data and extracted ion chromatograms (EICs) were created for all metabolites targeted within one polarity. For this purpose, the *m/z* vector of each MS^1 scan was compared with the exact *m/z*-value of the precursor ion. *m/z*-values and corresponding intensities, which differed less than Δ=0.003 Da from the theoretical *m/z*-value, were used for the EIC. If several matching *m/z*-values were found, the one with the highest intensity was used for the EIC. The three MS^2 scans that were in between the MS^1 scans with the highest and second highest intensity for the precursor ion were used to calculate the MS^2 spectrum. Ion peaks in all three MS^2 scans were picked with the *findpeaks.m* function of MATLAB (Height Filter: 400, Prominence: 400). The MS^1 scan with the highest intensity of the precursor ion was used to check precursor ion purity, mass accuracy (3 mDa) and intensity. MS^2 fragments matching the precursor *m/z* and fragments bigger than the precursor *m/z* were not considered. Normalized MS^2 fragments intensities were calculated by normalizing the peak intensity on the highest peak within a spectrum. MS^2 fragments with a normalized intensity smaller 0.05 were not considered.

Predicted Spectra

Predicted spectra were generated with CFM-ID 4.0[25]. For this purpose, the docker image was downloaded (https://hub.docker.com/r/wishartlab/cfmid, wishartlab/cfmid). To obtain SMILES code for all metabolites measured in LC-MS/MS experiments, MOL-Files were downloaded from the Kegg[47] database using a customized MATLAB script. Files were then converted into SMILES codes using the online tool ChemDB Chemoinformatics Portal Babel[48]. A text file containing all SMILES codes was then used to predict spectra with the Docker image of CFM-ID 4.0. SMILES codes of metabolites from the *i*ML1515 that do not possess a KEGG ID were manually searched (e.g. from ChEBI database[49], MetaNetX[50], EcoCyc[46]). Predicted spectra of isobaric reactants were merged and then compared to measured spectrum. Comparison of measured spectrum with predicted fragments was performed with 3 mDa tolerance.

Quantification of Intermediates in Chorismate Biosynthesis

The AroC strain and the control strain were cultivated in M9 with aTc in shake flasks (n = 3). Samples for metabolomics were collected by fast filtration[28]. Metabolite extracts were measured with a triple quadrupole mass spectrometer (Agilent TQ 6495) coupled to an Agilent 1290 Infinity II UHPLC in MRM mode. MRM transitions for intermediates of chorismate biosynthesis were obtained from targeted LC-MS/MS screen (Table S6). LC was performed with a SeQuant® ZIC®-pHILIC column (5 µm, polymeric, 50x2.1 mm, Merck) as described for targeted LC-MS/MS analysis. Amino acids were analyzed with an isotope ratio approach[28] on HILICZ column (Agilent InfinityLab Poroshell 120 HILIC-Z 2.7 µm, 2.1x150mm) with mobile phase A: 20 mM ammonium acetate pH 9.3 + 5 µM medronic acid and mobile phase B: acetonitrile, a flow rate of 0.4 mL*min^{-1} and the following gradient: 0 min 90% B, 1 min 90% B, 8 min 78% B, 12 min 60% B, 15 min 10% B, 19 min 90% B, 23 min 90% B. Column temperature was set to 15 °C and 3 µL was injected.

Identification of Non-Annotated *m/z* Features in the MetE Strain

The MetE strain was cultivated in shake flasks in triplicates and analyzed with targeted LC-MS/MS. The accumulating and non-annotated *m/z* features from the FI-MS screen were used as precursor ions (Table S7). The settings were set as described in the targeted LC-MS/MS section. For a first screen, triplicates were pooled. *m/z* features with proper chromatographic peak shape and MS^2 fragments were remeasured in triplicates. Data analysis was performed with mzMine 4.5.0[51]. EICs were extracted from mzMine with a tolerance of 0.003 Da or 20 ppm. Structure prediction was performed with SIRIUS 6.0.7[52] including CSIFingerID – Fingerprint Prediction & CANOPUS and CSI:FingerID – Structure Database Search[53,54,55,56]. The top 3 SIRIUS results per *m/z* feature are shown in Table S8.

Quantification of Carotenoid Levels

The genes *crtB*, *crtE*, *crtI*, *crtW*, *crtY* from *Pantoea ananatis* were expressed from a plasmid and transformed into the control strain and the IspB strain. Glycerol stocks of these strains were used to inoculate LB medium and incubated for 5 h at 37 °C, 220 rpm. Cultures were normalized to OD_{600} 0.05 in aTc–containing M9 medium and incubated for 24 h at 37 °C, 220 rpm. Carotenoids were quantified by centrifugation of 2 mL of each culture for 60 sec at 37 °C, 17,000 rpm. The supernatant was removed and 200 µL acetone was added for extraction. Extracts were incubated in the dark for 15 min at 55 °C with intermittent vortex steps. Extracts were centrifuged for 5 min at 37 °C, 17,000 rpm, 150 µL supernatant were transferred to a 1.5 mL reaction tube and stored at 4 °C till measurement. Extracts were diluted 5-fold in ethanol and absorbance was measured at 470 nm in a plate reader (Spark Tecan). Resulting data was normalized to the OD_{600} at the time point of sampling.

Bibliography

1. Cornish-Bowden, A. One hundred years of Michaelis–Menten kinetics. *Perspectives in Science* **4**, 3–9 (2015).
2. Reznik, E. *et al.* Genome-Scale Architecture of Small Molecule Regulatory Networks and the Fundamental Trade-Off between Regulation and Enzymatic Activity. *Cell Reports* **20**, 2666–2677 (2017).
3. Xu, Y.-F., Amador-Noguez, D., Reaves, M. L., Feng, X.-J. & Rabinowitz, J. D. Ultrasensitive regulation of anapleurosis via allosteric activation of PEP carboxylase. *Nat Chem Biol* **8**, 562–568 (2012).
4. Kacser, H., Burns, J. A., Kacser, H. & Fell, D. A. The control of flux. *Biochemical Society Transactions* **23**, 341–366 (1995).
5. Bennett, B. D. *et al.* Absolute metabolite concentrations and implied enzyme active site occupancy in *Escherichia coli*. *Nat Chem Biol* **5**, 593–599 (2009).
6. Alam, M. T. *et al.* The self-inhibitory nature of metabolic networks and its alleviation through compartmentalization. *Nat Commun* **8**, 16018 (2017).
7. de Lorenzo, V., Sekowska, A. & Danchin, A. Chemical reactivity drives spatiotemporal organisation of bacterial metabolism. *FEMS Microbiol Rev* **39**, 96–119 (2015).
8. Hartline, C. J., Schmitz, A. C., Han, Y. & Zhang, F. Dynamic control in metabolic engineering: Theories, tools, and applications. *Metabolic Engineering* **63**, 126–140 (2021).
9. Monk, J. M. *et al.* iML1515, a knowledgebase that computes *Escherichia coli* traits. *Nat Biotechnol* **35**, 904–908 (2017).
10. Gerosa, L. *et al.* Pseudo-transition Analysis Identifies the Key Regulators of Dynamic Metabolic Adaptations from Steady-State Data. *cels* **1**, 270–282 (2015).
11. Chubukov, V. *et al.* Transcriptional regulation is insufficient to explain substrate-induced flux changes in *Bacillus subtilis*. *Mol Syst Biol* **9**, 709 (2013).
12. Radoš, D., Donati, S., Lempp, M., Rapp, J. & Link, H. Homeostasis of the biosynthetic *E. coli* metabolome. *iScience* **25**, (2022).
13. Mahieu, N. G. & Patti, G. J. Systems-Level Annotation of a Metabolomics Data Set Reduces 25 000 Features to Fewer than 1000 Unique Metabolites. *Anal. Chem.* **89**, 10397–10406 (2017).
14. Wang, L. *et al.* Peak Annotation and Verification Engine for Untargeted LC–MS Metabolomics. *Anal. Chem.* **91**, 1838–1846 (2019).
15. Hartl, J. *et al.* Untargeted metabolomics links glutathione to bacterial cell cycle progression. *Nat Metab* **2**, 153–166 (2020).
16. Fendt, S.-M. *et al.* Tradeoff between enzyme and metabolite efficiency maintains metabolic homeostasis upon perturbations in enzyme capacity. *Mol Syst Biol* **6**, 356 (2010).
17. Fuhrer, T., Zampieri, M., Sévin, D. C., Sauer, U. & Zamboni, N. Genomewide landscape of gene–metabolome associations in *Escherichia coli*. *Molecular Systems Biology* **13**, 907 (2017).
18. Donati, S. *et al.* Multi-omics Analysis of CRISPRi-Knockdowns Identifies Mechanisms that Buffer Decreases of Enzymes in *E. coli* Metabolism. *Cell Systems* **12**, 56-67.e6 (2021).
19. Rachwalski, K., Tu, M. M., Madden, S. J., Hansen, D. M. & Brown, E. D. A mobile CRISPRi collection enables genetic interaction studies for the essential genes of *Escherichia coli*. 2023.04.21.537703 Preprint at https://doi.org/10.1101/2023.04.21.537703 (2023).
20. Anglada-Girotto, M. *et al.* Combining CRISPRi and metabolomics for functional annotation of compound libraries. *Nat Chem Biol* **18**, 482–491 (2022).

21. Hawkins, J. S. *et al.* Mismatch-CRISPRi Reveals the Co-varying Expression-Fitness Relationships of Essential Genes in *Escherichia coli* and *Bacillus subtilis*. *Cell Syst* **11**, 523-535.e9 (2020).
22. Fuhrer, T., Heer, D., Begemann, B. & Zamboni, N. High-throughput, accurate mass metabolome profiling of cellular extracts by flow injection-time-of-flight mass spectrometry. *Analytical Chemistry* **83**, 7074–7080 (2011).
23. Farke, N., Schramm, T., Verhülsdonk, A., Rapp, J. & Link, H. Systematic analysis of in-source modifications of primary metabolites during flow-injection time-of-flight mass spectrometry. *Analytical Biochemistry* **664**, 115036 (2023).
24. Kumar, V. *et al.* Free spermidine evokes superoxide radicals that manifest toxicity. *eLife* **11**, e77704 (2022).
25. Wang, F. *et al.* CFM-ID 4.0: More Accurate ESI-MS/MS Spectral Prediction and Compound Identification. *Anal. Chem.* **93**, 11692–11700 (2021).
26. Guo, A. C. *et al.* ECMDB: The *E. coli* Metabolome Database. *Nucleic Acids Research* **41**, D625–D630 (2013).
27. Sajed, T. *et al.* ECMDB 2.0: A richer resource for understanding the biochemistry of *E. coli*. *Nucleic Acids Research* **44**, D495–D501 (2016).
28. Guder, J. C., Schramm, T., Sander, T. & Link, H. Time-Optimized Isotope Ratio LC–MS/MS for High-Throughput Quantification of Primary Metabolites. *Anal. Chem.* **89**, 1624–1631 (2017).
29. Rath, P. *et al.* Hybrid Chemoenzymatic Synthesis of C7-Sugars for Molecular Evidence of in vivo Shikimate Pathway Inhibition. *ChemBioChem* **23**, e202200241 (2022).
30. Hadi, T., Hazra, S., Tanner, M. E. & Blanchard, J. S. Structure of MurNAc 6-Phosphate Hydrolase (MurQ) from *Haemophilus influenzae* with a Bound Inhibitor. *Biochemistry* **52**, 9358–9366 (2013).
31. Park, J. T. & Uehara, T. How Bacteria Consume Their Own Exoskeletons (Turnover and Recycling of Cell Wall Peptidoglycan). *Microbiol Mol Biol Rev* **72**, 211–227 (2008).
32. Krömer, J. O., Heinzle, E., Schröder, H. & Wittmann, C. Accumulation of Homolanthionine and Activation of a Novel Pathway for Isoleucine Biosynthesis in *Corynebacterium glutamicum* McbR Deletion Strains. *Journal of Bacteriology* **188**, 609–618 (2006).
33. Lee, S. Y. *et al.* A comprehensive metabolic map for production of bio-based chemicals. *Nat Catal* **2**, 18–33 (2019).
34. Joice, R., Yasuda, K., Shafquat, A., Morgan, X. C. & Huttenhower, C. Determining Microbial Products and Identifying Molecular Targets in the Human Microbiome. *Cell Metabolism* **20**, 731–741 (2014).
35. Nothias, L.-F. *et al.* Feature-based molecular networking in the GNPS analysis environment. *Nat Methods* **17**, 905–908 (2020).
36. Pahl, V., Lubrano, P., Petras, D. & Link, H. Intact protein barcoding enables one-shot identification of CRISPRi strains and their metabolic state. 2024.06.05.597362 Preprint at https://doi.org/10.1101/2024.06.05.597362 (2024).
37. Egloff, P. *et al.* Engineered Peptide Barcodes for In-Depth Analyses of Binding Protein Ensembles. *Nat Methods* **16**, 421–428 (2019).
38. Huang, Y. *et al.* High-throughput microbial culturomics using automation and machine learning. *Nat Biotechnol* **41**, 1424–1433 (2023).
39. Yang, J. Y. *et al.* Primer on Agar-Based Microbial Imaging Mass Spectrometry. *Journal of Bacteriology* **194**, 6023–6028 (2012).
40. Choudhury, S., Narayanan, B., Moret, M., Hatzimanikatis, V. & Miskovic, L. Generative machine learning produces kinetic models that accurately characterize intracellular metabolic states. *Nat Catal* **7**, 1086–1098 (2024).
41. Lawson, M. J. *et al.* In situ genotyping of a pooled strain library after characterizing complex phenotypes. *Molecular Systems Biology* **13**, 947 (2017).

42. Qi, L. S. *et al.* Repurposing CRISPR as an RNA-guided platform for sequence-specific control of gene expression. *Cell* **152**, 1173–1183 (2013).
43. Hazra, S. & Blanchard, J. Crystal Structure of MurQ from *H. influenzae* with bound inhibitor: 4lzj. https://doi.org/10.2210/pdb4lzj/pdb (2014).
44. Chambers, M. C. *et al.* A cross-platform toolkit for mass spectrometry and proteomics. *Nat Biotechnol* **30**, 918–920 (2012).
45. Moore, L. R. *et al.* Revisiting the y-ome of *Escherichia coli*. *Nucleic Acids Research* **52**, 12201–12207 (2024).
46. Karp, P. D. *et al.* The EcoCyc Database (2023). *EcoSal Plus* **11**, eesp-0002-2023 (2023).
47. Kanehisa, M. & Goto, S. KEGG: Kyoto Encyclopedia of Genes and Genomes. *Nucleic Acids Res.* **28**, 27–30 (2000).
48. Chen, J. H., Linstead, E., Swamidass, S. J., Wang, D. & Baldi, P. ChemDB update—full-text search and virtual chemical space. *Bioinformatics* **23**, 2348–2351 (2007).
49. Hastings, J. *et al.* ChEBI in 2016: Improved services and an expanding collection of metabolites. *Nucleic Acids Research* **44**, D1214–D1219 (2016).
50. Ganter, M., Bernard, T., Moretti, S., Stelling, J. & Pagni, M. MetaNetX.org: a website and repository for accessing, analysing and manipulating metabolic networks. *Bioinformatics* **29**, 815–816 (2013).
51. Schmid, R. *et al.* Integrative analysis of multimodal mass spectrometry data in MZmine 3. *Nat Biotechnol* **41**, 447–449 (2023).
52. Dührkop, K. *et al.* SIRIUS 4: a rapid tool for turning tandem mass spectra into metabolite structure information. *Nat Methods* **16**, 299–302 (2019).
53. Dührkop, K. *et al.* Systematic classification of unknown metabolites using high-resolution fragmentation mass spectra. *Nat Biotechnol* **39**, 462–471 (2021).
54. Djoumbou Feunang, Y. *et al.* ClassyFire: automated chemical classification with a comprehensive, computable taxonomy. *Journal of Cheminformatics* **8**, 61 (2016).
55. Kim, H. W. *et al.* NPClassifier: A Deep Neural Network-Based Structural Classification Tool for Natural Products. *J. Nat. Prod.* **84**, 2795–2807 (2021).
56. Dührkop, K., Shen, H., Meusel, M., Rousu, J. & Böcker, S. Searching molecular structure databases with tandem mass spectra using CSI:FingerID. *Proceedings of the National Academy of Sciences* **112**, 12580–12585 (2015).

Dissertation Conclusion

This dissertation describes the development and application of an arrayed CRISPRi library for functional genomics in *Escherichia coli*. The platform enables scalable, high-resolution perturbation studies under both metabolic and antibiotic stress conditions. Through the integration of CRISPRi-based gene knockdown strategies with untargeted and targeted metabolomics, transcriptomics, and proteomics, this work provides a framework for linking gene function and cellular response in bacterial systems.

Chapter 1 introduced the model organism *E. coli*, the role of antibiotics and bacterial survival strategies, the CRISPR-Cas system and its derivatives (CRISPRi and CRISPRa), and key omics approaches used throughout this work.

Chapter 2 demonstrated the successful construction and validation of an arrayed CRISPRi library derived from a pooled resource. The modular assembly and rigorous quality control yielded a high-confidence set of knockdown strains targeting the iML1515 metabolic model. This platform overcomes key limitations of pooled approaches by enabling the individual tracking and phenotyping of strains, which in turn allows direct follow-up with transcriptomic, proteomic, or metabolomic analysis.

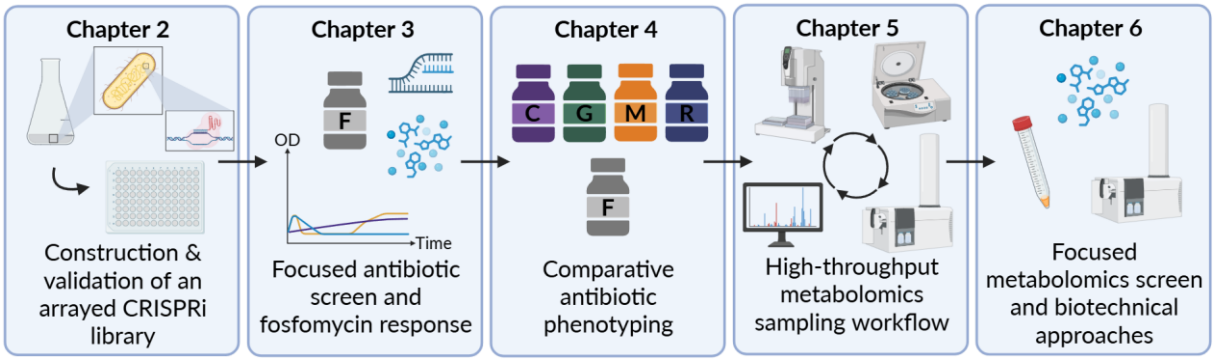

Figure 1. Overview of the dissertation workflow and key focus areas across Chapters 2-6. Chapter 2: Construction and validation of an arrayed CRISPR interference (CRISPRi) library covering the *E. coli* iML1515 metabolic model. **Chapter 3:** Antibiotic screening with a focus on fosfomycin (F), integrating growth dynamics with metabolomic and transcriptomic profiling. **Chapter 4:** Comparative phenotyping under multiple antibiotics - ciprofloxacin (C), gentamicin (G), meropenem (M), rifampicin (R), and fosfomycin (F) - to identify shared and drug-specific mechanisms of tolerance, resistance, and susceptibility. **Chapter 5:** Development of a high-throughput sampling workflow for metabolomics analysis in arrayed formats. **Chapter 6:** Application of the library in a focused metabolomics screen combined with biotechnical approaches.

In **Chapter 3**, the library was used to investigate how metabolic gene knockdowns influence bacterial responses to antibiotic stress, with a focus on fosfomycin. By combining metabolomic and transcriptomic profiling, specific gene targets, particularly *atpH* and *pykF*, were found to alter susceptibility phenotypes, pointing to a mechanistic connection between core metabolism and antibiotic responses. A visual overview of the workflow and major contributions across all chapters involving data generation is shown in Figure 1, serving as a closing summary of this dissertation.

Chapter 4 extended the antibiotic screen to include four additional clinically relevant compounds, enabling comparison of drugs with distinct cellular targets. This revealed shared as well as compound-specific tolerance mechanisms, including novel roles for metabolic slowdown, membrane stress responses, and redox regulation in non-inherited antibiotic survival. The arrayed format allowed for detailed phenotypic dissection beyond traditional growth inhibition, capturing regrowth dynamics, susceptibility, and metabolic adaptation.

Chapter 5 introduced a high-throughput sampling protocol optimized for metabolomics applications, tailored specifically to arrayed formats. The workflow allows for reproducible, scalable extraction of metabolites under defined culture conditions, overcoming a key limitation in metabolome-wide screens.

Chapter 6 applied the arrayed CRISPRi library in a genome-wide untargeted metabolomics screen to map the metabolic consequences of gene repression. The results revealed metabolite accumulation profiles linked to both annotated and unmodeled metabolic reactions, showing evidence of metabolic buffering, pathway crosstalk, and potential engineering opportunities. Follow-up experiments on these engineering targets were conducted, further validating the observed metabolic phenotypes. The integration of targeted MS/MS data further extended the resolution of phenotype mapping.

In sum, this work provides both a validated experimental resource and a framework for high-resolution studies of bacterial gene function. The CRISPRi library, in combination with robust omics pipelines, offers a versatile platform for system-level interrogation of metabolic and stress responses in *E. coli*. The insights gained here not only advance our understanding of bacterial physiology but also support the rational design of metabolic interventions and combinatorial antimicrobial strategies.

List of Publications

Schramm, T.; Lubrano, P.; Pahl, V.; Stadelmann, A.; **Verhülsdonk, A.**; Link, H. Mapping Temperature-sensitive Mutations at a Genome Scale to Engineer Growth Switches in Escherichia Coli. *Molecular Systems Biology* **2023**, *19* (10), e11596. https://doi.org/10.15252/msb.202311596.

Farke, N.; Schramm, T.; **Verhülsdonk, A.**; Rapp, J.; Link, H. Systematic Analysis of In-Source Modifications of Primary Metabolites during Flow-Injection Time-of-Flight Mass Spectrometry. Analytical Biochemistry 2023, 664, 115036. https://doi.org/10.1016/j.ab.2023.115036.

Rapp, J.; **Verhülsdonk, A.**; Garcke, A.; Stadelmann, A.; Farke, N.; Trossmann, F.; Kronenberger, T.; Alverado, A.; Petras, D.; Link, H. Metabolite accumulation in CRISPRi strains identifies principles of metabolic robustness and targets for engineering. Manuscript submitted to Cell Systems in August 2025.

Verhülsdonk, A.; Stadelmann, A.; Rapp, J.; Straub, D.; Link, H. CRISPR interference identifies metabolic genes that reduce susceptibility of *E. coli* to fosfomycin. Manuscript submitted to ACS Infectious Diseases in July 2025.